CHEMICAL REVIEWS

pubs.acs.org/CR Review

Design Rules for Obtaining Narrow Luminescence from Semiconductors Made in Solution

Published as part of the Chemical Reviews virtual special issue "Emerging Materials for Optoelectronics".

Hao A. Nguyen, Grant Dixon, Florence Y. Dou, Shaun Gallagher, Stephen Gibbs, Dylan M. Ladd, Emanuele Marino, Justin C. Ondry, James P. Shanahan, Eugenia S. Vasileiadou, Stephen Barlow, Daniel R. Gamelin, David S. Ginger, David M. Jonas, Mercouri G. Kanatzidis, Seth R. Marder, Daniel Morton, Christopher B. Murray, Jonathan S. Owen, Dmitri V. Talapin, Michael F. Toney, and Brandi M. Cossairt*

Cite This: https://doi.org/10.1021/acs.chemrev.3c00097 Read Online

ACCESS | Metrics & More | Article Recommendations

ABSTRACT: Solution-processed semiconductors are in demand for present and next-generation optoelectronic technologies ranging from displays to quantum light sources because of their scalability and ease of integration into devices with diverse form factors. One of the central requirements for semiconductors used in these applications is a narrow photoluminescence (PL) line width. Narrow emission line widths are needed to ensure both color and single-photon purity, raising the question of what design rules are needed to obtain narrow emission from semiconductors made in solution. In this review, we first examine the requirements for colloidal emitters for a variety of applications including light-emitting diodes, photodetectors, lasers, and quantum information science. Next, we will delve into the sources of spectral broadening, including "homogeneous" broadening from dynamical broadening mechanisms in single-particle spectra, heterogeneous broadening from static structural differences in ensemble spectra, and spectral diffusion. Then, we compare the current state of the art in terms of emission line width for a variety of colloidal materials including II–VI quantum dots (QDs) and nanoplatelets, III–V QDs, alloyed QDs, metal–halide perovskites including nanocrystals and 2D structures, doped nanocrystals, and, finally, as a point of comparison, organic molecules. We end with some conclusions and connections, including an outline of promising paths forward.

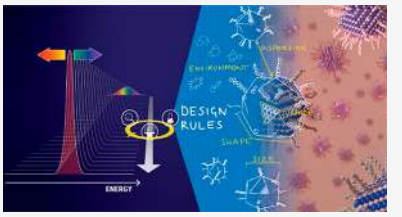

CONTENTS

Received: February 14, 2023

1. INTRODUCTION

Luminescent materials that can be made and processed in the solution phase are in demand for a range of present and next-generation optoelectronic technologies because of their scalability and ease of integration into devices with diverse form factors. Among these, colloidal semiconductors, i.e., dispersions made in solution of nanocrystals of the same inorganic materials that are semiconductors in the bulk, stand out as effective and proven solutions in many applications (Figure 1). We should note that the terms colloidal semiconductor, nanocrystal (or nanoparticle), and quantum dot (QD) have different origins and different connotations for different communities. However, in today's literature they have become practically synonymous and are generally used interchangeably. Rather than fight what has become almost colloquial usage for these terms, we too will use them interchangeably throughout this review. These terms are distinct from semiconductors grown in solution which may not necessarily form stable colloids of the final material. In this review, we will discuss both colloidal semiconductor nanocrystals and emerging semiconductor materials which can be grown in solution. Over the past 40 years, colloidal semiconductors have been used in a range of optoelectronic technologies, including light-emitting diodes (LEDs),[1,2] solar cells,[3,4] photodiodes,[5] photoconductors,[6,7] and field-effect transistors,[8] as well as for in vivo and in vitro imaging and sensing.[9,10] Some early commercial applications of emissive colloidal semiconductors were as remote phosphors for the backlighting of liquid-crystal and LED displays[11−13] and visible and near-infrared optical downconverters for inorganic and organic solid-state lighting sources.[1,14] While these applications are expected to continue to grow and develop in the coming years, new technology opportunities are on the horizon. These include electrically driven LEDs and lasers[1,2,15,16] and single-photon sources for optical quantum information platforms and related quantum technologies.[14,16−19]

All of these applications require narrow photoluminescence (PL) line widths to ensure both color and single-photon purity, raising the question of how to design narrow-emitting semiconductor materials that can be made in solution. Early efforts focused on controlling the ensemble-size heterogeneity of colloidal emitters, but it has become increasing clear that as technologies push us to the limit of requiring total line widths limited by the Fourier transform of the purely radiative decay of the single-exciton state, important sources of broadening come from a myriad of other sources, including other sources of static heterogeneous broadening related to composition, surfaces and interfaces, dynamic "homogeneous" broadening from fine-structure and exciton−phonon interactions that occur for a single dot but can vary from dot to dot, spectral diffusion, and environmental factors.

In this review, we first discuss the requirements for colloidal emitters for a variety of applications including displays, LEDs, photodetectors, lasers, and quantum information. We then discuss the mechanisms that place lower limits on achievable line widths: "homogeneous" broadening from dynamical broadening of single-dot spectra, static heterogeneous broadening in ensemble spectra, and spectral diffusion. We then survey emission line widths for different material classes: II−VI QDs and nanoplatelets, III−V QDs, alloyed QDs, colloidal metal−halide perovskites including nanocrystals and 2D structures, and doped nanocrystals. We also briefly survey the line widths achievable using organic molecules as a point of reference and critical comparison. Finally, we summarize the previous detailed sections, offer conclusions and connections, and suggest worthwhile avenues for future work.

2. REQUIREMENTS FOR COLLOIDAL EMITTERS BY APPLICATION

To motivate this review, we start by exploring the requirements for luminescent semiconductors made in solution by application. Given our focus on optoelectronics, we will highlight requirements in four primary technology areas, including displays and LED, photodetectors, lasers, and quantum information.

2.1. Displays and Light-Emitting Diodes

Current light-emitting technologies have limitations,[20] which in turn provide unique opportunities for improvement across a range of structural (i.e., solution, size, etc.), operational (i.e., stability, brightness, efficiency), and spectral (i.e., line width, spectral purity) parameters.[13,14,21−23] Colloidal QDs have emerged over the last 25 years as promising materials for overcoming several of these issues.[14] While QDs possess several desirable properties for emissive applications (high photoluminescence quantum yield (PLQY), solution processability, small size, high photostability), their tunable emission wavelengths across the visible spectrum and narrow emission line widths are fueling the pursuit of QD emitters for next-generation, ultrahigh-resolution wide color gamut displays.[24,25]

Emissive devices that possess a wide color gamut can represent real objects accurately in terms of color. Several standards have been introduced to define how a display renders the color spectrum to meet a benchmark of interest. These standards are quantified on Commission International de l'Eclairage (CIE) color space, which graphs the color gamut in terms of the hue and saturation of each emitter.[26] The space within the coordinate triangle defined by a set of red, green, and blue vertices represents the range of human-visible (trichromat) colors that can be recreated by a given light source (Figure 2).

Relevant gamut standards for this discussion are NTSC (National Television Standard Committee), Rec.709 for high-definition TV's and Rec2020 for ultrahigh-definition TV's (UHDTVs). The highest standard to date, Rec2020, represents the color gamut capable of reproducing the entire range of colors

https://doi.org/10.1021/acs.chemrev.3c00097
Chem. Rev. XXXX, XXX, XXX−XXX

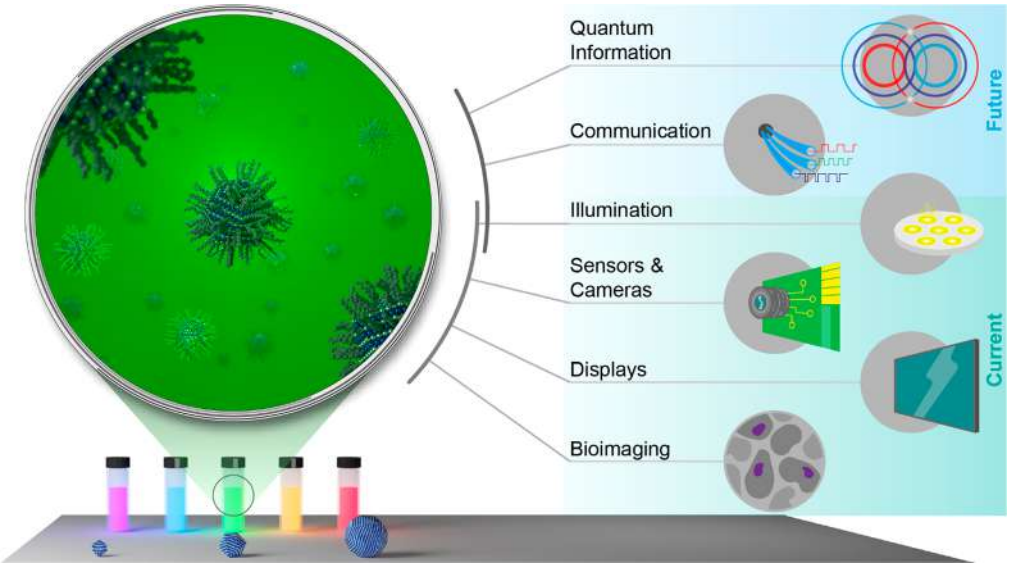

Figure 1. Present and potential future applications of luminescent solution-processed semiconductors.

that human eyes can detect in nature (i.e., the triangle vertices are defined by RGB monochromatic laser light), and encompasses all other existing gamut standards.[13,25,27,28] One of the greatest hurdles to overcome in LED and display technology is the spectral purity required to realize next-generation wide color gamut displays that meet the Rec2020 ultrahigh definition color gamut standard.[1,13,26−30]

Most current display technology relies on passive PL, which means it relies on the downconversion of high-energy blue light to produce an image. A classic example of this system is an LCD display where a broadly emitting yellow cerium-doped yttrium aluminum garnet (Ce:YAG) phosphor is pumped by an InGaN blue LED backlight to generate a visible spectrum. This light is then modulated by a liquid-crystal and color-filter array to generate an image. Because color gamut coverage is dictated by the hue (wavelength) and saturation (line width) of the red, green, and blue emitters that produce the image, the broad emission of the Ce:YAG phosphor and requisite color filtering results in subpar color gamut coverage (~70% NTSC) and decreased operating efficiencies.[31]

The narrow emission line widths of semiconductor QDs impart a competitive advantage to these technologies for generating highly color-pure and realistic displays.[1,23,27,30] When the traditional Ce:YAG phosphors in LCD displays are replaced with traditional red and green inorganic phosphors (fwhm ≈ 40−65 nm), gamut coverage can be increased to ~80% NTSC.[24] However, when spectrally pure QDs are employed as phosphors in so-called "photoenhanced" QD-LCDs (Figure 3, top), gamut coverage can be extended to over 95% of the Rec2020 gamut.[28] Tuning the R/G emission to match the color filters (i.e., not producing light that will be filtered out) also leads to improvements in energy efficiency and brightness over traditional LCD displays.[23] However, this type of display is transmissive; that is, it relies on filtering out roughly two-thirds of the transmitted light to generate the image, and as such is inherently less efficient than their emissive counterparts.[29]

QDs are also used as color converters (Figure 3, middle) to make photoluminescent LCD displays. In these systems, a QD film replaces the color filter component of LCD displays. Images are generated via the modulation of blue light from an LED backlight by the liquid crystal through red and green subpixels,

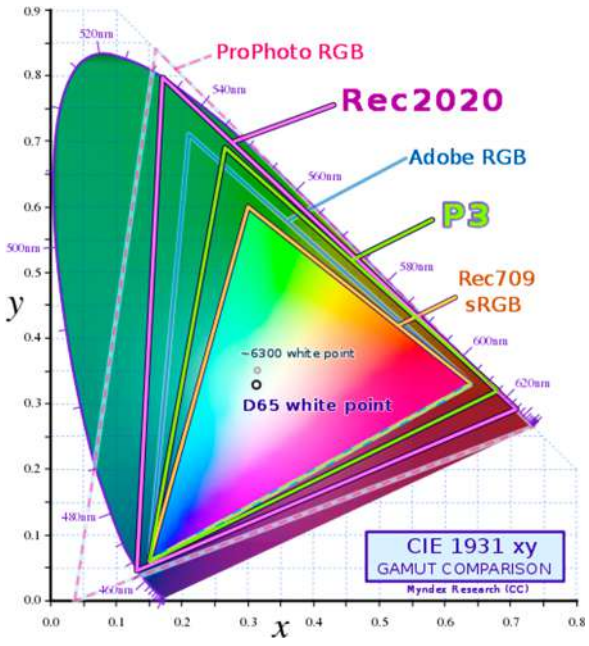

Figure 2. CIE chromaticity diagram used to quantify the quality of color for display technologies. In all cases, three primary colors (red, green, and blue) are mixed to obtain entire color palette. The Rec2020 color standard is shown in by the pink triangle. This image was reproduced from Wikimedia Commons, https://commons.wikimedia.org/wiki/File:CIE1931xy_gamut_comparison_of_sRGB_P3_Rec2020.svg.

which downconvert the light. This system allows each pixel on the screen to be individually modulated and produce only the wavelengths generated by the LED and red/green QDs, thus providing a color saturation advantage over transmissive displays.[23] The absence of color filters results in an increase in light throughput—an advantage over the high-loss color filter LCDs. Photoluminescent displays offer numerous advantages over transmissive displays, such as a wider viewing angle, better contrast, much improved efficiency, and plug-and-play compatibility with existing LCD and OLED technologies.[23,29,31]

The next frontier of QD display technologies and indeed the domain where they can truly exhibit all their advantages is in

https://doi.org/10.1021/acs.chemrev.3c00097
Chem. Rev. XXXX, XXX, XXX−XXX

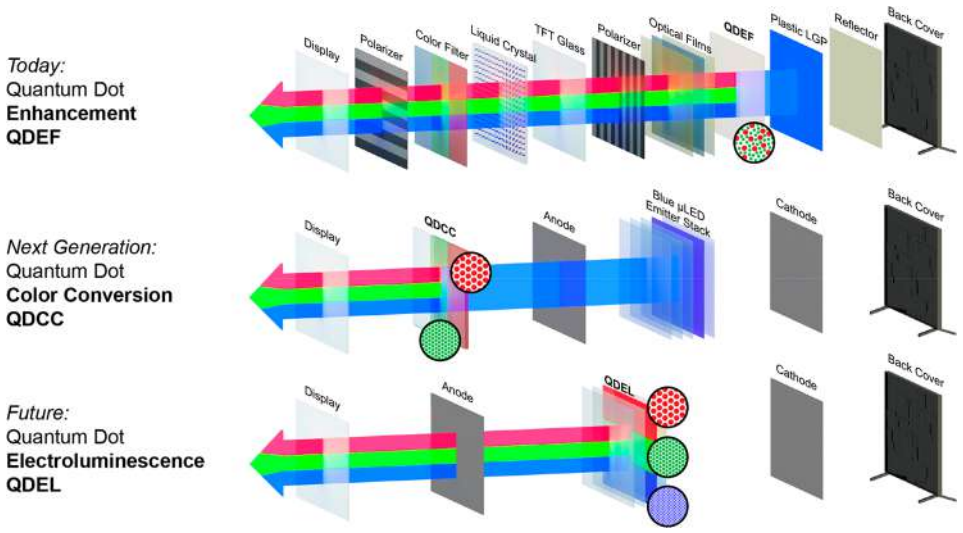

Figure 3. Diagram showing the development of QD displays from QD enhancement films to color conversion and beyond to electroluminescent implementations.

electroluminescent (EL) QD-LED displays (Figure 3, bottom). Contrary to downconverting photoluminescent displays, EL displays rely on the direct conversion of electricity to light. In other words, the all-blue LED backlight is rendered unnecessary, and the display is produced by an electrically driven circuit of QLEDs containing separate red, green, and blue emitters. The switch to an EL system requires efficient and balanced charge transport from the electron- and hole-injection layers as well as additional characterization metrics that consider the relationship of current density to emission characteristics, such as quantum efficiency, turn-on voltage, brightness, and lifetime.

Today's state-of-the-art EL displays are dominated by organic LEDs (OLEDs), which, despite their successful commercialization for some display applications, particularly in mobile phones and wearable devices, suffer from some limitations that reduce their desirability as emissive materials. Although organic molecules can exhibit narrow luminescence line widths (tens of nanometers, see section 4.4), those of materials used in many commercial OLEDs (fwhm ≈ 100 nm) do not currently compete with state-of-the-art inorganic emitters (fwhm ≈ 20−30 nm), and the devices generally exhibit slower response times (milliseconds in OLEDs vs nanoseconds in QLEDs) due to lower carrier mobilities and are more sensitive to operating temperature. Devices based on conventional fluorescent emitters also suffer from potential inefficiencies stemming from the spin statistics of electroluminescence, resulting in the formation of nonemissive triplet excited states in a 3:1 ratio.[24,30,32] However, this challenge has largely been overcome through strategies such as metal-containing phosphorescent emitters or of organic emitters that by virtue of small singlet−triplet separations exhibit thermally activated delayed fluorescence (TADF).[33] Notably, however, both of these emitter classes tend to have relatively broad PL, although a solution to this issue can be obtained by using a blend of emitters, whereby a TADF EL emitter is capable of singlet energy transfer to a conventional fluorescent molecule with a narrow emission.[34]

The spectral purity and gamut coverage of QLEDs qualifies them as formidable competitors in wide color gamut displays, and their solution processability, size, and stability impart various advantages in device engineering/cost, pixel resolution, and gamut coverage and can also offer the possibility of thin, flexible, and wearable electronics.[14,21,23,24,30,35] Despite examples of QLEDs outperforming other state-of-the-art emitters in terms of line width and efficiency, issues with their implementation and subsequent performance in devices serves as a bottleneck to production on an industrial scale.[21,22] For QLEDs to be a viable commercial product moving forward, progress on patterning, device engineering, and subsequent performance is crucial.

Current QLED patterning efforts take advantage of the solution processability of colloidal QDs and are dominated by inkjet printing, contact and photolithography, and microcontact transfer printing.[24,29,30,35] Fabrication techniques such as photolithography are compatible with existing production facilities, which will allow QLED commercialization to benefit from the existing OLED infrastructure.[1,24,29] Additionally, the resolution requirements of next-generation UHDTV and augmented/virtual reality displays dictate that display resolution surpasses the number of pixels that can be resolved by 20/20 vision in humans, which highlights the importance of efforts toward precise, reproducible patterning techniques that yield high pixel resolution.[30]

While surface ligands of colloidal QDs are often selected to optimize their photoluminescent properties, their direct involvement in the charge injection process of EL devices necessitates careful consideration of their electronic properties and electrochemical stability as well. The electrochemical stability of QD cores implies that electrochemical degradation of QDs under device operation stems from issues at the organic−inorganic interface. Pu et al. addressed this issue by showing that electroluminescent performance is ligand dependent for QDs of identical core composition and PL properties.[36] Red-emitting CdSe/CdS QDs (PLQY = ∼90%) exchanged with electrochemically stable amine ligands showed an average external quantum efficiency (EQE) of 18.6%, internal quantum efficiency (IQE) of ∼80%, and half-life (T_{50}) of 90 000 h at 100 cd m^{-2}, which represents a drastic increase in performance compared to the native carboxylate-capped QDs (EQE = 0.2%; T_{50} = ∼0.3 h). For blue-emissive CdSeS/ZnSeS/ZnS QDs, peak EQE increases from ∼2% in carboxylate-capped QDs to ∼10% in the amine-exchanged QDs. Additionally, the operational lifetime was calculated to be >10 000 h at 100 cd m^{-2}, which was

https://doi.org/10.1021/acs.chemrev.3c00097
Chem. Rev. XXXX, XXX, XXX−XXX

the most stable blue QLED reported at the time.[36] Bridging the gap between photoluminescent and electroluminescent QLED performance will require modified design rules that also consider the electrochemical resiliency of the ligand shell.

The most pertinent outstanding issues facing QLED development can be understood by following the operational principles of the LEDs themselves. Unbalanced charge injection, operational instability, short device lifetimes, and subpar performance metrics are all directly related to charge-carrier dynamics, which are in turn influenced by QD synthetic outcomes and photophysical properties, the role of interfaces and core/shell structures, ligand environment, patterning method, and injection layer composition and electronics. Thus, it is evident that efforts toward bright, stable, and high-performance QLEDs for next-generation display technology will require thoughtful and synergistic efforts across each phase of production, from QD synthesis to final device characterization. From a materials development perspective, efforts toward narrow-line-width emitters for QLEDs should be mindful of not only how shelling and passivation strategies affect photophysical properties but also how conducive these methods are toward device integration and electrochemical/operational stability. For instance, certain ligand environments might excel at passivating surface trap states that facilitate nonradiative recombination but also inhibit facile patterning or charge injection when integrated into a device. Notably, these considerations also affect the performance of QDs in both photodetector and quantum information applications, providing common chemical themes that unite these seemingly disparate engineering applications, as we discuss below.

2.2. Photodetectors

The detection of infrared (IR) light, which is based on the conversion of incident photons in the 0.75−12 μm wavelength range to electric signals, encompasses several applications including spectroscopy, medical diagnosis, night vision, military, astronomy, environmental mapping, and optical communication. Narrow PL line widths are not necessarily required for photodetectors, but this property often directly reports on the ability of the material to also serve as a narrow-band absorber. Traditional IR photodetectors using single-crystal IV, II−VI, or III−V semiconductors ($Hg_xCd_{1-x}Te$, silicon, $In_xGa_{1-x}As$, InSb, etc., Figure 4), despite having high responsivity and detectivity, remain expensive due to material-growth conditions and show poor modularity due to their fixed band gaps dictated by substrate lattice matching requirements. Device fabrication using these single-crystal materials for many applications, especially for narrow-band photodetection technologies, is limited by high implementation cost from the cryogenic cooling requirement. Typical device architectures for narrow-band photodetection to realize spectral discrimination combine broad-band photodetecting layers with interference filters, which not only increases the implementation cost but also introduces signal loss from transmission. Existing alternative narrow-band photodetection technologies include magnification of absorption in a selected wavelength range by the plasmonic effect, manipulation of the external quantum efficiency by charge collection narrowing, and the use of an absorber with a narrow absorption spectrum. For the latter, colloidal QDs, among other material candidates such as organic semiconductors, have been chosen to develop a new class of photodetectors to replace the conventional technology. The main advantages of photodetectors using colloidal QDs are (1) their spectral tunability from the quantum confinement of these nanocrystals, which promotes filterless narrow-band photodetection technologies, and (2) their room-temperature and low-cost solution processability enabling scalable fabrication with a variety of substrates via spin-coating, inkjet-printing, or spray-casting techniques. In addition, the above advantages also enable advanced on-chip manipulations that may not be possible for traditional wafer technologies.[6] This includes coupling the QD absorption with plasmonic structures to increase the absorption of thin layers, producing QD bilayer heterojunctions with different semiconductors to facilitate the exciton dissociation,[37,38] and creation of multispectral or full-color detectors.[39,40]

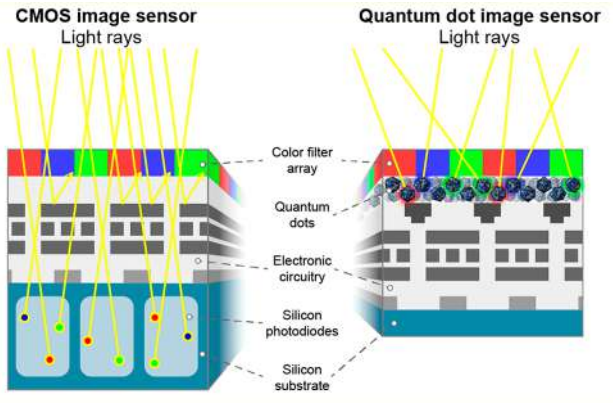

Figure 4. CMOS image sensor versus a QD image sensor in a photodetector.

To date, PbS and HgTe QDs are the leading materials for detection in the near- and mid-IR regions, respectively. State-of-the-art solution-processed QD photoconductors using the stacked image sensor technique from these materials have shown performance that overcomes classical photodetectors and enables facile integration to CMOS sensor arrays. However, besides the high toxicities of both Pb and Hg, there are still several major remaining challenges for QD-based photodetectors. In particular, the response speed of PbS-based photodetectors is typically significantly slower than that of conventional devices. Most HgTe-based photodetectors reported to date are single-pixel devices in the mid- and short-IR regions, while performance in the long-IR region is significantly poorer than that of commercial devices. Compared with PbS QDs, the emission line width and absorption edge in other infrared-absorbing QDs are typically less sharp, indicating a poor QD size distribution that negatively affects the charge-carrier mobilities in the photodetector material. Guyot-Sionnest et al. showed that this effect is larger on the intraband photodetecting properties of HgSe QDs than the interband properties.[41] Investigations that synthetically reduce the nanocrystal size distribution in order to reduce the dark current by deepening the conductivity gap of these materials could significantly boost the performance of QD IR photodetectors. Furthermore, the detectivity of colloidal QDs is usually unstable at high temperature and pressure, hindering their current promise for applications in harsh environments. Finally, it is also necessary to explore other nontoxic QDs that emit and absorb in the IR regions and other IR colloidal systems with higher efficiency and sharper absorption edge such as confined structured nanoplatelets.

https://doi.org/10.1021/acs.chemrev.3c00097
Chem. Rev. XXXX, XXX, XXX−XXX

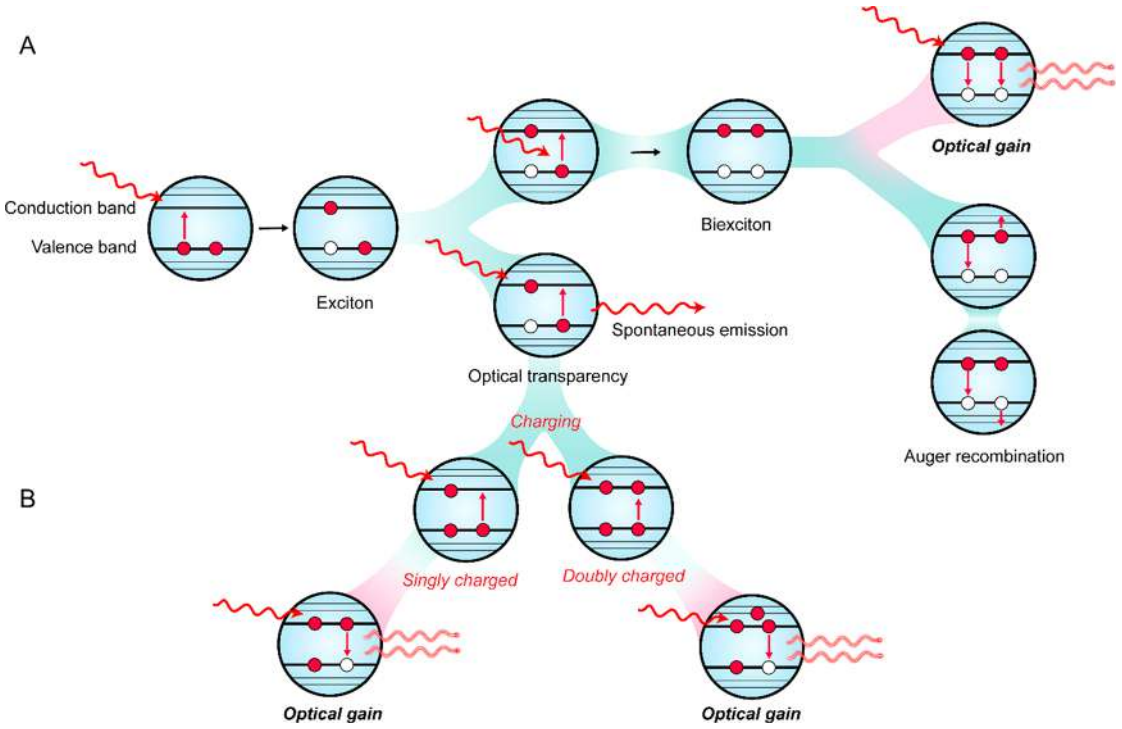

Figure 5. Diagram showing the mechanism to achieve optical gain through (A) biexciton and (B) sub-single-exciton mechanisms.

2.3. Lasers

Another important application of colloidal materials is in the field of lasing. The span of applications of lasers is vast. Lasers with a narrow line width are in high demand because of their ability to exhibit high temporal and spatial coherence and low-phase noise, which are important for holography, high-resolution measurements and detections, laser spectroscopy, and optical communication.[42] Since the very first demonstrations of microdisk lasers based on colloidal nanomaterials,[43] photonic crystals,[44] and nanowires,[45] nanolasers have been quickly developed.[17,46−49] Lasers from solution-processed materials can be operated under both electrical and optical pumping. The characteristics that make colloidal QDs excellent candidates for lasing are their atomic-like electronic states, large optical oscillator strengths, solution processability, continuous spectral tunability, and high thermal stability. In addition, QD nanolasers are a flexible solution that allow for property modifications through heterostructuring, surface chemistry, and incorporation with "functional" defects.

Exciton−exciton interactions play a crucial role in the optical gain of colloidal QD, as they determine the likelihood of a QD having a biexciton versus staying in the ground state. To achieve colloidal QD lasing, biexciton gain can be achieved by increasing the number of excitons per QD to more than 1 (Figure 5A).[47] However, this method leads to complications such as fast nonradiative multicarrier Auger recombination and high lasing thresholds, which reduce optical gain lifetimes to tens of picoseconds and have a significant negative impact on continuous-wave optical and direct-current electric pumping.[46,47,49] Lower laser gain thresholds have been achieved through facet-selective epitaxy to prevent thermal depopulation of the valence-band-edge states.[46] Toward optical gain without the need of biexcitons, more recent developments in engineering the multiexciton nature have shown ways to lower optical gain threshold to below the one-exciton limit (Figure 5B) through charging colloidal QDs with electrons or holes, electrochemically or photochemically, to bleach the ground-state absorption.[48,50−54] through facet-selective epitaxy to prevent thermal depopulation of the valence-band-edge states. Alternative ways to reduce optical gain thresholds include using materials with a large volume of nanocrystal such as nanoplatelets, which exhibit an ultranarrow emission line width due to extreme quantum confinement.[55−57]

In general, nanocrystal lasing materials are coupled with an external optical cavity structure to magnify their emission to a narrow spectral range due to the Purcell effect. The QD-cavity-coupled system allows narrowing of the gain line width of the active medium, enhancing laser coherence. The line width of the lasing resonance peak in these systems depends on the quality factor (Q) of the corresponding cavity mode, with narrower line widths resulting from higher Q and pump intensity.[58]

2.4. Quantum Information

Quantum computation and quantum information science are foundations for future technologies that are predicted to revolutionize computing, communication, security, and sensing. The current stage of quantum technology development is focused on physical realizations of scalable platforms that can perform quantum operations using quantum bits (qubits) with negligible errors and high stability. Among qubit candidates, photonic qubit systems have advantages based on their ability to operate at room temperature, the preservation of quantum states of photons due to weak interaction with external environments, and the potential for use in long-distance optical quantum communication.[59] A quantum device using optical qubits requires a reliable single-photon source that can emit one photon at a time. These single photons must have a high level of indistinguishability, i.e., photons with identical spectral, temporal, and spatial modes, for manipulations such as interference and entanglement. Investigations in stable solid-state single-photon emitters in the past decades have not found

https://doi.org/10.1021/acs.chemrev.3c00097
Chem. Rev. XXXX, XXX, XXX−XXX

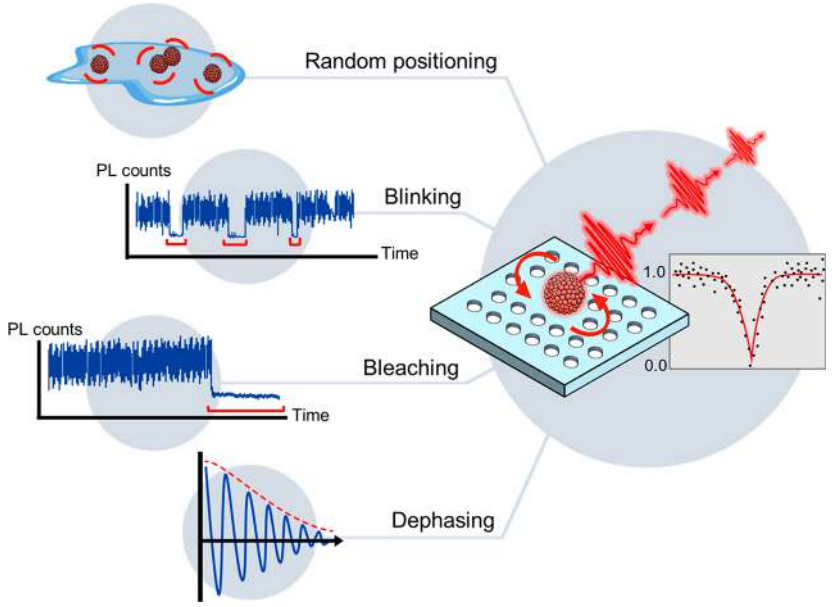

Figure 6. Challenges in making scalable photonic platforms with colloidal QD single-photon sources.

an ideal emissive material that meets all requirements. Another crucial obstacle for quantum nanophotonic development is scalability since future quantum nanophotonic devices would need to contain many coherent quantum light sources to perform quantum tasks simultaneously.

Considering all of these challenges, solution-processable materials such as QDs hold great promise to build a scalable, room-temperature-operating, and electrically driven quantum nanophotonic system. Quantum information science applications of colloidal QDs take advantage of their solution processability for the creation of scalable platforms based on photon-, spin-, or defect-based qubits. There have been many demonstrations where device-integrated colloidal QDs show a high single-photon emitting purity.[17,18,60−63] However, photonic applications beyond single-photon emission from colloidal QDs are still limited mainly due to (1) their random spatial positioning, (2) unwanted optical behaviors (inhomogeneous spectral broadening, blinking, and bleaching), and (3) low coherence lifetimes relative to their PL lifetimes (Figure 6). A scalable quantum photonic platform that uses QDs requires many identical single-photon-emitting building blocks, where single QDs are precisely positioned to couple with optical cavities. While deterministic placements and patterning of single QDs have been achieved,[64,65] coupling these patterned single QDs with cavities in a scalable fashion has yet to be realized. When coupled to a photonic cavity, a narrow QD emission line width increases the QD quality factor, thus improving the spontaneous emission rate enhancement through the Purcell effect.[66] Blinking or PL intermittency occurs when the QD emission is disrupted or switched to an "off" state by transitions to a nonradiative or a weakly emitting state. After a short duration, the QD PL is recovered. Photobleaching in QDs is an irreversible process, where the PL intensity of the QD is significantly reduced under continuous photoexcitation. Blinking and bleaching behaviors in QD single-photon emitters decrease single-photon purity by directly interfering with the photon generation. These behaviors have been extensively studied and effectively suppressed by several strategies developed in the past 20 years.[67−72] A room-temperature colloidal QD usually has exciton decoherence on a ∼100 fs time scale due to loss of wave function overlap from exciton−phonon interactions. For single-photon emitters, a long coherence time is necessary for quantum information science applications. Recent literature has suggested that perovskite materials, particularly lead halide perovskites, may be suitable candidates for this purpose, as they possess narrow emission line widths, (∼25 μeV) comparable to (5 times larger than) the transform limit from the radiative rate for single-photon emission due to defect tolerance, which in turn leads to longer coherence times.[62,73] However, cryogenic temperatures were required as this type of material has very low thermal stability. Consequently, the search for solution-processable materials that can exhibit high stability and long optical coherence time for single-dot emitters is still ongoing. Success will require a detailed understanding of the origins of spectral broadening as detailed in section 3.

3. SOURCES OF SPECTRAL BROADENING

In this section we will review the fundamental sources of spectral broadening in solution-phase semiconductors. We broadly classify the sources of broadening in three bins (Figure 7). The first is "homogeneous" broadening, which encompasses dynamic processes intrinsic to a single semiconductor particle itself, including population relaxation, decoherence (part of decoherence is sometimes referred to as "pure dephasing"), orientational relaxation, ligand vibrations, and solvent motions. The second is inhomogeneous, heterogeneous, or static broadening, which consists of practically static effects resulting from ensemble averaging, including dispersity in size, shape, and composition. Finally, we will consider confounding environmental factors that contribute to slow spectral diffusion.

3.1. "Homogeneous" Broadening—Dynamic Broadening in Single-Particle Spectra

The line width of the transition from the ground state to the first exciton, i.e., the lowest lying electronic excited state, has contributions from both dynamic broadening mechanisms that arise for a single nanocrystal, such as size-dependent exciton−phonon coupling,[74] and static inhomogeneous broadening that arises from differences between nanocrystals in an ensemble,

https://doi.org/10.1021/acs.chemrev.3c00097
Chem. Rev. XXXX, XXX, XXX−XXX

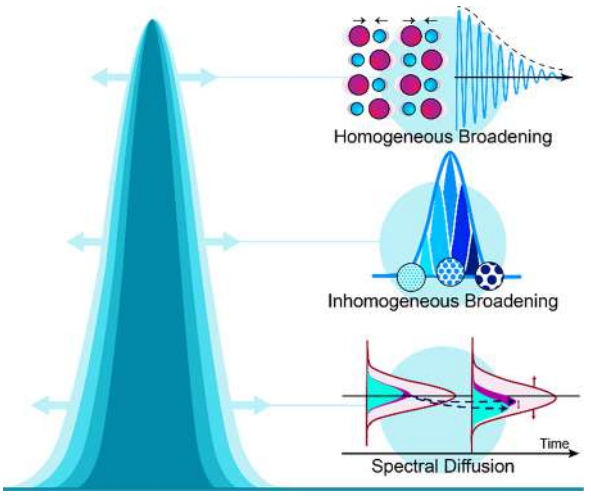

Figure 7. Three categories of sources of PL spectral broadening.

such as size dispersion.[75] Atomically resolved transmission electron microscopy (TEM) studies show that colloidal QD samples usually contain QDs with a wide variety of atomic structures, and single-dot spectroscopy has revealed a corresponding diversity of emission spectra. It has long been known that the line width varies systematically with size.[74] Furthermore, single-dot spectroscopy suggests that even QDs with the same band gap can have different emission line widths.[76,77] Simply put, most QD samples *do not have* a "homogeneous line shape" that is the same for all QDs in the sample. For this reason, Park et al. defined the dynamic line shape as the average single-dot line shape for all QDs with the same band gap and the static inhomogeneous line shape as the distribution of band gaps in a sample.[78] The dynamic line shape arises from the motions of electrons, holes, and spins, vibrations of the atomic lattice, and motion of ligands and the surrounding solvent. Every homogeneous or single-dot line shape is a dynamic line shape, but a dynamic line shape does not need to be homogeneous or match any single-dot line shape. Dynamic line shapes can be measured by single-dot or nonlinear spectroscopy,[52,78] while photon correlation Fourier spectroscopy[79−81] measures a symmetrized correlation function of the dynamic line shape. The dynamic/static terminology also has the advantage of emphasizing that the initial conditions matter so that the dynamic line shape is different for absorption versus emission and that the distinction between dynamic and static line shapes is always a question of measurement time scale, which is important for the slow dynamics known as spectral diffusion.

Theoretical work implies that band-gap inhomogeneity can be greater than the size/shape inhomogeneity[82,83] due to variations in stoichiometry,[84] faceting,[82] symmetry,[85] and surface passivation.[86] Surface inhomogeneities may become dominant for syntheses with single atomic layer control. Transmission electron microscopy (TEM) is the most widely used primary technique for quantifying size dispersion in semiconductor nanocrystals, despite well-known drawbacks such as magnification errors, decreased sensitivity to surface layers,[87] particle selection bias,[88] and ambiguities in determining particle boundaries,[89,90] leading to a 10% uncertainty in size dispersion when analyzing approximately 1000 nanocrystals.[78] Figure 8 compares size/shape dispersion band-gap inhomogeneities calculated from TEM measurements and total band-gap inhomogeneities determined from 2D spectra for colloidal

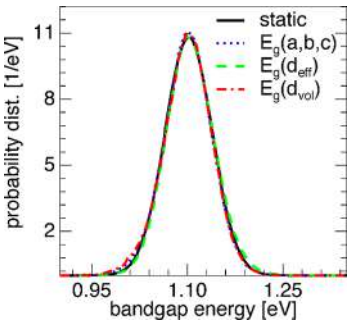

Figure 8. Full width half maximum total band-gap inhomogeneity extracted from two-dimensional Fourier transform spectra of colloidal PbSe QDs. This is compared to three static inhomogeneous band-gap distributions estimated from the full annular dark field-scanning tunneling electron microscopy size/shape distribution using a diameter-shifted/band-gap-matched version of the band-gap-sizing curve from Moreels et al.[91] The average QD has a prolate ellipsoidal shape with short axis lengths of 3.4 nm and a long axis length of 4.4 nm in the images. The short axis length distributions have a standard deviation slightly less than the thickness of one atomic layer. Although the discrete long-axis length distribution is significantly non-Gaussian, the size/shape band-gap distributions calculated from three different ways of accounting for the effect of shape (additive 1D confinement energies, equivalent diameter in the effective mass approximation, and an equivalent spherical volume diameter) all approximately match the Gaussian distribution obtained from the 2D spectra. Adapted with permission from ref 78. Copyright 2017 American Chemical Society.

PbSe QDs. This comparison indicates little to no dependence on the particle shape distribution and places upper bounds on the surface inhomogeneities.[78] The shape of the band-gap distribution is approximately Gaussian.

An approximately Gaussian band-gap inhomogeneity was also reported from two-dimensional Fourier transform spectra of slightly oblate colloidal PbS QDs with 4 nm diameter.[52] Ryu et al. also showed that if the QDs were diluted sufficiently to prevent energy transfer between QDs before luminescence, 1D absorption and PL spectra could also be used to accurately obtain the same band-gap inhomogeneity measured in the 2D spectra. This determination from 1D spectra relied on a generalized Einstein relationship between the dynamic line width Δ_{dyn} and the Stokes shift (2λ) for Gaussian spectra

$$\Delta_{dyn}^2 = (2\lambda)k_B T \tag{1}$$

where Δ_{dyn}^2 is the variance of the Gaussian dynamic line width, 2λ is the Stokes shift between maxima of the absorption and stimulated emission line shapes, k_B is the Boltzmann constant, T is the absolute temperature, and the line width and shift are measured in the same energy units as $k_B T$. Precise determination of the Stokes shift requires conversion of the PL spectrum (which has a spontaneous emission line shape) into a stimulated emission line shape and conversion of the absorption spectrum into an absorption line shape. For Gaussian spectra, the static inhomogeneous line width can be determined from the total line width and the additivity of variances

$$\Delta_{tot}^2 = \Delta_{dyn}^2 + \Delta_{inh}^2 \tag{2}$$

where Δ_{tot}^2 and Δ_{inh}^2 are the variances of the total and inhomogeneous line widths, respectively. Further, Ryu et al. showed that the above relationship between ensemble Stokes shift and dynamic line width also held for the Gaussian dynamic line widths obtained from photon-correlation Fourier spectros-

https://doi.org/10.1021/acs.chemrev.3c00097
Chem. Rev. XXXX, XXX, XXX−XXX

copy by Caram et al. for colloidal PbS QD samples with average diameters ranging from 2 to 6 nm.[81]

However, the 2D spectra show,[52] in agreement with low-temperature single-molecule spectroscopy and with theory,[77] that the PbS dynamical line shapes are asymmetric, primarily due to fine-structure broadening. Because the PbS fine-structure splittings are comparable to k_BT at room temperature, the absorption and emission spectra have different dynamic line shapes. With such non-Gaussian dynamic line shapes, the above approach becomes approximate. Ryu et al. described another approach, based on the generalized Einstein relations between single-molecule absorption and emission spectra, that enables determination of the inhomogeneous line shape from 1D absorption and PL spectra of PbS QDs with sub-meV accuracy.[52]

Tovstun et al. have used the Gaussian approximation to analyze the excitation−emission matrix of InP/ZnS core/shell QDs.[92] Although the Gaussian approximations to the excitation and emission spectra had different widths, the diagonal elongation of the excitation−emission matrix (which is similar to the static inhomogeneous diagonal elongation of two-dimensional Fourier transform spectra) was used to extract inhomogeneous line widths ranging from 19 to 22 nm (at ∼500 nm) depending on the method used; this amounts to an ∼14 meV range for estimates of the inhomogeneous line width (as measured by the Gaussian standard deviation). They attributed the larger overall line width in absorption than emission to larger homogeneous broadening (dynamic broadening in the sense distinguished here) in absorption than emission.

For smaller PbS QDs up to ∼1.75 nm diameter, Chakraborty et al. performed numerical calculations of the band gap for sets of one million structures with the same fixed stoichiometry.[93] Their results show a significantly skewed band-gap distribution. These spectra are homogeneous in the sense that all of the structures probed occur for a single stoichiometry, but a variety of structures (for example, different surface facet sizes seen in TEM) will give inhomogeneous broadening or spectral diffusion unless interconversion between structures is rapid on the electronic spectroscopy time scale.

Dynamic line shapes should be understood based on the underlying single-molecule line shapes. A single-molecule line shape is determined by the interaction between the observed system, its surroundings or bath, and the measurement. In this context, the system is measured while the bath influences those measurements indirectly through its effect on the system. Since the system and bath are coupled, there is no system-only wave function, and the system must be described by a reduced density matrix. Through system−bath interactions, the evolution of the reduced density matrix makes a transition from coherent quantum dynamics to dissipative-level kinetics in some preferred basis (the pointer basis preferred by the interacting system, bath, and measurement).[94] Coherence decay or decoherence quantifies this transition in the evolution of the system we can measure. So long as the transition moment is independent of the bath degrees of freedom (which can require that some degrees of freedom be considered part of the system), decoherence determines the single-dot line shape.[95−97]

In certain limits, decoherence can be mathematically viewed as arising from bath-induced changes in the system state (for example, lifetime broadening) plus either bath-induced phase "uncertainty" for the system (pure dephasing) or system-induced changes in bath overlap (pure decoherence).[96,97] For a spectroscopic transition, system-induced changes in bath overlap arise as the bath parts of an overall system−bath wave function develop differently with the initial and final states of the system in the transition. For example, if the electrons are taken as the system, the bath for excitonic decoherence will include spins, phonons, ligand motions, and the solvent. Excitonic decoherence will occur through the electronic coupling to spins that produces excitonic fine structure, exciton−phonon coupling, etc. The excitonic pure decoherence due to loss of overlap between phonon wavepackets on the ground (zero-exciton) and one-exciton states is readily visualized. This loss of phonon overlap occurs because of differences in exciton−phonon coupling or equilibrium lattice geometry between the ground and the one-exciton states. Starting from an equilibrated ground state, excitonic decoherence between the ground state and the one-exciton state gives the single-dot absorption line shape, while starting from an equilibrated one-exciton state gives the emission line shape.

QD excitonic decoherence times are typically 10−100 fs at room temperature and significantly longer at low temperature.[98] There is also evidence that the overall dynamic line width for the first exciton transition can be significantly altered by QD surface modifications. Using photon correlation Fourier spectroscopy, Cui et al. measured the dynamic emission line width for CdSe QDs with and without a passivating ZnS shell. For CdSe cores with the first exciton absorption at 508 nm, they reported that 3−4 monolayers of passivating ZnS shell reduced the dynamic emission line width from ∼90 to ∼60 meV.[80] With one exception, the reductions seen for other CdSe QD core sizes were smaller than this factor of 1/3 reduction. Using 2DFT relaxation spectroscopy, Ryu et al. compared the dynamic line width for two colloidal PbS QD samples with the same band gap and found that the half-width decreased from 43 to 36 meV with a 3-fold reduction in oleate ligand coverage. This ligand-coverage reduction in dynamic line width by a factor of 1/6 for PbS is comparable to the ZnS shell reduction in dynamic line width for the majority of CdSe QD sizes from the study of Cui et al.[80] This study attributed the CdSe line width reduction to decreased exciton−phonon coupling with a passivating shell. Computations on CdSe QDs have predicted that ligands can promote faster nonadiabatic interband relaxation[99] and slower adiabatic pure decoherence;[100] these make counterbalancing contributions to the total decoherence. In the case of PbS, the cause is uncertain because TEM images show a change in nanocrystal shape with ligand coverage;[52] the calculations from Poddubny et al. indicate changes in structure may affect intervalley and fine-structure broadening in PbS.[85]

In molecules, the overlap picture has been used to show that vibronic pure decoherence (pure decoherence between vibrational states of two different electronic states) can be slower than electronic pure decoherence between the same two electronic states.[101] Transferring intramolecular vibrations from the bath into the system has two counterbalancing effects on total decoherence: first, it slows down pure decoherence through the loss of bath overlap because intramolecular vibrational wavepacket overlap no longer contributes; second, it speeds up bath-induced changes in the system state by augmenting electronic internal conversion with vibrational population relaxation. Since vibrational population relaxation is typically ∼100 times slower than intramolecular vibrational overlap loss for large molecules in room-temperature condensed phases, total vibronic decoherence is slower than total electronic decoherence.

In QDs, specifying the total electron + spin angular momentum removes fine-structure wavepacket overlap decay

https://doi.org/10.1021/acs.chemrev.3c00097
Chem. Rev. XXXX, XXX, XXX−XXX

and incorporates relaxation between fine-structure levels; how this trade-off affects total decoherence is less clear. For example, in colloidal lead chalcogenide nanocrystals, measurements of electron + spin angular momentum relaxation using pulses with durations ranging from 20 to 50 fs resolved "fast" exponential time constants ranging from 150 (PbTe) to 300 fs (PbS) with an unresolved "very fast" relaxation.[102] For PbS QDs, the calculated intervalley and fine structure from Hu et al., which is supported by the dynamic absorption and emission spectra from Ryu et al.,[52] would generate a nonmonotonic wavepacket overlap decay, first dropping to 50% overlap after around ∼90 fs. It is not clear whether the unresolved "very fast" relaxation involves angular momentum wavepacket overlap decay, population relaxation between fine-structure states, or both, but intervalley/fine-structure overlap and population relaxation time scales can have the same order of magnitude at room temperature. The angular momentum relaxation time scale is a factor of 2 slower at 77 K and below.[102] More study is needed to determine how total decoherence times for excitonic fine structure relate to total decoherence times for excitons at room temperature.

The temperature dependence of total decoherence between the zero-exciton state and the lowest bright intervalley/fine-structure level of the one-exciton state of PbS QDs has been measured by 2DFT correlation spectroscopy.[98] Decoherence from exciton−phonon coupling accounted for 2D antidiagonal line widths that increased from ∼3 meV fwhm at 5 K to 10 meV fwhm at 80 K. A similar trend was observed in single-dot emission spectroscopy: at 4 K, single PbS core−shell QDs had a range of line widths from 8 to 25 meV fwhm, with an average line width of 16 meV; tracking single-dot spectra as a function of temperature, exciton−phonon coupling caused dot-dependent line width increases with temperature but roughly doubled the 5 K line widths by 60 K. Narrowed antidiagonal line widths are expected in 2DFT correlation spectra because 2DFT correlation spectra have no delay between excitation and detection steps, so that phonon motions are "frozen" during the femtosecond experiment;[103] In contrast, phonons fully relax on a time scale much faster than the exciton lifetime in single-dot emission. Single-dot emission can be broadened by spectral diffusion between emission events. Above 100 K, exciton fine structure begins contributing a high-energy shoulder to the single-dot emission line shape.[77] Fully relaxed 2DFT relaxation spectra, in which the excitation and detection steps are separated by a time delay sufficient for complete fine-structure and phonon relaxation, indicate an exciton−phonon coupling contribution to the dynamic line width of ∼60 meV (fwhm) for 4 nm diameter colloidal PbS QDs at room temperature;[52] given the surface-mediated differences in dynamic line width mentioned above, this is in reasonable agreement with the ∼55 meV exciton−phonon coupling line width expected from the lower temperature single-dot emission.

Based on the generalized Einstein relations, such single-dot line widths are incompatible with the "nearly-zero" Stokes shifts reported for PbS by Voznyy et al.[104] Their conclusion that aggregation and energy transfer can increase the measured Stokes shift at high concentrations is undoubtedly correct—the concentration-dependent effects of both nonradiative and radiative energy transfer on PL spectra, lifetimes, and quantum yields are well known.[105] If not an artifact arising from difficulties in measuring absorption at high dilution, the near-zero Stokes shifts reported by Voznyy et al.[104] would imply near elimination of both exciton−phonon coupling and intervalley/fine-structure splittings by chloride surface treatment.

QD PL lifetimes are often significantly lengthened by the intervalley/fine-structure equilibrium[106] and by the equilibrium between bright and dark excitons. The QD bright exciton/dark exciton equilibrium is related to the phenomenon of "delayed fluorescence" in molecules. After intersystem crossing, delayed fluorescence arises from the small equilibrium population of the first excited singlet state above that of the energetically lower first triplet state; thermally activated delayed fluorescence has the spectrum of fluorescence and the lifetime of phosphorescence.[107] Recent experiments on CdSe QDs by Ruhman and co-workers[108] showed that the electron spin flips needed for bright exciton−dark exciton equilibrium are orders of magnitude slower than the time scale for angular momentum relaxation within the bright state.[109] In QDs, the dark exciton is much closer in energy to the bright exciton and can indirectly emit through equilibrium with the bright exciton.[52] Compared to molecules, indirect emission occurs at lower temperatures and with higher yields in QDs.

The size-dependent emission spectra of PbS QDs exhibit two overlapping features at room temperature.[52] Caram et al. attributed the dominant emission feature to an ever-present defect state and reported that time-resolved PL from 4.1 nm diameter PbS QDs exhibited biexponential decay with sub-200 ns and ∼2 μs lifetimes.[81] The calculated intervalley/fine-structure splittings reported by Hu et al. give two bright features that account for the peak and high-energy shoulder in both single-dot emission at temperatures from 100 to 235 K[77] and dynamic emission from 2D spectra at room temperature.[52] Using the intervalley/fine-structure and the generalized Einstein relations to calculate the radiative lifetime for the equilibrated bright exciton gives ∼200 ns;[52] this radiative decay rate is only about 15% slower than what one would expect from a calculation using the Strickler−Berg relation,[110] the absorption spectrum, the shape of the PL spectrum, and the 8-fold degeneracy model[111] for the bright exciton. Using the same model and approach, the radiative rate for bright and dark excitons in equilibrium at room temperature is substantially slowed (up to ∼2 μs).[52] The simplest interpretation of this slowing is that the fully equilibrated exciton emits only from the 8 states of the bright exciton but spends most of its time in the more numerous dark states (the equilibrated bright-dark exciton is 64-fold degenerate). Both of these simple degeneracy-model interpretations are quantitatively modified by intervalley coupling and fine structure splittings.[77] The above picture for fully equilibrated PbS QD emission is directly analogous to the picture of microsecond radiative lifetimes for PbSe QDs proposed by Zunger and co-workers;[106] their calculations also showed that the intervalley/fine-structure splittings and intensities generate two size-dependent features in PbSe QD absorption. The agreement outlined above suggests that the two features in the spectra arise from intervalley/fine-structure splitting and that the slowest (2 μs) time constant in PbS PL decay arises from the fully equilibrated bright-dark exciton, which indirectly emits through the bright exciton at room temperature.[52] This is QD delayed fluorescence.

Ryu et al. reported a stimulated emission contribution to the 2D spectrum that was about 10% of the maximum 2D signal and appeared with the Stokes shift observed in PL spectra within 1 ps after band-edge excitation. The strength of this signal matches that for stimulated emission from the equilibrated bright exciton, so Ryu et al. attributed it to single-exciton stimulated emission.[52]

https://doi.org/10.1021/acs.chemrev.3c00097
Chem. Rev. XXXX, XXX, XXX−XXX

Since early experiments, QD lasing has usually been considered to require population of the biexciton state in order to avoid losses from exciton to biexciton absorption;[112] however, there is precedent for single-exciton lasing in QDs with a Stokes shift that is large relative to the linewidth.[46] (This mechanism for single-exciton stimulated emission through a large Stokes' shift is not shown in Figure 5.) In comparison to the dynamical line widths of 70 and 80 meV fwhm, the PbS QDs studied by Ryu et al. had a 70 meV Stokes shift, so that stimulated emission (which does not require laser gain) stands out above the red edge of the dynamical absorption spectrum. In agreement with the ∼7 meV red shift of biexciton emission reported by Heinz and co-workers,[113] Ryu et al. found a ∼ 7 meV red shift of exciton to biexciton absorption,[52] so induced absorption to the biexciton state does not interfere with measurement of stimulated emission. However, Ruhman and co-workers were unable to detect stimulated emission in recent spectrally resolved pump−probe and spectator exciton experiments on larger PbS nanocrystals.[114] This might be due to the combined effect of the relatively small stimulated emission signal (10% of maximum 2D signal), the ±5−10% error bars on the spectrally resolved pump−probe experiment, the obscuring effect of any sample heterogeneity in spectrally resolved pump−probe experiments, and extensive absorption−PL overlap noted for their sample (the Stokes shift decreases as size increases; the data of ref 81 suggests the Stokes shift might be a factor of 3 smaller). Thus, all available evidence from both theory and experiment is consistent with the bright exciton having a radiative lifetime of ∼200 ns, but this does not prove that the bright exciton lives long enough to account for the sub-200 ns decay reported in PL.

The time scale for equilibration between the bright and the dark exciton in PbS QDs is not settled. In contrast to CdSe,[108] spectator exciton experiments did not detect a spin blockade for PbS,[114] and the authors noted that a rapid spin-flip hypothesis would reduce but not eliminate the blockade at the band edge. One possible explanation, not suggested by the authors, is that rapid intervalley scattering among the four valleys in PbS could provide a way around any spin blockade created by up to 3 spectator excitons (the experiments probed 1 and 2 spectator excitons). This seems plausible for a variety of reasons: intervalley scattering typically has a ∼100 fs time scale in the bulk;[115] a different intervalley scattering process takes ∼100 fs in PbS QDs,[116] and it has been suggested[117] that intervalley coupling at the band edge is responsible for the residual low-temperature decoherence not accounted for by exciton−phonon coupling.[77,98,117] We are thus left with bright−dark exciton equilibration taking place sometime after 1 ps (when the bright exciton was observed in 2D experiments) and before 200 ns (soon after that, PL decays with the ∼2 μs exponential lifetime of the equilibrated bright−dark exciton). Ruhman's spin-blockade experiments on CdSe QDs yielded electron spin-flip times of ∼25 ps.[108] The 2D experiments establish that the radiative lifetime of the PbS QD bright exciton is ∼200 ns.[52] However, unless the carrier angular momentum flip times are orders of magnitude longer in PbS than CdSe, defect[81] or trap states may be necessary to explain the sub-200 ns decay component in PbS QD PL.

In summary, the heterogeneity within QD ensembles makes their line broadening quite different from the molecular homogeneous−inhomogeneous paradigm.

(1) The combination of size-dependent quantum confinement effects on line width and size dispersion means that most quantum dot ensembles do not have a truly homogeneous line shape that is the same for all quantum dots in the ensemble. Furthermore, quantum dots with the same band gap exhibit different single-dot line shapes, and their average can be correctly called a dynamical line shape. Measurements by single-dot spectroscopy, photon correlation Fourier spectroscopy, and two-dimensional spectroscopy indicate that the dynamics and dynamical line broadening that result from exciton interactions with spins, phonons, and ligands are significant and subject to synthetic control.

(2) The dynamic line shape can be contrasted with the static inhomogeneous line shape arising from the band-gap distribution, which is dominated by size dispersion without significant shape dependence in experiments to date. The dynamic line shape is determined by total decoherence in the time domain. In certain limits, total decoherence arises from bath-induced changes in system state (for example, lifetime broadening) and system-induced changes in bath wave function overlap (pure decoherence). Pure decoherence is sometimes described as bath-induced relative phase uncertainty between parts of the system wave function (pure dephasing).

(3) Provided the quantum dot sample is dilute enough to prevent energy transfer between quantum dots, the Stokes shift between ensemble absorption and emission maxima provides information on the dynamic line width. For the same line shape, a larger Stokes shift implies a larger dynamic line width. Simple quantitative relationships between the Stokes shift and the dynamic line width hold for Gaussian line shapes. For modern syntheses with low polydispersity, changes in dynamic line broadening can be so important that broader ensemble spectra no longer indicate greater size dispersion; in such circumstances, the ensemble Stokes shift should be used as a diagnostic for changes in dynamic line width.

3.1.1. Phonons. The second largest contribution to "homogeneous" or dynamic line broadening and single-dot decoherence is called collision broadening. For exciton wave functions, the pure dephasing picture of collision broadening is that random phase jumps can cause the wave function of the ground plus one exciton superposition state to lose phase information, commonly due to elastic collisions with phonons (or vibrational modes of a crystalline lattice). The random phase jumps will introduce additional frequency components and therefore broaden the spectrum of the exciton's wave function. Analogous to Franck−Condon vibronic coupling in molecules, the exciton of a nanocrystal may couple to phonons in the lattice due to some displacement Δ of the excited state along a (dimensionless) phonon coordinate, described by the Huang−Rhys parameter $S = \Delta^2/2$.[118] (The displacement Δ here and in ref 118 is not the same kind of quantity as the subscripted Δs used for line shape variances in section 3.1; the displacement Δ here is equal to d in ref 101.) This is known as exciton−phonon coupling. The result is additional phonon side-band transitions and, consequently, a broadened emission line width. Crystalline solids have acoustic and optical phonons. Acoustic phonons are longitudinal modes in which the atoms vibrate parallel to the direction of energy transport and are typically lower in energy than optical phonons, where atoms move in different directions. For narrow-emitting colloidal semiconductor nanocrystals, weak

https://doi.org/10.1021/acs.chemrev.3c00097
Chem. Rev. XXXX, XXX, XXX−XXX

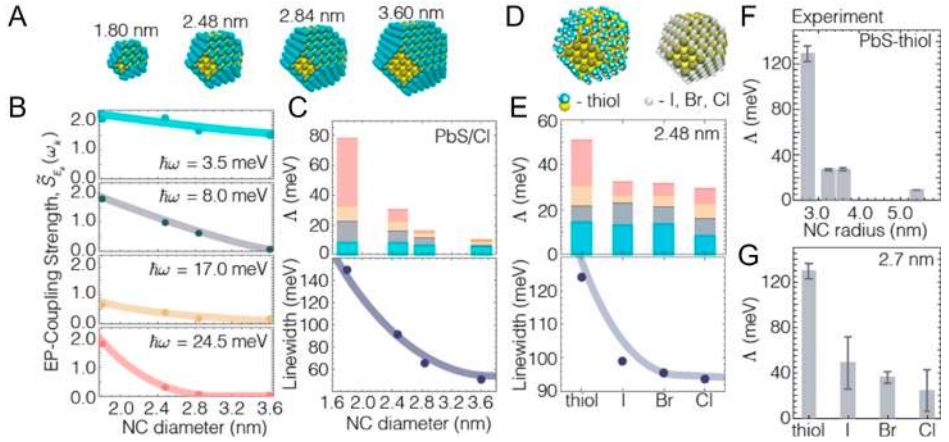

Figure 9. Size and ligand dependence of exciton−phonon coupling. (A) Atomistic models of the four PbS/Cl nanocrystal sizes considered here. (B) Exciton−phonon coupling strengths, $\tilde{S}_{E_g}(\omega_k)$, and (C) reorganization energies, Λ, and room-temperature line widths for the transition across the band gap. The plots of Λ are decomposed into the contributions to Λ from each of the four modes using the color scheme in B. (D) Atomistic models for 1.24 nm nanocrystals with methanethiol ligands and halide ligands. (E) Extracted Λ and line widths. In B, C, and E, the semitransparent lines are guides for the eye. Experimentally measured reorganization energies, Λ, as a function of nanocrystal size for (F) thiol-terminated PbS and (G) 2.7 nm diameter PbS nanocrystals with thiol and different halide passivations. Adapted with permission from ref 123. Copyright 2020 American Chemical Society.

phonon coupling is desirable, and the coupling can change as a function of size and surface composition.

It is generally accepted that as nanocrystal size increases, emission line width narrows. Bawendi et al. notably demonstrated this for both a continuous synthesis of CdSe cores (aliquot measurements) and multiple batches of CdSe of different sizes,[80] which shows that the effect was not a result of size focusing. This size dependence has also been shown to hold true for other systems.[81,119,120] This effect may be attributed to decreased coupling between the exciton and the surface phonon modes, which are generally more abundant and higher in energy than interior modes. As size increases, the surface area−volume ratio decreases and the exciton is better confined within the core. Rabani et al. showed that for a small 2.2 nm CdSe QD, 92% of phonon modes were localized to the outer monolayer of atoms and were responsible for 99% of the total reorganization energy (∼89 meV).[121] In this strongly confined system, the exciton wave function extends well to the surface and couples strongly with surface phonons. For a larger 4.7 nm CdSe QD (Bohr radius = 5.4 nm), the total reorganization energy becomes smaller (∼31 meV) and contributions become dominated by interior phonon modes (78%). There are some systems where this trend does not hold true, namely, nanoplatelets.[122] The effect of size on the exciton−phonon coupling strength and subsequent emission line width is therefore largely material dependent and requires an intimate understanding of the dominant phonon modes of the specific system.

Since many phonon modes are found on the surface, it follows that surface ligands can play a large role in exciton−phonon coupling. One of the major ways ligands affect this coupling is through surface passivation and dangling bonds or surface defects. In a computational study by Wood et al., thiol, iodide, bromide, and chloride terminations were compared on PbS QDs (Figure 9).[123] Exciton−phonon interactions were found to be suppressed in the halide systems compared to the thiol, which had many more underpassivated surface atoms and defects. The authors proposed that this resulted in more atomic displacement and extension of the excitonic wave function to the [111] surface facet. Surface defects may also lead to more localized dipoles, which can also couple to the exciton. The authors followed up on this work by both calculating and experimentally measuring emission line widths for these four terminations and found that the line width decreased with weaker phonon coupling.[124] Importantly, these effects were not a result of different electronic structures or trap states. Surface ligands have been calculated to reduce exciton−phonon coupling by reducing the vibrational amplitude of surface atoms through direct mechanical coupling.[100] Another proposed ligand phenomenon is damping of phonon modes. In a study by Dukovic et al., the authors compared the phonon behavior in CdTe and CdTe/CdSe QDs capped with aliphatic or chalcogenide ligands using transient absorption spectroscopy.[125] They found that the chalcogenide ligands were able to dissipate phonons into the solvent medium, resulting in severe damping behavior. While the authors did not study emission line widths, this behavior should be kept in mind when designing narrow emitters.

When a small, blue emitter is desired, one must therefore minimize the effect of the large surface area−volume ratio and multitude of surface defect sites and phonon modes. Where ligands fail, whether in terms of complete passivation or maintaining colloidal stability, an inorganic shell can be introduced around the QD core. Gradually introducing monolayers of a wide-band-gap material around the core to form a type-I heterostructure has been shown to decrease the emission line width.[80,126,127] Not only are surface defects passivated but also the electron and hole wave functions are localized to the core material only, preventing coupling to phonons on the surface. However, it has been observed that there can be an optimal shell thickness for the emission line width—for CdSe cores shelled with ZnS, the line width increases again beyond 5 monolayers of shelling.[80] The authors hypothesized that this may be due to increased strain on the core lattice, leading to reconstruction and new defect sites. For type-II shells, one charge-carrier wave function (typically the electron) can be delocalized into the shell; therefore, electron coupling to surface phonons cannot be mitigated, and emission is typically still broad.

https://doi.org/10.1021/acs.chemrev.3c00097
Chem. Rev. XXXX, XXX, XXX−XXX

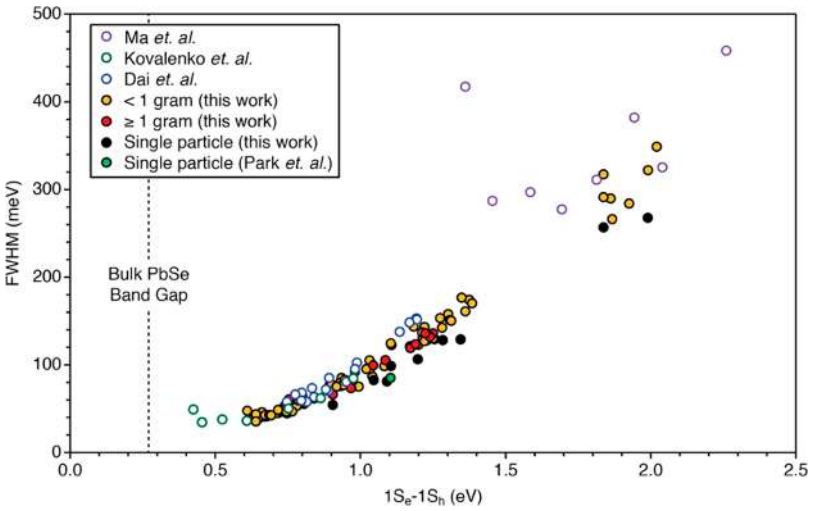

Figure 10. Full width half maximum of the lowest energy electronic transition versus its position ($1S_e-1S_h$) from a variety of selenourea precursors and reaction scales (solid yellow, solid red) and other reports (hollow violet,[132] hollow green,[133] and hollow blue[134]) compared to intrinsic single QD widths measured by hole burning (solid black) and 2D optical spectroscopy (solid green). The intrinsic broadening increases with smaller size, and the polydispersity is a relatively small contribution to the total line width in this case. Figure reproduced from ref 130. Copyright 2017 American Chemical Society.

3.2. Inhomogeneous Broadening—Static Broadening in Ensemble Spectra

For a collection of colloidal emitters that are inhomogeneously broadened, different emitters in the ensemble have different spectra—a different center frequency and/or line width. The overall spectrum of the collection of emitters is therefore a composite of the varied spectra of the individual emitters. In QDs, the primary sources of inhomogeneous or static broadening include size, shape, and composition or structural dispersity. We elaborate on each of these issues in the following sections.

3.2.1. Size and Shape Dispersity. Polydispersity in the size, shape, and surface termination of colloidal QDs contributes to the static inhomogeneous broadening of the PL spectrum. State-of-the-art QD synthesis produces polydispersities of a few percent[128] wherein the contribution to the optical line width is smaller than that of the dynamic broadening mechanisms described in section 3.1. Conventional estimates of the polydispersity, however, are obtained by ignoring the dynamic spectral broadening and converting the line width to a polydispersity using empirical relationships between the QD size and the band gap. This analysis overestimates the polydispersity,[129] particularly in CdSe, PbSe, and PbS nanocrystals where the dynamic width of a single QD is known to dominate the spectral width of the ensemble PL and is size dependent (Figure 10).[81,130,131] It is therefore important to be cautious when interpreting the absorption/emission line widths to assess the polydispersity.

Several other techniques can be used to directly measure the size polydispersity including small-angle X-ray scattering. This widely adopted approach enables direct in situ measurements of the polydispersity under realistic synthetic conditions.[135,136] However, both size polydispersity and shape contribute to the scattering line shape and are difficult to unambiguously deconvolute. These limitations inhibit the precise measurement of polydispersity using SAXS and limit its ability to distinguish between size distribution functions (e.g., Gaussian vs log normal).[137]

Electron microscopy remains the most widely practiced and direct method to measure size/shape dispersion. However, magnification errors, lower surface atom sensitivity, particle selection bias, ambiguities in particle boundary determination, and the thinness of the support limit its accuracy.[88,138] Algorithmic image analysis can eliminate user bias and improve high-resolution electron tomography.[139−142] Selection of the imaging technique (TEM vs ADF-STEM) and support film (e.g., 15−25 nm thick amorphous carbon vs <3 nm ultrathin carbon films) can improve the signal-to-noise ratios from 1:1 to 5:1; however, the change in support results in a decrease of the observed nanoparticle diameter.[78] Furthermore, analysis of the 2D images as projections of probability distributions of regular nonspherical shape distributions can improve the retrieval of the size/shape distribution of electron microscopy images; however, shape distributions do not contribute greatly to band-gap heterogeneity (Figure 8).[78] Further improvements may one day lead to statistical analysis of nanoparticle chemical formula distributions and a greater understanding of nanoparticle shape and surface polydispersity. Continued advances in the mass spectrometry of single particles may also lead to more precise measurements of polydispersity in size, shape, and chemical formula.[143]

3.2.2. Growth Mechanisms That Support Narrow Polydispersity. The nanoparticle size distribution is a direct consequence of the QD formation mechanism, a topic of long-standing interest for synthetic chemists. Recent reviews have covered mechanistic frameworks from classical and nonclassical nucleation theories[144] to growth models based on diffusion limitations[145,145] as well as digestive ripening[146] and aggregative processes.[147,148] A very recent review demonstrates the application of these models to the formation of metals and silicate nanoparticles.[149] Despite a relatively long history of study in this area, polydispersity is typically optimized empirically rather than being based on knowledge of the mechanism. Improved understanding of the connection between the polydispersity and the formation mechanism could eventually lead to rational methods to narrow the polydispersity and even narrower PL line widths.

https://doi.org/10.1021/acs.chemrev.3c00097
Chem. Rev. XXXX, XXX, XXX−XXX

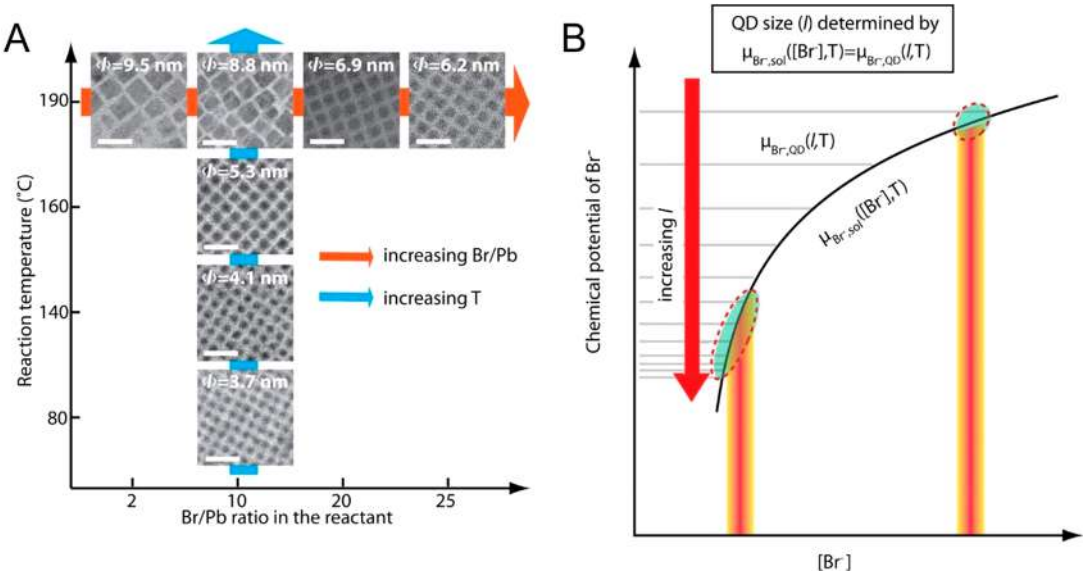

Figure 11. Size control via thermodynamic equilibrium in $CsPbBr_3$ QDs. (A) Dependence of the QD size on the Br to Pb ratio in the reactant and the reaction temperature. (B) A simple model illustrating the determination of the QD size via equilibrium of Br^- between the QD lattice and the solution medium. The QD size (l) for a given Br− concentration ($[Br^-]$) and temperature (T) is determined where the chemical potentials of Br^- in the QD (μBr^-, QD, series of gray horizontal lines for different l) and in the solution phase (μBr^-, sol, black curve) become equal. Adapted with permission from ref 176. Copyright 2018 American Chemical Society.

Canonical kinetic explanations of the polydispersity include the burst nucleation concept attributed to LaMer,[150] the size distribution focusing mechanism described by Reiss,[151] and the Ostwald ripening process described by Lifshitz−Slyozov−Wagner theory.[148] These mechanisms link the narrow polydispersity to a brief period of nucleation that precedes growth and a growth process that is limited by diffusion of monomers to the nanocrystals surface and a homogeneous ripening process that broadens the polydispersity while increasing the average size. However, recent kinetics investigations of InP,[152] CdSe,[153] PbS, and PbSe[131,154] QD syntheses have observed long nucleation periods that in some cases continue throughout the synthesis and are concurrent with growth as well as attachment-limited growth kinetics that support size distribution focusing. Indeed, a recent comprehensive review of semiconductor, metal, and oxide nanoparticle formation concluded that "compelling evidence for burst nucleation and diffusion-controlled growth in semiconductor nanoparticle formation is missing" and "a primary working hypothesis going forward to test and to try to disprove, is that nucleation may well more often be continuous".[145]

Size distribution focusing, for example, has been widely described since the first experimental demonstration with QDs.[129] Like many studies that followed, the absorption spectral line width was used to monitor the polydispersity under the assumption that the broadening is dominated by the polydispersity. However, since that time it has been demonstrated that the dynamic width of the single-QD optical spectrum is often the dominant contribution to the width of the ensemble emission (Figure 10). Moreover, the single-QD line width narrows as the size increases and can lead to erroneous claims of distribution focusing.[80,81,130,131] Another issue in this regard is the use of relative or percent polydispersities to argue on behalf of size focusing. True size focusing causes a reduction in the absolute polydispersity. On the other hand, the percent polydispersity of an unchanging absolute polydispersity will decrease as the average size grows. It is therefore important to measure and evaluate changes to the absolute polydispersity when analyzing the temporal evolution of the size distribution.

Size distribution focusing is well known to be a consequence of diffusion-limited growth kinetics.[151] As a result, claims of size focusing are often used in support of arguments for diffusion-limited growth mechanisms. This is largely because mechanisms limited by surface reactions are usually thought of as size independent. However, direct determination of the rate-limiting growth process requires the single-QD growth rate to be determined. In a homogeneous solution, the influence of the evolving solute concentration on QD growth kinetics should be determined, a technically challenging measurement that is rarely documented. Recent in situ electron microscopy in graphene liquid cells allowed the growth kinetics of individual colloidal metal nanoparticles to be directly measured.[155] In situ SAXS measurements of the growth and ex situ nuclear magnetic resonance measurements of the precursor concentration allowed the solute concentration and growth rate to be measured during growth of PbS QDs.[154] Population balance models based on these data support size-dependent growth kinetics that are slower than diffusion limitations and viscosity independent. The results clearly demonstrated that size distribution focusing under attachment-limited conditions can be attributed to the QD surface chemistry. Recent work on CdSe using a competitive growth strategy demonstrated a size-dependent reactivity that is greater than predicted by diffusion limitations.[153] Both the magnitude of the size dependence and its chemical origins across a variety of materials remain open areas of inquiry.

Recent studies of Ir[156] and Pd[157] nanoparticle growth have also concluded that size-dependent surface reactivity leads to size distribution focusing. In the case of Pd, the binding and coverage of phosphine ligands was argued to influence the solute attachment kinetics and cause the size focusing.[158] The size dependence of lead oleate binding to PbS[159] and the size-

https://doi.org/10.1021/acs.chemrev.3c00097
Chem. Rev. XXXX, XXX, XXX−XXX

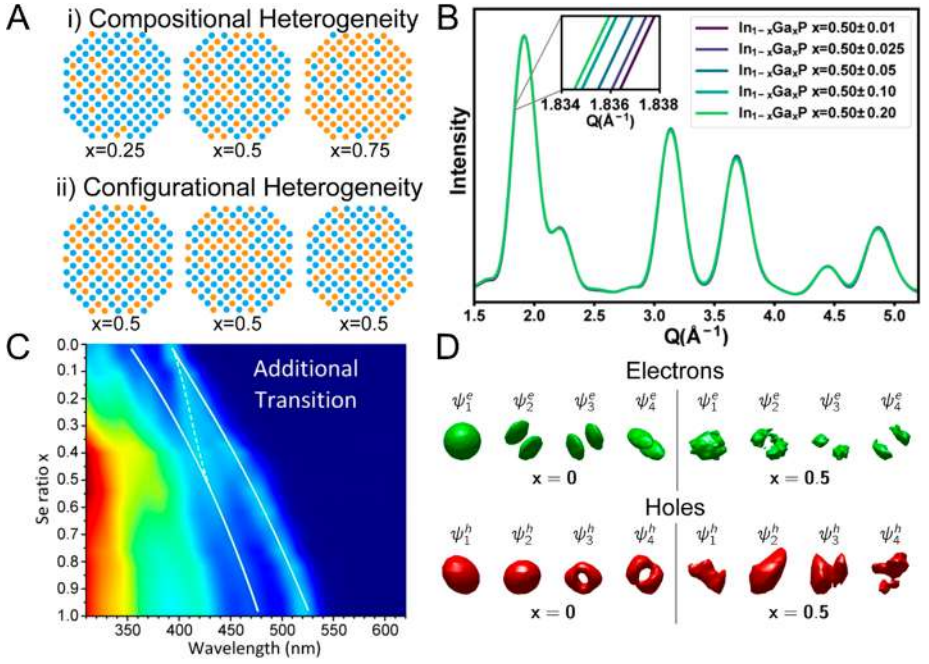

Figure 12. (A) Schematic representations of (i) compositional heterogeneity and (ii) configurational heterogeneity which can be present in an ensemble of alloyed semiconductor nanocrystals. (B) Simulated powder X-ray diffraction patterns for an ensemble of $In_{1-x}Ga_xP$ nanocrystals with different degrees of compositional heterogeneity. The resulting nearly identical diffraction patterns for samples with vastly different compositional heterogeneity show typical characterization methods cannot discern these important structural parameters. (C) UV−vis absorption spectra as a function of composition for $CdS_{1-x}Se_x$ showing the emergence of additional transitions at intermediate alloy compositions. (D) Electron (green) and hole (red) wave functions for pure CdS (left) and $CdS_{0.5}Se_{0.5}$ nanocrystals (right) showing the distortion of the electronic states due to alloying. Panel B reproduced with permission from ref 184. Copyright 2022 American Chemical Society. Panels C and D reproduced with permission from ref 186. Copyright 2014 American Chemical Society.

dependent surface reactivity of InP are also thought to determine the polydispersity of those materials.[152,160−162]

3.2.3. Thermodynamic Control over Size and Polydispersity. The recent observations of long nucleation times and size-dependent surface reactivity suggest an interesting evolution of the surface free energy with size that is reminiscent of so-called "magic size clusters". These "molecular" QDs have atomically precise formulas that result from the thermodynamic stability of their ligand coordination.[163−165] The high curvature of these small-sized nanocrystals provides the needed additional volume to pack surface ligands at high densities, preferentially stabilizing these small nanocrystals more effectively than large nanocrystals.[165] In line with this conclusion, it has been demonstrated that increasing the steric bulk of the ligand shell facilitates magic size cluster growth.[165]

Many reports have demonstrated that such clusters jump from one thermodynamically stable size to the next without accumulating intermediate sizes, a growth mode that could, in principle, lead to even more monodisperse QDs. Kinetics simulations of these growth pathways support kinetics that are limited by the nucleation of the subsequent 2D facet.[158,166−168] Several studies document cases where the stepwise size evolution is temperature dependent (CdSe,[169] ZnSe,[170] ZnTe,[171] PbSe,[172] InP,[173] and InAs[174]) such that growth to larger sizes requires higher temperatures. However, increasing the temperature eventually leads to polydisperse products.[170,175] Additionally, an interesting example of size and shape distribution control in the growth of $CsPbBr_3$ QDs appears to result from a thermodynamic equilibrium governed by surface ligand binding. The effect of temperature and bromide concentration on the particle size and size distribution is consistent with a control mechanism that results from dynamic exchange of Br^- with the QD lattice (Figure 11).[176] Cooling of the reaction mixture to less than 100 °C was found to inhibit the dynamic process and enable isolation of narrow size populations. Synthetic conditions that enable the thermodynamic control of particle sizes and distribution could provide powerful new methods to prepare highly monodisperse QDs.

3.2.4. Digestive Ripening. Another growth mode that creates extraordinarily narrow polydispersities is called digestive ripening. Experimental observations and theoretical understanding of this process were comprehensively summarized in a recent review.[146] Seminal observations in this field describe the ripening of polydisperse gold nanoparticles into monodisperse ensembles with a smaller average size upon heating with alkylthiols[177,178] or other ligands. The decrease in the average size and polydispersity is the inverse of conventional Ostwald ripening processes and suggests that digestive ripening lowers the total energy by maximizing the surface area. Such a conclusion requires that surfaces are thermodynamically favored structures, which might result from a high density of surface ligand bonds. The synthetic approach has been extended to CdSe QDs using tri-*n*-octylphosphine and hexadecylamine surfactants[179,180] and CdS, CdSe, $CsPbBr_3$, and $CuSnZnS_4$ using oleylamine.[181] A deeper understanding of driving forces can enhance our understanding of polydispersity control across different mechanisms while re-emphasizing the significance of surface structure in relation to the polydispersity and the resulting PL line width.

3.2.5. Compositional Variation of Alloys and Solid Solutions. Alloy compound semiconductors as core materials (e.g., $CdSe_{1-x}S_x$ and $In_{1-x}Ga_xP$)[182,183] and as gradient shell

https://doi.org/10.1021/acs.chemrev.3c00097
Chem. Rev. XXXX, XXX, XXX−XXX

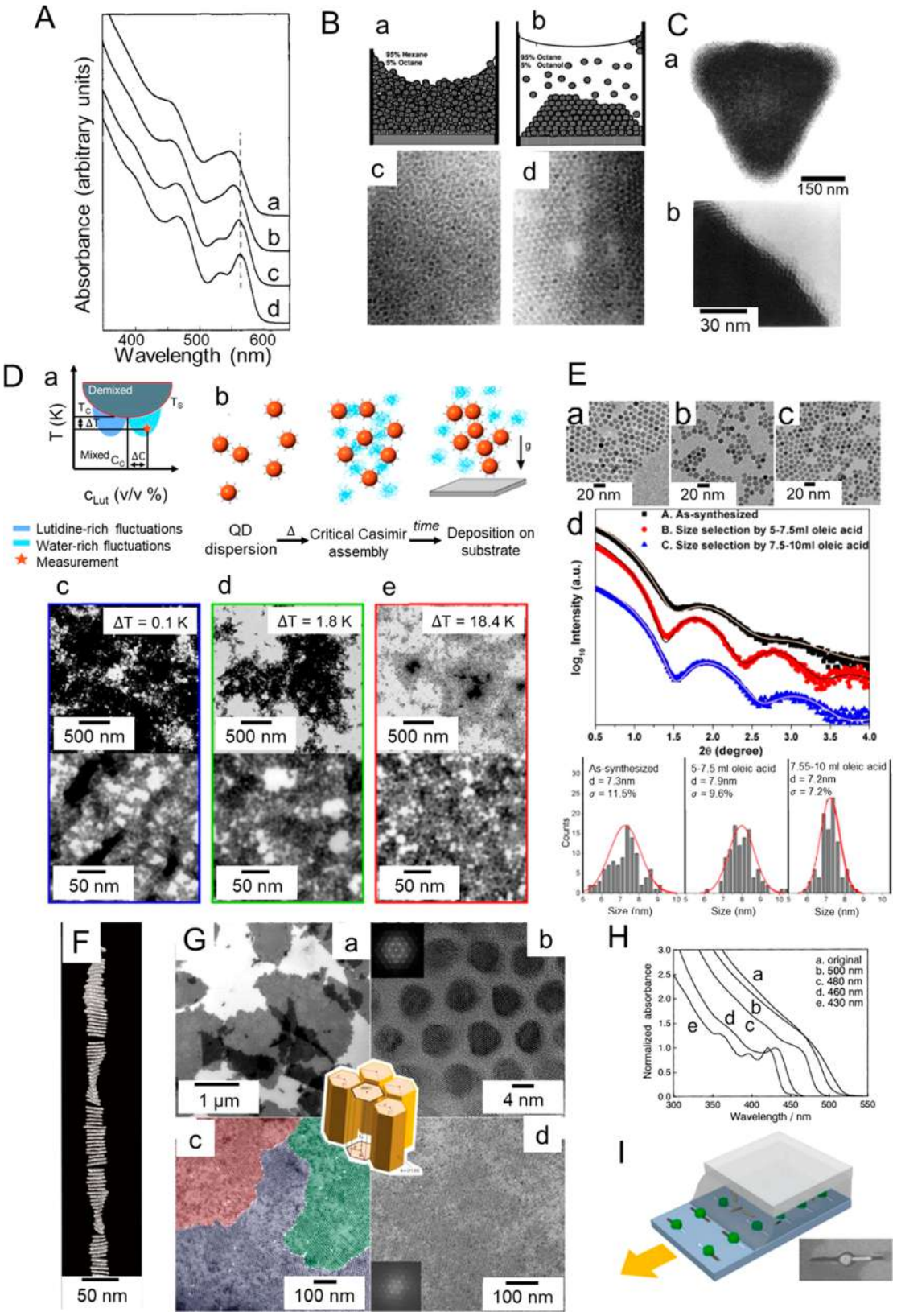

Figure 13. Strategies for the separation and purification of colloidal nanocrystals. (A) Absorption spectra of CdSe nanocrystals separated after the addition of increasing amounts of antisolvent. Adapted with permission from ref 189. Copyright 1993 American Chemical Society. (B) Glassy and crystalline structures self-assembled from CdSe colloidal nanocrystals undergoing flocculation under different conditions. Adapted with permission from ref 191. Copyright 1995 Massachusetts Institute of Technology. (C) CdSe nanocrystal superlattice self-assembled through the controlled addition of antisolvent. Adapted with permission from ref 192. Copyright 1995 The American Association for the Advancement of Science. (D) Critical Casimir forces induce the self-assembly of glassy structures of CdSe nanocrystals. Adapted with permission from ref 196. Copyright 2019 American Chemical Society. (E) The use of depletion forces through the controlled addition of oleic acid narrows the size distribution of

https://doi.org/10.1021/acs.chemrev.3c00097
Chem. Rev. XXXX, XXX, XXX−XXX

Figure 13. continued

$Mn_{0.44}Fe_{2.56}O_4$ nanocrystals. Adapted with permission from ref 202. Copyright 2016 American Chemical Society. (F) Ribbons of stacked CdSe nanoplatelets assembled through the addition of excess oleic acid. Adapted with permission from ref 204. Copyright 2017 Creative Commons Attribution Noncommercial License 4.0. (G) Crystalline superstructures of CdSe/CdS nanorods formed through the addition of excess oleic acid. Adapted with permission from ref 205. Copyright 2010 American Chemical Society. (H) Absorption spectra of CdS nanocrystals undergoing size selection through photoetching. Adapted with permission from ref 207. Copyright 1995 CSJ. (I) Trap-mediated separation of 130 nm gold nanorods and 80 nm $NaYF^4$:Yb^{3+}, Er^{3+} nanophosphors. Adapted with permission from ref 223. Copyright 2014 American Chemical Society.

materials (e.g., CdSe/$Cd_xZn_{1-x}S$, InP/$ZnSe_{1-x}S_x$) provide additional degrees of freedom for optimizing strained interfaces, band alignment, and confinement potential. However, this creates additional degrees of structural heterogeneity that can influence the line width, and thus, approaches to mitigate this synthetically must be developed. For typical compound semiconductors (e.g., CdSe, InP, etc.) the above-discussed size and shape distributions are the primary factors that govern static inhomogeneous broadening. These parameters also affect alloy semiconductors, indicating that key design principles, a narrow size distribution, and high shape purity remain as important considerations for alloy semiconductors as well. For alloy semiconductor nanocrystals, variation of the composition also has the potential to impact the line width in two ways: (1) compositional heterogeneity within the *ensemble* of nanocrystals, which we will denote as compositional heterogeneity (Figure 12Ai), and (2) heterogeneity in the distribution of the elements within *individual* nanocrystals, which we will denote as configurational heterogeneity (Figure 12Aii).

Compositional heterogeneity within the ensemble can affect the line width due to the composition-dependent band gap of semiconductor alloys. To first order, the band gap of an alloy semiconductor is simply a linear interpolation of the band gaps of the parent compounds (Vegard's law). Thus, nanocrystals that have compositions that deviate from the ensemble average will have different band gaps than the average, resulting in an ensemble line width that is broader than that of a given nonalloyed semiconductor. This effect is convoluted by other factors, such as the size/shape distribution and dynamic broadening. Empirically, ensemble line widths for alloy semiconductor nanocrystals are typically larger than their binary counterparts, suggesting additional heterogeneity is present in these samples; however, systematic studies precisely controlling for effects of the size distribution have not been reported. Synthetic challenges for preparing alloy semiconductor nanocrystals highlight potential ways in which compositional heterogeneity may be present in these samples, but the composition distribution cannot be easily determined experimentally. For example, in many cases, synthesis of alloy materials involves precursors with mismatched reactivity. This may result in nonuniform incorporation of the different alloy components depending on their size within the distribution. For example, in size-focusing growth, smaller nanocrystals grow faster to "catch up" in size to the larger ones; however, at this point in the reaction, the monomers may be depleted in the more reactive precursor. Cation exchange is another method for preparation of alloy nanocrystals which also has potential for introducing compositional heterogeneity. In these reactions, it has been determined that smaller nanocrystals undergo cation exchange faster than larger nanocrystals, potentially leading to a size-dependent composition within an ensemble upon cation exchange.[184] This potentially could exacerbate the effect of the size distribution if the alloy reaction creates a semiconductor with a larger band gap or counteracts the effect if the reaction creates a narrower band-gap semiconductor. Many discussions around compositional heterogeneity in alloy semiconductors remain qualitative and unproven mostly because direct quantification of the composition variation in nanocrystal ensembles is limited by the insensitivity of standard characterization tools to this parameter (Figure 12B). Thus, a systematic understanding of the effects of composition variation on line width in an ensemble of nanocrystals remains elusive.

Compositional heterogeneity in individual alloy nanocrystals is a second concern that can affect the emission line width. For a bulk crystal of a random alloy, all possible configurations are self-averaged, and thus, heterogeneity of their materials properties typically is not observed. For a finite-sized nanocrystal, the small size may not average over all alloy configurations and particle-to-particle variation in optoelectronic properties may result.[185] Thus, nanocrystals with identical nominal alloy compositions can display different emission energies or line widths. In addition, the configurational disorder resulting from alloying can distort the symmetry properties of electron or hole wave functions, increasing the oscillator strength of transitions which are dark in pure systems (Figure 12D). This can increase the number of energetically distinct states which a nanocrystal can emit light from and thus increase the line width or introduce new transitions (Figure 12C).[186]

3.2.6. Role of Postsynthesis Purification To Achieve Narrow Emission Line Widths. Purification and separation methods offer an often-overlooked strategy to obtain nanocrystal samples with narrow emission spectra. When static inhomogeneous broadening dominates the line width, the dependence of the confinement energy on the nanocrystal size[187] suggests that nanocrystal ensembles with a smaller size dispersion have narrower emission spectra. Size- and shape-selective techniques are widely used to produce nanocrystal ensembles with narrower emission. When static broadening dominates (which is not always true for modern syntheses, see sections 3.1 and 3.2.1), comparing the line width of the emission or absorption peaks before and after purification allows the quantification of the decrease in inhomogeneous broadening due to the increase in sample monodispersity.

Since their introduction, solvothermal heat-up[188] or hot-injection methods[189] have been accompanied by techniques that facilitate the selective extraction of a near-monodisperse fraction from a polydisperse ensemble. As a prime example, the controlled addition of a "bad" solvent, also known as an antisolvent, to a dispersion of nanocrystals has proven beneficial in separating and isolating specific sizes from a polydisperse ensemble. This technique is known as *size-selective precipitation*.[189,190] Murray et al. have shown how size-selective precipitation can be used to decrease the fwhm of the first exciton peak of CdSe nanocrystals from 25 nm (99 meV) to 17 nm (65 meV), as shown in Figure 13A.[189] Depending on sample parameters such as the choice of solvent/antisolvent pairs, the distributions of sizes, shapes, and compositions of nanocrystals within the ensemble, and the concentration of the dispersion,

https://doi.org/10.1021/acs.chemrev.3c00097
Chem. Rev. XXXX, XXX, XXX−XXX

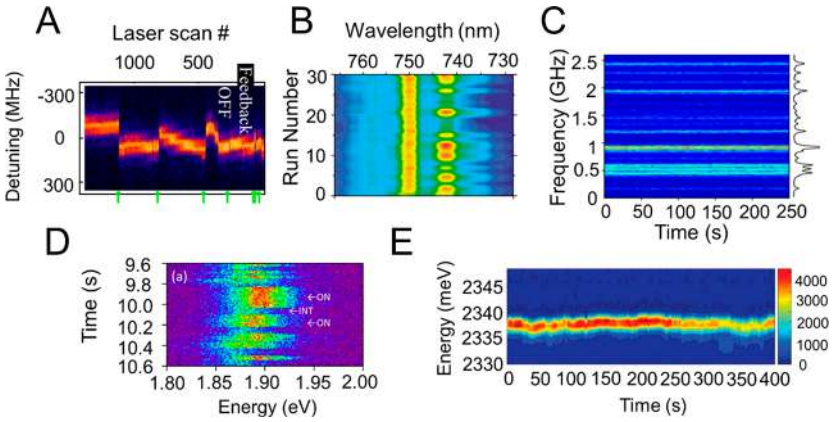

Figure 14. Tracking spectral diffusion via grating spectroscopy for (A) nitrogen vacancy centers,[229] (B) epitaxial III−V QDs,[230] (C) single organic molecules (dibenzoterrylene, DBT),[231] (D) II−VI colloidal QDs (CdSe/ZnS),[232] and (E) metal−halide perovskite QDs ($CsPbBr_3$).[62] Panel A is adapted with permission from ref 229. Copyright 2012 Creative Commons Attribution 3.0. Panel B is adapted from with permission ref 230. Copyright 2004 AIP Publishing. Panel C is adapted with permission from ref 231. Copyright 2019 John Wiley and Sons. Panel D is adapted with permission from ref 232. Copyright 2016 American Chemical Society. Panel E is adapted with permission from ref 62. Copyright 2018 The American Association for the Advancement of Science.

increasing the volume fraction of antisolvent within the mixture leads to nanocrystal aggregation (Figure 13B).[191] When this procedure is performed correctly, the final aggregates are known as *nanocrystal superlattices* as they incorporate nanocrystals of similar size into a crystalline lattice (Figure 13C).[192] A centrifugation step can be used to separate the superlattices from the remaining nanocrystal ensemble. The nanocrystal superlattices can then be redispersed in a good solvent, resulting in a dispersion with improved monodispersity compared to the initial ensemble. This separation process can be repeated until the desired range of nanocrystal sizes is obtained. More attractive nanocrystal species of the ensemble need milder destabilization conditions to reach flocculation, corresponding to a lower volume fraction of antisolvent. Since the magnitude of van der Waals forces increases with the square of the nanocrystal volume ($\propto R^6$, where R is the nanocrystal radius),[193] larger nanocrystals separate out at lower volume fractions of antisolvent than smaller nanocrystals. Furthermore, since the magnitude of van der Waals forces is higher for planar (plate-like) than round (rod-like or spherical) shapes,[193] size-selective precipitation remains the most effective, straightforward, and widespread mechanism to extract near-monodisperse samples from an initially polydisperse ensemble.

The temperature of the solvent mixture represents a crucial parameter in the separation and purification of nanocrystals. While this effect has been long known for microscale colloids,[194] it has been extended to the nanoscale only recently,[195] resulting in a growing area of interest.[196−198] When the solvent/antisolvent mixture is close to its critical point, solvent density fluctuations arise (Figure 13Da). The confinement of these fluctuations between the surfaces of nanocrystals leads to a net attractive force known as the critical Casimir force (Figure 13Db).[199] The magnitude of this force is sensitive to the size and shape of the nanocrystals and can be used to trigger the assembly of nanocrystals into aggregates with a temperature-sensitive morphology (Figure 13Dc−e).[195−197,200]

Besides the addition of an antisolvent, the use of other additives such as polymers or surfactants can induce the flocculation of nanocrystals through depletion interactions.[201] Since the magnitude of these interactions depends on the size of the additive relative to the nanocrystal ($\propto R/R_g$, where R_g is the gyration radius of the depletant) and its volume fraction in the mixture, depletion forces can be used to separate and isolate specific sizes and shapes of nanocrystals from a polydisperse ensemble. For instance, the use of the most common surfactant in nanocrystal synthesis, oleic acid, has allowed the size-selective precipitation of spherical nanocrystals of $Mn_{0.44}Fe_{2.56}O_4$, decreasing the sample polydispersity from 11.5% to 7.2% (Figure 13E).[202] Notably, depletion interactions are very sensitive to shape as this influences the magnitude of the depleted volume. Since planar structures result in larger depleted volumes than spheres, the addition of a depletant, such as oleic acid or cetyltrimethylammonium chloride, to the synthetic mixture of nanoplatelets[57,203] with spheres results in the efficient separation of the two populations. Upon addition of oleic acid, the CdSe nanoplatelets assemble into stacks or ribbons (Figure 13F),[204] allowing for the separation of nanocrystals by shape. The controlled use of depletion interactions can induce the formation of nanocrystal superlattices: In a successful demonstration, Baranov et al. triggered the crystallization of CdSe/CdS nanorods into superlattices by increasing the volume fraction of depletants such as oleic acid and poly(ethylene glycol) methacrylate (Figure 13G).[205] Since the magnitude of depletion interactions increases with thermal energy, Wu et al. were able to induce the self-assembly of nanocrystals into superlattices at temperatures higher than 230 °C.[206]

The use of external triggers, such as static or variable electromagnetic fields, can induce the assembly of nanocrystals to yield a more monodisperse product from a polydisperse ensemble. For instance, the resonant photoexcitation of semiconductor nanocrystals can induce photoetching, causing a shift in the distribution of sizes within the ensemble (Figure 13H).[207] This mechanism can be considered a particular case of hole burning[208] and has been studied in detail for aqueous dispersions of CdS[207,209−211] and more recently CdTe[212] nanocrystals. Since nanocrystals dispersed in water are usually charged, electric fields can be used to isolate specific fractions of the ensemble. This method, known as *electrophoresis*, has been explored in the literature since the 1990s as a way to deposit ordered films of nanocrystals on a substrate.[213−215] However, the possibility of using the charges attached to nanocrystals with different sizes for sorting purposes remains relatively unex-

https://doi.org/10.1021/acs.chemrev.3c00097
Chem. Rev. XXXX, XXX, XXX−XXX

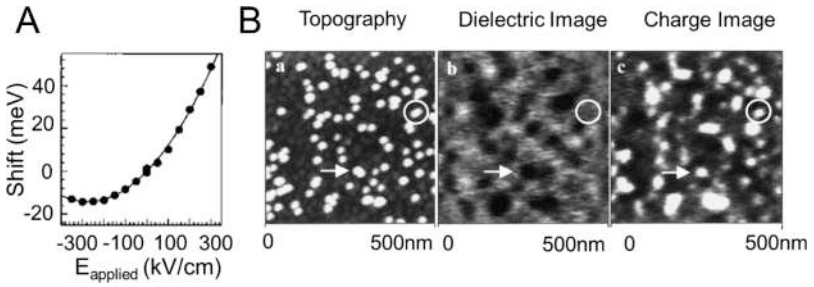

Figure 15. (A) Application of an external electric field to CdSe QDs between interdigitated electrodes. With the application of an external field, the emission energy of the QD shifts; this observed spectral diffusion behavior can be described with the quantum-confined Stark effect (QCSE).[266] (B) Electrostatic force microscopy of CdSe QDs on poly vinylbutyral (PVB) on highly oriented pyrolytic graphite (HOPG). (a, b, and c) Change in cantilever resonance frequency, at ω and 2ω. A neutral QD is indicated by the circle; the arrow indicates a positively charged QD.[258] Panel A is adapted with permission from ref 266. Copyright 1997 The American Association for the Advancement of Science. Panel B is adapted with permission from ref 258. Copyright 1999 American Physical Society.

plored. The same concept can also be extended to magnetically responsive nanocrystals with the use of static magnetic fields.[216,217] The main downside of using external triggers for nanocrystal separation consists in the lack of generalized approaches to identify nanocrystal/trigger pairs: each nanocrystal type needs to be responsive to the selected trigger for the method to succeed. The use of nanocrystal heterostructures that pair orthogonal physical responses within the same nanoscale colloid, such as heterodimers,[218−220] might eventually remove this limitation.

Specific designs of sample environment can also help extract predetermined sizes and shapes from a polydisperse nanocrystal ensemble. Recent advances in lithographic patterning have allowed the extension of template-assisted assembly from the microscale down to the nanoscale.[221,222] Pairing nanoscale patterning with self-assembly has resulted in the trapping of specific sizes and shapes of individual nanocrystals and their clusters in the nanometric recesses of solid-state substrates (Figure 13I).[223−227] The design of the trap must be carefully optimized to achieve the stable trapping of nanocrystals,[226] which can then be released to generate a monodisperse dispersion.[228] The trapping of nanocrystals with complementary properties within neighboring or adjacent trap sites can lead to the development of interesting new optical features. For instance, trapping a nanophosphor near a plasmonic nanocrystal results in the enhancement of the PL signal.[223] Instead, trapping several gold nanocrystals within the same trap can result in the development of optical features from the assembled structure as a whole; this has been demonstrated for the case of equilateral triangles of gold nanorods and metamolecules of gold nanospheres and nanopolygons.[223,225,227]

3.3. Spectral Diffusion—Broadening from Environmental Factors

Measured over short times (nanoseconds), the line widths of some colloidal QD emitters are already nearing the transform limit imposed by the radiative lifetime.[62] However, when measured over longer times, the emission peak position of almost all known quantum emitters (not just colloidal QDs) drifts over time (Figure 14). This drift of the emission peak, known as *spectral diffusion*, can be an important contributor to the line width of colloidal emitters. Spectral diffusion is a ubiquitous phenomenon and is often easily observed at cryogenic temperatures where the various phonon-broadening contributions from the emitter and its environment have been reduced. Indeed, spectral diffusion has been reported from single emitters in systems as diverse as diamond vacancies (Figure 14A),[229] epitaxially grown III−V QDs (Figure 14B),[230] single organic molecules (Figure 14C),[231] colloidal II−V QDs (Figure 14D),[232] and colloidal halide perovskite QDs (Figure 14E).[62] For colloidal materials, spectral diffusion has been reported for shapes including nanorods,[233] nanoplatelets,[234] and dot−rod heterostructures.[235] In many of these systems, not only does the instantaneous emission energy change with time but also the intensity (PL quantum yield) varies as well. This intensity variation is known as fluorescence intermittency,[236] blinking,[237] or flickering[238,239] and is often coupled with spectral diffusion as the nonradiative recombination rate and emission energy both fluctuate, sometimes due to related processes, as we discuss below.

Given its ubiquity, spectral diffusion has been studied in systems such as II−VI colloidal QDs and III−V epitaxial QDs[240−242] and less well in newer materials systems including halide perovskite QDs.[243,244] Consistent with the focus of this *Chemical Reviews* issue, we emphasize spectral diffusion in colloidal emitters. Nevertheless, it is useful to compare trends observed across many systems. For single colloidal emitters, spectral diffusion represents an important contribution to the total line width, especially at lower temperatures. Generally, spectral diffusion is less well studied than PL intermittency (i.e., blinking) in colloidal QDs, in part because of the drive to use colloidal QDs as fluorescent biological labels for single-particle tracking. However, as interest develops in employing colloidal emitters in quantum information science, including their use as single-photon sources and spin qubits,[243] it is important to understand and minimize spectral diffusion, so that emitters may approach transform-limited line widths needed for use as sources of coherent quantum light.

3.3.1. Causes of Spectral Diffusion Behavior in Colloidal Materials. One reason spectral diffusion is so common is that both the environment and the emitter fluctuate in time. Rearrangements of local bond geometries, dipole moments, and, notably, charges all perturb the potential energy landscape of both the ground and the excited states of a quantum emitter, leading to spectral shifts across many different time scales.[245−247] While some of these rearrangements can be frozen out at low temperature,[248−251] others are induced by the photoexcitation itself[252] and need to be understood and suppressed with different strategies.

Perhaps one of the most important sources of spectral diffusion and fluorescence intermittency (or blinking) in colloidal QDs is the photoinduced charge redistribution in the QD, its surface, and the surrounding environment. This effect is

https://doi.org/10.1021/acs.chemrev.3c00097
Chem. Rev. XXXX, XXX, XXX−XXX

known in the epitaxial semiconductor quantum-well literature[253] and explored by Bawendi et al. for CdSe QDs,[9] for which they explained spectral diffusion in terms of a quantum-confined Stark effect (QCSE). Importantly, they demonstrated, first, that applied electric fields could shift the PL of single CdSe emitters (Figure 15A) and, second, that the largest spectral jumps often accompany blinking-off and blinking-on events (Figure 15B).[11] This correlation between blinking events and spectral diffusion is highly suggestive, since dark states are widely attributed to photoionization events,[254−256] with the residual charge leading to a dark (nonemissive) dot via an efficient Auger process.[254−257] Further evidence in support of this mechanism was provided by direct confirmation of QD photoionization via electrostatic force microscopy[258] and also by the observation that QDs with wide-gap shells that prevent photoionization also tend to suppress blinking[259−262] and reduce spectral diffusion.[263−265]

Furthermore, in colloidal systems including CdSe, CdSe/ZnS, and $CsPbBr_3$, studies report that exciting a QD far above the band gap leads to increased spectral diffusion and blinking, presumably because the excess energy increases the chance of photoionization,[252,267−269] or that the excess above-gap energy can lead to rearrangements, including motion of trapped charge, at the QD surface.

Within a photoionization model, we expect the surface of the QD to play a critical role. Not only is the surface (or a strained core/shell interface) a likely source of charge trapping but also the ligands themselves can play a role in charge localization. For instance, adsorption of a single QD surface ligand can result in near complete quenching of a QD fluorescence,[270] and we speculate that rearrangements in the organic ligand shell could be important. Indeed, Braam et al. used a simple model based on the Stark effect to calculate that the rearranging charges responsible for spectra diffusion residing either directly on the QD surface or in its ligand shell.[271] Using photon correlation Fourier spectroscopy (PCFS), Beyler et al. were able to probe spectral diffusion dynamics across microsecond time scales inaccessible to grating spectroscopy. They observed variations in the spectral diffusion rate and magnitude, which they rationalized as ligand rearrangement perturbing trapped carriers within the QD.[247] Other studies report that the magnitude of spectral diffusion is independent of the polymer matrix, again suggesting that the QD and its surface are essential variables.[76] Many other reports have implicated the surface chemistry in spectral diffusion. Early work by Empedocoles et al. compared organic-ligand-coated CdSe QDs with CdSe overcoated with ZnS.[252] They reported that QDs coated only with organic ligands exhibited larger spectral shifts, confirming the importance of surface states in spectral diffusion. Trapped surface charges have also been reported to modulate the strength of the exciton−phonon coupling via the Fröhlich interaction, which emphasizes the importance of controlling the surface chemistry in order to minimize the homogeneous/dynamic line width both at short (sub-ns) times as well as at the longer times over which spectral diffusion is most important.[272]

Finally, multiexciton and Auger physics can also play a role in spectral diffusion in colloidal QDs. Although the exact threshold is system dependent, high-intensity illumination, on the order of ~20 $\mu J/cm^2$ for single CdSe/ZnS QDs[273] (as often occurs in confocal systems trying to achieve high signal levels), can excite biexciton states, which, in addition to opening high-efficiency Auger decay pathways leading to charged QDs,[269,274] can also have spectrally distinct emission features.[275,276] As a result, QDs excited at higher excitation *intensities* also tend to exhibit more spectral diffusion and blinking[267,252] as well as more complex spectral line shapes associated with the radiative decay of species such as biexcitons and trions.[232,277,278]

3.3.2. Prospects for Reducing Diffusion and Blinking. In some ways, the importance of photoinduced charge fluctuations in controlling spectral diffusion of QDs is similar to the significance of surface state charge fluctuations in diamond vacancy emission. This suggests that improved understanding of interface and surface passivation in QDs could potentially reduce spectral diffusion. For nitrogen vacancy (NV) centers in diamond, great progress was made in reducing lifetime variation,[279] spectral diffusion, and fluorescence intermittency[280] in near-surface defects, improving the quality of shallow, implanted defect centers relative to naturally occurring vacancies by optimizing fabrication and implementation conditions.[281] For example, pulsed optically detected magnetic resonance (ODMR) measurements (Figure 16A),

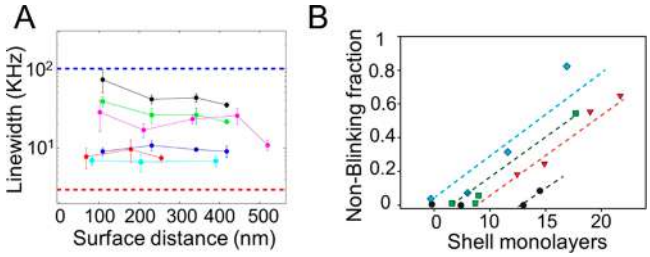

Figure 16. Surface control of line width and intermittency. (A) Pulsed optically detected magnetic resonance (ODMR) line width for single nitrogen vacancy (NV) centers grown by incorporation during growth of a purified ^{12}C film. Each trace represents the line width of a single defect center after successive etch steps. The blue trace represents typical NV center line widths (10^2 kHz ≡ 4.14×10^{-10} eV). The red trace represents the minimal possible line width due to microwave broadening.[282] (B) Nonblinking fraction of "giant-shell" CdSe/CdS for different core diameters as a function of shell thickness: black = 2.2 nm, red = 3.0 nm, green = 4.0 nm, and blue = 5.5 nm.[260] Panel A is adapted with permission from ref 282. Copyright 2012 American Chemical Society. Panel B is adapted with permission from ref 260. Copyright 2012 American Chemical Society.

which allow for estimation of the NV center line width, of the as-fabricated NV centers demonstrated improved line widths compared to previously reported values for defect centers.[282]

In contrast, while much is known for colloidal materials, there is still much that is unknown. It remains an open question, for instance, if the high dielectric constant of halide perovskites[283] and large polaron physics[284] might contribute to making them more resistant to local environmental charge fluctuations (at least on slower time scales) or if shelling strategies reaching atomic precision with sufficient thickness can eliminate coupling to surface defects entirely, thereby suppressing the largest sources of spectral diffusion.

3.3.2.1. Surface and Interface Control for Reducing Blinking and Spectral Diffusion. As previously mentioned, growing wide-band-gap inorganic shells over colloidal QDs has been a subject of intense study and is known to help suppress blinking and, to a less-studied extent, spectral diffusion as well.[256] In early work, ZnS shells minimized spectral diffusion for CdSe, though large dot−dot variations in the effectiveness of this approach suggested that early shelling strategies yielded incomplete shell coverage or led to the incorporation of defects at the CdSe/ZnS interface.[252] Later synthetic work improved

https://doi.org/10.1021/acs.chemrev.3c00097
Chem. Rev. XXXX, XXX, XXX−XXX

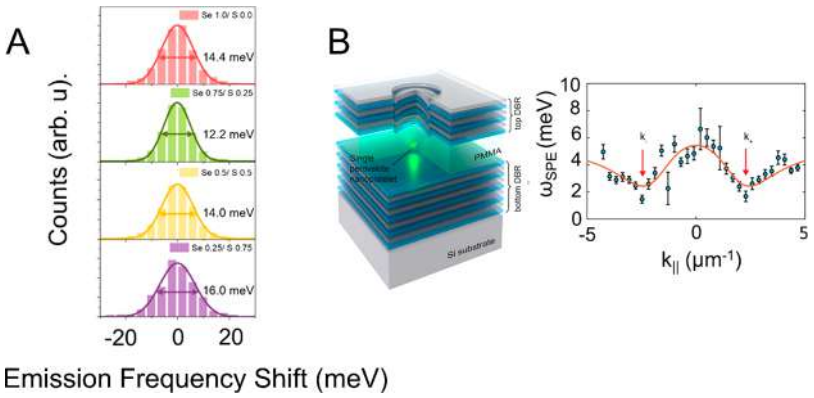

Figure 17. Mitigation strategies for spectral diffusion. (A) Surface engineering to reduce spectral diffusion in varying interface compositions (Se to S ratio) of core−shell−shell InP/$ZnSe_{1-x}S_x$/ZnS QDs. Frequency shift histograms are plotted for 40−60 single-dot QDs, fit to Gaussian functions, and the fwhm's are used compare the magnitude of spectral diffusion that occurs in each QD composition. The fwhm's of the Gaussian peaks are shown.[265] (B) Cavity integration and reduction of spectral diffusion. Angle-resolved emission (emission angle measured at $\theta = \sin^{-1}(k_{\parallel}/k_0)$ line width of the perovskite nanoplatelet ($CsPbBr_3$) ω_{SPE} integrated with a quasi-2D cavity (schematic left) of $k_{\parallel}$ measured at 35 K. k_+ and k_- mark the positive and negative $k_{\parallel}$ values where line width broadening is suppressed (minimal emitter and cavity detuning) via minimization of spectral diffusion channels.[295] Panel A is adapted with permission from ref 265. Copyright 2022 American Chemical Society. Panel B is adapted with permission from ref 295. Copyright 2022 American Chemical Society.

the quality of core−shell interfaces by optimizing shell thickness and composition, resulting in QDs displaying suppressed blinking, with 68% of QDs remaining bright for measurement times of 5 min with minimal blinking.[255] Interestingly, the authors found that the nonblinking fraction depended strongly on the number of shell monolayers, highlighting the importance of optimizing thicker shells for achieving nonblinking QDs. Further improvements in ensemble PLQY and reductions in dot-to-dot inhomogeneity were achieved by optimizing the synthesis of giant shells (>10 shell monolayers);[259] in this case, the percentage of nonblinking QDs depends on both the core diameter and the number of shell monolayers (Figure 16B).[259] In later work, Ghosh et al. reported that the fraction of nonblinking giant shell CdSe/ZnS QDs synthesized via successive ionic layer adsorption and reaction (SILAR) could be as high at 85% during 60 min of continuous observation.[260] Similar work in III−IV InP QDs corroborated the importance of the core−shell interfaces in those materials. Lee et al. investigated varying interface compositions of core−shell−shell InP/$ZnSe_{1-x}S_x$/ZnS QDs and attributed reduced blinking and spectral diffusion to strain reduction via gradient shells: a midshell composition of $ZnSe_{0.75}S_{0.25}$ led to minimization of defects at the interface through reduced lattice strain, resulting in a decrease in the overall PL line width (Figure 16A) compared to other gradient midshell compositions.[265]

3.3.2.2. Cavity Control. Another promising, though less studied, strategy for mitigating spectral diffusion is the use of optical cavities or nanoscale plasmonic antenna to modulate the emissive properties of colloidal QDs. For a quantum emitter weakly coupled to a photonic cavity or antenna structure, the radiative decay rate is given by Fermi's golden rule

$$\Gamma_{i\to f} = \frac{2\pi}{\hbar}\langle\psi_f|H'|\psi_i\rangle^2\rho(E) \quad (3)$$

Here, the intrinsic radiative decay rate, $\Gamma_{i\to f}$, is given by the transition matrix elements $\langle\psi_f|H'|\psi_i\rangle$, where ψ_i and ψ_f represent the wave functions of the initial and final states (this same relationship determines the absorption coefficient). Importantly, the density of states term contains a contribution from the local photonic mode density (or local density of optical states LDOS $\rho(E)$),[285] which quantifies the density of electromagnetic modes available at that point in space. Classic cavity structures including microcavities,[285] waveguides,[286] and metasurfaces[287] and plasmonic structures such as metal nanoparticles[288−291] can all modify the local photonic mode density, enhancing (or suppressing) the radiative decay rate of an emitter.[292] Cavity coupling is frequently used with quantum emitters because enhancing the radiative decay rate (reducing the population lifetime (T_1)) is advantageous when seeking to obtain a transform-limited line width. However, we note that cavity coupling can also help reduce spectral diffusion and fluorescence blinking; by increasing the radiative decay rate, light emission can more easily outcompete nonradiative processes such as photoionization events that contribute to spectral diffusion and blinking. Indeed, cavity integration has been shown to reduce spectral diffusion in epitaxial QDs, likely through radiative rate enhancement.[291,293,294] The effects of cavity coupling on the spectral diffusion of colloidal emitters has been less well studied; however, Huang et al. reported that cavity integration suppressed spectral diffusion and reduced the emitter line width for temperatures of up to 40 K for halide perovskite nanoplatelets coupled to a quasi-2D cavity (Figure 17B).[295] While there are fairly few studies of spectral diffusion of colloidal QDs in cavities, we can infer the positive effects might be more general by examining the larger literature on the effect of cavity integration on the related problem of blinking statistics of colloidal emitters. For example, Novotny et al. found that a QD emitter coupled to a plasmonic cavity emitter shows a slowed on-to-off state transition, resulting in a reduction in PL blinking relative to uncoupled QDs.[291] Similar results were demonstrated by Yuan et al., who coupled a CdSe/$Cd_xZn_{1-x}S$ gradient shell QD to a metallic mirror and observed 3.6-fold enhancement of the radiative lifetime as well as a reduction in the photoionization rate.[296] Given the rapid advances that have been made in nanophotonics, metasurfaces, and cavity integration, we speculate that working to maximize radiative rate enhancement could be fertile ground to explore in the quest to reduce spectral diffusion and blinking in colloidal materials. For instance, improvements in radiative rates by maximizing the Purcell factor can be realized through novel cavity designs for colloidal

https://doi.org/10.1021/acs.chemrev.3c00097
Chem. Rev. XXXX, XXX, XXX−XXX

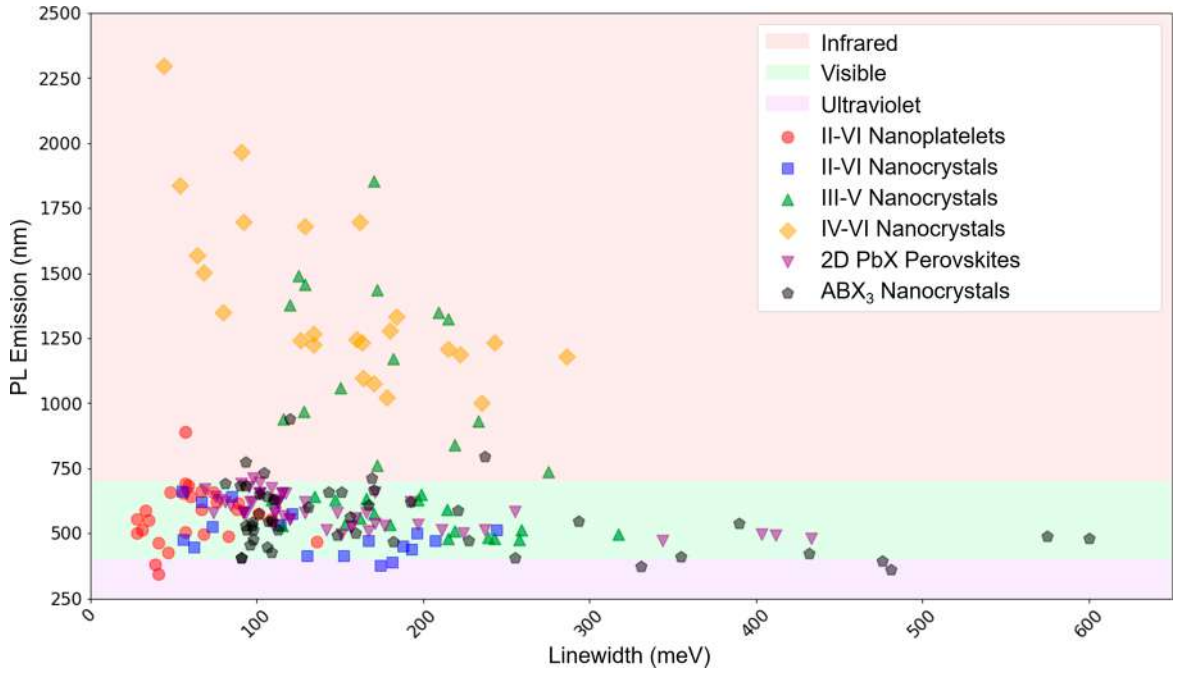

Figure 18. PL emission maximum versus emission line width of different materials summarized in section 4.

Table 1. Ensemble Line Widths of Representative II−VI Colloidal Nanoplatelets[a]

composition	PL emission	PL line width	PLQY (%)	refs
CdSe	395 nm (2 ML)			324
CdSe	463 nm (3 ML)	41 meV		325
CdSe	513 nm (4 ML)	31 meV		325
CdSe	550 nm (5 ML)	35 meV		325
CdSe	586 nm (6 ML)	9 nm (32.5 meV)	45	326
ZnSe	345 nm (4 ML)	41 meV		327
ZnSe	380 nm	39 meV		327
CdTe	428 nm	47 meV		328
CdTe	500 nm	28 meV		328
CdTe	556 nm	28 meV		328
HgTe	890 nm	57 meV		329
$CdSe/Cd_{0.7}Zn_{0.3}S$	1.93 eV	60 meV	60	330
4 ML $CdSe/Cd_xZn_{1-x}S$	1.89 eV	56 meV	88	331
6 ML $CdSe/Cd_xZn_{1-x}S$	1.79 eV	57 meV	92	331
CdSe/CdS/ZnS	1.87 eV	67 meV	78	331
CdSe/ZnS	2.00 eV	76 meV	52	331
CdSe/ZnSe	1.81 eV	59 meV	47	331
4 ML CdSe/1−6 ML CdS	2.10−1.88 eV	74−67 meV	70	306
4 ML CdSe/5 ML CdS/2 ML CdSe	1.88 eV	47.5 meV		306
$CdSe_{0.85}S_{0.15}$, 4 ML	505 nm (2.45 eV)	57 meV		332
$CdSe_{0.75}S_{0.25}$, 4 ML	495 nm (2.50 eV)	68.2 meV		332
$CdSe_{0.7}S_{0.3}$, 4 ML	488 nm (2.54 eV)	83 meV		332
$CdSe_xS_{1-x}/ZnS$, (x = 0.15−0.37)	554−593 nm 2.23−2.09 eV	109−88 meV		333
$CdSe_xS_{1-x}/Cd_yZn_{1-y}S$ (x = 0.15−0.37, y = 0.25−0.54), 4.5 ML	575−615 nm (2.15−2.01)	101−89 meV		333
$CdSe_{0.2}S_{0.8}/CdS$	468 nm (2.65 eV)	136 meV (24 nm)		334

[a]For PL emission energies and line widths expressed as ranges, the line width ranges are for the extrema of the emission wavelengths. For references where the authors did not directly report the emission peak properties, they were extracted from the published figures using the WebPlotDigitizer tool.[335]

materials integration[297] and also by development of methods for nanoscale positioning and integration of solution-processable emitters.[298,299]

3.3.2.3. External Tuning. Finally, beyond the surface chemistry and the integration of colloidal materials with nanophotonic cavities to control the environment, we propose it may also prove useful to develop mechanisms to tune emitters, which could conceivably be used to actively cancel residual spectral diffusion at longer time scales. As one possible strategy, one could use the quantum-confined Stark effect (QCSE) via an

https://doi.org/10.1021/acs.chemrev.3c00097
Chem. Rev. XXXX, XXX, XXX−XXX

Table 2. Ensemble Line Widths of Representative II−VI Colloidal Nanocrystals[a]

composition	PL emission	PL line width	PLQY (%)	refs
CdSe/CdS	620 nm (2.00 eV)	20 nm (67 meV)	97	336
CdSe/CdS	640 nm (1.94 eV)	28−32 nm (85−97 meV)	>97	314
CdSe	1.87−1.76 eV	∼55 meV		316
CdSe/ZnS	532 nm (2.33 eV)	26 nm (114 meV)	75	337
CdS/ZnS	2.69−2.58 eV	134−150 meV		338
CdS/ZnS	3.29−2.63 eV	174−207 meV		339
ZnSe/ZnS	446 nm (2.78 eV)	10 nm (62 meV)	95	25
ZnSe/ZnS	415 nm (2.99 eV)	<18 nm (130 meV)	>85	340
$CdSe_{1-x}S_x$ (x = 0.7)	414 nm (2.99 eV)	21 nm (152 meV)		341
$CdSe_{1-x}S_x$/CdS (x = 0.2−0.8)	439−515 nm (2.82−2.41 eV)	30−52 nm (193−244 meV)	10−40	342
$CdSe_{1-x}S_x$ (x = 0.25−0.75)	452−503 nm (2.74−2.46 eV)	31−40 nm (188−196 meV)		343
$CdSe_{1-x}Te_x$ (x = 0.4−0.66)	756−822 nm (1.64−1.51 eV)	35−47 nm (74−86 meV)	30−60	344
$Cd_{1-x}Zn_xSe$ (x = 0.26−0.81)	472−574 nm (2.63−2.16 eV)	30−32 nm (167−121 meV)		345
$Cd_{1-x}Zn_xSe$	2.61−2.36 eV	56−73 meV		345
$Zn_xCd_{1-x}S_ySe_{1-y}$ (x = 0.1−0.9, y = 0.11−0.89)	440−647 nm (2.82−1.92 eV)	36−45 nm (231−133 meV)	40−65	346
$ZnSe_{1-x}S_x$ (x = 0.4)	388 nm (3.20 eV)	22 nm (181 meV)	65	347

[a]For PL emission energies and line widths expressed as ranges, the line width ranges are for the extrema of the emission wavelengths. For references where the authors did not directly report the emission peak properties, they were extracted from the published figures using the WebPlotDigitizer tool.[335]

external applied electric field to tune the emitter to the cavity mode. Along these lines, Le Thomas et al. demonstrated that spectral diffusion can naturally bring an emitter into cavity resonance and thereby exhibit strong emitter/cavity coupling, an important proof of concept for applying an external electric field to tune an emitter into cavity resonance.[300] It is possible that other effects could be used to tune the emission energy rapidly and dynamically, for example, strain tuning of the emitter resonance, which was shown to shift the band gap of a single-halide perovskite QD coupled to a gap−plasmon cavity.[301] In general, while active tuning approaches have not received significant attention for colloidal materials to date, we predict they will be of increasing interest as technologies for synthesizing high-quality QDs and integrating them into cavity structures become more mature.

Overall, while spectral diffusion contributes to the broadening of spectral lines in a wide range of colloidal materials, we believe the field has not yet reached the ultimate limit of suppressing diffusion, and there exist both intrinsic chemical strategies, such as control over surface chemistry, as well as technological strategies, such as the use of cavity structures or active feedback to mitigate spectral diffusion in specific applications.

4. CURRENT STATE OF KNOWLEDGE AND TECHNOLOGY BY MATERIAL

In this final main section of the review, we document our current state of knowledge and the current state-of-the-art when it comes to narrow emission across the different classes of semiconductors made in solution. Specifically, we will focus on (i) QDs including II−VI, IV−VI, and III−V compositions, (ii) halide perovskites including 3D and 2D structures as well as nanocrystals, (iii) transition-metal- and rare-earth-doped nanocrystals, and (iv) organic molecules. Graphical and tabular summaries are provided in Figure 18 and Tables 1−7 for quick reference.

4.1. Quantum Dots and Nanoplatelets: II−VI, IV−VI, and III−V

Early efforts toward solution synthesis of colloidal semiconductors resulted in materials with size-tunable absorption onsets and diffuse absorption features arising from ensemble heterogeneity.[302] Over more than three decades, new synthetic approaches have been developed and synthetic parameters have been optimized to minimize the line widths of both excitonic absorption features and PL emission.[189,303] In this section, we will discuss the current state-of-the-art for ensemble PL line widths of colloidal II−VI, IV−VI, and III−V QDs and related nanoplatelets synthesized in solution.

We begin with colloidal nanoplatelets. The optical properties of II−VI nanoplatelets, in particular, and their potential for light-emitting applications have been well reviewed.[304,305] Since these materials are atomically defined in the critical quantum-confined dimension, we do not observe inhomogeneous broadening, and ensemble line widths are dictated by a truly homogeneous dynamic broadening in each case (Table 1).[56] This is true across the binary compositions of the II−VI materials (CdSe, ZnSe, CdTe, etc.), where ensemble line widths are in the range of 32−47 meV. Upon shell growth, with a wider band-gap shell, the quantum yield generally increases above 50% for CdSe-based heterostructures; however, this is accompanied by an increase in the PL line width in the range of 60−74 meV. Some of this may come from inhomogeneous shell growth leading to particle-to-particle variation or dynamic (possibly not truly homogeneous) broadening factors resulting from shell growth. Synthesis strategies for growing shells with atomic precision (e.g., colloidal ALD) allow for inhomogeneous broadening-free platelets to maintain this feature after overcoating with a wide-band-gap shell.[306,307] Despite the atomic precision for shell growth, these materials still have broader line widths than corresponding core-only platelets. One standout example is a multishell structure of 4CdSe/5CdS/2CdSe, which achieved a record narrow PL line width for solution-grown platelet emitters of 47 meV. The exact origins of the narrow PL line width in these complex systems are still unclear; however, this approach has great potential considering the vast composition/layer sequence parameter space available. Better understanding of the origins of the narrow PL line width in these complex systems is needed for future rational design in this materials space. At low temperatures, nanoplatelets display dual-band emission emerging from an emissive trion state[308,309] which will need to be addressed for application of these materials as single-photon emitters. The one

https://doi.org/10.1021/acs.chemrev.3c00097
Chem. Rev. XXXX, XXX, XXX−XXX

Table 3. Ensemble Line Width of Representative III−V Colloidal Nanocrystals[a]

composition	PL emission[a]	PL line width[a]	PLQY (%)	refs
InP/ZnSe/ZnS	528 nm (2.35 eV)	36 nm (115 meV)	95	319
InP/ZnSe/ZnS	630 nm (1.97 eV)	35 nm (109 meV)	∼100	320
InP/ZnSeS/ZnS	532 nm (2.33 eV)	35 nm (153 meV)	97	348
InP/ZnS	480−590 nm (2.58−2.10 eV)	40−60 nm (215−214 meV)	50−70	349
InP/GaP/ZnS	484 nm (blue)	45 nm	71	350
InP/Zn(Se,S)/ZnS	480−630 nm	45 nm	>90	351
InP/ZnS		60 nm	60	349
InP/ZnS, InP/ZnSe	510−630 nm (2.43−1.96 eV)	46−63 nm (219−197 meV)	80	352
InP/ZnSe	629 nm (1.97 eV)	47 nm (147 meV)	65	69
In(Zn)P/ZnSe/ZnS	488−641 nm (2.54−1.93 eV)	36 nm (green), 45 nm (red) (187−135 meV)	67, 56	353
InP/ZnSe/ZnS		42 nm (red)	93	354
InAs	760−970 nm (1.63−1.28 eV)	80−97 nm (172−128 meV)	∼1	355
InAs	1171−1348 nm (1.06−0.92 eV)	200−303 (182−209 meV)		S356
InAs/CdSe	940−1490 nm (1.31−0.83 eV)	116−125 meV	∼10	357
InAs/CdSe/CdS	930−1438 nm (1.33−86 eV)	161−284 nm (233−172 meV)	16−82	358
InSb	1458 nm (0.85 eV)	220 nm (129 meV)		359
InSb	1854 nm (0.67 eV)	466 nm (170 meV)		360
InSb	0.9−1.17 eV	120−150 meV		361
$In_{1-x}Ga_xP/ZnS$ (x = 0−0.6)	497−635 nm (2.49−1.95 eV)	∼63−54 (317−166 meV)	46	183
$In_{1-x}Ga_xAs/CdS$ (x = 0.5)	842 nm (1.47 eV)	∼125 nm (219 meV)	9.8	183
$In_{1-x}Ga_xP/(DDA)_2S$ (x = 0.5−0.7)	560 nm (2.21 eV)	∼41−47 nm (162−186 meV)		182
$In_{1-x}Ga_xP/ZnS$ (x = 0.7)	476−514 nm (2.60−2.41 eV)	∼47−55 nm (258−259 meV)		362
$In_{1-x}Ga_xP/ZnSe$ (x = 0.5)	532−574 nm (2.33−2.16 eV)	∼41−45 nm (180−170 meV)		362
$InAs_{1-x}P_x$ (x = 0.18−0.66)	652−738 nm (1.90−1.68 eV)	68−120 nm (199−275 eV)	1−2	363
$InAs_{1-x}Sb_x$ (x = 0.5)	1325 nm (0.94 eV)	300 nm (215 meV)		364

[a]For PL emission energies and line widths expressed as ranges, the line width ranges are for the extrema of the emission wavelengths. For references where the authors did not directly report the emission peak properties, they were extracted from the published figures using the WebPlotDigitizer tool.

case where narrow line widths have not been achieved is in alloy II−VI colloidal nanoplatelets. In these materials, despite atomic precision in the quantum-confined dimension, other sources of broadening due to inhomogeneous composition distributions (either within single particles or within the ensembles) are at play. To date, it is unclear if the single-particle line widths of alloy platelets result from truly homogeneous broadening, dynamic broadening that is not homogeneous, or static inhomogeneous broadening.

For the II−VI QDs, especially CdSe, the synthesis and surface chemistry have been thoroughly refined such that today it is possible to routinely obtain ensemble line widths that are nearly identical with those of single particles at room temperature (Table 2). The optical properties of II−VI QDs and their potential for light-emitting applications have also been well reviewed.[14,19,47,310−313] Given the volume of excellent examples, instead of tabulating data for CdSe, we instead provide an example of a representative synthesis that leads to such performance. State-of-the-art CdSe/CdS core/shell nanocrystals are typically prepared via a 2-step reaction. First, wurtzite CdSe cores are synthesized via a well-optimized hot injection method at 380 °C using a Cd−octadecylphosphonic acid complex as the cadmium source, trioctylphosphine−Se as the selenium source, and trioctylphosphine oxide as the solvent. After purification, the CdS shell is then slowly grown at high temperatures using Cd−oleate as the Cd source, 1-octanethiol as the sulfur source, and 1-octadecene as the solvent. These materials display narrow ensemble emission line widths (67 meV at room temperature). Further, this synthesis strategy also results in a record quantum efficiency of 99.6 ± 0.2% measured using photothermal threshold quantum yield measurements.[314] Importantly, this quantum yield measurement technique decreases the uncertainty to 0.2% compared to relative dye methods and integrating sphere techniques, which intrinsically have 2−5% uncertainty. This high luminescence efficiency and narrow line width make these materials competitive for applications beyond color conversion for displays including optical refrigeration, thermophotovoltaics, and thermal energy storage in optical cavities.[31,315]

In addition to the impressive quantum efficiency and line widths of the CdSe/CdS system, they also have single-particle line widths that are the same as the ensemble line width at room temperature. This indicates that synthesis science for these materials has achieved sufficient size, shape, etc., control such that homogeneous broadening dominates, and thus, developing strategies to narrow the homogeneous line width at room temperature is needed. It is known that the homogeneous line width of QD emitters decreases at low temperature; thus, for well-developed II−VI materials such as CdSe/CdS, a new goal could be to achieve identical single-particle and ensemble line widths at low temperature. While the CdSe/CdS system is the most well developed in terms of line width and stability for dot-based emitters, it is limited due to the toxicity of cadmium—particularly, for thick-shelled samples, the mole percent of cadmium per dot can be quite high.

Other II−VI QD materials systems have been explored to expand the accessible emission wavelengths or to minimize/eliminate concerns relating to Cd toxicity. For example, CdSe/ZnS emitters are advantageous because they have less Cd per dot as only the small volume core contains cadmium. However, the large lattice mismatch limits the thickness of the shell which can be gown, and the strain leads to nonuniform shell growth. As a

https://doi.org/10.1021/acs.chemrev.3c00097
Chem. Rev. XXXX, XXX, XXX−XXX

Table 4. Ensemble Line Widths of Representative IV−VI Colloidal Nanocrystals[a]

composition	PL emission	PL line width	PLQY (%)	refs
PbS	1024−1501 nm (1.21−0.83 eV)	178−68 meV		322
PbSe	1095−1265 nm (1.13−0.98 eV)	164−134 meV		130
PbSe	1.00 eV	126 meV		365
PbSe/CdSe	0.73−0.63 eV	162−91 meV		366
PbS/CdS	1.05−0.93 eV	286−184 meV		367
PbS/CdS	0.97 eV	180 meV		368
PbS/CdS	0.73−0.54 eV	92−44 meV		368
PbS	1.15−0.79 eV	170−64 meV		128
PbS	0.92 eV	80 meV		369
$PbS_{1-x}Se_x$ (x = 0.3)	1225 nm (1.01 eV)	∼161 nm (134 meV)		370
$PbS_{1-x}Se_x$ (x = 0.2−0.8)	1000−1188 nm (1.24−1.04 eV)	188−250 nm (235−222 meV)		371
$PbS_{1-x}Se_x$ (x = 0.11−0.86)	1233−1836 nm (1.01−0.67 eV)	199−147 nm (163−54 meV)		372
$PbTe_{1-x}Se_x$ (x = 0.09−0.69)	1248−1681 nm (0.99−0.74 eV)	200−291 nm (160−129 meV)		372
$PbTe_{1-x}S_x$ (x = 0.15−0.86)	1207−1234 nm (1.03−1.00 eV)	250−294 nm (215−243 meV)		372

[a]For PL emission energies and line widths expressed as ranges, the line width ranges are for the extrema of the emission wavelengths. For references where the authors did not directly report the emission peak properties, they were extracted from the published figures using the WebPlotDigitizer tool.[335]

result, state-of-the-art CdSe/ZnS emitters display broader emission line widths and lower quantum yield compared to their CdSe/CdS counterparts. To get blue emission, CdS/ZnS and ZnSe/ZnS materials have been explored, and both materials systems have accessed wavelength ranges inaccessible to the CdSe system. For the CdS/ZnS system, it is likely that the small size of the CdS core needed to achieve blue luminescence means this system is very sensitive to the size distribution—the small size likely leads to significant dynamic broadening. For the ZnSe/ZnS system, blue emission is feasible from weakly confined systems, and thus, ZnSe/ZnS emitting at 2.78 eV displayed a narrow (62 meV) PL line width and high (95%) quantum yield, representing a powerful path forward.

More generally, the size dependence of the emission energy is intrinsically tied to the band structure (carrier effective masses and dielectric constant) of a given material and thus provides intuition for the sensitivity of the inhomogeneous broadening to polydispersity. A loose trend can be seen that materials with larger Bohr radii show broader ensemble emission line widths than materials with smaller Bohr radii. Therefore, preparing nanocrystals with size larger than the Bohr exciton radius is another design principle for narrow ensemble emission line widths. In this weak confinement regime, the weak size dependence of the emission energy makes the emission properties much less sensitive to the size distribution. Examples of this include most lead halide perovskite nanocrystals (discussed in the next section), large ZnSe/ZnS nanocrystals, large CdZnSe, and large CdSe cubes.[316] To highlight the power of this approach, strongly confined ZnSe/ZnS nanocrystals display a broad 130 meV line width at 2.99 eV compared to large, weakly confined ZnSe/ZnS nanocrystals that display a much narrower 68 meV line width at 2.78 eV. A drawback of this approach is that the emission energy is no longer able to be broadly tuned by size, thus limiting wavelength options when designing materials. One way to mitigate this effect is to use ternary alloy systems to achieve narrow PL line widths in large alloy nanocrystals.

Due to the comparatively reactive precursors and larger bond energies, synthesis science in colloidal III−V nanocrystals has progressed more slowly than the II−VI materials in terms of size and shape control, although significant strides have been made in recent years.[317,318] As such, ensemble line widths in these materials are typically broader than their corresponding single-particle line widths (Table 3). For visible display relevant emission energies, InP/ZnE (E = S, Se) is the most well-developed system. In this class, PL emission line widths are typically in the range of 115−220 meV, which is significantly broader than their respective II−VI visible emitter counterparts (e.g., CdSe/CdS). Importantly single-particle line widths of InP-based QDs are nearly identical with II−VI-based systems, which suggests that further improvement in synthetic control of the size distribution and other sources of heterogeneous spectral broadening should enable the community to eliminate inhomogeneous broadening. There are additional challenges with InP intrinsic to the material. For example, the Bohr exciton radius of InP is 15 nm compared to 5.3 nm for CdSe. This results in a stronger size dependence of the emission energy; thus, for the same size polydispersity, InP will have a broader emission line width compared to CdSe. The best-performing InP/ZnE QDs required careful control of the core size distribution by regulating the reactivity of the In and P precursors and the formation of a highly crystalline and uniform ZnSe/ZnS multishell heterostructure. Using this strategy, 95% PLQY and 36 nm fwhm for green-emitting InP QDs have been achieved.[319] Taking these strategies one step further, InP/ZnSe/ZnS QDs with unity quantum yield and fwhm of 35 at 630 nm allowed for preparation of red LEDs with EQE of 21%.[320] In this example, the uniformity of the InP core was achieved through separation of nucleation and growth through continuous precursor injection. A 3.6 nm ZnSe interlayer was deposited with in situ etching of the oxide surface of the InP using hydrofluoric acid.

InP remains the most developed III−V colloidal nanocrystal system due to its relevance for display applications. For visible applications, other candidates include small GaAs nanocrystals and $In_{1-x}Ga_xP$ nanocrystals which have band gaps suitable for quantum-confined visible emission. Thus far, solution-grown GaAs nanocrystals have yet to display band-edge emission. Preparation of ternary gallium-containing III−V phases such as $In_{1-x}Ga_xP$ has developed quite slowly due to the reactivity and oxophilicity of gallium at high temperatures. Direct synthesis routes and conversion routes using molten salt solvents to perform gallium cation exchange on InP nanocrystals have achieved $In_{1-x}Ga_xP$ nanocrystals with emission line widths in the range of 170−317 meV, which is broader than comparable

https://doi.org/10.1021/acs.chemrev.3c00097
Chem. Rev. XXXX, XXX, XXX−XXX

InP-based emitters. Potential other III−V visible emitters such as GaP, AlAs, and AlP all have indirect band gaps in bulk, limiting their application for light emission applications. $In_{1-x}Ga_xN$ represents a final candidate for visible-emitting III−V colloidal nanocrystals; however, to date, synthetic methods to synthesize these materials have not been developed. Progress has been made with the colloidal synthesis of GaN nanocrystals and nanorods; however, band-edge emission still remains elusive in solution-derived III−N materials.[321] Promisingly, the success of nitride-based visible and UV emitters synthesized from gas-phase CVD and MBE growth suggests that these materials have considerable potential. Based on this, there remain many opportunities for synthesis science developments to realize generalized preparation of visible III−V emitters in solution.

To achieve materials with NIR emission, nanocrystals made of materials with narrower band gaps are needed. One important class of materials in this space is the IV−VI nanocrystals; in particular, the PbE (E = S, Se, Te) materials provide tunable band gaps across the near- and mid-IR region (Table 4). Synthesis science in these materials also developed more slowly than the visible-absorbing CdE materials; however, recent development of tunable thio- and selenourea precursors enable synthesis of a narrow size distribution across a broad size range. For large sizes, the PL emission line widths are quite narrow (down to ∼65 meV) for PbS nanocrystals.[322] For smaller nanocrystals of both PbS and PbSe, the PL line widths are still quite broad (>130 meV) despite the nearly monodisperse sizes that have been achieved with well-controlled thio- and selenourea precursors. For PbS, the nanocrystals show a sharp increase in Stokes shift for the small-sized materials, consistent with strong contribution from surface phonons. One approach to address surface coupling limiting the performance of small nanocrystals is to grow a wide-band-gap shell to localize the exciton wave function away from the surface. Unfortunately, for the lead chalcogenides there are not wide-band-gap isostructural materials available for shelling. Some success in terms of luminescence efficiency has been made by preparing PbS/CdS and PbSe/CdSe core/shell heterostructures via cation exchange. Unfortunately, wide-band-gap shells created by partial cation exchange do not drastically improve the ensemble PL line widths for small nanocrystals. Low-temperature growth of CdS shells on large PbS nanocrystals via colloidal ALD has demonstrated narrow PL line widths (from 92 to 44 meV for emission energies from 0.73 to 0.54 eV, respectively). However, the same overgrowth approaches on small PbS nanocrystals (0.97 eV emission) results in a much broader (180 meV) emission line width. Thus, it appears that for large PbX colloidal nanocrystals there is a path toward materials with emission line widths of ∼50 meV; however, in the short-wave IR range, considerable development is needed to improve the line width.

There are concerns related to the toxicity of lead for colloidal QD IR emitters. As such, other candidate materials for NIR and mid-IR emission include InAs and InSb, both of which have narrow band gaps and a size-tunable emission across the IR region. Like other III−V materials, the synthesis science of InAs has lagged that of comparable IV−VI materials. In many cases, the ensemble PL line widths for InAs nanocrystals with various shell materials is in the ∼200−300 meV range. One prodigious example that stands out is the synthesis of InAs/CdSe using indium(I) chloride and tris(dimethylamino)arsine as indium and arsenic precursors, respectively, which displays well-defined excitonic absorption peaks across the near- and mid-IR. Subsequent growth of wide-band-gap CdSe shells results in bright emission (∼10%) and narrow (116−125 meV) line widths for emission energies from 1.31 to 0.83 eV. Importantly, narrow line widths are still achieved for the smallest core sizes, filling an important spectral range where small PbE emitters have thus far struggled to achieve narrow emission. For redder emission energies, the narrow bulk band gap of InSb enables the material to span further into the infrared compared to InAs. This material has demonstrated ensemble line widths from 120 to 170 meV across emission energies from 1.17 to 0.67 eV, demonstrating performance on par with the more well-developed InAs system. However, InSb is very unstable to oxygen and moisture; as such, robust shell growth approaches that do not increase the line width are needed. A final candidate for IR emission is InN; however, due to the band alignments of this material, it is heavily doped and typically shows plasmonic features as colloidal nanocrystals.[323] Alloying InN with Ga to make colloidal $In_xGa_{1-x}N$ would allow tuning of the NIR emission across the visible and NIR; however, there are not yet established methods to synthesize alloy nitride materials using colloidal methods.

To summarize, for II−VI, IV−VI, and III−V QDs and nanoplatelets, the following factors should be considered *in tandem* when designing bright, tunable, less toxic, narrow emitters.

(1) Atomically precise synthesis of core emitters—this is most clearly demonstrated in the cases of nanoplatelets and II−VI QD systems, where synthetic procedures have been optimized such that there is atomic control in the quantum-confined dimension. Synthesis of III−V and NIR emitters lags behind; however, an increasing understanding and control of precursor conversion kinetics means that these materials will advance rapidly.

(2) Minimally strained shells—here, CdSe/CdS is the golden standard where a near-unity quantum yield and narrow emission has been achieved. Again, atomically precise shell growth techniques are now possible, and when the lattice strain between the core and the shell material is minimized, extremely narrow and bright emission will be possible for other materials as well. Shells also interrupt coupling with surface phonon modes to minimize the effect of homogeneous broadening.

(3) Alloying—where an unstrained shell is not feasible or a material does not have a direct band gap, a synthetic alternative to shelling could be alloying to achieve narrow band-edge emission, especially in less common spectral ranges (NIR).

(4) Using materials with small Bohr exciton radii—since some materials are more susceptible to inhomogeneous broadening as the size and spectral window is tuned, an alternative to developing atomically precise synthesis is to judiciously choose a material with a smaller Bohr exciton radius in the desired spectral window. This may necessitate using a combination of materials to cover wider emission ranges.

4.2. Metal Halide Perovskites: 3D, 2D, and Nanocrystals

4.2.1. 3D Perovskites. Hybrid halide perovskites have ascended into a central class of semiconductor research due to their tunable optoelectronic properties, low-temperature solution synthesis, and processibility into thin films.[373−391] 3D halide perovskites with the general formula AMX_3, where A is a monovalent cation (Cs^+, $CH_3NH_3^+$ (MA^+), $HC(NH_2)_2^+$ (FA^+),

https://doi.org/10.1021/acs.chemrev.3c00097
Chem. Rev. XXXX, XXX, XXX−XXX

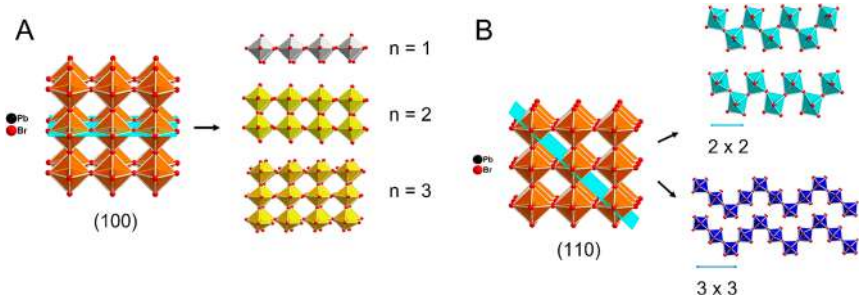

Figure 19. Schematic representation of the dimensional reduction of the $MAPbBr_3$ parent cubic 3D perovskite structure into (A) (100)-orientated 2D perovskite and (B) corrugated (110)-oriented 2D perovskite, where organic cations are omitted. Adapted with permission from ref 427. Copyright 2021 John Wiley and Sons.

or, recently, $CH_3NH_2NH_2^+$ [392,393] and $(CH_2)_2NH_2^+$),[394] M is a divalent metal (Ge^{2+}, Sn^{2+}, Pb^{2+}),[395] and X is a halide (Cl^-, Br^-, or I^-),[396,397] are direct band-gap semiconductors with noteworthy emissive properties. The 3D perovskite structure consists of a 3D network of corner-sharing metal halide $[MX_6]^{4-}$ octahedra with the A-site cation occupying the center of the cuboctahedral cavities. From the start of their academic investigation in the late 1980s[398−402] continuing to their present investigation,[403] the narrow light emission of hybrid lead halide perovskites offers tremendous potential for a broad range of commercial applications, including the design of photovoltaic devices with record high power conversion efficiency,[395,404−407] light emission,[382,383,391] radiation detection,[384−388] and lasing.[389,390]

A deeper connection between the underlying structural and photophysical properties in hybrid halide perovskites is essential for tuning their emission properties to optimize perovskite devices for commercialization. The optoelectronic properties of perovskite semiconductors are dependent on the chemical composition, electronic structure, and lattice dynamics of charge carriers.[408] Furthermore, structural defects need to be accounted for as well when considering resultant optoelectronic−emissive properties since these semiconductors are solution processable.[408] In general, inorganic emitters exhibit narrow emission when exciton−phonon interactions are weak and the defect concentration is controlled through expensive high-temperature production processes.[408,409] In 3D hybrid halide perovskites, the high dielectric constant and weak electron−hole binding energies result in free charge carriers, the species predominantly responsible for the PL emission at room temperature.[410] At low temperatures, free excitonic emission is observed in single-crystal 3D lead halide perovskites with a fwhm of 5 meV.[411] In comparison, 3D lead perovskite thin films display an absence of free excitonic emission at low temperatures, and instead, trap-state bands are dominant due to factors related to the crystallinity of the film samples.[411] Further spectroscopic study in parallel with structural characterization of 3D perovskites in bulk single crystals and thin films will enable the rational engineering of emission line widths in 3D perovskite-based optoelectronic devices.

4.2.2. 2D Perovskites. The 3D hybrid halide perovskite structure can be dimensionally reduced to layers of 2D structure, chains of 1D structure, or 0D clusters of $[MX_6]^{4-}$ octahedra by incorporating diverse ammonium cations.[412] The incorporation of certain organic cations larger than the aforementioned A-site cations leads to the family of 2D perovskites with formula $(A')_m(A)_{n-1}M_nX_{3n+1}$, where A′ is a monovalent ($m = 2$) or divalent ($m = 1$) cation and n is the number of inorganic layers in each "slab" of perovskite structure (Figure 19). The 2D halide perovskite structure can be conceptually derived from the 3D parent structure by slicing along specific crystallographic directions; the (100)-oriented perovskite family (Figure 19A), in which the parent cubic perovskite is sliced across the octahedral apices, is the most prevalent. Alternatively, if the 3D cubic perovskite structure is cut across the octahedral edges, the (110)-oriented perovskite family is obtained (Figure 19B). The arrangement of alternating semiconducting inorganic layers with insulating organic layers produces a natural 2D quantum-well superlattice in a bulk crystal with a layered structure. As a result of the quantum confinement, there is an increase in the band-gap energy (E_g) and the exciton binding energy (E_b) in 2D hybrid halide perovskites in comparison to their 3D parent structures.[410,413−418]

The 2D perovskite heterostructure can be synthetically fine tuned through the number of the inorganic layers n and the A′ organic "spacer" cation.[412,419,420] As the n-layer thickness increases, the 2D perovskite structure's optical and electronic properties (E_b, E_g, and PL) successively progress toward that of the 3D material.[419−422] On the other hand, the organic "spacer" cation indirectly influences the structure of the inorganic framework through its resultant noncovalent templating and through properties such as crystallinity, solubility, mechanical behavior, and thermochemical stability.[423−429] The superior environmental stability of 2D hybrid lead iodide perovskites and their inherent structural flexibility has rendered them attractive alternatives to 3D perovskites for the fabrication of environmentally robust optoelectronic devices.[68,377,428,430−438]

Photophysical studies have mainly been focused on lead halide perovskites due to their strong, excitonic PL emission. In the early 1990s, Thorn and colleagues published the first evidence of thick-layer lead halide perovskites ($n > 1$) producing thin films with the compositions $(C_9H_{19}NH_3)_2(CH_3NH_3)Pb_2I_7$ and $(C_9H_{19}NH_3)_2(CH_3NH_3)_{n-1}Pb_nBr_{3n+1}$ ($n = 1-3$) by incorporating the nonylammonium spacer cation and films of $(PhNH_3)_2(CH_3NH_3)Pb_2I_7$ containing the anilinium cation.[439] Although Thorn and colleagues were unable to acquire the single-crystal structures at that time, they observed the excitonic absorption peak of $(C_9H_{19}NH_3)_2(CH_3NH_3)Pb_2Br_7$ films at 430 nm and $(C_9H_{19}NH_3)_2(CH_3NH_3)_2Pb_3Br_{10}$ at 450 nm, lower in energy than their $n = 1$ member.[439] In 2000, Ishigure and co-workers rationally expanded the phase space of thick-layer perovskites by preparing and characterizing $n = 2$ perovskite films: $(C_mH_{2m+1}NH_3)_2(CH_3NH_3)Pb_2Br_7$ ($m = 2$, 3, 4, and 6).[440] Ishigure and co-workers showed that optical tunability and homogeneous emission lines can be obtained when using halide

https://doi.org/10.1021/acs.chemrev.3c00097
Chem. Rev. XXXX, XXX, XXX−XXX

Table 5. Structural and Optical Properties of Representative 2D Lead Halide Perovskites

composition	layer thickness (n)	PL emission	PL line width	equatorial Pb−X−Pb angle (deg)	bond angle variance of PbX_6 (deg)	carrier lifetime	refs
$(AA)_2(MA)_2Pb_3I_{10}$, AA = allylammonium	n = 3	1.99 eV	~60 nm	165.9	3.65	75.4 ps	429
$(EA)_3Pb_3Br_{10}$, EA = ethylammonium	n = 3	2.64 eV	61 nm	167.30	16.2	0.58 ns	489
$(EA)_3Pb_3Cl_{10}$, EA = ethylammonium	n = 3	2.48 eV	151 nm	161.53	40.45	1.77 ns	489
$(C4)_2PbI_4$, C4 = butylammonium	n = 1	2.36 eV	~35 nm	153.7	5.7	189 ps	419, 493, 494
$(C4)_2(MA)Pb_2I_7$, C4 = butylammonium	n = 2	2.14 eV	89 meV ~30 nm	167.2	3.4	223.52 ps	419, 495
$(C4)_2(MA)Pb_2Br_7$, C4 = butylammonium	n = 2	2.42 eV	~50 nm	155.7	20.1	3.91 ns	426, 429
$(C4)_2(DMA)Pb_2I_7$, C4 = butylammonium	n = 2	~2.23 eV	106 meV ~30 nm	166.6	17.4	56.45 ps	495
$(C4)_2(FA)Pb_2I_7$, C4 = butylammonium	n = 2	~2.15 eV	79 meV ~25 nm	169.4	5.7	117.42 ps	495
$(C4)_2(GA)Pb_2I_7$, C4 = butylammonium	n = 2	~2.19 eV	89 meV ~30 nm	168.1[8]	5.7	43.82 ps	495
$(C4)_2(EA)_2Pb_3I_{10}$, C4 = butylammonium	n = 3	2.12 eV	~ 70 nm	166.1	19.3	5.37 ps	496
$(C4)_2(MA)_2Pb_3I_{10}$, C4 = butylammonium	n = 3	2.00 eV	~35 nm	169.4	15.6		419
$(C4)_2(MA)_3Pb_4I_{13}$, C4 = butylammonium	n = 4	1.90 eV	~35 nm	170.4	16.3		419
$(C4)_2(MA)_4Pb_5I_{16}$, C4 = butylammonium	n = 5	1.83 eV	~35 nm	169.5	13.9		497
$(C4)_2(MA)_5Pb_6I_{19}$, C4 = butylammonium	n = 6	1.78 eV	~40 nm	168.6	14.5		498
$(C4)_2(MA)_6Pb_7I_{22}$, C4 = butylammonium	n = 7	1.74 eV	~40 nm	163.7	2.3		
$(C5)_2PbI_4$, C5 = pentylammonium	n = 1	2.42 eV	~30 nm	150.2	13.5	113 ps	450
$(C5)_2(MA)Pb_2I_7$, C5 = pentylammonium	n = 2	2.14 eV	~35 nm	166.5	19.7	310 ps	
$(C5)_2(MA)_2Pb_3I_{10}$, C5 = pentylammonium	n = 3	2.00 eV	~35 nm	167.5	18.3	253 ps	
$(C5)_2(MA)_3Pb_4I_{13}$, C5 = pentylammonium	n = 4	1.90 eV	~35 nm	168.5	15.9	263 ps	
$(C5)_2(MA)_5Pb_6I_{19}$, C5 = pentylammonium	n = 5	1.79 eV	~35 nm	169.7	14.7		
$(C6)_2PbI_4$, C6 = hexylammonium	n = 1	2.36 eV	~35 nm	155.1	8.3	255 ps	
$(C6)_2(MA)Pb_2I_7$, C6 = hexylammonium	n = 2	2.14 eV	~40 nm	160.2	24.9	303 ps	
$(C6)_2(MA)Pb_2Br_7$, C6 = hexylammonium	n = 2	2.58 eV	~80 nm	161.82	2.1	6.16 ns	426
$(C6)_2(MA)_2Pb_3I_{10}$, C6 = hexylammonium	n = 3	2.00 eV	~40 nm	168.8	20.3	113 ps	450
$(C6)_2(MA)_3Pb_4I_{13}$, C6 = hexylammonium	n = 4	1.90 eV	~40 nm	168.4	18.2	113 ps	
$(C7)_2(MA)Pb_2Br_7$, C7 = heptylammonium	n = 2	2.52 eV	~80 nm	165.1	3.4	1.27 ns	426
$(C8)_2(MA)Pb_2Br_7$, C8 = octylammonium	n = 2	2.49 eV	~80 nm	165.7	3.1	0.44 ns	
$(H_3N−C7−NH_3)PbI_4$, $H_3N−C7−NH_3$ = heptane-1,7-diammonium	n = 1	2.41 eV	~45 nm	155.01	4.56		449
$(H_3N−C7−NH_3)(MA)$ Pb_2I_7, $H_3N−C7−NH_3$ = heptane-1,7-diammonium	n = 2	2.14 eV	~30 nm				
$(H_3N−C7−NH_3)(MA)_2Pb_3I_{10}$, $H_3N−C7−NH_3$ = heptane-1,7-diammonium	n = 3	1.99 eV	~30 nm			τ_1 = 38 ps	
$(H_3N−C8−NH_3)PbI_4$, $H_3N−C8−NH_3$ = octane-1,8-diammonium	n = 1	2.50 eV	~30 nm	156.05	6.89		
$(H_3N−C8−NH_3)(MA)$ Pb_2I_7, $H_3N−C8−NH_3$ = octane-1,8-diammonium	n = 2	2.14 eV	~20 nm	162.4	7.11		
$(H_3N−C8−NH_3)(MA)_2Pb_3I_{10}$, $H_3N−C8−NH_3$ = octane-1,8-diammonium	n = 3	2.00 eV	~30 nm	168.7	3.39	τ_1 = 59 ps	
$(H_3N−C8−NH_3)(MA)_3Pb_4I_{13}$, $H_3N−C8−NH_3$ = octane-1,8-diammonium	n = 4	1.89 eV	~40 nm	169.39 [9]	4.93		
$(H_3N−C9−NH_3)PbI_4$, $H_3N−C9−NH_3$ = nonane-1,9-diammonium	n = 1	2.34 eV	~25 nm	153.26	4.33		
$(H_3N−C9−NH_3)(MA)$ Pb_2I_7, $H_3N−C9−NH_3$ = nonane-1,9-diammonium	n = 2	2.14 eV	~25 nm	167.88	3.05		
$(H_3N−C9−NH_3)(MA)_2Pb_3I_{10}$, $H_3N−C9−NH_3$ = nonane-1,9-diammonium	n = 3	2.00 eV	~25 nm	168.70	3.73	τ_1 = 45 ps	
$(H_3N−C9−NH_3)(MA)_3Pb_4I_{13}$, $H_3N−C9−NH_3$ = nonane-1,9-diammonium	n = 4	1.89 eV	~40 nm				
$(3AMP)PbI_4$, 3AMP = 3-(ammoniomethyl)piperidinium	n = 1	2.22 eV	~40 nm	165.2	36.1	0.08 ns	451
$(3AMP)(MA)Pb_2I_7$, 3AMP = 3-(ammoniomethyl)piperidinium	n = 2	2.00 eV	~35 nm	163.1	6.7	0.28 ns	
$(3AMP)(MA)_2Pb_3I_{10}$, 3AMP = 3-(ammoniomethyl)piperidinium	n = 3	1.90 eV	~35 nm	163.6	4.9	0.27 ns	
$(3AMP)(MA)_3Pb_4I_{13}$, 3AMP = 3-(ammoniomethyl)piperidinium	n = 4	1.84 eV	~40 nm	162.2	12.3	0.25 ns	451, 499
$(4AMP)PbI_4$, 4AMP = 4-(ammoniomethyl) piperidinium	n = 1	2.33 eV	~45 nm	154.5	9.5	0.11 ns	451

https://doi.org/10.1021/acs.chemrev.3c00097
Chem. Rev. XXXX, XXX, XXX−XXX

Table 5. continued

composition	layer thickness (n)	PL emission	PL line width	equatorial Pb−X−Pb angle (deg)	bond angle variance of PbX_6 (deg)	carrier lifetime	refs
(4AMP)(MA) Pb_2I_7, 4AMP = 4-(ammoniomethyl)piperidinium	n = 2	2.13 eV	~25 nm	156.4	6.0	0.10 ns	
$(4AMP)(MA)_2Pb_3I_{10}$, 4AMP = 4-(ammoniomethyl)piperidinium	n = 3	1.97 eV	~35 nm	158	5.3	0.08 ns	
$(4AMP)(MA)_3Pb_4I_{13}$, 4AMP = 4-(ammoniomethyl)piperidinium	n = 4	1.88 eV	~60 nm	160.3	10.7	0.11 ns	
$(3AMPy)PbI_4$, 3AMPy = 3-(ammoniomethyl)pyridinium	n = 1	2.23 eV	~30 nm	166.3	6.0	0.25 ns	499
(3AMPy)(MA) Pb_2I_7, 3AMPy = 3-(ammoniomethyl)pyridinium	n = 2	2.04 eV	~25 nm	168.9	4.0	0.16 ns	
$(3AMPy)(MA)_2Pb_3I_{10}$, 3AMPy = 3-(ammoniomethyl)pyridinium	n = 3	1.93 eV	~25 nm	168.0	3.3	0.29 ns	
$(3AMPy)(MA)_3Pb_4I_{13}$, 3AMPy = 3-(ammoniomethyl)pyridinium	n = 4	1.85 eV	~25 nm	168.8	2.7	0.27 ns	
$(4AMPy)PbI_4$, 4AMPy = 4-(ammoniomethyl)pyridinium	n = 1			149.2	0.7		
(4AMPy)(MA) Pb_2I_7, 4AMPy = 4-(ammoniomethyl)pyridinium	n = 2	2.14 eV	~45 nm	153.9	0.6	0.15 ns	
$(4AMPy)(MA)_2Pb_3I_{10}$, 4AMPy = 4-(ammoniomethyl)pyridinium	n = 3	1.97 eV	~25 nm	155.9[10]	0.73	0.20 ns	
$(4AMPy)(MA)_3Pb_4I_{13}$, 4AMPy = 4-(ammoniomethyl)pyridinium	n = 4	1.89 eV	~20 nm	157.3	1.3	0.20 ns	
$(mPDA)PbI_4$, mPDA = *m*-phenylenediammonium	n = 1	2.43 eV	~35 nm	143.7	234.2		500
(mPDA)(MA) Pb_2I_7, mPDA = *m*-phenylenediammonium	n = 2	2.14 eV	~25 nm	152.4	1.1		
$(mPDA)(MA)_2Pb_3I_{10}$, mPDA = *m*-phenylenediammonium	n = 3	1.99 eV	~35 nm	155.0	3.0		
$(4AMP)(MA)Pb_2Br_7$, 4AMP = 4-(ammoniomethyl)piperidinium	n = 2			159.9	4.54		501
$(4AMP)(FA)Pb_2Br_7$, 4AMP = 4-(ammoniomethyl)piperidinium	n = 2	2.34 eV	~40 nm	163.9	10.91	2.3 ns	
$(3AMP)(MA)Pb_2Br_7$, 3AMP = 3-(ammoniomethyl)piperidinium	n = 2			178.2	6.21		
$(3AMP)(FA)Pb_2Br_7$, 3AMP = 3-(ammoniomethyl)piperidinium	n = 2	2.30 eV	~40 nm	176.5[11]	4.66	1.8 ns	
$(4AMP)(FA)_{0.5}(MA)_{0.5}Pb_2Br_7$, 3AMP = 3-(ammoniomethyl)piperidinium	n = 2	2.48 eV	~45 nm	160.2	2.64		

binary alloys as a result of the robustness of the 2D Wannier exciton.[440]

The PL of most 2D lead halide perovskites $(A')_m(A)_{n-1}Pb_nX_{3n+1}$ yields free excitonic, narrow emission with a reduced Stokes shift.[441,442] When excited by above band-gap radiation, the fwhm is typically around 100 meV. Solution-processed 2D perovskite films typically contain multiple n-layer members with a broad width distribution, where the quantum-well inhomogeneity leads to charge funneling into the lowest band-gap n member, which accelerates Auger recombination.[443] Recently, there has been progress in obtaining phase-pure 2D perovskite films with $n > 1$,[444−446] where narrow line width emission attests to suppressed energetic disorder and indicates a homogeneous energy landscape.[443,447] A main advantage of producing 2D perovskites as single crystals is that a uniform phase of n-layer thickness is obtained, providing the opportunity to measure and analyze the inherent characteristics of this class of solution-processable 2D materials. Thus, we focus our discussion here on bulk 2D perovskites where, to the best of our knowledge, there has not been a holistic assessment targeted specifically toward design rules of narrow emission in 2D bulk perovskites.

The emission wavelength of 2D halide perovskites can cover the spectral regions between the UV and the NIR through tuning their chemical composition.[448] Here, we examine a wide representation of bulk 2D perovskites to initiate the extraction of design principles for the targeted synthesis of narrow-band 2D perovskite light-emitting crystals based on tailoring their chemical composition and/or their crystal growth/quality (Table 5). Regarding the chemical composition, we deduce three main chemical composition variables related to the resultant emission line width: (i) organic A′ spacer cation, (ii) A-site cation, and (iii) halide anion.

4.2.2.1. Tuning the A′ Spacer Cation. The organic A′ spacer cations primarily tailor the structure−property relationship in 2D lead halide perovskites through their electrostatic interaction with the inorganic layers. This can induce tilting of $[MX_6]^{4-}$ octahedra, deviation of the equatorial Pb−X−Pb angles from 180°, and distortions of the octahedra from ideal geometry, while the intrinsic dielectric nature of the spacer cation can influence the exciton-binding energy and crystallization kinetics of the 2D perovskite. As mentioned, the choice of organic cation directly dictates the distortions within the 2D inorganic lattice, contributing to the band-gap values and band-edge emission (Table 5). As seen in Table 5, between the comparison of known 2D lead iodide perovskites with tunable linear alkyl mono-ammonium cations $(C_mH_{2m+1}NH_3)_2(MA)_{n-1}Pb_nI_{3n+1}$, m = 4−6) and linear alkyl diammonium cations $((H_3NC_mH_{2m+1}NH_3)(MA)_{n-1}Pb_nI_{3n+1}$, m = 7−9) there is not a significant observed difference in the emission line width

https://doi.org/10.1021/acs.chemrev.3c00097
Chem. Rev. XXXX, XXX, XXX−XXX

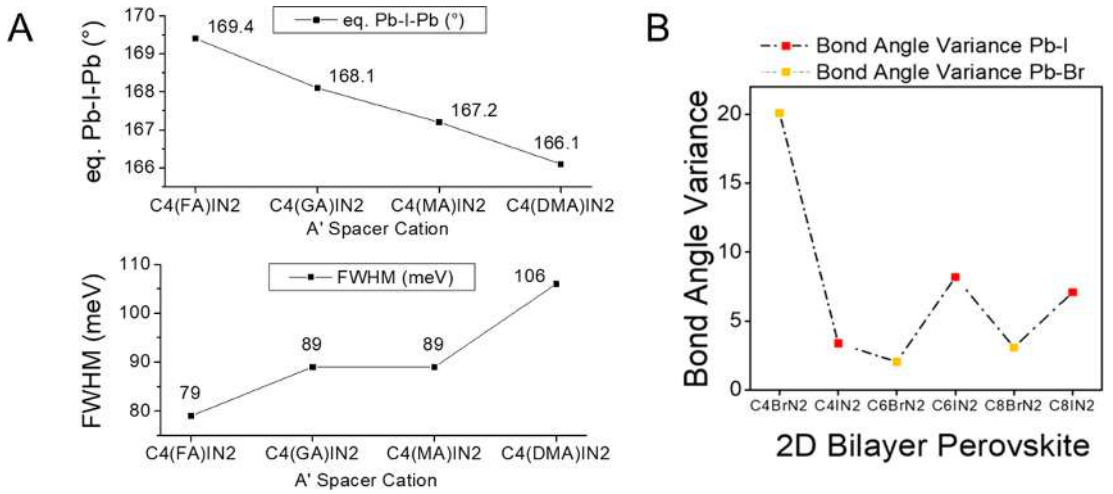

Figure 20. (A) Average equatorial Pb−I−Pb angle in correlation with the fwhm of $(C_4H_9NH_3)_2(A)Pb_2I_7$ (A = MA, FA, DMA, and GA) perovskites.[495] Abbreviations: $(C_4H_9NH_3)_2(FA)Pb_2I_7$ = C4(FA)IN2, $(C_4H_9NH_3)_2(GA)Pb_2I_7$ = C4(GA)IN2, $(C_4H_9NH_3)_2(MA)Pb_2I_7$ = C4(MA)IN2, and $(C_4H_9NH_3)_2(DMA)Pb_2I_7$ = C4(DMA)IN2. (B) Bond angle variance (degrees) of octahedral $[PbX_6]$ distortions in C4BrN2, C6BrN2, and C8BrN2 versus C4IN2, C6IN2, and C8IN2. Abbreviations: C4BrN2 = $(C_4H_9NH_3)_2(MA)Pb_2Br_7$, C6BrN2 = $(C_6H_{13}NH_3)_2(MA)Pb_2Br_7$, C8BrN2 = $(C_8H_{17}NH_3)_2(MA)Pb_2Br_7$, C4IN2 = $(C_4H_9NH_3)_2(MA)Pb_2I_7$, C6IN2 = $(C_6H_{13}NH_3)_2(MA)Pb_2I_7$, and C8IN2 = $(C_8H_{17}NH_3)_2(MA)Pb_2I_7$. Bond angle variance calculated from the formula $\sigma^2 = \sum_{i=1}^{12} \frac{(\theta_i - 90)^2}{11}$ of the individual $[PbX_6]^{4-}$ octahedra. Adapted with permission from ref 426. Copyright 2021 American Chemical Society.

between the two families.[419,449,450] This is the case among various *n*-layer thickness members between the two families, although there are different distortion levels within the $[PbI_6]^{4-}$ layers. The 2D lead iodide perovskites $(C_mH_{2m+1}NH_3)_2(MA)_{n-1}Pb_nI_{3n+1}$, m = 4−6) incorporating the linear monoammonium cations belong to the Ruddlesden−Popper (RP) family where the successive $[PbI_6]^{4-}$ inorganic layers are "staggered" with respect to one another in the *a* and *b* (in-plane) directions, often being described as a (1/2, 1/2) displacement. 2D lead iodide perovskites incorporating the linear diammonium cations $(H_3NC_mH_{2m+1}NH_3)(MA)_{n-1}Pb_nI_{3n+1}$, m = 7−9) also afford a staggered arrangement of the inorganic layers but with a divalent diammonium cation.

Another important substructure family of 2D halide perovskites is the Dion−Jacobson (DJ) perovskites. The DJ structure is composed of divalent spacer cations that template an eclipsed arrangement of successive inorganic halide layers, such that there are no relative displacements.[451] An attractive property of the DJ series $(3AMP)(MA)_{n-1}Pb_nI_{3n+1}$ and $(4AMP)(MA)_{n-1}Pb_nI_{3n+1}$ (n = 1−4), where 3AMP and 4AMP = 3- and 4-(ammoniomethyl)piperidinium, respectively, is the considerably lower band-gap and PL emission energies in comparison with the RP perovskites $(C_mH_{2m+1}NH_3)_2(MA)_{n-1}Pb_nI_{3n+1}$, m = 4−6). Although the distortions of the equatorial Pb−I−Pb angles in the DJ series $(3AMP)(MA)_{n-1}Pb_nI_{3n+1}$ and $(4AMP)(MA)_{n-1}Pb_nI_{3n+1}$ are larger than those in the RP series (Table 5), the band-gap values are lower. The lower band gaps were inferred to be related to small I···I distances between adjacent $[Pb_nI_{3n+1}]$ slabs and the resulting more dispersive electronic bands along the stacking axis.[451] Again, although the nature of the organic A′ spacer cation is significantly different and imposes drastic structural effects that lead to different substructure families of 2D perovskites with different distortion levels, the carrier lifetimes and emission line width of RP and DJ perovskites are comparable (Table 5). In summary, an area of focus when characterizing 2D perovskite compounds among a homologous series should be extracting structural correlations between tuning the A′ spacer cation with the emission line width and carrier lifetime.

4.2.2.2. Tuning the A-Site Cation. The effect of the A-site cation in 2D perovskites seems to impose important variances in the PL properties of layered perovskites. The study of the structural evolution of the series with the butylammonium spacer cation $(C_4H_9NH_3)_2(A)Pb_2I_7$ (A = MA, FA, EA, DMA, and GA; where FA = formamidinium, EA = ethylammonium, DMA = dimethylammonium, and GA = guanidinium) as a function of A cation size showed that the enlarged A cations (EA, DMA, and GA) lead to significant decreases in PL intensity and lifetime as a result of a more pronounced nonradiative decay.[495] Moreover, among this series $(C_4H_9NH_3)_2(A)Pb_2I_7$, the distortion of the average equatorial Pb−I−Pb angle slightly increases as follows: $(C_4H_9NH_3)_2(FA)Pb_2I_7$ with 169.4° < $(C_4H_9NH_3)_2(GA)Pb_2I_7$ with 168.1° < $(C_4H_9NH_3)_2(MA)Pb_2I_7$ with 167.2° < $(C4)_2(DMA)Pb_2I_7$ with 166.1°. In a similar manner, the emission line width slightly narrows as the average equatorial Pb−I−Pb angles' distortion decreases with $(C_4H_9NH_3)_2(FA)Pb_2I_7$ having the smallest fwhm of 79 meV versus $(C_4H_9NH_3)_2(DMA)Pb_2I_7$ that has a fwhm of 106 meV (Figure 20A). Similar observations were found between thick-layer $(C_4H_9NH_3)_2(MA)_2Pb_3I_{10}$ and $(C_4H_9NH_3)_2(EA)_2Pb_3I_{10}$, where the PL intensity is quenched with the increasing amount of EA added into the 2D structure.[452] It was found that the larger $[PbI_6]^{4-}$ octahedral distortions and the longer Pb−I bond lengths in $(C4)_2(EA)_2Pb_3I_{10}$ result in stronger PL quenching and a more asymmetric PL peak, where transient absorption spectroscopy revealed a broad distribution of trap states below the band gap. Consequently, it can be deduced that the nature of the A-site cation and the strain it imposes on the 2D perovskite structure has more direct effects on the PL properties than the A′ spacer cation.

4.2.2.3. Tuning the Halide Anion. Tuning the halide anion suggests having the most profound effect on the emission line width. The comparison of 2D lead halide perovskites with the

https://doi.org/10.1021/acs.chemrev.3c00097
Chem. Rev. XXXX, XXX, XXX−XXX

same organic cation but different halide anions demonstrates considerable changes: the lead bromide perovskites generally have broader emission than their iodide counterparts. Specifically, the comparison of the n = 2, RP family of perovskites $(C_mH_{2m+1}NH_3)_2(MA)Pb_2X_7$ (m = 6−8, X = Br, I) offers insight into the photophysical differences between 2D lead bromide and 2D lead iodide perovskites.[426] First, from a structural viewpoint, the $(C_mH_{2m+1}NH_3)_2(MA)Pb_2Br_7$ (m = 6−8) perovskites present a smaller distortion of the $[PbX_6]$ octahedra in comparison with their lead iodide congeners. As seen in Figure 20B, $(C_6H_{13}NH_3)_2(MA)Pb_2I_7$ and $(C_8H_{17}NH_3)_2(MA)Pb_2I_7$ have consistently larger distortions of the individual $[PbI_6]^{4-}$ octahedra than $(C_6H_{13}NH_3)_2(MA)Pb_2Br_7$ and $(C_8H_{17}NH_3)_2(MA)Pb_2Br_7$, respectively. Thus, it seems that the $[MX_6]^{4-}$ octahedral distortion does not have a direct correlation with the emission line width when the X halide anion is varied, while it does correlate as a function of tuning the A′ spacer cation among perovskites with the same halide anion as discussed earlier.

From a photophysical stance, the bulk lead bromide perovskites $(C_mH_{2m+1}NH_3)_2(CH_3NH_3)Pb_2Br_7$ (m = 6−8) feature broader emissions and longer lifetimes (on the nanoseconds scale) than their lead iodide analogs. Based on the significantly longer PL lifetime of the mentioned n = 2 bromide materials, the band dispersion and effective mass in the in-plane direction were investigated to gain insight on the radiative electronic transitions where the computed in-plane average lattice strain was calculated.[426] It was found that the lattice mismatch with the related 3D perovskite $MAPbBr_3$ was significantly smaller for the $(C_4H_9NH_3)_2(MA)Pb_2Br_7$ layered perovskite, in contrast to the lattice mismatch of the lead iodide analogue $(C_4H_9NH_3)_2(MA)Pb_2I_7$ to $MAPbI_3$. Hence, the internal lattice strain in 2D perovskites increases from bromide to iodide when tuning the halide anion in the n = 2 lead perovskites, leading to an increase of the nonradiative recombination and decrease of the carrier lifetime.[426] Overall, it appears that the reduced lattice mismatch and thus enhanced lattice rigidity of the bromide compounds compared to the iodide analogues is beneficial in limiting nonradiative recombination as discussed earlier. However, it may in turn limit the possibility of growth of high n-layer thickness perovskites and give rise to broader emission. Lastly, the comparison of the emission line width between n = 2 lead bromide perovskite RP $(C_mH_{2m+1}NH_3)_2(CH_3NH_3)Pb_2Br_7$ (m = 6−8) and DJ (4AMP)(FA)Pb_2Br_7 and (3AMP)(FA)Pb_2Br_7 shows similar broad emissions with a nanoseconds time scale carrier lifetime, in stark comparison with their lead iodide analogues (Table 5).

4.2.2.4. Broad-Band Emission Coexisting with Narrow Emission in 2D Perovskites. In general, the PL emission in 2D perovskites is a complex phenomenon where narrow emission is not the sole emission observed and various other emission mechanisms are present such as broad emission and edge states.[453−456] There is still much unknown regarding how to eradicate or exploit edge emission through synthetic design. The observation of broad Stokes-shifted PL emission in layered lead halide perovskites has sparked great interest for white lighting applications.[457−460] Emission is typically considered as "broad" when having fwhm > 100 meV and has been attributed to sub-band-gap trap states generated from self-trapped excitons (STEs), instead of excitonic emission.[461] The formation of STEs is due to strong electron−phonon coupling within a soft lattice.[454,461,462] The softness of the halide perovskite lattice can promote strong exciton−phonon interactions that may lead to the movement of the exciton being interrupted at a lattice site, resulting in its self-trapping inside the self-induced potential barriers (Figure 21).[463,464] Consequently, self-trapped excitons produce transient, light-induced lattice deformations that can be thought of as "excited-state" defects, in contrast to more permanent lattice defects such as vacancies and interstitials, which are preserved in the ground state as well.

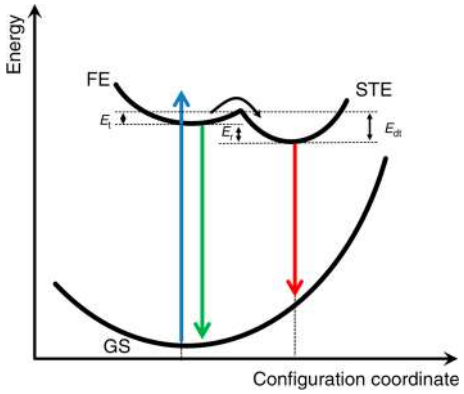

Figure 21. Photophysical processes leading to low-energy emission. Free (FEs) and self-trapped excitons (STEs) are shown in a configuration coordinate model. Excitation from the ground state (GS) generates FEs or free carriers (not shown), which can self-trap when overcoming a barrier, E_t. The accompanying lattice deformation decreases the minimum of the STE by the relaxation energy E_r with respect to FEs. STEs can also become FEs again when a detrapping barrier E_{dt} is overcome. Defect states within the bulk (left) or at the surface (right) of a material can also evoke low-energy luminescence. Adapted with permission from ref 468. Copyright 2020 Creative Commons Attribution 4.0 International.

There is still much investigation in the perovskite community of whether the formation of STEs giving rise to broad emission is intrinsic or extrinsic in nature.[427,461,465−468] In brief, intrinsic STEs create transient lattice distortions without permanent material defects, while extrinsic STEs are facilitated by the local environment of lattices when the electron−phonon coupling is too weak to generate STEs themselves. Besides the states in the bulk of a crystal, defects can occur at the surface of a material and can lead to radiative recombination, as shown in Figure 21. In the case of the extrinsic origin of broad emission, the below-band-gap excitation can create in-gap states caused by defects within the bulk crystal that are responsible for the broad emission.[468] A more detailed analysis of the mechanism of broad-band emission in hybrid halide perovskites is outside the scope of this review, but a review of related research advances can be found elsewhere.[460,462] To rationally harness the broad emission presented in layered halide perovskites for application perspectives, it is important to assign critically the nature of the broad emission (through the use of a combination of spectroscopic techniques) as intrinsic self-trapping may not always be responsible for broad emission.

In parallel with the spectroscopic investigation, there is an emerging image on the structure−property relationships defining broad emission in 2D halide perovskites. Specifically, many n = 1 lead chloride $(A')_mPbCl_4$ and lead bromide $(A')_mPbBr_4$ perovskites exhibit broad emission or a combination of both broad and narrow emission.[346,454,461,464,469−483] In comparison, there are fewer reports of broad emission in lead iodide perovskites, most commonly at low temperature and for n = 1 $(A')_mPbI_4$ members.[429,456,484] Hence, free excitons and

https://doi.org/10.1021/acs.chemrev.3c00097
Chem. Rev. XXXX, XXX, XXX−XXX

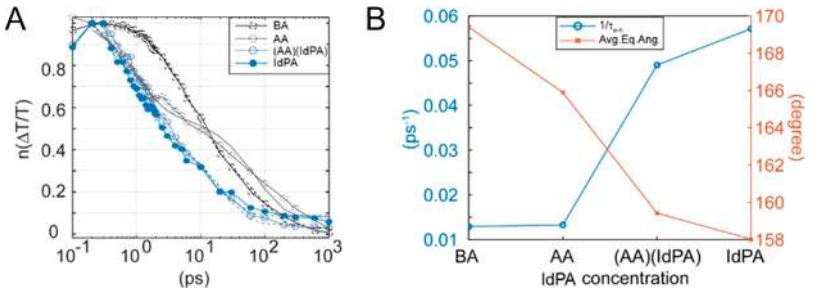

Figure 22. (A) The normalized transient absorption (TA) signal intensity extracted at the band gaps shows the recombination dynamics at the band gaps of crystals containing different cations: BA (butylammonium), AA (allylammonium), and IdPA (iodopropylammonium). (B) Correlation between the lattice distortion and the recombination lifetimes. The left axis shows the speed of the recombination, and the right axis shows the average equatorial Pb−I−Pb bond angle from X-ray crystallography, indicating the level of distortion within the inorganic structures. A clear negative correlation between the level of distortion and the speed of recombination can be observed, suggesting the direct effect of lattice distortion on excited-state dynamics. Adapted with permission from ref 429. Copyright 2022 American Chemical Society.

STEs can coexist in the same material, leading to the observation of both narrow and broad bands in layered perovskites. All (110)-oriented lead bromide perovskites reported broad-band emission—this is attributed to the large distortions of the corrugated lead bromide crystal lattice producing STEs.[465,471−474,481,483,485−487] A critical assessment of the structure−property−luminescent relationships in lead bromide perovskites with structural design principles for targeted synthesis and correlation to narrow emission and broad emission was published recently.[427] In the present context, the structural prerequisites of organic spacer cations that can template the (110)-orientated lead bromide structure are (i) organic cations with an extended ability for hydrogen-bonding and electrostatic interactions inherited from functional groups such as diamine/polyamines, electronegative heteroatoms, and/or aromaticity and (ii) organic cations with small steric hindrance.[474,479,486,488,489] Finally, in (110)-perovskites, larger octahedral distortions correlate with broader PL emission.[488]

Originally, broad emission was observed in the (110)-oriented perovskites; however, subsequently, multiple examples of n = 1, (100)-oriented $(A')_mPbX_4$ perovskites were described displaying both narrow-band and broad-band emission.[465,475,490,491] The (100)-oriented perovskites usually feature broad-band emission at low temperature (<100 K), suggesting that this emission feature is not exclusive to a specific structural geometry but a general property of the distorted, 2D perovskite emitters.[491] It is a common observation among the numerous studies of broad emission in (100)-oriented $(A')_mPbX_4$ perovskites that the distortions and torsions of the inorganic lattice are the main source of STEs.[346,492] Several correlations between structural distortion parameters and STE broad emission have been proposed to interpret the broad emission in (100)-oriented perovskites such as distortion angles within the Pb−X−Pb inorganic layers,[461] the degree of octahedral distortion quantified from the bond angle variance,[488,489] octahedral Pb−X bond elongation,[488,489] and substitution positions of functional groups of the organic spacer cation.[476,479] Additionally, for n = 1 halide perovskites, tuning the identity of the A′ organic spacer plays a crucial role on the resultant distortions within the inorganic lattice and on the excitonic−STE emission. Finally, broad emission is much more common in n = 1 perovskites versus the thick-layer perovskites (n > 1).

Recently, spectroscopic and structural analysis on thick-layer perovskites (n > 1) of various compositions in the A-site cation and A′ spacer cation revealed direct correlations of the broad STE emission with structural distortions when the A-site cation was tuned from MA to FA, while there was not a strong dependence when adjusting the identity of the A′ spacer cation from butylammonium ($C_4H_9NH_3$) to pentylammonium ($C_5H_{11}NH_3$) and hexylammonium ($C_6H_{13}NH_3$).[467] In the thick-layer systems, the A-site cations support the Pb−X inorganic layers, relieving the inorganic layers from the steric strain imposed by the organic spacers nearby.[467] Furthermore, the influence of the emission line width from different functional groups on the A′ spacer cation in n > 1 perovskites is largely unexplored. The incorporation of the 3-iodopropylammonium cation (IdPA) with the heavy and sterically large iodine atom into the 2D perovskite lattice was demonstrated to be directly related to the formation of long-lived (∼100 ps) trap states with broad-band emission in the visible region (Figure 22).[429] In the series $(IdPA)_2(MA)_{n-1}Pb_nI_{3n+1}$ (n = 1−4), the IdPA cation creates significant lattice distortions (Figure 22B) and leads to the creation of new, broad-band ensembles of states deep into the band gap that quickly depopulate the band-edge excitons but elongate the lifetimes of photoexcited carriers.[429] In summary, the appearance of lower energy emission features that can broaden the PL emission is dependent on an interplay of effects related to the chemical composition of the 2D perovskite (n-layer thickness, A-site cation, A′ spacer cation, halide anion) to structural defects, and to sub-band-gap trap states.

4.2.3. Perovskite Nanocrystals. On the heels of 3D bulk metal−halide perovskites, solution-processed nanocrystal analogues (MHP nanocrystals) have made a similarly explosive entrance to the field of nanotechnology for conventional and quantum optoelectronics within the past decade. The volume of research activity on MHP nanocrystals prompted us to defer to numerous reviews, all published since 2019, that detail the current states of MHP nanocrystal synthesis,[502,503] characterization,[504] stability,[505−508] doping,[509] shelling and heterostructures,[510,511] self-assembly,[512] encapsulation,[513] device applications,[514−519] and more,[520−524] with a particularly comprehensive review of the MHP nanocrystal state-of-the-art published in 2021.[525] Here, we aim to present the major considerations for achieving bright, efficient, and narrow emission from nanoscale ABX_3 structures synthesized in solution.

Optical characterization of $NaMgF_3$ nanocrystals synthesized in oleic acid solution was reported as early as 2009 (without the use of MHP terminology).[526] Nontemplated solution synthesis of Pb-based MHP nanocrystals, however, would gain momentum later with initial reports from 2014 to 2016 of both hybrid organic−inorganic,[527,528] and all-inorganic[529]

https://doi.org/10.1021/acs.chemrev.3c00097
Chem. Rev. XXXX, XXX, XXX−XXX

Table 6. Ensemble Line Widths of Representative MHP Colloidal Nanocrystals[a]

composition	NC diameter	PL emission	PL line width	PLQY (%)	refs
$CsPbCl_3$	5−15 nm	405 nm (3.06 eV)	12 nm (91 meV)	50−90	529
$CsPbCl_3$		405 nm (3.06 eV)	12 nm (91 meV)	10	531
$CsPbCl_xBr_{3-x}$	5−15 nm	426 nm (2.91 eV)	16 nm (109 meV)	50−90	529
$CsPbCl_{1.5}Br_{1.5}$		455 nm (2.72 eV)	16 nm (96 meV)	37	531
$CsPbClBr_2$		478 nm (2.59 eV)	18 nm (98 meV)	70	531
$CsPbBr_3$	11 nm	513 nm (2.42 eV)	20 nm (94 meV)	95	531
$CsPbBr_3$	5−15 nm	513 nm (2.42 eV)	24 nm (113 meV)	50−90	529
$CsPbBr_xI_{3-x}$	5−15 nm	545−577 nm (2.27−2.15 eV)	26−27 nm (109−101 meV)	50−90	529
$CsPbBr_2I$		548 nm (2.26 eV)	26 nm (107 meV)	78	531
$CsPbBr_{1.5}I_{1.5}$		600 nm (2.07 eV)	38 nm (131 meV)	72	531
$CsPbBr_{1.2}I_{1.8}$		628 nm (1.97 eV)	35 nm (110 meV)	80	531
$CsPbBrI_2$		640 nm (1.94 eV)	35 nm (106 meV)	70	531
$CsPbI_3$	5−15 nm	652 nm (1.90 eV)	35 nm (102 meV)	50−90	529
$CsPbI_3$	5−15 nm	685 nm (1.81 eV)	34 nm (90 meV)	50−90	529
$CsPbI_3$	11 nm	690 nm (1.80 eV)	31 nm (81 meV)	∼100	550
$MAPbCl_3$		373 nm (3.32 eV)	37 nm (331 meV)		530
$MAPbCl_3$		407 nm (3.05 eV)	34 nm (255 meV)		530
$MAPbCl_xBr_{3-x}$		446−493 nm (2.78−2.51 eV)	17−29 nm (106−148 meV)		530
$MAPbBr_3$		530 nm (2.34 eV)	21 nm (93 meV)		527
$MAPbBr_3$	3.3 ± 0.7 nm	515 nm (2.41 eV)	21 nm (98 meV)	50−70	530
$MAPbBr_xI_{3-x}$		565−660 nm (2.19−1.88 eV)	40−53 nm (156−151 meV)		530
$MAPbI_3$		734 nm (1.69 eV)	45 nm (104 meV)		530
$FAPbBr_3$	5 nm	474 nm (2.62 eV)	41 nm (227 meV)		528
$FAPbBr_3$	8 nm	499 nm (2.48 eV)	32 nm (160 meV)		528
$FAPbBr_3$	12 nm	530 nm (2.34 eV)	22 nm (97 meV)	85	528
$FAPbBr_3$	>50 nm	542 nm (2.29 eV)	23 nm (97 meV)		528
$FAPbBr_xI_{3-x}$		586−713 nm (2.12−1.74 eV)	61−69 nm (221−169 meV)		551
$FAPbI_3$	10−15 nm	775 nm (1.60 eV)	45 nm (93 meV)	>70	551
$FA_{0.1}Cs_{0.9}PbI_3$	10−15 nm	685 nm (1.81 eV)	35 nm (93 meV)	>70	551
$Cs_3Bi_2Cl_9$		393 nm (3.15 eV)	59 nm (476 meV)	26	552
$Cs_3Bi_2Br_9$	3.88 ± 0.67 nm	410 nm (3.02 eV)	48 nm (355 meV)	19	552
$Cs_3Bi_2I_9$		545 nm (2.27 eV)	70 nm (293 meV)	0.02	552
MA_3BiCl_9		360 nm (3.44 eV)	50 nm (481 meV)	15	553
$MA_3Bi_2Br_9$		423 nm (2.93 eV)	62 nm (432 meV)	12	553
$MA_3Bi_2I_9$		540 nm (2.30 eV)	91 nm (390 meV)	0.03	553
$CsSnCl_3$		480 nm (2.58 eV)	110 nm (600 meV)		554
$CsSnCl_xBr_{3-x}$	7.6	490 nm (2.53 eV)	110 nm (575 meV)		554
$CsSnBr_3$	10.7	660 nm (1.88 eV)	50 nm (143 meV)		554
$CsSnBr_xI_{3-x}$	10.1	795 nm (1.56 eV)	120 nm (237 meV)		554
$CsSnI_3$	9.9 nm	940 nm (1.32 eV)	85 nm (120 meV)		554

[a]For PL emission energies and line widths expressed as ranges, the line width ranges are for the extrema of the emission wavelengths. For references where the authors did not directly report the emission peak properties, they were extracted from the published figures using the WebPlotDigitizer tool.[335]

cuboidal nanocrystal ensembles with low polydispersity, emission line widths of tens of nanometers, and solution PLQYs of up to 90% as represented in Table 6. The initial success of hot-injection synthesis was soon followed by ligand-assisted reprecipitation (LARP)[530] and supersaturated recrystallization[531] methods, offering room-temperature routes for producing monodisperse colloidal ensembles enabled by the ionic bonding inherent to MHP. Controlling the fast kinetics of MHP nanocrystal formation remains an area of active synthesis research, particularly critical for achieving smaller particle diameters. Most recently, the judicious choice of trioctylphosphine oxide as a complexing agent has demonstrated a self-limiting equilibrium of precursor, monomer, and nanocrystal constituents in solution for size control.[532] Templated synthesis in porous media has also been investigated as a strategy for growth of small MHP nanocrystals, assisted by the defect-tolerant nature of MHP.[533,534] Postsynthetic strategies such as size-selective precipitation are also useful for narrowing the size distribution at small diameters if nanocrystal stability and reasonable yield can be maintained throughout the process (Figure 23).[535]

4.2.3.1. X-site Halide Anion and Emission Wavelength. MHP nanocrystals enjoy the same band-gap tunability as their 3D bulk counterparts, as mixed-halide compositions can be achieved either directly during synthesis[529−531] or by reversible anion exchange postsynthesis,[536,537] enabling full coverage of the visible range. This is an advantage over binary inorganic semiconductors, as MHP nanocrystals can be synthesized in the weak confinement regime to mitigate inhomogeneous broadening[538] but maintain coverage of the visible spectrum through compositional alloying. The high ionic mobility that enables facile halide exchange, however, also leaves MHP nanocrystals

https://doi.org/10.1021/acs.chemrev.3c00097
Chem. Rev. XXXX, XXX, XXX−XXX

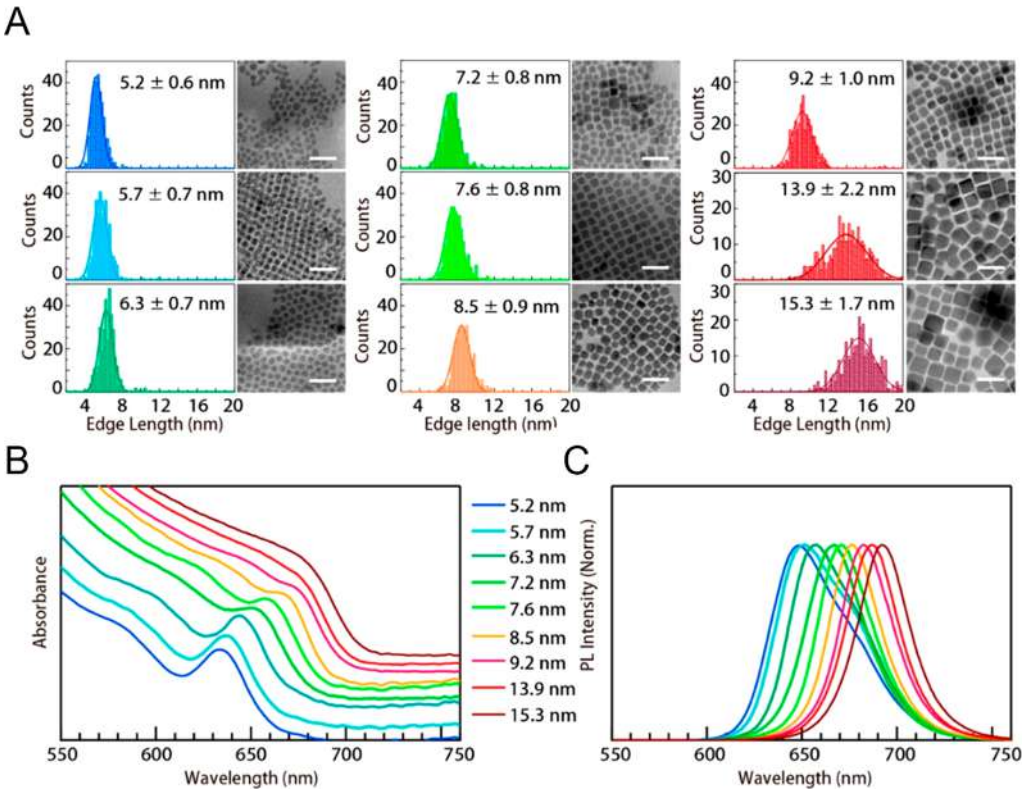

Figure 23. (A) TEM images and size distributions of $CsPbI_3$ nanocrystals with mean edge lengths (assuming a cubic shape) of 5.2−15.3 nm (scale bars = 30 nm). (B) Offset optical absorption spectra normalized by the first excitonic peak and (C) PL spectra for each nanocrystal size. Adapted with permission from ref 535. Copyright 2020, American Chemical Society.

prone to halide segregation driven by applied field or illumination, particularly observable in the broadening and splitting of electroluminescence emission spectra from devices.[539−541] Akin to the compositional and configurational heterogeneity in alloyed compound semiconductors discussed in section 3.2.5, both intra- and internanocrystal halide segregation contribute to line width broadening at the ensemble and individual particle levels. Ongoing efforts to suppress halide segregation in MHP nanocrystals include the use of multidentate ligands to reduce the presence of halide Frenkel defects at the nanocrystal surface, which facilitate halide migration.[541]

4.2.3.2. B-Site Metal Cation and PLQY. The defect-tolerant nature in MHP nanocrystal systems is due to the absence of midgap trap-state formation, despite easily formed halide vacancies, and the resulting suppression of nonradiative recombination pathways. This is another advantage over traditional colloidal QDs, which often require electronic surface passivation via an insulating shell. Intragap trap states are often limited to the surface environments of MHP nanocrystals, and specifically, the presence of excess Pb at the surface can promote nonradiative recombination and a reduction in the PLQY due to the contribution of the Pb 6s and 6p orbitals at the band edges.[542] Methods of removing or coordinating surface Pb to restore surface stoichiometry, such as thiocyanate treatment reported by Koscher et al. or surface treatments involving halides or other strongly coordinating ligands, have all shown decisive improvement, especially in inorganic $CsPbX_3$ nanocrystals, by driving the PLQY to values near unity and improving long-term stability.[543−546]

While the topic of transition-metal and lanthanide doping will be specifically discussed in section 4.3, a wealth of research has been executed concerning the doping of MHP nanocrystals with various metals. By substituting Pb^{2+}, metal doping can have mixed effects on optical performance and nonradiative recombination. B-site dopants have been reported as effective ways to improve the thermodynamic stability and band alignment for both $CsPbI_3$ (Bi^{3+}, Sr^{2+}) and $MAPbI_3$ (Co^{2+}, Cu^{2+}, Mg^{2+}, Mn^{2+}, Ni^{2+}, Sn^{2+}, Sr^{2+}, and Zn^{2+}).[542] Cd^{2+} and Ni^{2+} doping has demonstrated near-unity PLQY enhancements in $CsPbCl_3$ nanocrystals.[547] While Sn^{2+} doping and the use of Sn^{2+} as the sole B-site ion have stirred excitement as PL enhancement dopants, IR emitters and a nontoxic Pb alternative Sn-containing perovskites generally suffer from a low PLQY hindered by the favored oxidation of Sn^{II} to Sn^{IV} and resulting trap states, in stark contrast to the defect tolerance of pure Pb MHPs.[542,548,549]

4.2.3.3. A-Site Cation and Nanocrystal Structure. While MHP nanocrystal emission wavelength is primarily tuned by QD size or halide mixing, mixed A-site compositions offer an additional avenue of control for emission and improving stability, and such as the red emission of $FA_xCs_{1-x}PbI_3$.[551] MHP nanocrystals may exhibit thermal phase transitions, as observed in bulk MHP, from a global high-temperature cubic (α) phase to a tetragonal (β) form and then a low-temperature orthorhombic (γ) form driven by octahedral tilting along one or two principal axes. The crystal structure and symmetry exhibited by MHP nanocrystals is readily tuned via mixing of A-site cations with varied effective radii as framed by the Goldschmidt tolerance factor. $FAPbI_3$ and $CsPbI_3$, for which bulk material can also form nonperovskite phases at room temperature, are stabilized in α and γ perovskite phases, respectively, as nanocrystals.[551,555] Moreover, synchrotron grazing incidence wide-angle X-ray scattering (GIWAXS) studies indicate that the

https://doi.org/10.1021/acs.chemrev.3c00097
Chem. Rev. XXXX, XXX, XXX−XXX

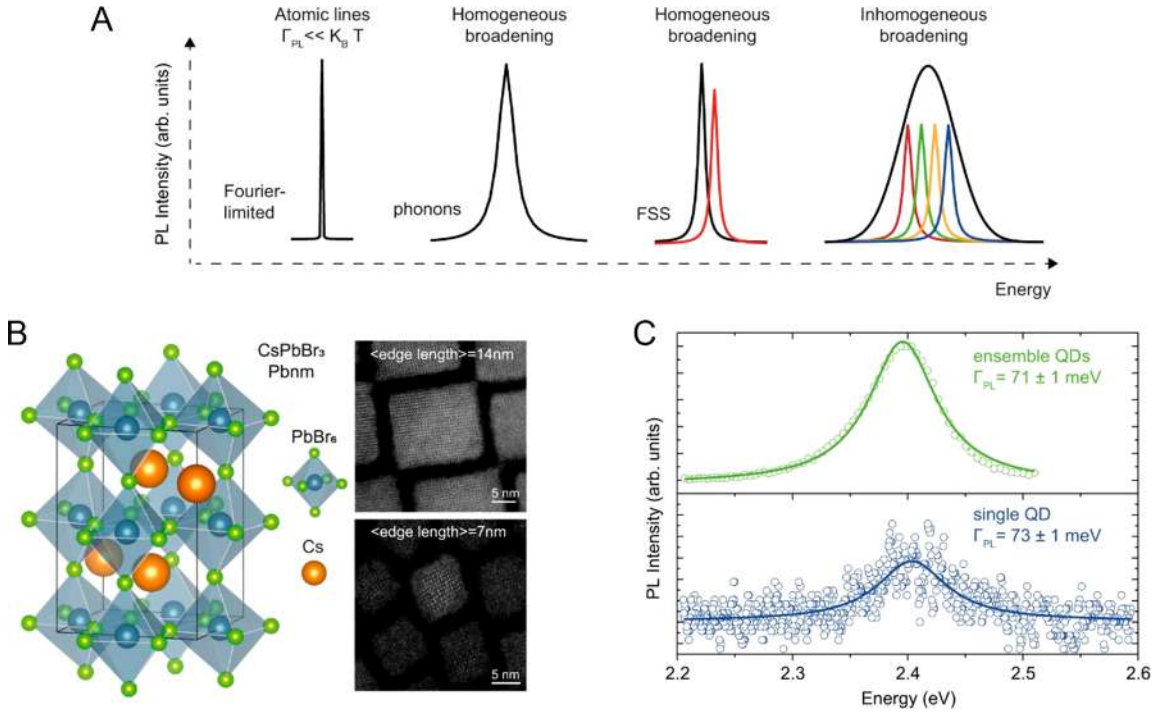

Figure 24. (A) Sketch of PL linewidth (Γ_{PL}) broadening mechanisms. (B) $CsPbBr_3$ orthorhombic crystal structure and HAADF-STEM images of two size-controlled ensembles. (C) Room-temperature PL spectra of QD ensemble (top) and single QD (bottom) fit to Lorentzian line shapes and exhibiting similar broadening. Adapted with permission from ref 126. Copyright 2022, Creative Commons Attribution 4.0 International.

crystal symmetry may be modulated across α, β, and γ phases by increasing the Cs:FA ratio in $FA_xCs_{1-x}PbI_3$. Unique nanocrystal stability is in-part contributed to a modified MHP phase space introduced at the nanoscale, where high surface-to-volume ratios allow surface energy a significant role in moderating the degree of octahedral tilting via size-dependent tensile strain.[535,556] It should be noted that accurate structure determination of MHP systems often requires care and high-resolution diffraction data, the lack of which has historically driven debate over reported structures in the literature. Subtle diffraction peak splitting for the lower symmetry perovskite phases in combination with Scherrer peak-broadening effects of nanocrystals and twinning contribute to difficult phase identification.[555−557] This goes even without mentioning dynamic local order distinct from the observed average crystal structure, necessitating inelastic and total scattering techniques.[558,559] Further study of static and dynamic local order in MHP nanocrystals is necessary to accurately describe sources of homogeneous line width broadening in the soft ionic lattices that are otherwise ill described from an assignment of the average crystal structure.[557,560]

4.2.3.4. Current State of $CsPbX_3$. The inorganic $CsPbX_3$ MHP nanocrystals are the most frequently studied systems, generally due to their narrow, excitonic, and nanosecond radiative decay but also due to their relative stability compared to hybrid systems with more volatile components.[538,561] These properties have prompted micro-PL studies of single MHP nanocrystals that demonstrate single-photon emission and exciton fine structure of interest in quantum emitter technologies.[562−565] Adl et al. in 2021 completed a micro-PL study of single-nanocrystal and nanocrystal ensembles of both $CsPbBr_3$ and $CsPbI_3$ to illuminate the dominant line width broadening phenomena in these systems. Room-temperature single-particle and ensemble measurements were comparable for both material systems with a fwhm of approximately ∼100 meV for both $CsPbBr_3$ and $CsPbI_3$ samples. This suggests that at ambient temperature, inhomogeneous broadening contributions, at least outside of the strong confinement regime (∼10 nm nanocrystal diameters vs $CsPbBr_3$ and $CsPbI_3$ Bohr exciton radii of ∼7 and 4.6 nm, respectively[529,538,566]), are less significant than homogeneous broadening contributions of individual nanocrystals. The authors discuss the clear presence of exciton−phonon interactions, primarily discussing coupling to a longitudinal optical (LO) phonon mode as observed in other published experimental and ab initio efforts.[124,567,568] Subsequent measurements at 4 K demonstrated zero phonon lines of between 1 and 5 meV for $CsPbBr_3$ and between 0.1 and 0.5 meV for $CsPbI_3$. At this low temperature, inhomogeneous broadening from ensemble polydispersity now dominates in the absence of exciton−phonon coupling. In this work, remaining homogeneous contributions at 4 K are suggested to be the product of exciton fine structure and possible spectral diffusion from local dynamic electric field fluctuations.[568]

In a subsequent 2022 micro-PL study,[126] Rainò et al. further interrogated the phenomena driving homogenous broadening of single $CsPbBr_3$ QDs (Figure 24). In this case, cuboidal nanocrystal samples of 7 nm and 14 nm edge lengths and capped in stability-enhancing zwitterionic ligands were measured at room temperature.[126,543] The authors observed a linear increase in single QD line widths with higher PL peak energies and smaller QD sizes, also observed by photon-correlation spectroscopy and in ensembles.[120,176,569] The authors executed ab initio molecular dynamics simulations (AIMD) for a range of QD sizes from 1.8 to 4.2 nm from which the phonon density of states and electron−phonon coupling strength as the Huang−Rhys factor were obtained in agreement with experimental results.[570] AIMD simulations identified three phonon modes: two at low energy (∼2 and ∼7 meV) and the higher energy LO

https://doi.org/10.1021/acs.chemrev.3c00097
Chem. Rev. XXXX, XXX, XXX−XXX

phonon mode (~17 meV). Notably, Huang–Rhys factor calculations show the nanocrystal-size-dependent electron–phonon coupling strength to the two lower energy phonon modes, in contrast to the size-independent nature of the coupling strength to the LO phonon. As the QD size decreases, electron–phonon coupling to the low-energy modes becomes stronger, and for the smallest simulated QDs of 1.8 nm, the Huang–Rhys factor of both low-energy modes is significantly greater than that of the LO phonon. The size-dependent coupling strength could arise from quantum confinement of carriers, surface-localized phonon modes, or a combination of the two. Rainò et al. simulated a core–shell perovskite nanocrystal with Type-I alignment and demonstrated that the size-dependent phonon coupling strength does not arise from stronger carrier confinement but rather that low-energy phonon modes are enhanced at the nanocrystal surface, consistent with the positive correlation of the surface-to-volume ratio and increasingly broad line widths. These findings point to the benefits of a wide-gap epitaxial shell to distance carriers from the localized phonons at the nanocrystal surface. While the growth of epitaxial shells has proven more difficult for MHP nanocrystals compared to conventional QDs, the authors demonstrated surface treatments with trace water content to form wide-gap shells on $CsPbBr_3$. These core–shell $CsPbBr_3$ QDs have demonstrated record RT line widths as low as 35 meV for single QDs and overall improvements for the ensemble with a mean of 60–70 meV.[126]

Even in the absence of phonon line broadening, a remaining contributor to homogeneous broadening impeding Fourier transform-limited line widths in MHP nanocrystals is exciton fine-structure splitting (FSS). FSS arising from reduced symmetry in the crystal structure or nanocrystal shape anisotropy has been characterized for colloidal MHP nanocrystals.[560,571−578] The most recent report[578] investigating exciton FSS by Han et al. has identified splitting by up to 1.6 meV of the bright triplet exciton as a direct result of the lower symmetry orthorhombic phase in $CsPbI_3$ for the smallest QD diameter of 4.9 nm (Figure 25). The observation of a single quantum beat frequency is made in accordance with modeling the exciton fine structure by planes of the persistent cuboidal shape of the nanocrystal rather than the orthorhombic crystal planes.[576,578] While such detailed ventures into low-magnitude line width broadening may be negligible for many conventional MHP nanocrystal device applications, the control of FSS phenomena will be critical to apply MHP nanocrystals as quantum emitters. It should be re-emphasized that efforts toward detailed understanding and control of the local structural order, lattice dynamics, and resulting symmetry in MHP nanocrystal systems will play a key role in the mitigation (or utilization) of exciton FSS and advance ever closer to lifetime-limited narrow emission.

In general, for the perovskite family of materials, several parameters may affect emission line broadening.

(1) Composition—changing the cation or anion can affect the lattice distortion, strain, or self-trapped exciton, leading to changes in emission line width that are material dependent.

(2) Sample inhomogeneity—many of the problems contributing to inhomogeneous broadening discussed in section 4.1 also affect perovskites. Particularly, halide segregation leads to structural subpopulations that are detrimental to line width and must be avoided.

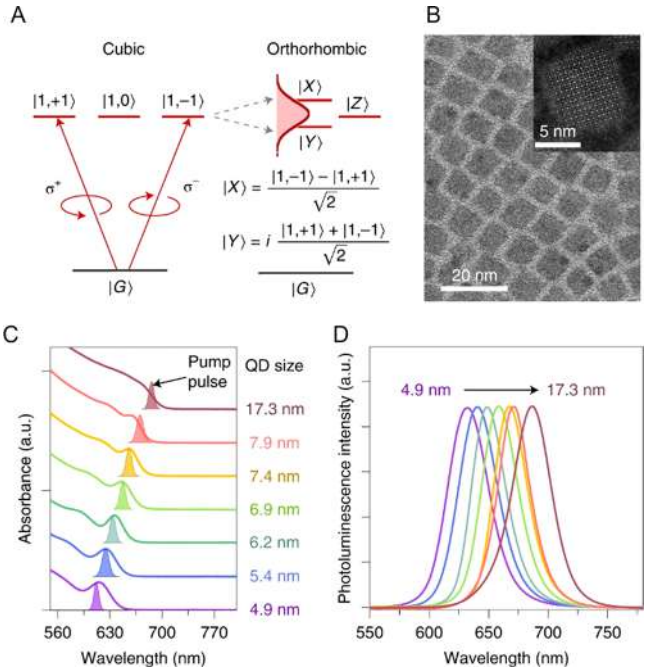

Figure 25. (A) Bright triplet $|1, \pm 1\rangle$ exciton states of cubic symmetry and their split into two eigenstates $|X\rangle$ and $|Y\rangle$ in orthorhombic QDs, the difference between which is ΔFSS, where crystal ground state is $|G\rangle$. The transition dipole of exciton state $|Z\rangle = |1,0\rangle$ is along the z-axis and for this illustration, the excitation is a circularly polarized pulse also directed along the z-axis with bandwidth > ΔFSS. (B) 7.9 nm QDs shown in bright and dark-field TEM. (C) Optical absorption and (D) PL spectra of sized QDs in hexane. Adapted with permission from ref 578. Copyright 2022 Springer Nature.

(3) Exciton–phonon coupling—as with QDs, perovskite emission is broadened via coupling to phonon modes on the surface and in the core. A shell is typically introduced to mitigate this; however, this is a large synthetic challenge for perovskites that is being actively explored.

(4) Exciton fine-structure splitting—greater control over local structural order and symmetry will enable harnessing or mitigating FSS phenomena.

4.3. Transition-Metal- and Rare-Earth-Doped Nanocrystals

Transition-metal and lanthanide dopants in nanocrystals can impart PL derived from emission localized at these ions, and in some cases, this emission can be very narrow. The line width of this emission is dependent on the electronic structure of the dopant ion, the surrounding lattice, and the interaction between the two. Beyond all of the extrinsic contributions to inhomogeneous broadening outlined elsewhere (above), such interactions can broaden even the *homogeneous* line shapes. When pursuing the narrowest emission from dopants, the first property to consider is how the electronic transition responsible for luminescence may distort the local bonding and thus alter whether vibronic (phonon-coupled) transitions are allowed. Figure 26 outlines four general categories of common dopant-centered electronic transitions and their relationships to emission line width in transition-metal- and lanthanide-doped nanocrystals in order of broadest to narrowest.

Charge-transfer transitions generally lead to the broadest emission among dopant-centered transition types. Here, transitions between ground and charge-transfer excited states involve formal charge transfer between localized dopant orbitals

https://doi.org/10.1021/acs.chemrev.3c00097
Chem. Rev. XXXX, XXX, XXX−XXX

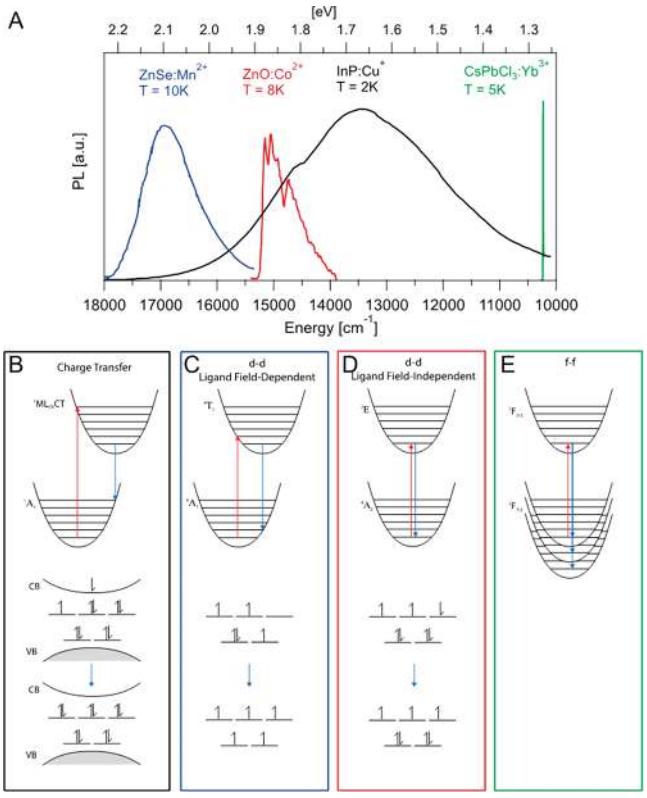

Figure 26. (A) Low-temperature PL spectra and (b–e) corresponding state and one-electron orbital splitting diagrams for four classes of dopant-centered radiative transitions observed in nanocrystals. (B) Charge transfer from localized dopant orbitals to the delocalized conduction band (CB) in InP:Cu^+ distorts the excited state along one or more nuclear coordinates, and this distortion broadens the resulting emission.[579] (C) Mn^{2+} emission when doped into ZnSe nanocrystals is broadened due to nuclear distortions arising from the ligand-field dependence of its lowest energy d–d transition.[580] (D) Emission from ZnO:Co^{2+} nanocrystals is sharper because there is no change in bonding between the ground ($^4A_2$) and the lowest energy excited (^2E) states, keeping them vertically aligned, i.e., this spin-flip d–d transition is ligand-field independent.[581] (e) Due to high shielding of the valence f orbitals, f–f transitions in lanthanides are accompanied by little lattice distortion, e.g., in $CsPbCl_3$:Yb^{3+} nanocrystals.[582] Such f–f emission is thus always ligand-field independent.

and either (i) a delocalized conduction or valence band of a host semiconductor or (ii) the valence orbitals of the surrounding ligands in insulating nanocrystals. This change in orbital occupancy causes a significant geometric distortion along one or more nuclear coordinate, illustrated schematically by the shift of the excited-state potential energy surface relative to the ground state in Figure 26B. Most of the emission will come from the lowest energy excited state. Due to the nuclear distortion, the emission probability is now distributed across a range of ground-state vibrational energy levels, resulting in an energy-broadened emission spectrum. As an illustrative example, Cu^+:InP nanocrystal (Figure 26A) luminescence involves radiative recombination of a conduction band electron with a d-orbital hole, corresponding to a $^1ML_{CB}CT$ to $^1A_1$ (ground-state) electronic transition.[579]

Although there is no charge transfer to or from the dopant, ligand-field-dependent d–d transitions of transition-metal ions also commonly show sizable vibronic broadening because they involve changes in orbital occupancy within the d subshell that still alter bonding because they either increase or decrease the population of σ-antibonding d orbitals. The resulting change in bonding creates a nuclear distortion that shifts the excited-state potential energy surface along one or more nuclear coordinates relative to the ground state, and this shift results in energy-broadened emission. Nuclear distortions in d–d excited states are typically not as large as those in charge-transfer excited states; hence, the corresponding d–d emission can be somewhat narrower. For Mn^{2+}:ZnSe nanocrystals (Figure 26C), for example, the $^6A_1$ ground state has five unpaired electrons with one in each of the five d orbitals.[580] The first excited state, $^4T_1$, results from a spin-flip excitation wherein an electron moves from the less stable t_2 orbital set and pairs with an electron in the more stable e set. The increase in the overall energy of this excitation is due to the high energetic cost of pairing spins. Because the t_2 set is more antibonding than the e set, the equilibrium bond lengths in the $^4T_1$ excited state are on average contracted and luminescence again involves emission probabilities distributed across a range of ground-state vibrational energy levels.

When d–d transitions between ground and excited states *do not* primarily involve a change in orbital occupancy but instead involve simply flipping an electron's spin, these are referred to as ligand-field-independent d–d transitions. Because no change in bonding occurs, the potential-energy surfaces for the two states involved in the emission process are nearly vertically aligned for every nuclear coordinate. At low temperature, PL intensity can be concentrated in the zero-phonon line (subject to symmetry restrictions). For example, for tetrahedral Co^{2+} in wurtzite ZnO nanocrystals (Figure 26D), the lowest energy excited state (^2E) is created when the spin of an electron in the t_2 orbital set is flipped relative to the ground state ($^4A_2$).[581] As a consequence, d–d emission from this ^2E excited state is concentrated in the spin–orbit split electronic origin (zero-phonon line) and can be very narrow. In colloidal nanostructures, this line width is broadened *inhomogeneously* with decreasing dimensionality, emphasizing the impact of nanocrystal interfaces even on highly localized dopants. Additionally, the proximity of the $^4T_1$ (P) excited state to the ^2E state combined with the different radiative transition probabilities of spin-allowed and spin-forbidden transitions in Co^{2+} leads to the observed additional broad emission to the lower energy side of the ^2E split origin. $^4T_1$ (P) emission is vibronically broadened following the mechanism described above.

For lanthanide (or rare earth, RE) dopants, the valence electrons are in f orbitals instead of d orbitals. Due to high f-orbital screening, electron–nuclear coupling is typically very small for the f shell, and the ground and excited states of f–f transitions are vertically aligned for every nuclear coordinate. In contrast to d–d transitions, all f–f transitions are thus ligand-field independent, and f–f emission is typically extremely narrow. The energy splitting between the ground and the f–f excited states results primarily from spin–orbit coupling, while the crystal-field splitting causes only relatively small splittings of each multiplet. For example, the $^2F_{7/2}$ ground and $^2F_{5/2}$ excited terms of Yb^{3+} shown in Figure 26E are each split by ~500 cm^{-1} (ca. 62 meV) due to crystal-field interactions, but the $^2F_{7/2}$–$^2F_{5/2}$ energy splitting is ~10 000 cm^{-1} (ca. 1.2 eV) due to spin–orbit coupling.[582]

Once a system has been selected that shows acceptably small vibronic broadening, additional factors contribute to determining the line widths of the remaining transitions. Generally, the zero-phonon line is narrowest, and its line width is dominated by extrinsic inhomogeneous effects, especially in nanocrystals. This

https://doi.org/10.1021/acs.chemrev.3c00097
Chem. Rev. XXXX, XXX, XXX–XXX

Table 7. Emission Characteristics of Selected Doped Colloidal Nanocrystals

material	emission transition	class	temp (K)	PL (cm^{-1}/meV)	PL fwhm (cm^{-1})[a]	PL lifetime (ms)	refs
$InP:Cu^{+}$	$^{1}ML_{CB}CT \rightarrow {}^{1}A_1$	charge transfer	2	13 150/1630	3180	5	579
$CdSe:Cu^{+}$	$^{1}ML_{CB}CT \rightarrow {}^{1}A_1$	charge transfer	15	12 260/1520	3065	2.4	579
$ZnS:Cu^{+}$	$^{1}ML_{CB}CT \rightarrow {}^{1}A_1$	charge transfer	4	21 050/2610	2222	20	587
$ZnSe:Mn^{2+}$	$^{4}T_1 \rightarrow {}^{6}A_1$	d−d, ligand-field dependent	10	17 244/2138	1210		580
$ZnSe:Mn^{2+}$	$^{4}T_1 \rightarrow {}^{6}A_1$	d−d, ligand-field dependent	298	17 244/2138	1613		580
$ZnSe:Mn^{2+}$	$^{4}T_1 \rightarrow {}^{6}A_1$	d−d, ligand-field dependent	298	17 543/2175	1788	290	588
$CdS:Mn^{2+}$	$^{4}T_1 \rightarrow {}^{6}A_1$	d−d, ligand-field dependent	5	16 949/2101	1390	1000	589
$ZnS:Mn^{2+}$	$^{4}T_1 \rightarrow {}^{6}A_1$	d−d, ligand-field dependent	300	16 667/2066	2232	1900	590
$ZnO:Co^{2+}$	$^{2}E \rightarrow {}^{4}A_2$	d−d, ligand-field independent	8	15 155/1879	90	0.015	591
$ZnO:Co^{2+}$	$^{2}E \rightarrow {}^{4}A_2$	d−d, ligand-field independent	8	15 160/1880	85	0.065	581
$CsPbCl_3:Yb^{3+}$	$^{2}F_{5/2} \rightarrow {}^{2}F_{7/2}$	f−f	5	10 233/1269	4	4000	582
$CaF_2:Yb^{3+}/Er^{3+}$	$^{4}S_{3/2} \rightarrow {}^{4}I_{15/2}$	f−f	298	18 480/2291	510		592
$NaYF_4:Yb^{3+}/Er^{3+}$	$^{4}S_{3/2} \rightarrow {}^{4}I_{15/2}$	f−f	298	18 480/2291	510		592
$SrS:Ce^{3+}$	$^{4}F_1 \rightarrow {}^{5}D_1$	d−f	298	20 576/2551	1624	0.056	593
$CdSe:Tb^{3+}$	$^{5}D_4 \rightarrow {}^{7}F_5$	f−f	298	18 350/2275	440	3000	594

[a]For spectra with multiple peaks, the peak of narrowest fwhm is reported.

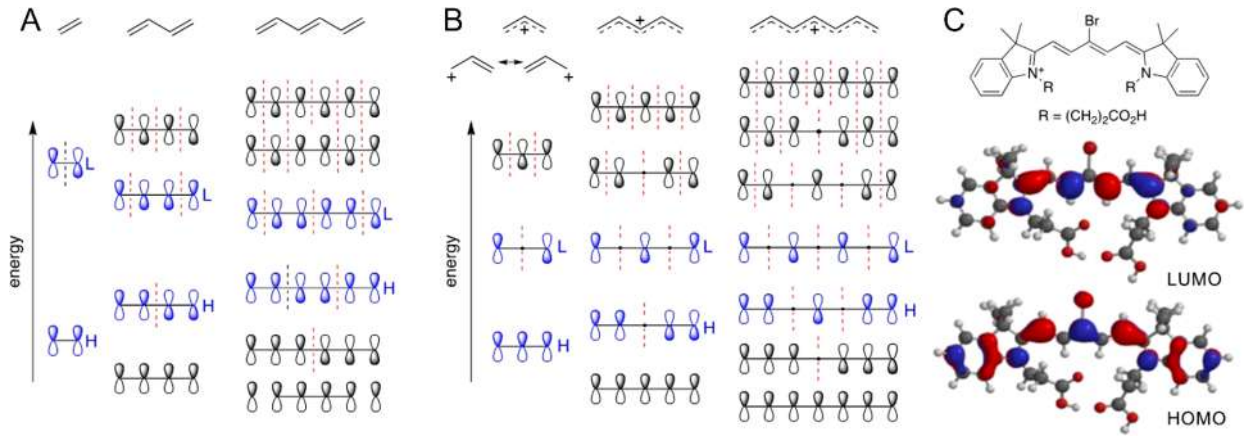

Figure 27. (A and B) Sketches of π orbitals for three polyenes and three polymethine cations, respectively, with the HOMO (H) and LUMO (L) in each case in blue and nodal planes perpendicular to the molecular axis denoted by dashed red lines. Note that the nodal planes shown as passing through atoms in the polymethines only do so precisely by symmetry for the central carbon atom; nonetheless, as shown in C, orbital coefficients on these atoms are at least very small according to quantum-chemical calculations. Also note that the LUMO and LUMO+1 of each polymethine cation correspond to the HOMO and LUMO, respectively, of the corresponding polymethine anion. (C) Structure and DFT HOMO and LUMO of an example of a cyanine dye (Reproduced with permission from ref 603. Copyright 2017 SAGE.) that contains a cationic heptamethine moiety. Note that these orbitals are similar to those sketched for the heptamethine cation in B with extra contributions from the indole nitrogen atom and, in the case of the HOMO, the Br substituent and the indole arene rings.

inhomogeneous broadening reflects the distribution of static local environments around the ensemble of dopants. In addition, there may be time-averaged and dynamic distributions of electric-field and magnetic environments resulting from the dopant's proximity to the surface, proximity to other defects, or nuclear hyperfine coupling that contribute to the dynamic line shape. In general, lifetime broadening is not the dominant contribution to the line width of dopant emission in nanocrystals. Table 7 collects the emission characteristics of ensembles of doped nanocrystals from the literature and classifies them according to the aforementioned criteria. The table represents just a handful of examples to illustrate the various categories of dopant-centered electronic transitions in colloidal nanocrystals and is not intended to be comprehensive. The reader is referred to additional reviews for more extensive discussion of each category.[583−586] The tabulated line widths show that f−f transitions and ligand-field-independent d−d transitions have the narrowest emission, reinforcing the above discussion.

To summarize, when utilizing doped nanocrystals as emitters, one must consider (1) the identity of the dopant and its electronic transitions, leading to varying degrees of vibronic coupling, and (2) extrinsic inhomogeneous effects also mentioned in sections 4.1 and 4.2, specifically leading to a distribution of local environments around each dopant.

4.4. Organic Molecules: Special Case of Solution-Phase Emitters

Here, we briefly review the ranges of PL line widths that may be seen for organic molecules (and their aggregates) in solution and, in less detail, in solid films. We note that some of these molecules also function as semiconductors in the solid state, but our main focus is on comparing the emission line widths that can be achieved with those discussed in preceding sections. As we have discussed in section 3, the line width of a particular absorption or emission band in a molecule is quantum mechanically related to both the electronic and the vibrational contributions to the transition dipole moment of the transition

https://doi.org/10.1021/acs.chemrev.3c00097
Chem. Rev. XXXX, XXX, XXX−XXX

in question, which measures the degree to which they are allowed. In π-conjugated organic molecules, relatively strong coupling between electronic and vibrational excitations results in so-called *vibronic* transitions. Quantum mechanically, such transitions are treated using time-dependent Hamiltonians that include a perturbation due the electric field of light (and rigorously also its magnetic field, although this is often neglected). Using the Born−Oppenheimer approximation, the Hamiltonian can be separated into parts that involve electron motions and nuclear motions because the motion of the relatively heavy nuclei is much slower than that of the much lighter electrons.

To understand the line width in π-conjugated organic molecules, it is helpful to consider two limiting cases of quasi-linear π systems

(1) polyene-like molecules $H(CH)_{2n}H$ and

(2) polymethine-like ions $[H(CH)_{2n+1}H]^{\pm 1}$

where n is a nonzero integer. This distinction has been used extensively to understand the linear[595,596] and nonlinear[597,598] optical properties of more elaborate conjugated molecules and reflects distinct differences in the nodal properties of the frontier orbitals of these molecules.

The simplest polyene—ethylene—can be considered as having both carbon and hydrogen atoms lying in the *x,y* plane with each carbon atom contributing a p_z orbital to the π system—this gives rise to two π molecular orbitals: (1) the highest occupied molecular orbital (HOMO), which is stabilized relative to an isolated p_z orbital and bonding in character and (2) the lowest unoccupied molecular orbital (LUMO), which, due to a node *between* the two carbon atoms, is destabilized with respect to a p_z orbital and antibonding in character. The simplest polymethine—allyl—consists of three carbon atoms that contribute p_z orbitals, leading to the formation of three molecular π orbitals: (1) the lowest has no nodes and is thus bonding between each adjacent pair of carbon atoms; (2) the highest has two nodes (between atoms, like the LUMO of ethylene) and is antibonding between each adjacent pair of carbons in the chain; (3) the π orbital at intermediate energy—the LUMO of the allyl cation and the HOMO of the allyl cation—is characterized by a nodal plane passing through the central carbon atom with contributions from only the p_z orbitals of the terminal atoms and thus, within the Hückel approximation, nonbonding and neither stabilized nor destabilized with respect to isolated p_z orbitals. Longer homologues exhibit similar patterns, as shown schematically for n = 2 and 3 polyenes and polymethines in Figure 27. The antibonding interaction between the central two carbon atoms in the HOMO of butadiene leads to this C−C bond in the ground-state molecule being considerably longer than the other two C−C bonds, i.e., to a significant bond-length alternation (BLA) between the bonds rendered as formally double and single in a valence-bond representation; this BLA is also seen in longer homologues such as hexatriene and β-carotene (a substituted n = 11 polyene). On the other hand, the two C−C bonds of the allyl cation (or anion) are equal in length. Even in pentadienyl or heptatrienyl cations (n = 2 and 3 polymethines), the filled π orbitals are all either bonding or nonbonding between adjacent carbons, and thus, there is relatively little variation between adjacent bond lengths and certainly not a pattern of *alternating* bond lengths. (As a caveat, we note that in long-chain polymethines, the charge is no longer delocalized over the entire chain length: in $[Ph(CH)_{2n+1}Ph]^-$ ions, the charge no longer reaches the terminal phenyl groups for $n \approx 15$, i.e., ca. 31 methines,[599] whereas in organic cyanines with more effective charge-stabilizing end groups, the charge becomes localized on one end group rather than shared by both with significant nonzero BLA in between, at $n \approx 4-6$, i.e., ca. 9−13 methine units, depending on the end group, solvent, and counter-ion.[600−602]) Furthermore, a one-electron HOMO−LUMO excitation in ethylene involves depopulating a C−C bonding orbital and populating a C−C antibonding orbital. Similarly, in butadiene, the electron is promoted to a LUMO in which the bonding and antibonding interactions between adjacent C atoms are reversed relative to those in the HOMO. Thus, the equilibrium excited-state C−C bond lengths of polyenes, reached after the geometric relaxation that follows excitation, differ considerably from those in the ground state. On the other hand, in polymethine cations (anions), a HOMO−LUMO excitation involves promotion from a partially bonding to a nonbonding orbital (from a nonbonding to a partially antibonding orbital) and thus to a smaller change in equilibrium C−C bond lengths.

Thus, in general, the ground and excited states of polyene-like molecules will have a much greater difference in their equilibrium geometries, specifically with respect to C−C bond lengths, than those of polymethine-like molecules. Returning to the Franck−Condon principle, the ground and excited states of molecules can be represented as shown in Figure 28, where the two electronic states are represented as parabolic wells, with the horizontal offset representing the differences in equilibrium geometry and where the horizontal "rungs" represent the C−C stretching modes in each state. For the polymethine dyes, the similarity of the ground- and excited-state geometries leads to strong vibrational overlap between the zeroth level in the ground state and the zeroth level in the excited state; thus, the so-called 0,0 transition (represented by the heaviest arrows) is dominant

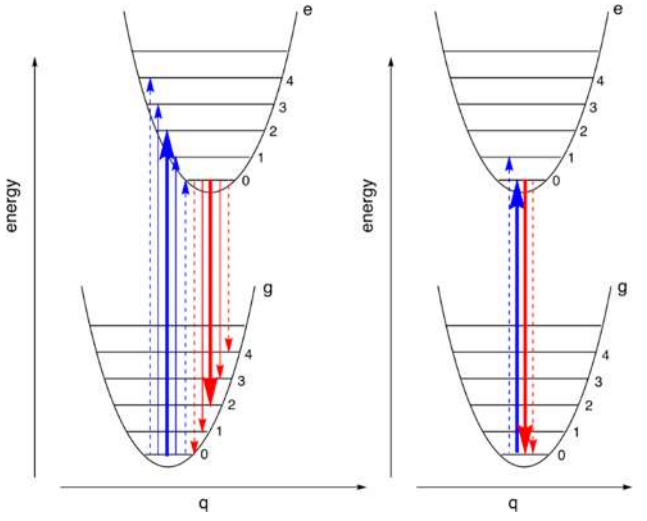

Figure 28. Schematics showing the ground-state (g) and excited-state (e) potential energy surfaces for (left) a molecule, such as a polyene, with significantly different ground- and excited-state geometries and (right) a molecule, such as a polymethine, with similar ground- and excited-state geometries. Absorption and fluorescence vibronic transitions are represented by blue and red arrows, respectively, with the heaviness of the arrows roughly denoting the relative strength of each transition. In both cases, q represents a coordinate representing the C−C bond lengths and the "rungs" in the ground and excited states reflect the vibrational levels associated with the C−C stretching modes in those states.

https://doi.org/10.1021/acs.chemrev.3c00097
Chem. Rev. XXXX, XXX, XXX−XXX

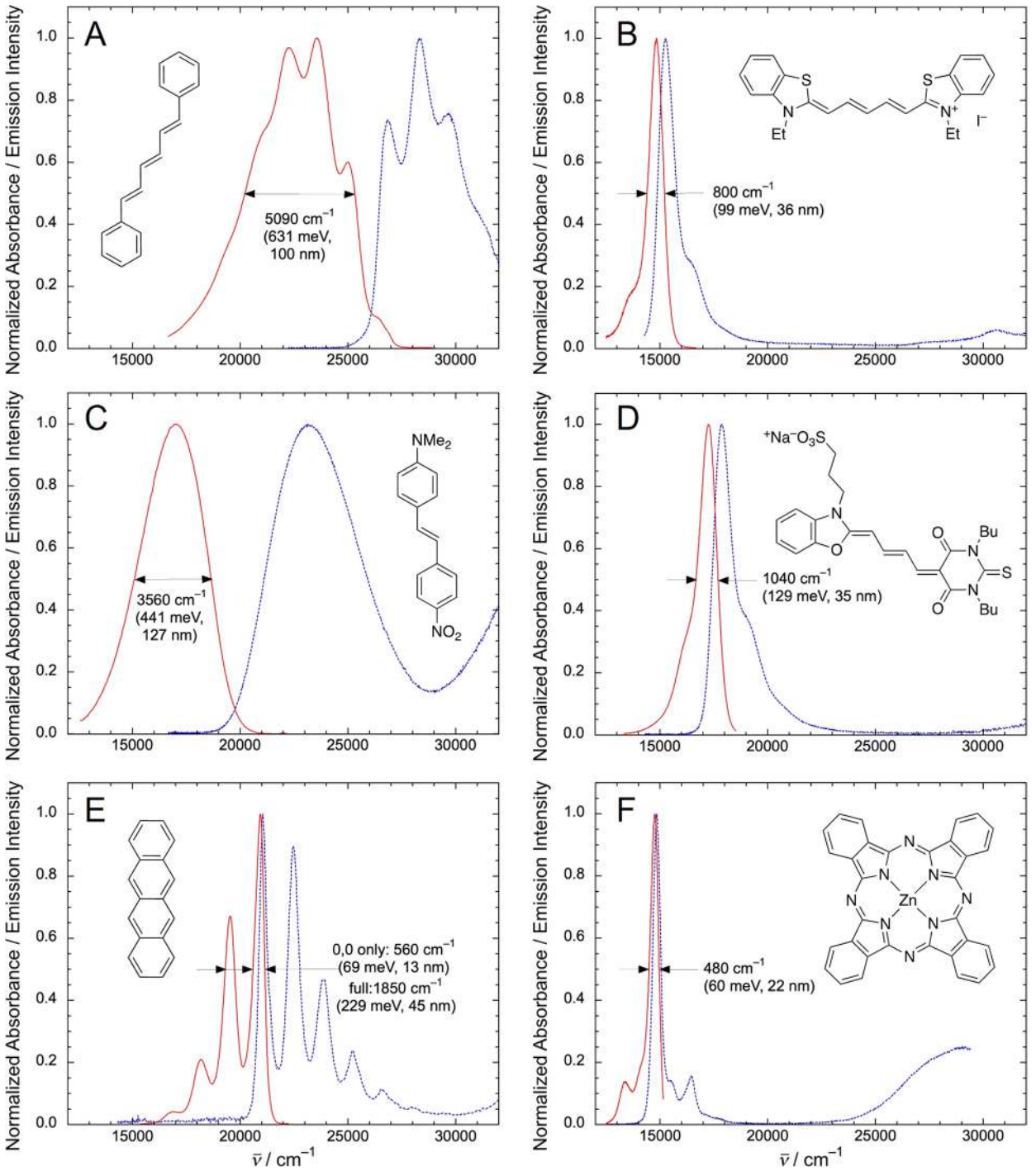

Figure 29. Solution absorption (blue) and emission (red) spectra of representative examples of various classes of organic chromophore, replotted using data available from the online PhotochemCAD database:[607−609] (A) a diphenylpolyene (in cyclohexane), (B) a cyanine (in ethanol), (C) a donor−(π-bridge)−acceptor molecule with a polyene-type structure (in benzene), (D) a merocyanine example of a donor−(π-bridge)−acceptor compound having a cyanine-like structure characterized by near-zero bond-length alternation (in ethanol), (E) a rigid aromatic (in benzene), and (F) a porphyrin-like heterocycle, specifically zinc phthalocyanine (in pyridine). In each case, the fwhm is given for the emission spectrum; note that values in wavenumber or energy units are more representative of each compound class, whereas the fwhm in wavelength units is dependent on both the compound class and the wavelength at which the specific example shown emits.

in both absorption and emission spectra. In addition, there is little difference in absorption and emission maxima (i.e., a small Stokes shift). On the other hand, for the polyene, the greatest overlap relevant to absorption is between the ground-state zeroth vibrational level and a higher (as drawn, the second) excited-state vibrational level, while for fluorescence, the zeroth vibrational level in the excited state overlaps most strongly with a higher (as drawn, second) ground-state vibrational level with, in both cases, appreciable oscillator strength for other vibronic sub-bands. Thus, polyene-like dyes are expected to exhibit broader absorption and emission bands than polymethines and to exhibit larger Stokes shifts. Simple unsubstituted polyenes and, especially, polymethine ions are not particularly stable species. However, the molecules in Figure 29A and 29B—a polyene with

https://doi.org/10.1021/acs.chemrev.3c00097
Chem. Rev. XXXX, XXX, XXX−XXX

stabilizing phenyl end groups and a cyanine dye in which a polymethine cation bears two charge-stabilizing end groups, respectively—illustrate the differences in absorption and emission line shapes between these two classes of molecules. Clearly, both the absorption and the emission bands of the first compound exhibit multiple vibronic sub-bands, are *not* 0,0 peaked, and are therefore relatively broad. (An additional complication with many polyenes, such as $Ph(CH{=}CH)_4Ph$,[604] is that the lowest singlet excited state, S_1, does not correspond to an allowed one-electron HOMO → LUMO excitation but rather to a state that can be described as resulting from configuration interaction between HOMO−1 → LUMO, HOMO → LUMO+1, and double HOMO → LUMO excitation,[605] which is forbidden for an ideal planar all-*E* geometry and thus only weakly emissive. In some studies, dual emission is seen, with both the S_1 and the S_2 (HOMO → LUMO) states contributing.[606] Nevertheless, the general principles discussed regarding absorption and emission broadening still stand.) The cyanine, on the other hand, exhibits a much smaller Stokes shift and 0,0-peaked spectra resulting in much narrower bandwidths.

Narrow cyanine-like spectra are also seen for molecules with related electronic structures that can also be represented as a superposition of two limiting equivalent resonance structures (Figure 30A) in which terminal atoms bear a charge and for which the frontier orbitals have similar nodal properties to those of polymethines; examples include squaraines, croconium dyes, rhodamines, fluoresceins, and BODIPY dyes (Figure 30C, 30D, 30E, 30F, and 30G, respectively). Unsymmetrical donor−(π-bridge)−acceptor molecules often exhibit broad spectra (Figure 29C), as discussed below, but in special cases, a suitable balance of donor and acceptor strengths can result in equal contributions from neutral and zwitterionic valence-bond structures and thus minimal bond-length alternation and cyanine-like spectra (Figure 29B and 29D); however, in dyes of this type, the energetic balance of the two valence-bond structures and thus the BLA and the spectral line shapes are typically highly sensitive to solvent polarity.

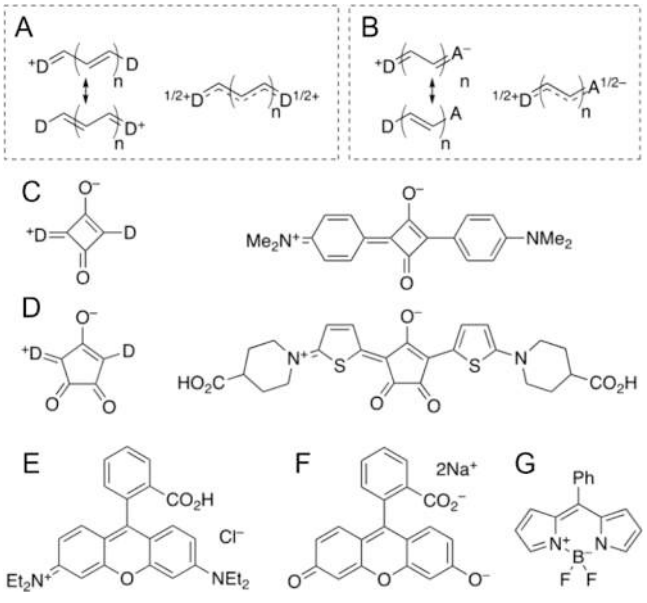

Figure 30. Cyanine-like dyes with narrow emission bands: (A) schematic showing how cyanine dyes can be represented by two extreme valence bond structures (D = π-donor); (B) schematic showing how the same can apply to D−(π-bridge)−A (A = π-acceptor) compounds in which D and A strengths are appropriately balanced, such as in the dye shown in Figure 28D; (C and D) generic structures of squaraine and croconium dyes, respectively, along with specific examples for which narrow emission spectra have been reported; (E, F, and G) structures of rhodamine B, fluorescein, and an example of BODIPY derivative, respectively. Spectra of compounds shown in C and E−G may be found in the PhotochemCAD database,[608,609] while spectra for the croconium dye shown in D are reported by Wang et al.[610]

Thus far, we have considered only geometric changes between ground and excited states associated with C−C bond length, i.e., vibronic coupling to relatively high-frequency C—C stretching modes. In addition, coupling to other modes can affect the line shape, with low-frequency in- and out-of-plane bends, for example, contributing to the line width of each subpeak of a vibronically structured spectrum. Thus, there is variation in the line widths of cyanine-like dyes with 0,0-peaked spectra due to the possibility of coupling to other modes; all else being equal, coupling to other modes will be suppressed in more rigid systems. This is also true in other rigid systems, notably fused-ring aromatics such as acenes (Figure 29E) and perylene diimides, for which individual sub-bands are often very narrow. However, coupling to C−C stretching modes is stronger in these species than in cyanine-like dyes (i.e., there are larger changes in equilibrium C−C bond lengths between ground and excited states), and so, although the 0,0 peaks are often the strongest in the absorption and emission spectra, the other sub-bands are much more significant than for cyanines, leading to a broader overall emission (although this broadness may or may not be captured by the commonly used fwhm measure, depending on the exact relative strengths of the 0,0 and 0,1 vibronic components). Examples of phthalocyanines, naphthalocyanines, and porphyrins can exhibit *both* very narrow 0,0 transitions, due to their rigid planar cyclic structures, *and* strongly 0,0 peaked spectra, due to weak coupling to C−C and C−N stretching modes, which in turn is attributable to frontier orbitals with similar nodal properties to those of polymethines (Figures 29F and 31).[611] It should be noted, however, that some choices of the central metal ion or substituents can lead to compounds that are nonemissive or have broad emissions with charge-transfer character.

More complex patterns of vibronic coupling can lead to less well-resolved vibronic structure, as can the presence of a range of solvation environments. The latter effect, which we have not so

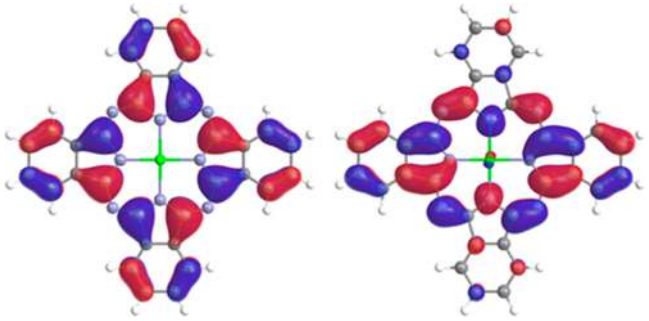

Figure 31. DFT HOMO (left) and LUMO (right, one of a pair of degenerate orbitals) of zinc phthalocyanine (see Figure 29F for structure and spectra). Adapted with permission from ref 611. Copyright 2019 American Chemical Society. Note that the eight nitrogen atoms all lie on nodal planes in the HOMO.

https://doi.org/10.1021/acs.chemrev.3c00097
Chem. Rev. XXXX, XXX, XXX−XXX

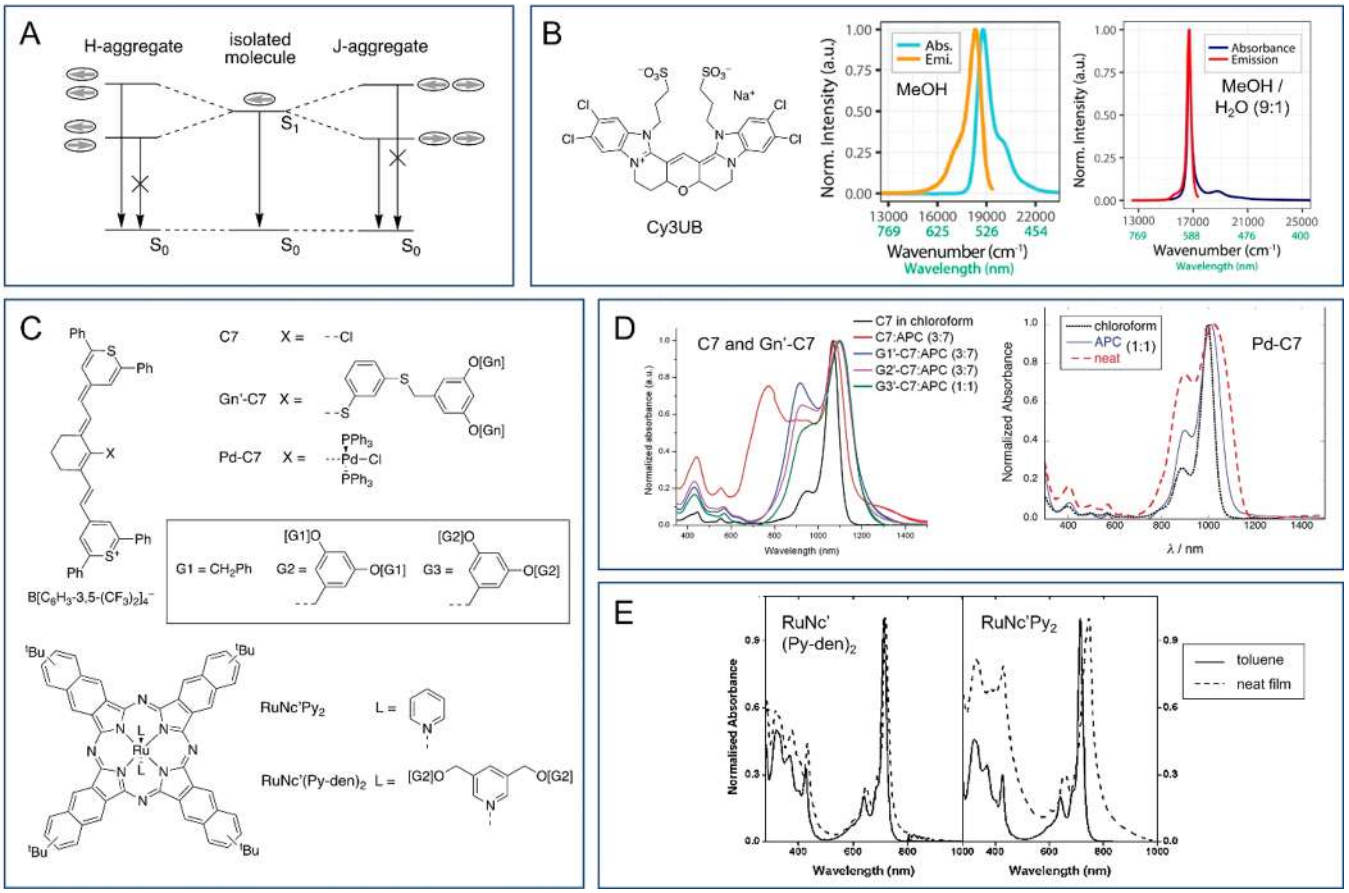

Figure 32. (A) Schematic showing how a side-by-side (H-aggregate) alignment of chromophore transition dipoles leads to a low-energy nonemissive state but how end-to-end (J-aggregate) alignment leads to an emissive state lower in energy than that of the monomer. (B) Structure of Cy3UB, an example of a cyanine dye reported to form J aggregates, along with absorption and emission spectra of monomeric Cy3UB in MeOH and of Cy3UB J aggregates in 9:1 MeOH/H_2O. Spectra reproduced with permission from ref 616. Copyright 2022 American Chemical Society. (C) Examples of the use of bulky substituents to attempt to achieve "site isolation" of chromophores in the solid state. (D) Absorption spectra of C7 derivatives shown in C in solution and in high-concentration films, showing the limited effectiveness of the Fréchet-type dendron approach (left) vs the use of a rigidly out-of-plane bulky organometallic substituent (right) in preserving solution-like spectra in films. Spectra reproduced from refs 617 and 621. Copyright 2012 American Chemical Society and copyright 2018 Royal Society of Chemistry. (E) Absorption of ruthenium naphthalocyanine derivatives shown in C in solution and in neat films, showing that, in this case, the use of Fréchet-type dendrons leads to solution-like spectra in the solid state. Spectra reproduced from ref 618. Copyright 2011 Royal Society of Chemistry.

far explicitly considered, is particularly important for polar molecules, and in general, transitions that have dipolar charge-transfer character are relatively broad and featureless. Figure 29C shows an example of a donor−(π-bridge)−acceptor molecule with a polyene-type structure (strong bond-length alternation in the vinylene bridge). The band appears as a not quite symmetrical featureless Gaussian envelope due to the combination of a non-0,0-peaked spectrum and these additional broadening mechanisms "smearing out" any vibrational structure.

Thus far, we have considered isolated chromophores. In the solid state and, in some cases, in solution at high concentrations or in solvents that poorly solvate the monomeric species, the shapes of both absorption and emission spectra solutions can also be impacted by intermolecular aggregation phenomena. Aggregation can have a variety of effects on spectra, some of which lead to spectral broadening; however, of most relevance to obtaining narrow PL are so-called J aggregates. H and J aggregates are types of ordered assemblies in which coupling between two or more chromophores results in excitons lower and higher in energy than the excited state of the isolated molecule; H and J aggregates can be classified according to whether the aggregate absorption is blue and red shifted, respectively, relative to the that of the isolated chromophore. Within the exciton theory of Kasha,[612] which considers only Coulombic coupling between parallel transition dipoles in adjacent molecules, H aggregates are found when the angle between the transition dipoles and the vector connecting the centers of adjacent dipoles is greater than 54.7°, with the largest coupling and largest blue shift obtained when the angle is 90° (side-by-side dipoles); for these, the inversion symmetry of the lowest energy aggregate exciton means that fluorescence is forbidden (Figure 32A). On the other hand, the lowest energy excitons in J aggregates, in which the angle is less than 54.7° and the coupling largest at 0° (end-to-end dipoles), are strongly coupled to the ground state and thus potentially fluorescent. We note, however, that in some aggregates other coupling mechanisms can contribute and, in some cases, lead to different geometric criteria for observation of the characteristic spectroscopic features of each aggregate type.[613] Compared to the corresponding isolated chromophores, J-aggregate emission spectra are (i) red shifted (as explained by the cartoon of Figure 32A), (ii) more strongly 0,0 peaked, and (iii) in many strongly coupled cases characterized by narrower widths for each sub-

https://doi.org/10.1021/acs.chemrev.3c00097
Chem. Rev. XXXX, XXX, XXX−XXX

band. The increased relative intensity of the 0,0 subpeak can been explained using quantum-mechanical analysis of the vibronic structure,[614] while the 0,0 peak is narrowed due to rapid motion of the exciton between different sites.[615] As an example, the left portion of Figure 32B shows the structure of a recently reported J-aggregate-forming dye, Cy3UB.[616] Like many such aggregate-forming dyes, this is a cyanine dye, the planarity and large polarizability of which favors aggregate formation in poor solvents, and even the isolated molecule shows a fairly narrow emission spectrum (Figure 32B, center), with the aggregate (Figure 32B, right) clearly showing the three characteristics of J-aggregate spectra noted above, notably a narrower 0,0 emission.

As noted above, narrow absorption and emission features can be obtained in the solid state for dyes that form highly ordered J aggregates. However, for many dyes, considerable broadening and in some cases emission quenching is obtained due to H-aggregate formation, due to the formation of aggregates in which there are multiple different interchromophore couplings, and/or due to disorder affording a range of different chromophore environments. An alternative approach to retaining or partially retaining solution-like narrow bands in the solid state is through site isolation. This, in principle, can be achieved using dilution in an "optically innocent" host material or by functionalizing the chromophore with groups intended to disrupt interchromophore interactions (Figure 32C). Unfortunately, the classes of dyes that exhibit narrow features in dilute solution, especially at longer wavelengths, such as cyanines, tend to be highly polarizable, which makes disruption of interchromophore interactions particularly challenging. For example, the left panel of Figure 32D shows absorption spectra for films of a cyanine dye diluted in amorphous polycarbonate (APC) *and* functionalized by increasingly bulky Fréchet dendrons (structures shown in Figure 32C); although the largest dendron does lead to the narrowest solid-state absorption, this feature is still considerably broader than that seen in solution.[617] The specific point of dendron attachment and the flexible bridge between the dye and the dendron evidently does not effectively protect the π systems of the dyes from approaching those of their neighbors. On the other hand, similar dendrons attached to axial ligands in metal phthalocyanines and naphthalocyanines have led to successful preservation of narrow line widths, presumably because in these cases the dendron effectively blocks the π faces of the chromophores (Figure 32E).[618] Returning to cyanines, an approach that has been more successful is to use substituents (both organic[619,620] and, as shown in Figure 32C and the right panel of Figure 32D, organometallic moieties[621,622]) that are rigidly out-of-plane immediately adjacent to the π system. This approach has also been somewhat successful with other cyanines and other classes of dyes including merocyanines and perylene diimides.[622]

In summary, this section has emphasized that the organic molecules with the narrowest molecular emissions are those with minimal geometry changes between the ground and the excited states, which lead to the following design guidelines.

(1) Cyanines and related dyes (Figure 31) that have frontier orbitals with nodes lying on (or nearly on), rather than between, atoms exhibit spectra that are narrow due to being dominated by 0,0 transitions, whereas in polyene dyes with nodes lying between atoms, strong coupling to high-frequency C−C modes leads to much broader emission.
(2) The 0,0 transitions of dyes are generally narrower when low-frequency out-of-plane modes are suppressed by incorporation into rings so that, for example, phthalocyanines often exhibit narrower emissions than cyanines.
(3) Strong solvent−dye interactions result in a distribution of dye−solvent complexes, each absorbing at different energies, so that highly dipolar dyes tend to have the broadest spectra and thus should be avoided.

Finally, J-aggregate formation can lead to further narrowing of emission, but other forms of aggregation, including H-aggregate formation, which lead to broader spectra and largely quenches fluorescence, should be avoided or suppressed through site-isolation strategies.

5. CONNECTIONS, CONCLUSIONS, AND CHARTING A PATH FORWARD

By virtue of their scalability, processability, and versatility, solution-processed semiconductors have transformed the landscape of emissive technologies and are poised to play a prominent role in their further development. As discussed in section 2, colloidal QDs, for example, already make up the "Q" in QLED and the "QD" in QD-OLED displays but are currently being developed by companies, including Nanosys, for electroluminescent QD screens. Looking further to the future, solution-processed semiconductors will be a leading contender as scalable components for quantum information science. However, as highlighted in sections 2 and 3, challenges from a fundamental research standpoint remain. Focusing first on opportunities opened by gaps in our fundamental understanding of solution-processed semiconductors, new strategies to control the structure and surface of individual nanocrystals, including vibrational coupling with the surface and the environment, are needed to control dynamic or homogeneous broadening. We must better understand how to design and harness growth mechanisms that support narrow polydispersity as well as leverage techniques that enable size selection postsynthetically including digestive ripening, size-selective purification, and crystallization. Finally, we must develop new approaches to minimize broadening from environmental factors by carefully controlling interfacial structure and bonding as well as control the environments themselves, including cavity integration, as part of a systems-level approach to controlling colloidal semiconductor PL.

In section 4, we discussed the factors influencing PL line widths in a variety of solution-processed semiconductor materials. Dynamic or homogeneous broadening in binary semiconductor nanocrystals leads to PL emissions with fwhm values often on the order of 20−40 meV, somewhat narrower than the narrowest emissions observed for nonaggregated organic dyes in solution. However, static inhomogeneous broadening associated with nanocrystal size dispersity is often a limitation, and synthetic strategies to prepare more monodisperse samples and purify ensembles with size selection are still needed. With their more recent emergence from a research and development standpoint, metal−halide perovskites have had a disruptive impact on the field of colloidal semiconductors. 3D metal−halide perovskites have PL line widths that are comparably narrow relative to binary semiconductors, both in the bulk and in the nanocrystal form. 2D metal−halide perovskites tend to exhibit somewhat broader emission than their 3D counterparts, some examples giving very broad emissions attributable to the formation of self-trapped excitons. Excitingly, there is a lot of room to tune emission

AQ

energies and line widths through design of the organic spacer molecules. Doping of colloidal semiconductors with isolated d- or f-block ions can result in a wide range of different transition types and thus a wide range of PL line widths. Exceptionally narrow emission (down to ca. 0.5 meV) can be obtained when the lowest such states are f−f transitions associated with lanthanide ions, which are relatively insensitive to their chemical environment, but often suffer from weak intensities due to being Laporte forbidden. In the special case of molecular semiconductors, organic molecules with the narrowest molecular emissions are those with minimal geometry changes between the ground and the excited states. Further narrowing of emission spectra can be obtained in these molecular systems through the formation of supramolecular J aggregates.

We hope that this review will serve as a tutorial for newcomers to the area of solution-phase semiconductors as well as a go-to resource for researchers and technology practitioners alike.

AUTHOR INFORMATION

Corresponding Author

Brandi M. Cossairt − *Department of Chemistry, University of Washington, Seattle, Washington 98195-1700, United States;* orcid.org/0000-0002-9891-3259; Email: cossairt@uw.edu

Authors

Hao A. Nguyen − *Department of Chemistry, University of Washington, Seattle, Washington 98195-1700, United States;* orcid.org/0000-0001-6742-1748

Grant Dixon − *Department of Chemistry, University of Washington, Seattle, Washington 98195-1700, United States*

Florence Y. Dou − *Department of Chemistry, University of Washington, Seattle, Washington 98195-1700, United States*

Shaun Gallagher − *Department of Chemistry, University of Washington, Seattle, Washington 98195-1700, United States*

Stephen Gibbs − *Department of Chemistry, University of Washington, Seattle, Washington 98195-1700, United States*

Dylan M. Ladd − *Department of Materials Science and Engineering, University of Colorado Boulder, Boulder, Colorado 80303, United States;* orcid.org/0000-0002-9242-4382

Emanuele Marino − *Department of Chemistry, University of Pennsylvania, Philadelphia, Pennsylvania 19104, United States; Dipartimento di Fisica e Chimica, Università degli Studi di Palermo, 90123 Palermo, Italy*

Justin C. Ondry − *Department of Chemistry, James Franck Institute, and Pritzker School of Molecular Engineering, University of Chicago, Chicago, Illinois 60637, United States;* orcid.org/0000-0001-9113-3420

James P. Shanahan − *Department of Chemistry, Columbia University, New York, New York 10027, United States*

Eugenia S. Vasileiadou − *Department of Chemistry, Northwestern University, Evanston, Illinois 60208, United States;* orcid.org/0000-0002-5714-9207

Stephen Barlow − *Renewable and Sustainable Energy Institute, University of Colorado Boulder, Boulder, Colorado 80303, United States;* orcid.org/0000-0001-9059-9974

Daniel R. Gamelin − *Department of Chemistry, University of Washington, Seattle, Washington 98195-1700, United States;* orcid.org/0000-0003-2888-9916

David S. Ginger − *Department of Chemistry, University of Washington, Seattle, Washington 98195-1700, United States;* orcid.org/0000-0002-9759-5447

David M. Jonas − *Department of Chemistry, University of Colorado Boulder, Boulder, Colorado 80309, United States; Renewable and Sustainable Energy Institute, University of Colorado Boulder, Boulder, Colorado 80303, United States;* orcid.org/0000-0002-1085-8161

Mercouri G. Kanatzidis − *Department of Chemistry, Northwestern University, Evanston, Illinois 60208, United States;* orcid.org/0000-0003-2037-4168

Seth R. Marder − *Department of Chemistry, University of Colorado Boulder, Boulder, Colorado 80309, United States; Renewable and Sustainable Energy Institute, University of Colorado Boulder, Boulder, Colorado 80303, United States; Department of Chemical and Biological Engineering, University of Colorado Boulder, Boulder, Colorado 80303, United States;* orcid.org/0000-0001-6921-2536

Daniel Morton − *Renewable and Sustainable Energy Institute, University of Colorado Boulder, Boulder, Colorado 80303, United States*

Christopher B. Murray − *Department of Chemistry, University of Pennsylvania, Philadelphia, Pennsylvania 19104, United States*

Jonathan S. Owen − *Department of Chemistry, Columbia University, New York, New York 10027, United States;* orcid.org/0000-0001-5502-3267

Dmitri V. Talapin − *Department of Chemistry, James Franck Institute, and Pritzker School of Molecular Engineering, University of Chicago, Chicago, Illinois 60637, United States;* orcid.org/0000-0002-6414-8587

Michael F. Toney − *Department of Materials Science and Engineering and Renewable and Sustainable Energy Institute, University of Colorado Boulder, Boulder, Colorado 80303, United States; Department of Chemical and Biological Engineering, University of Colorado Boulder, Boulder, Colorado 80303, United States;* orcid.org/0000-0002-7513-1166

Complete contact information is available at: https://pubs.acs.org/10.1021/acs.chemrev.3c00097

Author Contributions

CRediT: **Hao Anh Nguyen** visualization, writing-original draft, writing-review & editing; **Grant Dixon** writing-original draft, writing-review & editing; **Florence Y. Dou** visualization, writing-original draft, writing-review & editing; **Shaun Gallagher** visualization, writing-original draft, writing-review & editing; **Stephen Gibbs** visualization, writing-original draft, writing-review & editing; **Dylan M. Ladd** visualization, writing-original draft, writing-review & editing; **Emanuele Marino** visualization, writing-original draft, writing-review & editing; **Justin C. Ondry** visualization, writing-original draft, writing-review & editing; **James P. Shanahan** visualization, writing-original draft, writing-review & editing; **Eugenia S. Vasileiadou** visualization, writing-original draft, writing-review & editing; **Stephen Barlow** conceptualization, data curation, visualization, writing-original draft, writing-review & editing; **Daniel R. Gamelin** project administration, supervision, writing-original draft; **David S Ginger** conceptualization, funding acquisition, project administration, visualization, writing-original draft, writing-review & editing; **David M. Jonas** visualization, writing-original draft; **Mercouri G. Kanatzidis** project administration, supervision, writing-original draft; **Seth R. Marder** conceptualization, project administration, supervision, writing-original draft, writing-review & editing; **Daniel Morton** visualization,

writing-review & editing; **Christopher B. Murray** supervision, writing-original draft; **Jonathan S. Owen** supervision, visualization, writing-original draft, writing-review & editing; **Dmitri V. Talapin** supervision, writing-original draft, writing-review & editing; **Michael F Toney** project administration, supervision, writing-original draft, writing-review & editing; **Brandi M. Cossairt** conceptualization, funding acquisition, project administration, resources, supervision, visualization, writing-original draft, writing-review & editing.

Notes

The authors declare no competing financial interest.

Biographies

Hao A. Nguyen received his B.S. degree in Chemistry from Texas A&M University in 2020. He is pursuing his Ph.D. degree in Chemistry at the University of Washington under the supervision of Brandi Cossairt. His research interests include developing inorganic shelling techniques for Cd-, In-, and Pb-based quantum dots and other emissive colloidal systems. Additionally, he aims to leverage machine-learning algorithms to aid in the synthesis of nanocrystals. His overarching research goal is to develop a stable, efficient, scalable, and highly emissive platform for quantum photonics applications.

Grant Dixon received his B.S. degree in Chemistry from the University of Richmond in 2020 and is currently a second-year graduate student in the lab of Brandi Cossairt at the University of Washington. He is focused on exploring the relationships between the surface structure, ligand chemistry, and photophysical properties of colloidal InP nanocrystals through synthetic development.

Florence Y. Dou grew up in Trinidad and Tobago. As an international student, she received her B.S. degree in Chemistry from Trinity College (Hartford, CT), where she worked in Timothy Curran's lab. She then worked as a Research Technician at the Dana-Farber Cancer Institute in Boston, MA in Bruce Spiegelman's lab. In 2018, she joined the Department of Chemistry at University of Washington and is currently a Ph.D. candidate in Brandi Cossairt's lab. She studies the synthesis and design of semiconductor nanocrystals as organic photoredox catalysts. She has been the recipient of the Mickey and Karen Schurr Endowed Fellowship, a Clean Energy Institute Graduate Fellowship, and an Education Fellowship from the NSF Center for Integration of Modern Optoelectronic Materials on Demand.

Shaun Gallagher received his B.S. degree in Chemistry and his B.A. degree in Foreign Languages and Literatures from the University of Florida. He is currently pursuing his Ph.D. degree in Chemistry at the University of Washington under the supervision of David Ginger. His research focuses on the development and application of optical microscopies to study how the surface chemistry of perovskite quantum dots impacts photoluminescence blinking and spectral diffusion.

Stephen Gibbs obtained his B.S. degree in Chemical Engineering from the University of Florida. He then earned his Ph.D. degree in Chemical Engineering from the University of Texas at Austin while studying doped nanocrystal plasmonics under Delia Milliron's advising. He is currently a postdoctoral researcher at the University of Washington and is studying the magneto-optics of doped quantum dots in Daniel Gamelin's lab.

Dylan M. Ladd received his B.S. degree in Chemical Engineering from Montana State University in 2019 and worked as a semiconductor process engineer for Micron Technology through 2021. He is now an NSF graduate research fellow and second year Ph.D. student in Materials Science and Engineering at the University of Colorado Boulder advised by Michael F. Toney. His research focuses on local structural characterization of hybrid metal halide perovskites and colloidal nanocrystals to understand and control their emergent properties.

Emanuele Marino is a Junior Assistant Professor at the Department of Physics and Chemistry of the University of Palermo, Italy. He received his Ph.D. degree in Physics from the University of Amsterdam with a thesis on nanocrystal self-assembly. Afterward, he moved to the University of Pennsylvania as a postdoctoral researcher in the group of Chris Murray to explore the formation mechanism of multicomponent and multifunctional nanocrystal superstructures. His research focuses on understanding nanocrystal self-assembly to build functional superstructures characterized by deterministic structure–property relationships.

Justin C. Ondry received his B.S. degree in Chemistry/Materials Science from the University of California, Los Angeles, in 2015 where he performed undergraduate research with Sarah H. Tolbert. He received his Ph.D. degree in Physical Chemistry (Advisor A. Paul Alivisatos) from the University of California, Berkeley, in 2020. He primarily studied dislocations and their dynamics in imperfectly attached colloidal nanocrystals using in situ transmission electron microscopy. Currently, he is a postdoctoral scholar with Dmitri Talapin at the University of Chicago, where he is developing molten salt solvents for synthesis and transformation of colloidal nanocrystals.

James P. Shanahan earned his Ph.D. degree at the University of Michigan, advised by Nathaniel K. Szymczak. He is currently a postdoctoral research scientist at Columbia University working with Jonathan S. Owen, where his research focuses on precursor design strategies to prepare atomically precise metal–chalcogenide clusters.

Eugenia S. Vasileiadou received her B.S. degree in Chemistry (2017) with Dean's Distinction from the Aristotle University of Thessaloniki. She earned her Ph.D. degree (2022) from the Chemistry Department of Northwestern University under the direction of Mercouri Kanatzidis. As a recipient of the Dr. John N. Nicholson fellowship during her Ph.D. studies, she worked on the synthetic design of novel, hybrid metal halide perovskites and studied their structure–property–stability relationships for optoelectronic applications. Her research currently focuses on the rational synthetic design and characterization of functional materials for energy conversion and energy storage applications.

Stephen Barlow has been an associate research professor in the Renewable and Sustainable Energy Institute at the University of Colorado Boulder since 2021. He received his B.A. (1992) and D.Phil. (1996) degrees in Chemistry from the University of Oxford in the United Kingdom. After postdoctoral work at Caltech, he was lecturer in Inorganic Chemistry at Oxford for 3 years and then held Research Scientist positions at the University of Arizona and Georgia Tech. His research interests include the structural, optical, and electronic properties of a wide range of organic, organometallic, and metal–organic materials.

Daniel R. Gamelin holds the Nicole A. Boand Endowed Chair in Chemistry at the University of Washington. He began at the UW as an assistant professor in 2000 following a postdoctoral appointment at the University of Bern, Switzerland, and obtaining his Ph.D. degree at Stanford University. His research at the UW involves the development of new inorganic materials with unique electronic structures that give rise to desirable photophysical, photochemical, magnetic, or magneto-optical properties. Recent interests include luminescent materials for solar spectral conversion, magneto-optical materials for spin photonics, redox and photoredox properties of quantum dots, and 2D quantum materials.

https://doi.org/10.1021/acs.chemrev.3c00097
Chem. Rev. XXXX, XXX, XXX−XXX

David S. Ginger earned dual B.S. degrees in Chemistry and Physics at Indiana University in 1997. He completed his Ph.D. degree in Physics studying CdSe nanocrystals with Neil C. Greenham in the Optoelectronics group at the University of Cambridge (UK) in 2001. After a joint NIH and DuPont Postdoctoral Fellowship at Northwestern University in Chad Mirkin's lab, he joined the faculty at the University of Washington where he is currently the B. Seymour Rabinovitch Endowed Chair in Chemistry, Washington Research Foundation Distinguished Scholar in Clean Energy, and Adjunct Professor of Physics and Materials Science and Engineering and serves as the Chief Scientist of the Washington state-funded UW Clean Energy Institute. He is the founding director of the NSF Science and Technology Center for the Integration of Modern Optoelectronic Materials on Demand (IMOD). His research centers on the physical chemistry of nanostructured materials with applications in optoelectronics, energy, and sensing, and his group makes use of techniques ranging from scanning probe microscopy to optical spectroscopy. He is also an associate editor of the ACS journal *Chemical Reviews*.

David M. Jonas received his B.S. degree in Chemistry and an A.B. degree in Mathematics from UC Berkeley in 1986, completed his Ph.D. degree in Physical Chemistry with Robert W. Field and Robert J. Silbey at MIT in 1992, and carried out postdoctoral work with Graham R. Fleming at the University of Chicago before joining the faculty of the Department of Chemistry and Biochemistry at the University of Colorado in 1995. He and his group demonstrated and developed femtosecond two-dimensional Fourier transform spectroscopy as the optical analog of two-dimensional nuclear magnetic resonance. They currently study the fast electronic motions required for efficient electronic processes in molecules, nanomaterials, and photosynthesis. He has served as Chair of the International Conference on Ultrafast Phenomena (Optical Society of America) and as Chemistry Department Chair at the University of Colorado (2018−2021). He has won the Ahmed Zewail Award in Ultrafast Science and Technology from the American Chemical Society (2013), the Bomem-Michelson Award from the Coblentz Society (2015), the Earle K. Plyler Prize in Molecular Spectroscopy and Dynamics from the American Physical Society (2018), and the E. Bright Wilson Award in Spectroscopy from the American Chemical Society (2023).

Mercouri G. Kanatzidis received his Chemistry diploma from the Aristotle University, Greece, and his Ph.D. degree in Chemistry from the University of Iowa in 1984. He was a postdoctoral research fellow at the University of Michigan and Northwestern University from 1985 to 1987. At Northwestern University, he is the Charles E. and Emma H. Morrison Professor and carries a joint appointment as a Senior Scientist at Argonne National Laboratory. He is active in the field of solar energy materials, thermoelectric materials, halide perovskites, and synthesis science.

Seth R. Marder is the Director of the Renewable and Sustainable Energy Institute, which is joint between the University of Colorado Boulder (CU Boulder) and the NREL. At CU, he is also a professor of Chemical and Biological Engineering Chemistry and a Fellow of the Materials Science and Engineering Program. He is also a Senior Research Fellow at NREL. He is a Fellow of the American Association for the Advancement of Science, the Optical Society of America, SPIE, the Royal Society of Chemistry, the American Physical Society, the Materials Research Society, and the National Academy of Inventors and a Member of the World Cultural Council.

Daniel Morton earned his Ph.D. degree in Synthetic Organic Chemistry from the University of East Anglia (UK) in 2004. After postdoctoral fellowships at the University of Leeds (UK) and then at Emory University, he joined Reddy's Laboratories in Cambridge (UK). In 2013, he returned to Emory University as the Managing Director of the NSF Center for Selective C−H Functionalization. In 2019, he moved to the Georgia Institute of Technology as the Technical Program Manager for the Generation Two Reinvented Toilet Program. In 2021, he moved to the University of Colorado Boulder, joining the Renewable and Sustainable Energy Institute (RASEI) with part of his role acting as the Director of Communications for the NSF Center for Integrated Modern Optoelectronic Materials on Demand (IMOD).

Christopher B. Murray holds the Richard Perry University Professorship in Chemistry and Materials Science at the University of Pennsylvania, where his research focuses on the preparation, characterization, and integration of nanomaterials. Before joining the University of Pennsylvania, he was a Staff Scientist and Manager in IBM's Research Division from 1995 to 2006, where he led the "Nanoscale Materials & Devices" Department at the T. J. Watson Research Center. He received his B.Sc. degree with Honors in Chemistry from St. Mary's University in Halifax Nova Scotia, Canada (1988) and spent 1 year as a Rotary International Fellow at the University of Auckland, New Zealand, studying Chemistry and Materials Science before pursuing his Ph.D. degree in Chemistry at the Massachusetts Institute of Technology under the supervision of Moungi G. Bawendi.

Jonathan S. Owen received his B.S. degree in Chemistry from the University of Wisconsin, Madison in 2000 and his Ph.D. degree in Chemistry from the California Institute of Technology in 2005. After postdoctoral research at the University of California Berkeley, he began his independent career at Columbia University in 2009, where he is currently Associate Professor of Chemistry. His research group studies the coordination chemistry of colloidal semiconductor crystals using liquids nuclear magnetic resonance spectroscopy and the mechanisms of nanocrystal nucleation and growth using X-ray scattering methods.

Dmitri V. Talapin is Ernest DeWitt Burton Distinguished Service Professor in the Department of Chemistry, James Franck Institute, and Pritzker School of Molecular Engineering at the University of Chicago. His group's research interests focus on inorganic and hybrid organic−inorganic nanomaterials, from synthetic methodology to self-assembly to electronic and optoelectronic devices. His recognitions include an ACS Inorganic Nanoscience Award, a MRS Outstanding Young Investigator Award, the David and Lucile Packard Fellowship in Science and Engineering, and others. He was elected a Fellow of the Royal Society of Chemistry in 2014.

Michael F. Toney received his B.S. degree from Caltech and his Ph.D. degree in Physics from the University of Washington. After a NATO Postdoctoral Fellowship, he joined the IBM Research Division to focus on the use of X-ray scattering methods for structure determination for polymer thin films and interfaces. After working at the Stanford Synchrotron Radiation Lightsource, he joined CU Boulder in 2020. Toney is a pioneer in the use of X-ray diffraction for in situ investigations of thin films and of atomic structure at electrified interfaces and for studies of the molecular structure of polymers. He is a Fellow of the American Physical Society.

Brandi M. Cossairt received her B.S. degree in Chemistry from the California Institute of Technology in 2006 and her Ph.D. degree from the Massachusetts Institute of Technology in 2010. She then trained as an NIH NRSA Postdoctoral Fellow at Columbia University before joining the Department of Chemistry at the University of Washington in 2012, where she is now the Lloyd. E. and Florence M. West Endowed Professor. Her research group examines the nucleation, growth, surface chemistry, and reactivity of nanoscale materials to enable next-generation technologies in the diverse areas of displays, lighting, catalysis, quantum information, and hybrid matter. Outside of the lab, she is an Associate Editor at the ACS journal *Inorganic Chemistry* and is

https://doi.org/10.1021/acs.chemrev.3c00097
Chem. Rev. XXXX, XXX, XXX−XXX

the cofounder of the Chemistry Women Mentorship Network (ChemWMN).

ACKNOWLEDGMENTS

This material is based upon work supported by the National Science Foundation via the Center for Integration of Modern Optoelectronic Materials on Demand Science and Technology Center under Grant No. DMR-2019444.

REFERENCES

(1) Shirasaki, Y.; Supran, G. J.; Bawendi, M. G.; Bulović, V. Emergence of Colloidal Quantum-Dot Light-Emitting Technologies. *Nat. Photonics* **2013**, *7*, 13−23.
(2) Veldhuis, S. A.; Boix, P. P.; Yantara, N.; Li, M.; Sum, T. C.; Mathews, N.; Mhaisalkar, S. G. Perovskite Materials for Light-Emitting Diodes and Lasers. *Adv. Mater.* **2016**, *28*, 6804−6834.
(3) Kirmani, A. R.; Luther, J. M.; Abolhasani, M.; Amassian, A. Colloidal Quantum Dot Photovoltaics: Current Progress and Path to Gigawatt Scale Enabled by Smart Manufacturing. *ACS Energy Lett.* **2020**, *5*, 3069−3100.
(4) Carey, G. H.; Abdelhady, A. L.; Ning, Z.; Thon, S. M.; Bakr, O. M.; Sargent, E. H. Colloidal Quantum Dot Solar Cells. *Chem. Rev.* **2015**, *115*, 12732−12763.
(5) García de Arquer, F. P.; Armin, A.; Meredith, P.; Sargent, E. H. Solution-Processed Semiconductors for next-Generation Photodetectors. *Nat. Rev. Mater.* **2017**, *2*, 16100.
(6) Lhuillier, E.; Guyot-Sionnest, P. Recent Progresses in Mid Infrared Nanocrystal Optoelectronics. *IEEE J. Sel. Top. Quantum Electron.* **2017**, *23*, 1−8.
(7) Guyot-Sionnest, P.; Ackerman, M. M.; Tang, X. Colloidal Quantum Dots for Infrared Detection beyond Silicon. *J. Chem. Phys.* **2019**, *151*, 060901.
(8) Kahmann, S.; Shulga, A.; Loi, M. A. Quantum Dot Light-Emitting Transistors—Powerful Research Tools and Their Future Applications. *Adv. Funct. Mater.* **2020**, *30*, 1904174.
(9) Kargozar, S.; Hoseini, S. J.; Milan, P. B.; Hooshmand, S.; Kim, H.-W.; Mozafari, M. Quantum Dots: A Review from Concept to Clinic. *Biotechnol. J.* **2020**, *15*, 2000117.
(10) Gil, H. M.; Price, T. W.; Chelani, K.; Bouillard, J.-S. G.; Calaminus, S. D. J.; Stasiuk, G. J. NIR-Quantum Dots in Biomedical Imaging and Their Future. *iScience* **2021**, *24*, 102189.
(11) Hong, Q.; Lee, K.-C.; Luo, Z.; Wu, S.-T. High-Efficiency Quantum Dot Remote Phosphor Film. *Appl. Opt.* **2015**, *54*, 4617−4622.
(12) Luo, Z.; Xu, D.; Wu, S.-T. Emerging Quantum-Dots-Enhanced LCDs. *J. Dispersion Technol.* **2014**, *10*, 526−539.
(13) Zhu, R.; Luo, Z.; Chen, H.; Dong, Y.; Wu, S.-T. Realizing Rec. 2020 Color Gamut with Quantum Dot Displays. *Opt. Express* **2015**, *23*, 23680−23693.
(14) García de Arquer, F. P.; Talapin, D. V.; Klimov, V. I.; Arakawa, Y.; Bayer, M.; Sargent, E. H. Semiconductor Quantum Dots: Technological Progress and Future Challenges. *Science* **2021**, *373*, No. eaaz8541.
(15) Lu, M.; Zhang, Y.; Wang, S.; Guo, J.; Yu, W. W.; Rogach, A. L. Metal Halide Perovskite Light-Emitting Devices: Promising Technology for Next-Generation Displays. *Adv. Funct. Mater.* **2019**, *29*, 1902008.
(16) Kagan, C. R.; Lifshitz, E.; Sargent, E. H.; Talapin, D. V. Building Devices from Colloidal Quantum Dots. *Science* **2016**, *353*, aac5523.
(17) Chen, Y.; Sharp, D.; Saxena, A.; Nguyen, H.; Cossairt, B. M.; Majumdar, A. Integrated Quantum Nanophotonics with Solution-Processed Materials. *Adv. Quantum Technol.* **2022**, *5*, 2100078.
(18) Kagan, C. R.; Bassett, L. C.; Murray, C. B.; Thompson, S. M. Colloidal Quantum Dots as Platforms for Quantum Information Science. *Chem. Rev.* **2021**, *121*, 3186−3233.
(19) Kim, J. Y.; Voznyy, O.; Zhitomirsky, D.; Sargent, E. H. 25th Anniversary Article: Colloidal Quantum Dot Materials and Devices: A Quarter-Century of Advances. *Adv. Mater.* **2013**, *25*, 4986−5010.
(20) Bae, W. K.; Brovelli, S.; Klimov, V. I. Spectroscopic Insights into the Performance of Quantum Dot Light-Emitting Diodes. *MRS Bull.* **2013**, *38*, 721−730.
(21) Bang, S. Y.; Suh, Y.-H.; Fan, X.-B.; Shin, D.-W.; Lee, S.; Choi, H. W.; Lee, T. H.; Yang, J.; Zhan, S.; Harden-Chaters, W.; et al. Technology Progress on Quantum Dot Light-Emitting Diodes for next-Generation Displays. *Nanoscale Horiz.* **2021**, *6*, 68−77.
(22) Osypiw, A. R. C.; Lee, S.; Jung, S.-M.; Leoni, S.; Smowton, P. M.; Hou, B.; Kim, J. M.; Amaratunga, G. A. J. Solution-Processed Colloidal Quantum Dots for Light Emission. *Mater. Adv.* **2022**, *3*, 6773.
(23) Zhongsheng, L.; Yurek, J. Quantum Dots: The Technology Platform for All Future Displays. *Light-Emitting Devices, Materials, and Applications*; SPIE, 2019; Vol. *10940*, p 1094010. DOI: 10.1117/12.2508088.
(24) Liu, Z.; Lin, C.-H.; Hyun, B.-R.; Sher, C.-W.; Lv, Z.; Luo, B.; Jiang, F.; Wu, T.; Ho, C.-H.; Kuo, H.-C.; et al. Micro-Light-Emitting Diodes with Quantum Dots in Display Technology. *Light Sci. Appl.* **2020**, *9*, 83.
(25) Gao, M.; Yang, H.; Shen, H.; Zeng, Z.; Fan, F.; Tang, B.; Min, J.; Zhang, Y.; Hua, Q.; Li, L. S.; et al. Bulk-like ZnSe Quantum Dots Enabling Efficient Ultranarrow Blue Light-Emitting Diodes. *Nano Lett.* **2021**, *21*, 7252−7260.
(26) *Parameter Values for Ultra-High Definition Television Systems for Production and International Programme Exchange*; BT Series Broadcasting Service (television); International Broadcasting Service (Television), 2015; https://www.itu.int/dms_pubrec/itu-r/rec/bt/R-REC-BT.2020-2-201510-I!!PDF-E.pdf.
(27) Erdem, T.; Demir, H. V. Colloidal Nanocrystals for Quality Lighting and Displays: Milestones and Recent Developments. *Nanophotonics* **2016**, *5*, 74−95.
(28) Chen, H.-W.; Zhu, R.-D.; He, J.; Duan, W.; Hu, W.; Lu, Y.-Q.; Li, M.-C.; Lee, S.-L.; Dong, Y.-J.; Wu, S.-T. Going beyond the Limit of an LCD's Color Gamut. *Light Sci. Appl.* **2017**, *6*, No. e17043.
(29) Triana, M. A.; Hsiang, E.-L.; Zhang, C.; Dong, Y.; Wu, S.-T. Luminescent Nanomaterials for Energy-Efficient Display and Healthcare. *ACS Energy Lett.* **2022**, *7*, 1001−1020.
(30) Yang, J.; Choi, M. K.; Yang, U. J.; Kim, S. Y.; Kim, Y. S.; Kim, J. H.; Kim, D.-H.; Hyeon, T. Toward Full-Color Electroluminescent Quantum Dot Displays. *Nano Lett.* **2021**, *21*, 26−33.
(31) Steckel, J. S.; Ho, J.; Hamilton, C.; Xi, J.; Breen, C.; Liu, W.; Allen, P.; Coe-Sullivan, S. Quantum Dots: The Ultimate down-Conversion Material for LCD Displays. *J. Soc. Inf. Dispersion* **2015**, *23*, 294−305.
(32) Chen, H.-W.; Lee, J.-H.; Lin, B.-Y.; Chen, S.; Wu, S.-T. Liquid Crystal Display and Organic Light-Emitting Diode Display: Present Status and Future Perspectives. *Light Sci. Appl.* **2018**, *7*, 17168−17168.
(33) Hosokai, T.; Matsuzaki, H.; Nakanotani, H.; Tokumaru, K.; Tsutsui, T.; Furube, A.; Nasu, K.; Nomura, H.; Yahiro, M.; Adachi, C. Evidence and Mechanism of Efficient Thermally Activated Delayed Fluorescence Promoted by Delocalized Excited States. *Sci. Adv.* **2017**, *3*, e1603282.
(34) Nakanotani, H.; Higuchi, T.; Furukawa, T.; Masui, K.; Morimoto, K.; Numata, M.; Tanaka, H.; Sagara, Y.; Yasuda, T.; Adachi, C. High-Efficiency Organic Light-Emitting Diodes with Fluorescent Emitters. *Nat. Commun.* **2014**, *5*, 4016.
(35) Huang, Y.-M.; James Singh, K.; Hsieh, T.-H.; Langpoklakpam, C.; Lee, T.-Y.; Lin, C.-C.; Li, Y.; Chen, F.-C.; Chen, S.-C.; Kuo, H.-C.; et al. Gateway towards Recent Developments in Quantum Dot-Based Light-Emitting Diodes. *Nanoscale* **2022**, *14*, 4042−4064.
(36) Pu, C.; Dai, X.; Shu, Y.; Zhu, M.; Deng, Y.; Jin, Y.; Peng, X. Electrochemically-Stable Ligands Bridge the Photoluminescence-Electroluminescence Gap of Quantum Dots. *Nat. Commun.* **2020**, *11*, 937.
(37) Klem, E.; Lewis, J.; Cunningham, G.; Temple, D.; D'Souxa, A.; Robinson, E.; Wijewarnasuriya, P. S.; Dhar, N. High-Performance SWIR Sensing from Colloidal Quantum Dot Photodiode Arrays. *Proc. SPIE* **2013**, *8868*, 06.
(38) Klem, E.; Gregory, C.; Temple, D.; Lewis, J. PbS Colloidal Quantum Dot Photodiodes for Low-Cost SWIR Sensing. *Proc. SPIE* **2015**, *9451*, 945104.

(39) Tang, X.; Ackerman, M. M.; Chen, M.; Guyot-Sionnest, P. Dual-Band Infrared Imaging Using Stacked Colloidal Quantum Dot Photodiodes. *Nat. Photonics* **2019**, *13*, 277−282.
(40) Kim, J.; Kwon, S.-M.; Kang, Y. K.; Kim, Y.-H.; Lee, M.-J.; Han, K.; Facchetti, A.; Kim, M.-G.; Park, S. K. A Skin-like Two-Dimensionally Pixelized Full-Color Quantum Dot Photodetector. *Sci. Adv.* **2019**, *5*, eaax8801.
(41) Chen, M.; Shen, G.; Guyot-Sionnest, P. Size Distribution Effects on Mobility and Intraband Gap of HgSe Quantum Dots. *J. Phys. Chem. C* **2020**, *124*, 16216−16221.
(42) Bai, Z.; Zhao, Z.; Tian, M.; Jin, D.; Pang, Y.; Li, S.; Yan, X.; Wang, Y.; Lu, Z. A Comprehensive Review on the Development and Applications of Narrow-Linewidth Lasers. *Microwave Opt. Technol. Lett.* **2022**, *64*, 2244.
(43) McCall, S. L.; Levi, A. F. J.; Slusher, R. E.; Pearton, S. J.; Logan, R. A. Whispering-gallery Mode Microdisk Lasers. *Appl. Phys. Lett.* **1992**, *60*, 289−291.
(44) Painter, O.; Lee, R. K.; Scherer, A.; Yariv, A.; O'Brien, J. D.; Dapkus, P. D.; Kim, I. Two-Dimensional Photonic Band-Gap Defect Mode Laser. *Science* **1999**, *284*, 1819−1821.
(45) Huang, M. H.; Mao, S.; Feick, H.; Yan, H.; Wu, Y.; Kind, H.; Weber, E.; Russo, R.; Yang, P. Room-Temperature Ultraviolet Nanowire Nanolasers. *Science* **2001**, *292*, 1897−1899.
(46) Fan, F.; Voznyy, O.; Sabatini, R. P.; Bicanic, K. T.; Adachi, M. M.; McBride, J. R.; Reid, K. R.; Park, Y.-S.; Li, X.; Jain, A.; et al. Continuous-Wave Lasing in Colloidal Quantum Dot Solids Enabled by Facet-Selective Epitaxy. *Nature* **2017**, *544*, 75−79.
(47) Park, Y.-S.; Roh, J.; Diroll, B. T.; Schaller, R. D.; Klimov, V. I. Colloidal Quantum Dot Lasers. *Nat. Rev. Mater.* **2021**, *6*, 382−401.
(48) Klimov, V. I.; Ivanov, S. A.; Nanda, J.; Achermann, M.; Bezel, I.; McGuire, J. A.; Piryatinski, A. Single-Exciton Optical Gain in Semiconductor Nanocrystals. *Nature* **2007**, *447*, 441−446.
(49) Jung, H.; Ahn, N.; Klimov, V. I. Prospects and Challenges of Colloidal Quantum Dot Laser Diodes. *Nat. Photonics* **2021**, *15*, 643−655.
(50) Dang, C.; Lee, J.; Breen, C.; Steckel, J. S.; Coe-Sullivan, S.; Nurmikko, A. Red, Green and Blue Lasing Enabled by Single-Exciton Gain in Colloidal Quantum Dot Films. *Nat. Nanotechnol.* **2012**, *7*, 335−339.
(51) Kozlov, O. V.; Park, Y.-S.; Roh, J.; Fedin, I.; Nakotte, T.; Klimov, V. I. Sub−Single-Exciton Lasing Using Charged Quantum Dots Coupled to a Distributed Feedback Cavity. *Science* **2019**, *365*, 672−675.
(52) Ryu, J.; Park, S. D.; Baranov, D.; Rreza, I.; Owen, J. S.; Jonas, D. M. Relations between Absorption, Emission, and Excited State Chemical Potentials from Nanocrystal 2D Spectra. *Sci. Adv.* **2021**, *7*, eabf4741.
(53) Park, Y.-S.; Bae, W. K.; Baker, T.; Lim, J.; Klimov, V. I. Effect of Auger Recombination on Lasing in Heterostructured Quantum Dots with Engineered Core/Shell Interfaces. *Nano Lett.* **2015**, *15*, 7319−7328.
(54) Lim, J.; Park, Y.-S.; Klimov, V. I. Optical Gain in Colloidal Quantum Dots Achieved with Direct-Current Electrical Pumping. *Nat. Mater.* **2018**, *17*, 42−49.
(55) Wu, M.; Ha, S. T.; Shendre, S.; Durmusoglu, E. G.; Koh, W.-K.; Abujetas, D. R.; Sánchez-Gil, J. A.; Paniagua-Domínguez, R.; Demir, H. V.; Kuznetsov, A. I. Room-Temperature Lasing in Colloidal Nanoplatelets via Mie-Resonant Bound States in the Continuum. *Nano Lett.* **2020**, *20*, 6005−6011.
(56) Tessier, M. D.; Javaux, C.; Maksimovic, I.; Loriette, V.; Dubertret, B. Spectroscopy of Single CdSe Nanoplatelets. *ACS Nano* **2012**, *6*, 6751−6758.
(57) She, C.; Fedin, I.; Dolzhnikov, D. S.; Dahlberg, P. D.; Engel, G. S.; Schaller, R. D.; Talapin, D. V. Red, Yellow, Green, and Blue Amplified Spontaneous Emission and Lasing Using Colloidal CdSe Nanoplatelets. *ACS Nano* **2015**, *9*, 9475−9485.
(58) Majumdar, A.; Faraon, A.; Kim, E. D.; Englund, D.; Kim, H.; Petroff, P.; Vučković, J. Linewidth Broadening of a Quantum Dot Coupled to an Off-Resonant Cavity. *Phys. Rev. B* **2010**, *82*, 045306.
(59) Slussarenko, S.; Pryde, G. J. Photonic Quantum Information Processing: A Concise Review. *Appl. Phys. Rev.* **2019**, *6*, 041303.
(60) Aharonovich, I.; Englund, D.; Toth, M. Solid-State Single-Photon Emitters. *Nat. Photonics* **2016**, *10*, 631−641.
(61) Lin, X.; Dai, X.; Pu, C.; Deng, Y.; Niu, Y.; Tong, L.; Fang, W.; Jin, Y.; Peng, X. Electrically-Driven Single-Photon Sources Based on Colloidal Quantum Dots with near-Optimal Antibunching at Room Temperature. *Nat. Commun.* **2017**, *8*, 1132.
(62) Utzat, H.; Sun, W.; Kaplan, A. E. K.; Krieg, F.; Ginterseder, M.; Spokoyny, B.; Klein, N. D.; Shulenberger, K. E.; Perkinson, C. F.; Kovalenko, M. V.; et al. Coherent Single-Photon Emission from Colloidal Lead Halide Perovskite Quantum Dots. *Science* **2019**, *363*, 1068−1072.
(63) Zhu, C.; Marczak, M.; Feld, L.; Boehme, S. C.; Bernasconi, C.; Moskalenko, A.; Cherniukh, I.; Dirin, D.; Bodnarchuk, M. I.; Kovalenko, M. V.; et al. Room-Temperature, Highly Pure Single-Photon Sources from All-Inorganic Lead Halide Perovskite Quantum Dots. *Nano Lett.* **2022**, *22*, 3751−3760.
(64) Nguyen, H. A.; Sharp, D.; Fröch, J. E.; Cai, Y.-Y.; Wu, S.; Monahan, M.; Munley, C.; Manna, A.; Majumdar, A.; Kagan, C. R.; et al. Deterministic Quantum Light Arrays from Giant Silica-Shelled Quantum Dots. *ACS Appl. Mater. Interfaces* **2023**, *15*, 4294−4302.
(65) Xie, W.; Gomes, R.; Aubert, T.; Bisschop, S.; Zhu, Y.; Hens, Z.; Brainis, E.; Van Thourhout, D. Nanoscale and Single-Dot Patterning of Colloidal Quantum Dots. *Nano Lett.* **2015**, *15*, 7481−7487.
(66) Gupta, S.; Waks, E. Spontaneous Emission Enhancement and Saturable Absorption of Colloidal Quantum Dots Coupled to Photonic Crystal Cavity. *Opt. Express* **2013**, *21*, 29612−29619.
(67) van Sark, W. G. J. H. M.; Frederix, P. L. T. M.; Bol, A. A.; Gerritsen, H. C.; Meijerink, A. Blueing, Bleaching, and Blinking of Single CdSe/ZnS Quantum Dots. *ChemPhysChem* **2002**, *3*, 871−879.
(68) Cao, H.; Ma, J.; Huang, L.; Qin, H.; Meng, R.; Li, Y.; Peng, X. Design and Synthesis of Antiblinking and Antibleaching Quantum Dots in Multiple Colors via Wave Function Confinement. *J. Am. Chem. Soc.* **2016**, *138*, 15727−15735.
(69) Chandrasekaran, V.; Tessier, M. D.; Dupont, D.; Geiregat, P.; Hens, Z.; Brainis, E. Nearly Blinking-Free, High-Purity Single-Photon Emission by Colloidal InP/ZnSe Quantum Dots. *Nano Lett.* **2017**, *17*, 6104−6109.
(70) Chen, Y.; Vela, J.; Htoon, H.; Casson, J. L.; Werder, D. J.; Bussian, D. A.; Klimov, V. I.; Hollingsworth, J. A. Giant" Multishell CdSe Nanocrystal Quantum Dots with Suppressed Blinking. *J. Am. Chem. Soc.* **2008**, *130*, 5026−5027.
(71) Pisanello, F.; Leménager, G.; Martiradonna, L.; Carbone, L.; Vezzoli, S.; Desfonds, P.; Cozzoli, P. D.; Hermier, J.-P.; Giacobino, E.; Cingolani, R.; et al. Non-Blinking Single-Photon Generation with Anisotropic Colloidal Nanocrystals: Towards Room-Temperature, Efficient, Colloidal Quantum Sources. *Adv. Mater.* **2013**, *25*, 1974−1980.
(72) Shi, J.; Sun, W.; Utzat, H.; Farahvash, A.; Gao, F. Y.; Zhang, Z.; Barotov, U.; Willard, A. P.; Nelson, K. A.; Bawendi, M. G. All-Optical Fluorescence Blinking Control in Quantum Dots with Ultrafast Mid-Infrared Pulses. *Nat. Nanotechnol.* **2021**, *16*, 1355−1361.
(73) Becker, M. A.; Scarpelli, L.; Nedelcu, G.; Rainò, G.; Masia, F.; Borri, P.; Stöferle, T.; Kovalenko, M. V.; Langbein, W.; Mahrt, R. F. Long Exciton Dephasing Time and Coherent Phonon Coupling in $CsPbBr_2Cl$ Perovskite Nanocrystals. *Nano Lett.* **2018**, *18*, 7546−7551.
(74) Rossetti, R.; Nakahara, S.; Brus, L. E. Quantum Size Effects in the Redox Potentials, Resonance Raman Spectra, and Electronic Spectra of CdS Crystallites in Aqueous Solution. *J. Chem. Phys.* **1983**, *79*, 1086−1088.
(75) Mittleman, D. M.; Schoenlein, R. W.; Shiang, J. J.; Colvin, V. L.; Alivisatos, A. P.; Shank, C. V. Quantum Size Dependence of Femtosecond Electronic Dephasing and Vibrational Dynamics in CdSe Nanocrystals. *Phys. Rev. B* **1994**, *49*, 14435−14447.
(76) Gómez, D. E.; van Embden, J.; Mulvaney, P. Spectral Diffusion of Single Semiconductor Nanocrystals: The Influence of the Dielectric Environment. *Appl. Phys. Lett.* **2006**, *88*, 154106.

https://doi.org/10.1021/acs.chemrev.3c00097
Chem. Rev. XXXX, XXX, XXX−XXX

(77) Hu, Z.; Kim, Y.; Krishnamurthy, S.; Avdeev, I. D.; Nestoklon, M. O.; Singh, A.; Malko, A. V.; Goupalov, S. V.; Hollingsworth, J. A.; Htoon, H. Intrinsic Exciton Photophysics of PbS Quantum Dots Revealed by Low-Temperature Single Nanocrystal Spectroscopy. *Nano Lett.* **2019**, *19*, 8519−8525.
(78) Park, S. D.; Baranov, D.; Ryu, J.; Cho, B.; Halder, A.; Seifert, S.; Vajda, S.; Jonas, D. M. Bandgap Inhomogeneity of a PbSe Quantum Dot Ensemble from Two-Dimensional Spectroscopy and Comparison to Size Inhomogeneity from Electron Microscopy. *Nano Lett.* **2017**, *17*, 762−771.
(79) Cui, J.; Beyler, A. P.; Marshall, L. F.; Chen, O.; Harris, D. K.; Wanger, D. D.; Brokmann, X.; Bawendi, M. G. Direct Probe of Spectral Inhomogeneity Reveals Synthetic Tunability of Single-Nanocrystal Spectral Linewidths. *Nat. Chem.* **2013**, *5*, 602−606.
(80) Cui, J.; Beyler, A. P.; Coropceanu, I.; Cleary, L.; Avila, T. R.; Chen, Y.; Cordero, J. M.; Heathcote, S. L.; Harris, D. K.; Chen, O.; et al. Evolution of the Single-Nanocrystal Photoluminescence Linewidth with Size and Shell: Implications for Exciton−Phonon Coupling and the Optimization of Spectral Linewidths. *Nano Lett.* **2016**, *16*, 289−296.
(81) Caram, J. R.; Bertram, S. N.; Utzat, H.; Hess, W. R.; Carr, J. A.; Bischof, T. S.; Beyler, A. P.; Wilson, M. W. B.; Bawendi, M. G. PbS Nanocrystal Emission Is Governed by Multiple Emissive States. *Nano Lett.* **2016**, *16*, 6070−6077.
(82) Wang, L.-W.; Zunger, A. Electronic Structure Pseudopotential Calculations of Large (∼1000 Atoms) Si Quantum Dots. *J. Phys. Chem.* **1994**, *98*, 2158−2165.
(83) Allan, G.; Delerue, C. Confinement Effects in PbSe Quantum Wells and Nanocrystals. *Phys. Rev. B* **2004**, *70*, 245321.
(84) Kim, D.; Kim, D.-H.; Lee, J.-H.; Grossman, J. C. Impact of Stoichiometry on the Electronic Structure of PbS Quantum Dots. *Phys. Rev. Lett.* **2013**, *110*, 196802.
(85) Poddubny, A. N.; Nestoklon, M. O.; Goupalov, S. V. Anomalous Suppression of Valley Splittings in Lead Salt Nanocrystals without Inversion Center. *Phys. Rev. B* **2012**, *86*, 035324.
(86) Chen, O.; Yang, Y.; Wang, T.; Wu, H.; Niu, C.; Yang, J.; Cao, Y. C. Surface-Functionalization-Dependent Optical Properties of II−VI Semiconductor Nanocrystals. *J. Am. Chem. Soc.* **2011**, *133*, 17504−17512.
(87) McBride, J. R.; Pennycook, T. J.; Pennycook, S. J.; Rosenthal, S. J. The Possibility and Implications of Dynamic Nanoparticle Surfaces. *ACS Nano* **2013**, *7*, 8358−8365.
(88) Pyrz, W. D.; Buttrey, D. J. Particle Size Determination Using TEM: A Discussion of Image Acquisition and Analysis for the Novice Microscopist. *Langmuir* **2008**, *24*, 11350−11360.
(89) Segets, D.; Lucas, J. M.; Klupp Taylor, R. N.; Scheele, M.; Zheng, H.; Alivisatos, A. P.; Peukert, W. Determination of the Quantum Dot Band Gap Dependence on Particle Size from Optical Absorbance and Transmission Electron Microscopy Measurements. *ACS Nano* **2012**, *6*, 9021−9032.
(90) Mondini, S.; Ferretti, A. M.; Puglisi, A.; Ponti, A. Pebbles and PebbleJuggler: Software for Accurate, Unbiased, and Fast Measurement and Analysis of Nanoparticle Morphology from Transmission Electron Microscopy (TEM) Micrographs. *Nanoscale* **2012**, *4*, 5356−5372.
(91) Moreels, I.; Lambert, K.; De Muynck, D.; Vanhaecke, F.; Poelman, D.; Martins, J. C.; Allan, G.; Hens, Z. Composition and Size-Dependent Extinction Coefficient of Colloidal PbSe Quantum Dots. *Chem. Mater.* **2007**, *19*, 6101−6106.
(92) Tovstun, S. A.; Gadomska, A. V.; Spirin, M. G.; Razumov, V. F. Extracting the Homogeneous and Inhomogeneous Linewidths of Colloidal Quantum Dots from the Excitation-Emission Matrix. *J. Lumin.* **2022**, *252*, 119420.
(93) Scher, J. A.; Govind, N.; Chakraborty, A. Evidence of Skewness and Sub-Gaussian Character in Temperature-Dependent Distributions of One Million Electronic Excitation Energies in PbS Quantum Dots. *J. Phys. Chem. Lett.* **2020**, *11*, 986−992.
(94) Zurek, W. H. Environment-Induced Superselection Rules. *Phys. Rev. D* **1982**, *26*, 1862−1880.
(95) Caldeira, A. O.; Leggett, A. J. Influence of Damping on Quantum Interference: An Exactly Soluble Model. *Phys. Rev. A* **1985**, *31*, 1059−1066.
(96) Stern, A.; Aharonov, Y.; Imry, Y. Phase Uncertainty and Loss of Interference: A General Picture. *Phys. Rev. A* **1990**, *41*, 3436−3448.
(97) Prezhdo, O. V.; Rossky, P. J. Relationship between Quantum Decoherence Times and Solvation Dynamics in Condensed Phase Chemical Systems. *Phys. Rev. Lett.* **1998**, *81*, 5294−5297.
(98) Bylsma, J.; Dey, P.; Paul, J.; Hoogland, S.; Sargent, E. H.; Luther, J. M.; Beard, M. C.; Karaiskaj, D. Quantum Beats Due to Excitonic Ground-State Splitting in Colloidal Quantum Dots. *Phys. Rev. B* **2012**, *86*, 125322.
(99) Kilina, S.; Velizhanin, K. A.; Ivanov, S.; Prezhdo, O. V.; Tretiak, S. Surface Ligands Increase Photoexcitation Relaxation Rates in CdSe Quantum Dots. *ACS Nano* **2012**, *6*, 6515−6524.
(100) Liu, J.; Kilina, S. V.; Tretiak, S.; Prezhdo, O. V. Ligands Slow Down Pure-Dephasing in Semiconductor Quantum Dots. *ACS Nano* **2015**, *9*, 9106−9116.
(101) Tiwari, V.; Peters, W. K.; Jonas, D. M. Electronic Energy Transfer through Non-Adiabatic Vibrational-Electronic Resonance. I. Theory for a Dimer. *J. Chem. Phys.* **2017**, *147*, 154308.
(102) Johnson, J. C.; Gerth, K. A.; Song, Q.; Murphy, J. E.; Nozik, A. J.; Scholes, G. D. Ultrafast Exciton Fine Structure Relaxation Dynamics in Lead Chalcogenide Nanocrystals. *Nano Lett.* **2008**, *8*, 1374−1381.
(103) Jonas, D. M. Two-Dimensional Femtosecond Spectroscopy. *Annu. Rev. Phys. Chem.* **2003**, *54*, 425−463.
(104) Voznyy, O.; Levina, L.; Fan, F.; Walters, G.; Fan, J. Z.; Kiani, A.; Ip, A. H.; Thon, S. M.; Proppe, A. H.; Liu, M.; et al. Origins of Stokes Shift in PbS Nanocrystals. *Nano Lett.* **2017**, *17*, 7191−7195.
(105) Kelley, A. M.; Kelley, D. F. Comment on "Dependence of the Fluorescent Lifetime τ on the Concentration at High Dilution". *J. Phys. Chem. Lett.* **2022**, *13*, 11942−11945.
(106) An, J. M.; Franceschetti, A.; Zunger, A. The Excitonic Exchange Splitting and Radiative Lifetime in PbSe Quantum Dots. *Nano Lett.* **2007**, *7*, 2129−2135.
(107) Parker, C. A. *Photoluminescence of Solutions*; Elsevier Publishing Co.: New York, 1968.
(108) Ghosh, T.; Dehnel, J.; Fabian, M.; Lifshitz, E.; Baer, R.; Ruhman, S. Spin Blockades to Relaxation of Hot Multiexcitons in Nanocrystals. *J. Phys. Chem. Lett.* **2019**, *10*, 2341−2348.
(109) Huxter, V. M.; Kim, J.; Lo, S. S.; Lee, A.; Nair, P. S.; Scholes, G. D. Spin Relaxation in Zinc Blende and Wurtzite CdSe Quantum Dots. *Chem. Phys. Lett.* **2010**, *491*, 187−192.
(110) Strickler, S. J.; Berg, R. A. Relationship between Absorption Intensity and Fluorescence Lifetime of Molecules. *J. Chem. Phys.* **1962**, *37*, 814−822.
(111) Kang, I.; Wise, F. W. Electronic Structure and Optical Properties of PbS and PbSe Quantum Dots. *J. Opt. Soc. Am. B* **1997**, *14*, 1632−1646.
(112) Klimov, V. I.; Mikhailovsky, A. A.; Xu, S.; Malko, A.; Hollingsworth, J. A.; Leatherdale, C. A.; Eisler, H.-J.; Bawendi, M. G. Optical Gain and Stimulated Emission in Nanocrystal Quantum Dots. *Science* **2000**, *290*, 314−317.
(113) Gesuele, F.; Sfeir, M. Y.; Koh, W.-K.; Murray, C. B.; Heinz, T. F.; Wong, C. W. Ultrafast Supercontinuum Spectroscopy of Carrier Multiplication and Biexcitonic Effects in Excited States of PbS Quantum Dots. *Nano Lett.* **2012**, *12*, 2658−2664.
(114) Dana, J.; Ghosh, T.; Gdor, I.; Shapiro, A.; Lifshitz, E.; Ruhman, S. Spectator Exciton Effects on Nanocrystal Photophysics II: PbS. *J. Phys. Chem. C* **2022**, *126*, 19304−19310.
(115) Shank, C. V.; Becker, P. Femtosecond Processes in Semiconductors. *Spectroscopy of Nonequilibrium Electrons and Phonons*; Shank, C. V.; Zakharchenya, B. P., Ed. Elsevier Science: Amsterdam, 1992; pp 215−243.
(116) Cho, B.; Peters, W. K.; Hill, R. J.; Courtney, T. L.; Jonas, D. M. Bulklike Hot Carrier Dynamics in Lead Sulfide Quantum Dots. *Nano Lett.* **2010**, *10*, 2498−2505.

https://doi.org/10.1021/acs.chemrev.3c00097
Chem. Rev. XXXX, XXX, XXX−XXX

(117) Masia, F.; Langbein, W.; Moreels, I.; Hens, Z.; Borri, P. Exciton Dephasing in Lead Sulfide Quantum Dots by *X*-Point Phonons. *Phys. Rev. B* **2011**, *83*, 201309.
(118) Kelley, A. M. Exciton-Optical Phonon Coupling in II-VI Semiconductor Nanocrystals. *J. Chem. Phys.* **2019**, *151*, 140901.
(119) Gellen, T. A.; Lem, J.; Turner, D. B. Probing Homogeneous Line Broadening in CdSe Nanocrystals Using Multidimensional Electronic Spectroscopy. *Nano Lett.* **2017**, *17*, 2809−2815.
(120) Cheng, O. H.-C.; Qiao, T.; Sheldon, M.; Son, D. H. Size- and Temperature-Dependent Photoluminescence Spectra of Strongly Confined CsPbBr (3) Quantum Dots. *Nanoscale* **2020**, *12*, 13113−13118.
(121) Jasrasaria, D.; Rabani, E. Interplay of Surface and Interior Modes in Exciton−Phonon Coupling at the Nanoscale. *Nano Lett.* **2021**, *21*, 8741−8748.
(122) Gramlich, M.; Lampe, C.; Drewniok, J.; Urban, A. S. How Exciton−Phonon Coupling Impacts Photoluminescence in Halide Perovskite Nanoplatelets. *J. Phys. Chem. Lett.* **2021**, *12*, 11371−11377.
(123) Yazdani, N.; Bozyigit, D.; Vuttivorakulchai, K.; Luisier, M.; Infante, I.; Wood, V. Tuning Electron−Phonon Interactions in Nanocrystals through Surface Termination. *Nano Lett.* **2018**, *18*, 2233−2242.
(124) Yazdani, N.; Volk, S.; Yarema, O.; Yarema, M.; Wood, V. Size, Ligand, and Defect-Dependent Electron−Phonon Coupling in Chalcogenide and Perovskite Nanocrystals and Its Impact on Luminescence Line Widths. *ACS Photonics* **2020**, *7*, 1088−1095.
(125) Schnitzenbaumer, K. J.; Dukovic, G. Comparison of Phonon Damping Behavior in Quantum Dots Capped with Organic and Inorganic Ligands. *Nano Lett.* **2018**, *18*, 3667−3674.
(126) Rainò, G.; Yazdani, N.; Boehme, S. C.; Kober-Czerny, M.; Zhu, C.; Krieg, F.; Rossell, M. D.; Erni, R.; Wood, V.; Infante, I.; et al. Ultra-Narrow Room-Temperature Emission from Single $CsPbBr_3$ Perovskite Quantum Dots. *Nat. Commun.* **2022**, *13*, 2587.
(127) Huang, L.; Ye, Z.; Yang, L.; Li, J.; Qin, H.; Peng, X. Synthesis of Colloidal Quantum Dots with an Ultranarrow Photoluminescence Peak. *Chem. Mater.* **2021**, *33*, 1799−1810.
(128) Weidman, M. C.; Beck, M. E.; Hoffman, R. S.; Prins, F.; Tisdale, W. A. Monodisperse, Air-Stable PbS Nanocrystals via Precursor Stoichiometry Control. *ACS Nano* **2014**, *8*, 6363−6371.
(129) Peng, X.; Wickham, J.; Alivisatos, A. P. Kinetics of II-VI and III-V Colloidal Semiconductor Nanocrystal Growth: "Focusing" of Size Distributions. *J. Am. Chem. Soc.* **1998**, *120*, 5343−5344.
(130) Campos, M. P.; Hendricks, M. P.; Beecher, A. N.; Walravens, W.; Swain, R. A.; Cleveland, G. T.; Hens, Z.; Sfeir, M. Y.; Owen, J. S. A Library of Selenourea Precursors to PbSe Nanocrystals with Size Distributions near the Homogeneous Limit. *J. Am. Chem. Soc.* **2017**, *139*, 2296−2305.
(131) Campos, M. P.; De Roo, J.; Greenberg, M. W.; McMurtry, B. M.; Hendricks, M. P.; Bennett, E.; Saenz, N.; Sfeir, M. Y.; Abécassis, B.; Ghose, S. K.; et al. Growth Kinetics Determine the Polydispersity and Size of PbS and PbSe Nanocrystals. *Chem. Sci.* **2022**, *13*, 4555−4565.
(132) Ma, W.; Swisher, S. L.; Ewers, T.; Engel, J.; Ferry, V. E.; Atwater, H. A.; Alivisatos, A. P. Photovoltaic Performance of Ultrasmall PbSe Quantum Dots. *ACS Nano* **2011**, *5*, 8140−8147.
(133) Kovalenko, M. V.; Talapin, D. V.; Loi, M. A.; Cordella, F.; Hesser, G.; Bodnarchuk, M. I.; Heiss, W. Quasi-Seeded Growth of Ligand-Tailored PbSe Nanocrystals through Cation-Exchange-Mediated Nucleation. *Angew. Chem., Int. Ed.* **2008**, *47*, 3029−3033.
(134) Dai, Q.; Wang, Y.; Li, X.; Zhang, Y.; Pellegrino, D. J.; Zhao, M.; Zou, B.; Seo, J.; Wang, Y.; Yu, W. W. Size-Dependent Composition and Molar Extinction Coefficient of PbSe Semiconductor Nanocrystals. *ACS Nano* **2009**, *3*, 1518−1524.
(135) Lei, Y.; Mehmood, F.; Lee, S.; Greeley, J.; Lee, B.; Seifert, S.; Winans, R. E.; Elam, J. W.; Meyer, R. J.; Redfern, P. C.; et al. Increased Silver Activity for Direct Propylene Epoxidation via Subnanometer Size Effects. *Science* **2010**, *328*, 224−228.
(136) Li, T.; Senesi, A. J.; Lee, B. Small Angle X-Ray Scattering for Nanoparticle Research. *Chem. Rev.* **2016**, *116*, 11128−11180.
(137) Maes, J.; Castro, N.; De Nolf, K.; Walravens, W.; Abécassis, B.; Hens, Z. Size and Concentration Determination of Colloidal Nanocrystals by Small-Angle X-Ray Scattering. *Chem. Mater.* **2018**, *30*, 3952−3962.
(138) Liu, J. Scanning Transmission Electron Microscopy and Its Application to the Study of Nanoparticles and Nanoparticle Systems. *J. Electron Microsc. (Tokyo)* **2005**, *54*, 251−278.
(139) Park, J.; Elmlund, H.; Ercius, P.; Yuk, J. M.; Limmer, D. T.; Chen, Q.; Kim, K.; Han, S. H.; Weitz, D. A.; Zettl, A.; et al. 3D Structure of Individual Nanocrystals in Solution by Electron Microscopy. *Science* **2015**, *349*, 290−295.
(140) Cheng, Z.; Wang, C.; Wu, X.; Chu, J. Review *in Situ* Transmission Electron Microscope with Machine Learning. *J. Semicond.* **2022**, *43*, 081001.
(141) Pelz, P. M.; Rakowski, A.; Rangel DaCosta, L.; Savitzky, B. H.; Scott, M. C.; Ophus, C. A Fast Algorithm for Scanning Transmission Electron Microscopy Imaging and 4D-STEM Diffraction Simulations. *Microsc. Microanal.* **2021**, *27*, 835−848.
(142) Wen, H.; Luna-Romera, J. M.; Riquelme, J. C.; Dwyer, C.; Chang, S. L. Y. Statistically Representative Metrology of Nanoparticles via Unsupervised Machine Learning of TEM Images. *Nanomaterials* **2021**, *11*, 2706.
(143) Jarrold, M. F. Applications of Charge Detection Mass Spectrometry in Molecular Biology and Biotechnology. *Chem. Rev.* **2022**, *122*, 7415−7441.
(144) Karthika, S.; Radhakrishnan, T. K.; Kalaichelvi, P. A Review of Classical and Nonclassical Nucleation Theories. *Cryst. Growth Des.* **2016**, *16*, 6663−6681.
(145) Whitehead, C. B.; Özkar, S.; Finke, R. G. LaMer's 1950 Model of Particle Formation: A Review and Critical Analysis of Its Classical Nucleation and Fluctuation Theory Basis, of Competing Models and Mechanisms for Phase-Changes and Particle Formation, and Then of Its Application to Silver Halide, Semiconductor, Metal, and Metal-Oxide Nanoparticles. *Mater. Adv.* **2021**, *2*, 186−235.
(146) Shimpi, J. R.; Sidhaye, D. S.; Prasad, B. L. V. Digestive Ripening: A Fine Chemical Machining Process on the Nanoscale. *Langmuir* **2017**, *33*, 9491−9507.
(147) Wang, F.; Richards, V. N.; Shields, S. P.; Buhro, W. E. Kinetics and Mechanisms of Aggregative Nanocrystal Growth. *Chem. Mater.* **2014**, *26*, 5−21.
(148) Thanh, N. T. K.; Maclean, N.; Mahiddine, S. Mechanisms of Nucleation and Growth of Nanoparticles in Solution. *Chem. Rev.* **2014**, *114*, 7610−7630.
(149) Li, J.; Deepak, F. L. In Situ Kinetic Observations on Crystal Nucleation and Growth. *Chem. Rev.* **2022**, *122*, 16911−16982.
(150) LaMer, V. K.; Dinegar, R. H. Theory, Production and Mechanism of Formation of Monodispersed Hydrosols. *J. Am. Chem. Soc.* **1950**, *72*, 4847−4854.
(151) Reiss, H. The Growth of Uniform Colloidal Dispersions. *J. Chem. Phys.* **1951**, *19*, 482−487.
(152) McMurtry, B. M.; Qian, K.; Teglasi, J. K.; Swarnakar, A. K.; De Roo, J.; Owen, J. S. Continuous Nucleation and Size Dependent Growth Kinetics of Indium Phosphide Nanocrystals. *Chem. Mater.* **2020**, *32*, 4358−4368.
(153) Prins, P. T.; Montanarella, F.; Dümbgen, K.; Justo, Y.; van der Bok, J. C.; Hinterding, S. O. M.; Geuchies, J. J.; Maes, J.; De Nolf, K.; Deelen, S.; et al. Extended Nucleation and Superfocusing in Colloidal Semiconductor Nanocrystal Synthesis. *Nano Lett.* **2021**, *21*, 2487−2496.
(154) Abécassis, B.; Greenberg, M. W.; Bal, V.; McMurtry, B. M.; Campos, M. P.; Guillemeney, L.; Mahler, B.; Prevost, S.; Sharpnack, L.; Hendricks, M. P.; et al. Persistent Nucleation and Size Dependent Attachment Kinetics Produce Monodisperse PbS Nanocrystals. *Chem. Sci.* **2022**, *13*, 4977−4983.
(155) Yuk, J. M.; Park, J.; Ercius, P.; Kim, K.; Hellebusch, D. J.; Crommie, M. F.; Lee, J. Y.; Zettl, A.; Alivisatos, A. P. High-Resolution EM of Colloidal Nanocrystal Growth Using Graphene Liquid Cells. *Science* **2012**, *336*, 61−64.

https://doi.org/10.1021/acs.chemrev.3c00097
Chem. Rev. XXXX, XXX, XXX−XXX

(156) Handwerk, D. R.; Shipman, P. D.; Whitehead, C. B.; Özkar, S.; Finke, R. G. Mechanism-Enabled Population Balance Modeling of Particle Formation En Route to Particle Average Size and Size Distribution Understanding and Control. *J. Am. Chem. Soc.* **2019**, *141*, 15827−15839.
(157) Mozaffari, S.; Li, W.; Thompson, C.; Ivanov, S.; Seifert, S.; Lee, B.; Kovarik, L.; Karim, A. M. Colloidal Nanoparticle Size Control: Experimental and Kinetic Modeling Investigation of the Ligand−Metal Binding Role in Controlling the Nucleation and Growth Kinetics. *Nanoscale* **2017**, *9*, 13772−13785.
(158) Mozaffari, S.; Li, W.; Dixit, M.; Seifert, S.; Lee, B.; Kovarik, L.; Mpourmpakis, G.; Karim, A. M. The Role of Nanoparticle Size and Ligand Coverage in Size Focusing of Colloidal Metal Nanoparticles. *Nanoscale Adv.* **2019**, *1*, 4052−4066.
(159) Kessler, M. L.; Dempsey, J. L. Mapping the Topology of PbS Nanocrystals through Displacement Isotherms of Surface-Bound Metal Oleate Complexes. *Chem. Mater.* **2020**, *32*, 2561−2571.
(160) Cossairt, B. M. Shining Light on Indium Phosphide Quantum Dots: Understanding the Interplay among Precursor Conversion, Nucleation, and Growth. *Chem. Mater.* **2016**, *28*, 7181−7189.
(161) Zhao, Q.; Kulik, H. J. Electronic Structure Origins of Surface-Dependent Growth in III−V Quantum Dots. *Chem. Mater.* **2018**, *30*, 7154−7165.
(162) Weishäupl, S. J.; Cui, Y.; Deger, S. N.; Syed, H.; Ovsianikov, A.; Hauer, J.; Pöthig, A.; Fischer, R. A. Coordination Polymers Based on Carbazole-Derived Chromophore Linkers for Optimized Multiphoton Absorption: A Structural and Photophysical Study. *Chem. Mater.* **2022**, *34*, 7402−7411.
(163) Palencia, C.; Yu, K.; Boldt, K. The Future of Colloidal Semiconductor Magic-Size Clusters. *ACS Nano* **2020**, *14*, 1227−1235.
(164) Busatto, S.; de Mello Donega, C. Magic-Size Semiconductor Nanostructures: Where Does the Magic Come From? *ACS Mater. Au* **2022**, *2*, 237−249.
(165) Hens, Z.; De Roo, J. Atomically Precise Nanocrystals. *J. Am. Chem. Soc.* **2020**, *142*, 15627−15637.
(166) Mule, A. S.; Mazzotti, S.; Rossinelli, A. A.; Aellen, M.; Prins, P. T.; van der Bok, J. C.; Solari, S. F.; Glauser, Y. M.; Kumar, P. V.; Riedinger, A.; et al. Unraveling the Growth Mechanism of Magic-Sized Semiconductor Nanocrystals. *J. Am. Chem. Soc.* **2021**, *143*, 2037−2048.
(167) ter Horst, J. H.; Kashchiev, D. Rate of Two-Dimensional Nucleation: Verifying Classical and Atomistic Theories by Monte Carlo Simulation. *J. Phys. Chem. B* **2008**, *112*, 8614−8618.
(168) Pun, A. B.; Mazzotti, S.; Mule, A. S.; Norris, D. J. Understanding Discrete Growth in Semiconductor Nanocrystals: Nanoplatelets and Magic-Sized Clusters. *Acc. Chem. Res.* **2021**, *54*, 1545−1554.
(169) Beecher, A. N.; Yang, X.; Palmer, J. H.; LaGrassa, A. L.; Juhas, P.; Billinge, S. J. L.; Owen, J. S. Atomic Structures and Gram Scale Synthesis of Three Tetrahedral Quantum Dots. *J. Am. Chem. Soc.* **2014**, *136*, 10645−10653.
(170) Wegner, K. D.; Häusler, I.; Knigge, X.; Hodoroaba, V.-D.; Emmerling, F.; Reiss, P.; Resch-Genger, U. One-Pot Heat-Up Synthesis of ZnSe Magic-Sized Clusters Using Thiol Ligands. *Inorg. Chem.* **2022**, *61*, 7207−7211.
(171) Groeneveld, E.; van Berkum, S.; Meijerink, A.; de Mello Donegá, C. Growth and Stability of ZnTe Magic-Size Nanocrystals. *Small* **2011**, *7*, 1247−1256.
(172) Yu, K.; Ouyang, J.; Leek, D. M. In-Situ Observation of Nucleation and Growth of PbSe Magic-Sized Nanoclusters and Regular Nanocrystals. *Small* **2011**, *7*, 2250−2262.
(173) Kwon, Y.; Kim, S. Indium Phosphide Magic-Sized Clusters: Chemistry and Applications. *NPG Asia Mater.* **2021**, *13*, 37.
(174) Ning, J.; Banin, U. Magic Size InP and InAs Clusters: Synthesis, Characterization and Shell Growth. *Chem. Commun.* **2017**, *53*, 2626−2629.
(175) Cossairt, B. M.; Owen, J. S. CdSe Clusters: At the Interface of Small Molecules and Quantum Dots. *Chem. Mater.* **2011**, *23*, 3114−3119.
(176) Dong, Y.; Qiao, T.; Kim, D.; Parobek, D.; Rossi, D.; Son, D. H. Precise Control of Quantum Confinement in Cesium Lead Halide Perovskite Quantum Dots via Thermodynamic Equilibrium. *Nano Lett.* **2018**, *18*, 3716−3722.
(177) Lin, X. M.; Wang, G. M.; Sorensen, C. M.; Klabunde, K. J. Formation and Dissolution of Gold Nanocrystal Superlattices in a Colloidal Solution. *J. Phys. Chem. B* **1999**, *103*, 5488−5492.
(178) Stoeva, S. I.; Zaikovski, V.; Prasad, B. L. V.; Stoimenov, P. K.; Sorensen, C. M.; Klabunde, K. J. Reversible Transformations of Gold Nanoparticle Morphology. *Langmuir* **2005**, *21*, 10280−10283.
(179) Cingarapu, S.; Yang, Z.; Sorensen, C. M.; Klabunde, K. J. Synthesis of CdSe Quantum Dots by Evaporation of Bulk CdSe Using SMAD and Digestive Ripening Processes. *Chem. Mater.* **2009**, *21*, 1248−1252.
(180) Prasad, B. L. V.; Stoeva, S. I.; Sorensen, C. M.; Klabunde, K. J. Digestive-Ripening Agents for Gold Nanoparticles: Alternatives to Thiols. *Chem. Mater.* **2003**, *15*, 935−942.
(181) Razgoniaeva, N.; Yang, M.; Garrett, P.; Kholmicheva, N.; Moroz, P.; Eckard, H.; Royo Romero, L.; Porotnikov, D.; Khon, D.; Zamkov, M. Just Add Ligands: Self-Sustained Size Focusing of Colloidal Semiconductor Nanocrystals. *Chem. Mater.* **2018**, *30*, 1391−1398.
(182) Hudson, M. H.; Gupta, A.; Srivastava, V.; Janke, E. M.; Talapin, D. V. Synthesis of In1−XGaxP Quantum Dots in Lewis Basic Molten Salts: The Effects of Surface Chemistry, Reaction Conditions, and Molten Salt Composition. *J. Phys. Chem. C* **2022**, *126*, 1564−1580.
(183) Srivastava, V.; Kamysbayev, V.; Hong, L.; Dunietz, E.; Klie, R. F.; Talapin, D. V. Colloidal Chemistry in Molten Salts: Synthesis of Luminescent In1−XGaxP and In1−XGaxAs Quantum Dots. *J. Am. Chem. Soc.* **2018**, *140*, 12144−12151.
(184) Gupta, A.; Ondry, J. C.; Chen, M.; Hudson, M. H.; Coropceanu, I.; Sarma, N. A.; Talapin, D. V. Diffusion-Limited Kinetics of Isovalent Cation Exchange in III−V Nanocrystals Dispersed in Molten Salt Reaction Media. *Nano Lett.* **2022**, *22*, 6545−6552.
(185) Mlinar, V.; Zunger, A. Effect of Atomic-Scale Randomness on the Optical Polarization of Semiconductor Quantum Dots. *Phys. Rev. B* **2009**, *79*, 115416.
(186) Mourad, D.; Guille, A.; Aubert, T.; Brainis, E.; Hens, Z. Random-Alloying Induced Signatures in the Absorption Spectra of Colloidal Quantum Dots. *Chem. Mater.* **2014**, *26*, 6852−6862.
(187) Brus, L. E. Electron−Electron and Electron-hole Interactions in Small Semiconductor Crystallites: The Size Dependence of the Lowest Excited Electronic State. *J. Chem. Phys.* **1984**, *80*, 4403−4409.
(188) Park, J.; An, K.; Hwang, Y.; Park, J.-G.; Noh, H.-J.; Kim, J.-Y.; Park, J.-H.; Hwang, N.-M.; Hyeon, T. Ultra-Large-Scale Syntheses of Monodisperse Nanocrystals. *Nat. Mater.* **2004**, *3*, 891−895.
(189) Murray, C. B.; Norris, D. J.; Bawendi, M. G. Synthesis and Characterization of Nearly Monodisperse CdE (E = Sulfur, Selenium, Tellurium) Semiconductor Nanocrystallites. *J. Am. Chem. Soc.* **1993**, *115*, 8706−8715.
(190) Chemseddine, A.; Weller, H. Highly Monodisperse Quantum Sized CdS Particles by Size Selective Precipitation. *Berichte Bunsenges. Für Phys. Chem.* **1993**, *97*, 636−638.
(191) Murray, C. B. Synthesis and Characterization of II-IV Quantum Dots and Their Assembly into 3D Quantum Dot Superlattices. Ph.D. Disseration, Massachusetts Institute of Technology: Cambridge, MA, 1995.
(192) Murray, C. B.; Kagan, C. R.; Bawendi, M. G. Self-Organization of CdSe Nanocrystallites into Three-Dimensional Quantum Dot Superlattices. *Science* **1995**, *270*, 1335−1338.
(193) Israelachvili, J. Van der Waals Forces between Particles and Surfaces. *Intermolecular and Surface Forces*, 3rd ed.; Academic Press, 2011; pp 253−390.
(194) Hertlein, C.; Helden, L.; Gambassi, A.; Dietrich, S.; Bechinger, C. Direct Measurement of Critical Casimir Forces. *Nature* **2008**, *451*, 172−175.
(195) Marino, E.; Kodger, T. E.; Hove, J. B. t.; Velders, A. H.; Schall, P. Assembling Quantum Dots via Critical Casimir Forces. *Nanotechnol. Gener. High Effic. Photovolt. NEXTGEN NANOPV Spring Int. Sch. Workshop* **2016**, *158*, 154−159.

https://doi.org/10.1021/acs.chemrev.3c00097
Chem. Rev. XXXX, XXX, XXX−XXX

(196) Marino, E.; Balazs, D. M.; Crisp, R. W.; Hermida-Merino, D.; Loi, M. A.; Kodger, T. E.; Schall, P. Controlling Superstructure−Property Relationships via Critical Casimir Assembly of Quantum Dots. *J. Phys. Chem. C* **2019**, *123*, 13451−13457.
(197) Vasilyev, O. A.; Marino, E.; Kluft, B. B.; Schall, P.; Kondrat, S. Debye vs. Casimir: Controlling the Structure of Charged Nanoparticles Deposited on a Substrate. *Nanoscale* **2021**, *13*, 6475−6488.
(198) Villanueva-Valencia, J. R.; Guo, H.; Castañeda-Priego, R.; Liu, Y. Concentration and Size Effects on the Size-Selective Particle Purification Method Using the Critical Casimir Force. *Phys. Chem. Chem. Phys.* **2021**, *23*, 4404−4412.
(199) Nguyen, V. D.; Dang, M. T.; Nguyen, T. A.; Schall, P. Critical Casimir Forces for Colloidal Assembly. *J. Phys.: Condens. Matter* **2016**, *28*, 043001.
(200) Marino, E.; Vasilyev, O. A.; Kluft, B. B.; Stroink, M. J. B.; Kondrat, S.; Schall, P. Controlled Deposition of Nanoparticles with Critical Casimir Forces. *Nanoscale Horiz.* **2021**, *6*, 751−758.
(201) Israelachvili, J. Steric (Polymer-Mediated) and Thermal Fluctuation Forces. *Intermolecular and Surface Forces*, 3rd ed.; Academic Press, 2011; pp 381−414.
(202) Li, D.; Yun, H.; Diroll, B. T.; Doan-Nguyen, V. V. T.; Kikkawa, J. M.; Murray, C. B. Synthesis and Size-Selective Precipitation of Monodisperse Nonstoichiometric $M_xFe_{3-x}O_4$ (M = Mn, Co) Nanocrystals and Their DC and AC Magnetic Properties. *Chem. Mater.* **2016**, *28*, 480−489.
(203) Scarabelli, L.; Liz-Marzán, L. M. An Extended Protocol for the Synthesis of Monodisperse Gold Nanotriangles. *ACS Nano* **2021**, *15*, 18600−18607.
(204) Jana, S.; de Frutos, M.; Davidson, P.; Abécassis, B. Ligand-Induced Twisting of Nanoplatelets and Their Self-Assembly into Chiral Ribbons. *Sci. Adv.* **2017**, *3*, e1701483.
(205) Baranov, D.; Fiore, A.; van Huis, M.; Giannini, C.; Falqui, A.; Lafont, U.; Zandbergen, H.; Zanella, M.; Cingolani, R.; Manna, L. Assembly of Colloidal Semiconductor Nanorods in Solution by Depletion Attraction. *Nano Lett.* **2010**, *10*, 743−749.
(206) Wu, L.; Willis, J. J.; McKay, I. S.; Diroll, B. T.; Qin, J.; Cargnello, M.; Tassone, C. J. High-Temperature Crystallization of Nanocrystals into Three-Dimensional Superlattices. *Nature* **2017**, *548*, 197−201.
(207) Matsumoto, H.; Sakata, T.; Mori, H.; Yoneyama, H. Narrowing Size Distribution of CdS Nanocrystals by Size Selective Photocorrosion. *Chem. Lett.* **1995**, *24*, 595−596.
(208) Völker, S. Hole-Burning Spectroscopy. *Annu. Rev. Phys. Chem.* **1989**, *40*, 499−530.
(209) Matsumoto, H.; Sakata, T.; Mori, H.; Yoneyama, H. Preparation of Monodisperse CdS Nanocrystals by Size Selective Photocorrosion. *J. Phys. Chem.* **1996**, *100*, 13781−13785.
(210) Miyake, M.; Torimoto, T.; Sakata, T.; Mori, H.; Yoneyama, H. Photoelectrochemical Characterization of Nearly Monodisperse CdS Nanoparticles-Immobilized Gold Electrodes. *Langmuir* **1999**, *15*, 1503−1507.
(211) Torimoto, T.; Kontani, H.; Shibutani, Y.; Kuwabata, S.; Sakata, T.; Mori, H.; Yoneyama, H. Characterization of Ultrasmall CdS Nanoparticles Prepared by the Size-Selective Photoetching Technique. *J. Phys. Chem. B* **2001**, *105*, 6838−6845.
(212) Uematsu, T.; Kitajima, H.; Kohma, T.; Torimoto, T.; Tachibana, Y.; Kuwabata, S. Tuning of the Fluorescence Wavelength of CdTe Quantum Dots with 2 nm Resolution by Size-Selective Photoetching. *Nanotechnology* **2009**, *20*, 215302.
(213) Giersig, M.; Mulvaney, P. Preparation of Ordered Colloid Monolayers by Electrophoretic Deposition. *Langmuir* **1993**, *9*, 3408−3413.
(214) Yu, Y.; Yu, D.; Orme, C. A. Reversible, Tunable, Electric-Field Driven Assembly of Silver Nanocrystal Superlattices. *Nano Lett.* **2017**, *17*, 3862−3869.
(215) Bass, J. D.; Ai, X.; Bagabas, A.; Rice, P. M.; Topuria, T.; Scott, J. C.; Alharbi, F. H.; Kim, H.-C.; Song, Q.; Miller, R. D. An Efficient and Low-Cost Method for the Purification of Colloidal Nanoparticles. *Angew. Chem., Int. Ed.* **2011**, *50*, 6538−6542.
(216) Yavuz, C. T.; Mayo, J. T.; Yu, W. W.; Prakash, A.; Falkner, J. C.; Yean, S.; Cong, L.; Shipley, H. J.; Kan, A.; Tomson, M.; et al. Low-Field Magnetic Separation of Monodisperse Fe_3O_4 Nanocrystals. *Science* **2006**, *314*, 964−967.
(217) Testa-Anta, M.; Liébana-Viñas, S.; Rivas-Murias, B.; Rodríguez González, B.; Farle, M.; Salgueiriño, V. Shaping Iron Oxide Nanocrystals for Magnetic Separation Applications. *Nanoscale* **2018**, *10*, 20462−20467.
(218) Rosen, D. J.; Yang, S.; Marino, E.; Jiang, Z.; Murray, C. B. In Situ EXAFS-Based Nanothermometry of Heterodimer Nanocrystals under Induction Heating. *J. Phys. Chem. C* **2022**, *126*, 3623−3634.
(219) Ye, X.; Reifsnyder Hickey, D.; Fei, J.; Diroll, B. T.; Paik, T.; Chen, J.; Murray, C. B. Seeded Growth of Metal-Doped Plasmonic Oxide Heterodimer Nanocrystals and Their Chemical Transformation. *J. Am. Chem. Soc.* **2014**, *136*, 5106−5115.
(220) Gordon, T. R.; Schaak, R. E. Synthesis of Hybrid Au-In_2O_3 Nanoparticles Exhibiting Dual Plasmonic Resonance. *Chem. Mater.* **2014**, *26*, 5900−5904.
(221) Yin, Y.; Lu, Y.; Gates, B.; Xia, Y. Template-Assisted Self-Assembly: A Practical Route to Complex Aggregates of Monodispersed Colloids with Well-Defined Sizes, Shapes, and Structures. *J. Am. Chem. Soc.* **2001**, *123*, 8718−8729.
(222) Keller, A. W.; Marino, E.; An, D.; Neuhaus, S. J.; Elbert, K. C.; Murray, C. B.; Kagan, C. R. Sub-5 Nm Anisotropic Pattern Transfer via Colloidal Lithography of a Self-Assembled GdF_3 Nanocrystal Monolayer. *Nano Lett.* **2022**, *22*, 1992−2000.
(223) Greybush, N. J.; Saboktakin, M.; Ye, X.; Della Giovampaola, C.; Oh, S. J.; Berry, N. E.; Engheta, N.; Murray, C. B.; Kagan, C. R. Plasmon-Enhanced Upconversion Luminescence in Single Nanophosphor−Nanorod Heterodimers Formed through Template-Assisted Self-Assembly. *ACS Nano* **2014**, *8*, 9482−9491.
(224) Greybush, N. J.; Liberal, I.; Malassis, L.; Kikkawa, J. M.; Engheta, N.; Murray, C. B.; Kagan, C. R. Plasmon Resonances in Self-Assembled Two-Dimensional Au Nanocrystal Metamolecules. *ACS Nano* **2017**, *11*, 2917−2927.
(225) Greybush, N. J.; Pacheco-Peña, V.; Engheta, N.; Murray, C. B.; Kagan, C. R. Plasmonic Optical and Chiroptical Response of Self-Assembled Au Nanorod Equilateral Trimers. *ACS Nano* **2019**, *13*, 1617−1624.
(226) Flauraud, V.; Mastrangeli, M.; Bernasconi, G. D.; Butet, J.; Alexander, D. T. L.; Shahrabi, E.; Martin, O. J. F.; Brugger, J. Nanoscale Topographical Control of Capillary Assembly of Nanoparticles. *Nat. Nanotechnol.* **2017**, *12*, 73−80.
(227) Cai, Y.-Y.; Fallah, A.; Yang, S.; Choi, Y. C.; Xu, J.; Stein, A.; Kikkawa, J. M.; Murray, C. B.; Engheta, N.; Kagan, C. R. Open- and Close-Packed, Shape-engineered Polygonal Nanoparticle Metamolecules with Tailorable Fano Resonances. *Adv. Mater.* **2023**.
(228) Zhang, M.; Magagnosc, D. J.; Liberal, I.; Yu, Y.; Yun, H.; Yang, H.; Wu, Y.; Guo, J.; Chen, W.; Shin, Y. J.; et al. High-Strength Magnetically Switchable Plasmonic Nanorods Assembled from a Binary Nanocrystal Mixture. *Nat. Nanotechnol.* **2017**, *12*, 228−232.
(229) Acosta, V. M.; Santori, C.; Faraon, A.; Huang, Z.; Fu, K. M. C.; Stacey, A.; Simpson, D. A.; Ganesan, K.; Tomljenovic-Hanic, S.; Greentree, A. D.; et al. Dynamic Stabilization of the Optical Resonances of Single Nitrogen-Vacancy Centers in Diamond. *Phys. Rev. Lett.* **2012**, *108*, 6−11.
(230) Rice, J. H.; Robinson, J. W.; Jarjour, A.; Taylor, R. A.; Oliver, R. A.; Briggs, G. A. D.; Kappers, M. J.; Humphreys, C. J. Temporal Variation in Photoluminescence from Single InGaN Quantum Dots. *Appl. Phys. Lett.* **2004**, *84*, 4110−4112.
(231) Moradi, A.; Ristanović, Z.; Orrit, M.; Deperasińska, I.; Kozankiewicz, B. Matrix-Induced Linear Stark Effect of Single Dibenzoterrylene Molecules in 2,3-Dibromonaphthalene Crystal. *ChemPhysChem* **2019**, *20*, 55−61.
(232) Ibuki, H.; Ihara, T.; Kanemitsu, Y. Spectral Diffusion of Emissions of Excitons and Trions in Single CdSe/ZnS Nanocrystals: Charge Fluctuations in and around Nanocrystals. *J. Phys. Chem. C* **2016**, *120*, 23772−23779.

https://doi.org/10.1021/acs.chemrev.3c00097
Chem. Rev. XXXX, XXX, XXX−XXX

(233) Müller, J.; Lupton, J. M.; Rogach, A. L.; Feldmann, J.; Talapin, D. V.; Weller, H. Monitoring Surface Charge Movement in Single Elongated Semiconductor Nanocrystals. *Phys. Rev. Lett.* **2004**, *93*, 2−5.
(234) Tessier, M. D.; Javaux, C.; Maksimovic, I.; Loriette, V.; Dubertret, B. Spectroscopy of Single CdSe Nanoplatelets. *ACS Nano* **2012**, *6*, 6751−6758.
(235) Lohmann, S. H.; Harder, P.; Bourier, F.; Strelow, C.; Mews, A.; Kipp, T. Influence of Interface-Driven Strain on the Spectral Diffusion Properties of Core/Shell CdSe/CdS Dot/Rod Nanoparticles. *J. Phys. Chem. C* **2019**, *123*, 5099−5109.
(236) Kuno, M.; Fromm, D. P.; Hamann, H. F.; Gallagher, A.; Nesbitt, D. J. "On"/"off" Fluorescence Intermittency of Single Semiconductor Quantum Dots. *J. Chem. Phys.* **2001**, *115*, 1028−1040.
(237) Kuno, M.; Fromm, D. P.; Hamann, H. F.; Gallagher, A.; Nesbitt, D. J. Nonexponential "Blinking" Kinetics of Single CdSe Quantum Dots: A Universal Power Law Behavior. *J. Chem. Phys.* **2000**, *112*, 3117−3120.
(238) Galland, C.; Ghosh, Y.; Steinbrück, A.; Sykora, M.; Hollingsworth, J. A.; Klimov, V. I.; Htoon, H. Two Types of Luminescence Blinking Revealed by Spectroelectrochemistry of Single Quantum Dots. *Nature* **2011**, *479*, 203−207.
(239) Seth, S.; Ahmed, T.; Samanta, A. Photoluminescence Flickering and Blinking of Single $CsPbBr_3$ Perovskite Nanocrystals: Revealing Explicit Carrier Recombination Dynamics. *J. Phys. Chem. Lett.* **2018**, *9*, 7007−7014.
(240) Cui, J.; Beyler, A. P.; Bischof, T. S.; Wilson, M. W. B.; Bawendi, M. G. Deconstructing the Photon Stream from Single Nanocrystals: From Binning to Correlation. *Chem. Soc. Rev.* **2014**, *43*, 1287−1310.
(241) Fernée, M. J.; Tamarat, P.; Lounis, B. Spectroscopy of Single Nanocrystals. *Chem. Soc. Rev.* **2014**, *43*, 1311−1337.
(242) Gómez, D. E.; Califano, M.; Mulvaney, P. Optical Properties of Single Semiconductor Nanocrystals. *Phys. Chem. Chem. Phys.* **2006**, *8*, 4989−5011.
(243) Kagan, C. R.; Bassett, L. C.; Murray, C. B.; Thompson, S. M. Colloidal Quantum Dots as Platforms for Quantum Information Science. *Chem. Rev.* **2021**, *121*, 3186−3233.
(244) Cao, Z.; Hu, F.; Zhang, C.; Zhu, S.; Xiao, M.; Wang, X. Optical Studies of Semiconductor Perovskite Nanocrystals for Classical Optoelectronic Applications and Quantum Information Technologies : A Review. *Adv. Photonics* **2020**, *2*, 8−10.
(245) Blanton, S. A.; Hines, M. A.; Guyot-Sionnest, P. Photoluminescence Wandering in Single CdSe Nanocrystals. *Appl. Phys. Lett.* **1996**, *69*, 3905−3907.
(246) Brokmann, X.; Marshall, L. F.; Bawendi, M. G. Revealing Single Emitter Spectral Dynamics from Intensity Correlations in an Ensemble Fluorescence Spectrum. *Opt. Express* **2009**, *17*, 4509.
(247) Beyler, A. P.; Marshall, L. F.; Cui, J.; Brokmann, X.; Bawendi, M. G. Direct Observation of Rapid Discrete Spectral Dynamics in Single Colloidal Cdse-Cds Core-Shell Quantum Dots. *Phys. Rev. Lett.* **2013**, *111*, 1−5.
(248) Fernée, M. J.; Littleton, B. N.; Cooper, S.; Rubinsztein-Dunlop, H.; Gómez, D. E.; Mulvaney, P. Acoustic Phonon Contributions to the Emission Spectrum of Single CdSe Nanocrystals. *J. Phys. Chem. C* **2008**, *112*, 1878−1884.
(249) Fernée, M. J.; Sinito, C.; Mulvaney, P.; Tamarat, P.; Lounis, B. The Optical Phonon Spectrum of CdSe Colloidal Quantum Dots. *Phys. Chem. Chem. Phys.* **2014**, *16*, 16957−16961.
(250) Strandell, D. P.; Kambhampati, P. The Temperature Dependence of the Photoluminescence of $CsPbBr_3$ Nanocrystals Reveals Phase Transitions and Homogeneous Linewidths. *J. Phys. Chem. C* **2021**, *125*, 27504−27508.
(251) Iaru, C. M.; Geuchies, J. J.; Koenraad, P. M.; Vanmaekelbergh, D.; Silov, A. Y. Strong Carrier-Phonon Coupling in Lead Halide Perovskite Nanocrystals. *ACS Nano* **2017**, *11*, 11024−11030.
(252) Empedocles, S. A.; Bawendi, M. G. Influence of Spectral Diffusion on the Line Shapes of Single CdSe Nanocrystallite Quantum Dots. *J. Phys. Chem. B* **1999**, *103*, 1826−1830.
(253) Bar-Joseph, I.; Klingshirn, C.; Miller, D. A. B.; Chemla, D. S.; Koren, U.; Miller, B. I. Quantum-Confined Stark Effect in InGaAs/InP Quantum Wells Grown by Organometallic Vapor Phase Epitaxy. *Appl. Phys. Lett.* **1987**, *50*, 1010−1012.
(254) Cordones, A. A.; Leone, S. R. Mechanisms for Charge Trapping in Single Semiconductor Nanocrystals Probed by Fluorescence Blinking. *Chem. Soc. Rev.* **2013**, *42*, 3209−3221.
(255) Mahler, B.; Spinicelli, P.; Buil, S.; Quelin, X.; Hermier, J. P.; Dubertret, B. Towards Non-Blinking Colloidal Quantum Dots. *Nat. Mater.* **2008**, *7*, 659−664.
(256) Efros, A. L.; Nesbitt, D. J. Origin and Control of Blinking in Quantum Dots. *Nat. Nanotechnol.* **2016**, *11*, 661−671.
(257) Galland, C.; Ghosh, Y.; Steinbrück, A.; Hollingsworth, J. A.; Htoon, H.; Klimov, V. I. Lifetime Blinking in Nonblinking Nanocrystal Quantum Dots. *Nat. Commun.* **2012**, *3*, 903.
(258) Krauss, T. D.; Brus, L. E. Charge, Polarizability, and Photoionization of Single Semiconductor Nanocrystals. *Phys. Rev. Lett.* **1999**, *83*, 4840−4843.
(259) Chen, Y.; Vela, J.; Htoon, H.; Casson, J. L.; Werder, D. J.; Bussian, D. A.; Klimov, V. I.; Hollingsworth, J. A. "Giant" Multishell CdSe Nanocrystal Quantum Dots with Suppressed Blinking. *J. Am. Chem. Soc.* **2008**, *130*, 5026−5027.
(260) Ghosh, Y.; Mangum, B. D.; Casson, J. L.; Williams, D. J.; Htoon, H.; Hollingsworth, J. A. New Insights into the Complexities of Shell Growth and the Strong Influence of Particle Volume in Nonblinking "Giant" Core/Shell Nanocrystal Quantum Dots. *J. Am. Chem. Soc.* **2012**, *134*, 9634−9643.
(261) Gao, F.; Bajwa, P.; Nguyen, A.; Heyes, C. D. Shell-Dependent Photoluminescence Studies Provide Mechanistic Insights into the Off-Grey-On Transitions of Blinking Quantum Dots. *ACS Nano* **2017**, *11*, 2905−2916.
(262) Hohng, S.; Ha, T. Near-Complete Suppression of Quantum Dot Blinking in Ambient Conditions. *J. Am. Chem. Soc.* **2004**, *126*, 1324−1325.
(263) Pal, B. N.; Ghosh, Y.; Brovelli, S.; Laocharoensuk, R.; Klimov, V. I.; Hollingsworth, J. A.; Htoon, H. "Giant" CdSe/CdS Core/Shell Nanocrystal Quantum Dots as Efficient Electroluminescent Materials: Strong Influence of Shell Thickness on Light-Emitting Diode Performance. *Nano Lett.* **2012**, *12*, 331−336.
(264) Lee, S. H.; Kim, Y.; Jang, H.; Min, J. H.; Oh, J.; Jang, E.; Kim, D. The Effects of Discrete and Gradient Mid-Shell Structures on the Photoluminescence of Single InP Quantum Dots. *Nanoscale* **2019**, *11*, 23251−23258.
(265) Lee, Y.; Jo, D. Y.; Kim, T.; Jo, J. H.; Park, J.; Yang, H.; Kim, D. Effectual Interface and Defect Engineering for Auger Recombination Suppression in Bright InP/ZnSeS/ZnS Quantum Dots. *ACS Appl. Mater. Interfaces* **2022**, *14*, 12479−12487.
(266) Empedocles, S. A.; Bawendi, M. G. Quantum-Confined Stark Effect in Single CdSe Nanocrystallite Quantum Dots. *Science* **1997**, *278*, 2114−2117.
(267) Knappenberger, K. L.; Wong, D. B.; Romanyuk, Y. E.; Leone, S. R. Excitation Wavelength Dependence of Fluorescence Lntermittency in CdSe/ZnS Core/Shell Quantum Dots. *Nano Lett.* **2007**, *7*, 3869−3874.
(268) Gibson, N. A.; Koscher, B. A.; Alivisatos, A. P.; Leone, S. R. Excitation Intensity Dependence of Photoluminescence Blinking in $CsPbBr_3$ Perovskite Nanocrystals. *J. Phys. Chem. C* **2018**, *122*, 12106−12113.
(269) Peterson, J. J.; Nesbitt, D. J. Modified Power Law Behavior in Quantum Dot Blinking: A Novel Role for Biexcitons and Auger Ionization. *Nano Lett.* **2009**, *9*, 338−345.
(270) Munro, A. M.; Jen-La Plante, I.; Ng, M. S.; Ginger, D. S. Quantitative Study of the Effects of Surface Ligand Concentration on CdSe Nanocrystal Photoluminescence. *J. Phys. Chem. C* **2007**, *111*, 6220−6227.
(271) Braam, D.; Mölleken, A.; Prinz, G. M.; Notthoff, C.; Geller, M.; Lorke, A. Role of the Ligand Layer for Photoluminescence Spectral Diffusion of CdSe/ZnS Nanoparticles. *Phys. Rev. B - Condens. Matter Mater. Phys.* **2013**, *88*, 1−6.

https://doi.org/10.1021/acs.chemrev.3c00097
Chem. Rev. XXXX, XXX, XXX−XXX

(272) Gellen, T. A.; Lem, J.; Turner, D. B. Probing Homogeneous Line Broadening in CdSe Nanocrystals Using Multidimensional Electronic Spectroscopy. *Nano Lett.* **2017**, *17*, 2809−2815.
(273) Fisher, B.; Caruge, J. M.; Zehnder, D.; Bawendi, M. Room-Temperature Ordered Photon Emission from Multiexciton States in Single CdSe Core-Shell Nanocrystals. *Phys. Rev. Lett.* **2005**, *94*, 1−4.
(274) Yuan, G.; Gómez, D. E.; Kirkwood, N.; Boldt, K.; Mulvaney, P. Two Mechanisms Determine Quantum Dot Blinking. *ACS Nano* **2018**, *12*, 3397−3405.
(275) Jha, P. P.; Guyot-Sionnest, P. Trion Decay in Colloidal Quantum Dots. *ACS Nano* **2009**, *3*, 1011−1015.
(276) Gómez, D. E.; van Embden, J.; Mulvaney, P.; Fernée, M. J.; Rubinsztein-Dunlop, H. Exciton-Trion Transitions in Single CdSe−CdS Core−Shell Nanocrystals. *ACS Nano* **2009**, *3*, 2281−2287.
(277) Htoon, H.; Malko, A. V.; Bussian, D.; Vela, J.; Chen, Y.; Hollingsworth, J. A.; Klimov, V. I. Highly Emissive Multiexcitons in Steady-State Photoluminescence of Individual "Giant" CdSe/CdS Core/Shell Nanocrystals. *Nano Lett.* **2010**, *10*, 2401−2407.
(278) Mueller, S.; Lüttig, J.; Brenneis, L.; Oron, D.; Brixner, T. Observing Multiexciton Correlations in Colloidal Semiconductor Quantum Dots via Multiple-Quantum Two-Dimensional Fluorescence Spectroscopy. *ACS Nano* **2021**, *15*, 4647.
(279) Tisler, J.; Balasubramanian, G.; Naydenov, B.; Kolesov, R.; Grotz, B.; Reuter, R.; Boudou, J. P.; Curmi, P. A.; Sennour, M.; Thorel, A.; et al. Fluorescence and Spin Properties of Defects in Single Digit Nanodiamonds. *ACS Nano* **2009**, *3*, 1959−1965.
(280) Bradac, C.; Gaebel, T.; Naidoo, N.; Sellars, M. J.; Twamley, J.; Brown, L. J.; Barnard, A. S.; Plakhotnik, T.; Zvyagin, A. V.; Rabeau, J. R. Observation and Control of Blinking Nitrogen-Vacancy Centres in Discrete Nanodiamonds. *Nat. Nanotechnol.* **2010**, *5*, 345−349.
(281) Wrachtrup, J.; Jelezko, F.; Grotz, B.; McGuinness, L. Nitrogen-Vacancy Centers Close to Surfaces. *MRS Bull.* **2013**, *38*, 149−154.
(282) Ishikawa, T.; Fu, K. M. C.; Santori, C.; Acosta, V. M.; Beausoleil, R. G.; Watanabe, H.; Shikata, S.; Itoh, K. M. Optical and Spin Coherence Properties of Nitrogen-Vacancy Centers Placed in a 100 nm Thick Isotopically Purified Diamond Layer. *Nano Lett.* **2012**, *12*, 2083−2087.
(283) De Roo, J.; Ibáñez, M.; Geiregat, P.; Nedelcu, G.; Walravens, W.; Maes, J.; Martins, J. C.; Van Driessche, I.; Kovalenko, M. V.; Hens, Z. Highly Dynamic Ligand Binding and Light Absorption Coefficient of Cesium Lead Bromide Perovskite Nanocrystals. *ACS Nano* **2016**, *10*, 2071−2081.
(284) Eperon, G. E.; Jedlicka, E.; Ginger, D. S. Biexciton Auger Recombination Differs in Hybrid and Inorganic Halide Perovskite Quantum Dots. *J. Phys. Chem. Lett.* **2018**, *9*, 104−109.
(285) Lodahl, P.; Mahmoodian, S.; Stobbe, S. Interfacing Single Photons and Single Quantum Dots with Photonic Nanostructures. *Rev. Mod. Phys.* **2015**, *87*, 347−400.
(286) Brorson, S. D.; Yokoyama, H.; Ippen, E. P. Spontaneous Emission Rate Alteration in Optical Waveguide Structures. *IEEE J. Quantum Electron.* **1990**, *26*, 1492−1499.
(287) Li, A.; Singh, S.; Sievenpiper, D. Metasurfaces and Their Applications. *Nanophotonics* **2018**, *7*, 989−1011.
(288) Hugall, J. T.; Singh, A.; Van Hulst, N. F. Plasmonic Cavity Coupling. *ACS Photonics* **2018**, *5*, 43−53.
(289) Munechika, K.; Chen, Y.; Tillack, A. F.; Kulkarni, A. P.; Plante, I. J. La; Munro, A. M.; Ginger, D. S. Spectral Control of Plasmonic Emission Enhancement from Quantum Dots near Single Silver Nanoprisms. *Nano Lett.* **2010**, *10*, 2598−2603.
(290) Chen, Y.; Munechika, K.; Jen-La Plante, I.; Munro, A. M.; Skrabalak, S. E.; Xia, Y.; Ginger, D. S. Excitation Enhancement of CdSe Quantum Dots by Single Metal Nanoparticles. *Appl. Phys. Lett.* **2008**, *93*, 053106.
(291) Bharadwaj, P.; Novotny, L. Robustness of Quantum Dot Power-Law Blinking. *Nano Lett.* **2011**, *11*, 2137−2141.
(292) Purcell, E. M. Spontaneous Emission Probabilities at Radio Frequencies. *Phys. Rev.* **1946**, *69*, 681.
(293) Liu, X.; Nakajima, H.; Li, Y.; Odashima, S.; Suemune, I.; Kumano, H. Optical Control of Spectral Diffusion with Single InAs Quantum Dots in a Silver-Embedded Nanocone. *Opt. Express* **2017**, *25*, 8073.
(294) Lyasota, A.; Jarlov, C.; Rudra, A.; Dwir, B.; Kapon, E. Limiting the Spectral Diffusion of Nano-Scale Light Emitters Using the Purcell Effect in a Photonic-Confined Environment. *Sci. Rep.* **2019**, *9*, 1−9.
(295) Huang, Y.; Su, R.; Wang, Y.; Zhu, C.; Feng, J.; Zhao, J.; Liu, Z.; Xiong, Q. A Fano Cavity - Photon Interface for Directional Suppression of Spectral Diffusion of a Single Perovskite Nanoplatelet. *Nano Lett.* **2022**, *22*, 8274.
(296) Yuan, G.; Gómez, D.; Kirkwood, N.; Mulvaney, P. Tuning Single Quantum Dot Emission with a Micromirror. *Nano Lett.* **2018**, *18*, 1010−1017.
(297) Chen, Y.; Sharp, D.; Saxena, A.; Nguyen, H.; Cossairt, B. M.; Majumdar, A. Integrated Quantum Nanophotonics with Solution-Processed Materials. *Adv. Quantum Technol.* **2022**, *5*, 2100078.
(298) Kim, J.-H.; Aghaeimeibodi, S.; Carolan, J.; Englund, D.; Waks, E. Hybrid Integration Methods for On-Chip Quantum Photonics. *Optica* **2020**, *7*, 291.
(299) Cohen, T. A.; Sharp, D.; Kluherz, K. T.; Chen, Y.; Munley, C.; Anderson, R. T.; Swanson, C. J.; De Yoreo, J. J.; Luscombe, C. K.; Majumdar, A.; et al. Direct Patterning of Perovskite Nanocrystals on Nanophotonic Cavities with Electrohydrodynamic Inkjet Printing. *Nano Lett.* **2022**, *22*, 5681.
(300) Le Thomas, N.; Schöps, O.; Woggon, U.; Artemyev, M. V.; Kazes, M.; Banin, U. Cavity QED with Semiconductor Nanocrystals. *Nano Lett.* **2006**, *6*, 557.
(301) Lee, H.; Woo, J. Y.; Park, D. Y.; Jo, I.; Park, J.; Lee, Y.; Koo, Y.; Choi, J.; Kim, H.; Kim, Y. H.; et al. Tip-Induced Strain Engineering of a Single Metal Halide Perovskite Quantum Dot. *ACS Nano* **2021**, *15*, 9057−9064.
(302) Steigerwald, M. L.; Alivisatos, A. P.; Gibson, J. M.; Harris, T. D.; Kortan, R.; Muller, A. J.; Thayer, A. M.; Duncan, T. M.; Douglass, D. C.; Brus, L. E. Surface Derivatization and Isolation of Semiconductor Cluster Molecules. *J. Am. Chem. Soc.* **1988**, *110*, 3046−3050.
(303) Peng, Z. A.; Peng, X. Formation of High-Quality CdTe, CdSe, and CdS Nanocrystals Using CdO as Precursor. *J. Am. Chem. Soc.* **2001**, *123*, 183−184.
(304) Diroll, B. T.; Guzelturk, B.; Po, H.; Dabard, C.; Fu, N.; Makke, L.; Lhuillier, E.; Ithurria, S. 2D II−VI Semiconductor Nanoplatelets: From Material Synthesis to Optoelectronic Integration. *Chem. Rev.* **2023**, *123*, 3543−3624.
(305) Bai, B.; Zhang, C.; Dou, Y.; Kong, L.; Wang, L.; Wang, S.; Li, J.; Zhou, Y.; Liu, L.; Liu, B.; et al. Atomically Flat Semiconductor Nanoplatelets for Light-Emitting Applications. *Chem. Soc. Rev.* **2023**, *52*, 318−360.
(306) Hazarika, A.; Fedin, I.; Hong, L.; Guo, J.; Srivastava, V.; Cho, W.; Coropceanu, I.; Portner, J.; Diroll, B. T.; Philbin, J. P.; et al. Colloidal Atomic Layer Deposition with Stationary Reactant Phases Enables Precise Synthesis of "Digital" II−VI Nano-Heterostructures with Exquisite Control of Confinement and Strain. *J. Am. Chem. Soc.* **2019**, *141*, 13487−13496.
(307) Ithurria, S.; Talapin, D. V. Colloidal Atomic Layer Deposition (c-ALD) Using Self-Limiting Reactions at Nanocrystal Surface Coupled to Phase Transfer between Polar and Nonpolar Media. *J. Am. Chem. Soc.* **2012**, *134*, 18585−18590.
(308) Antolinez, F. V.; Rabouw, F. T.; Rossinelli, A. A.; Keitel, R. C.; Cocina, A.; Becker, M. A.; Norris, D. J. Trion Emission Dominates the Low-Temperature Photoluminescence of CdSe Nanoplatelets. *Nano Lett.* **2020**, *20*, 5814−5820.
(309) Peng, L.; Otten, M.; Hazarika, A.; Coropceanu, I.; Cygorek, M.; Wiederrecht, G. P.; Hawrylak, P.; Talapin, D. V.; Ma, X. Bright Trion Emission from Semiconductor Nanoplatelets. *Phys. Rev. Mater.* **2020**, *4*, 056006.
(310) Panfil, Y. E.; Oded, M.; Banin, U. Colloidal Quantum Nanostructures: Emerging Materials for Display Applications. *Angew. Chem., Int. Ed.* **2018**, *57*, 4274−4295.
(311) Pu, C.; Qin, H.; Gao, Y.; Zhou, J.; Wang, P.; Peng, X. Synthetic Control of Exciton Behavior in Colloidal Quantum Dots. *J. Am. Chem. Soc.* **2017**, *139*, 3302−3311.

https://doi.org/10.1021/acs.chemrev.3c00097
Chem. Rev. XXXX, XXX, XXX−XXX

(312) Pietryga, J. M.; Park, Y.-S.; Lim, J.; Fidler, A. F.; Bae, W. K.; Brovelli, S.; Klimov, V. I. Spectroscopic and Device Aspects of Nanocrystal Quantum Dots. *Chem. Rev.* **2016**, *116*, 10513−10622.
(313) Reiss, P.; Protière, M.; Li, L. Core/Shell Semiconductor Nanocrystals. *Small* **2009**, *5*, 154−168.
(314) Hanifi, D. A.; Bronstein, N. D.; Koscher, B. A.; Nett, Z.; Swabeck, J. K.; Takano, K.; Schwartzberg, A. M.; Maserati, L.; Vandewal, K.; van de Burgt, Y.; et al. Redefining Near-Unity Luminescence in Quantum Dots with Photothermal Threshold Quantum Yield. *Science* **2019**, *363*, 1199−1202.
(315) Kang, S.; Kim, Y.; Jang, E.; Kang, Y.; Han, S. Fundamental Limit of the Emission Linewidths of Quantum Dots: An Ab Initio Study of CdSe Nanocrystals. *ACS Appl. Mater. Interfaces* **2020**, *12*, 22012−22018.
(316) Lv, L.; Liu, S.; Li, J.; Lei, H.; Qin, H.; Peng, X. Synthesis of Weakly Confined, Cube-Shaped, and Monodisperse Cadmium Chalcogenide Nanocrystals with Unexpected Photophysical Properties. *J. Am. Chem. Soc.* **2022**, *144*, 16872−16882.
(317) Shu, Y.; Lin, X.; Qin, H.; Hu, Z.; Jin, Y.; Peng, X. Quantum Dots for Display Applications. *Angew. Chem., Int. Ed.* **2020**, *59*, 22312−22323.
(318) Tamang, S.; Lincheneau, C.; Hermans, Y.; Jeong, S.; Reiss, P. Chemistry of InP Nanocrystal Syntheses. *Chem. Mater.* **2016**, *28*, 2491−2506.
(319) Kim, Y.; Ham, S.; Jang, H.; Min, J. H.; Chung, H.; Lee, J.; Kim, D.; Jang, E. Bright and Uniform Green Light Emitting InP/ZnSe/ZnS Quantum Dots for Wide Color Gamut Displays. *ACS Appl. Nano Mater.* **2019**, *2*, 1496−1504.
(320) Won, Y.-H.; Cho, O.; Kim, T.; Chung, D.-Y.; Kim, T.; Chung, H.; Jang, H.; Lee, J.; Kim, D.; Jang, E. Highly Efficient and Stable InP/ZnSe/ZnS Quantum Dot Light-Emitting Diodes. *Nature* **2019**, *575*, 634−638.
(321) Cho, W.; Zhou, Z.; Lin, R.; Ondry, J. C.; Talapin, D. V. Synthesis of Colloidal GaN and AlN Nanocrystals in Biphasic Molten Salt/Organic Solvent Mixtures under High-Pressure Ammonia. *ACS Nano* **2023**, *17*, 1315−1326.
(322) Hendricks, M. P.; Campos, M. P.; Cleveland, G. T.; Jen-La Plante, I.; Owen, J. S. A Tunable Library of Substituted Thiourea Precursors to Metal Sulfide Nanocrystals. *Science* **2015**, *348*, 1226−1230.
(323) Palomaki, P. K. B.; Miller, E. M.; Neale, N. R. Control of Plasmonic and Interband Transitions in Colloidal Indium Nitride Nanocrystals. *J. Am. Chem. Soc.* **2013**, *135*, 14142−14150.
(324) Meerbach, C.; Wu, C.; Erwin, S. C.; Dang, Z.; Prudnikau, A.; Lesnyak, V. Halide-Assisted Synthesis of Cadmium Chalcogenide Nanoplatelets. *Chem. Mater.* **2020**, *32*, 566−574.
(325) Ithurria, S.; Bousquet, G.; Dubertret, B. Continuous Transition from 3D to 1D Confinement Observed during the Formation of CdSe Nanoplatelets. *J. Am. Chem. Soc.* **2011**, *133*, 3070−3077.
(326) Cho, W.; Kim, S.; Coropceanu, I.; Srivastava, V.; Diroll, B. T.; Hazarika, A.; Fedin, I.; Galli, G.; Schaller, R. D.; Talapin, D. V. Direct Synthesis of Six-Monolayer (1.9 nm) Thick Zinc-Blende CdSe Nanoplatelets Emitting at 585 nm. *Chem. Mater.* **2018**, *30*, 6957−6960.
(327) Cunningham, P. D.; Coropceanu, I.; Mulloy, K.; Cho, W.; Talapin, D. V. Quantized Reaction Pathways for Solution Synthesis of Colloidal ZnSe Nanostructures: A Connection between Clusters, Nanowires, and Two-Dimensional Nanoplatelets. *ACS Nano* **2020**, *14*, 3847−3857.
(328) Pedetti, S.; Nadal, B.; Lhuillier, E.; Mahler, B.; Bouet, C.; Abécassis, B.; Xu, X.; Dubertret, B. Optimized Synthesis of CdTe Nanoplatelets and Photoresponse of CdTe Nanoplatelets Films. *Chem. Mater.* **2013**, *25*, 2455−2462.
(329) Izquierdo, E.; Robin, A.; Keuleyan, S.; Lequeux, N.; Lhuillier, E.; Ithurria, S. Strongly Confined HgTe 2D Nanoplatelets as Narrow Near-Infrared Emitters. *J. Am. Chem. Soc.* **2016**, *138*, 10496−10501.
(330) Mahler, B.; Nadal, B.; Bouet, C.; Patriarche, G.; Dubertret, B. Core/Shell Colloidal Semiconductor Nanoplatelets. *J. Am. Chem. Soc.* **2012**, *134*, 18591−18598.
(331) Rossinelli, A. A.; Rojo, H.; Mule, A. S.; Aellen, M.; Cocina, A.; De Leo, E.; Schäublin, R.; Norris, D. J. Compositional Grading for Efficient and Narrowband Emission in CdSe-Based Core/Shell Nanoplatelets. *Chem. Mater.* **2019**, *31*, 9567−9578.
(332) Kelestemur, Y.; Dede, D.; Gungor, K.; Usanmaz, C. F.; Erdem, O.; Demir, H. V. Alloyed Heterostructures of $CdSe_xS_{1-x}$ Nanoplatelets with Highly Tunable Optical Gain Performance. *Chem. Mater.* **2017**, *29*, 4857−4865.
(333) Altintas, Y.; Liu, B.; Hernández-Martínez, P. L.; Gheshlaghi, N.; Shabani, F.; Sharma, M.; Wang, L.; Sun, H.; Mutlugun, E.; Demir, H. V. Spectrally Wide-Range-Tunable, Efficient, and Bright Colloidal Light-Emitting Diodes of Quasi-2D Nanoplatelets Enabled by Engineered Alloyed Heterostructures. *Chem. Mater.* **2020**, *32*, 7874−7883.
(334) Izmir, M.; Sharma, A.; Shendre, S.; Durmusoglu, E. G.; Sharma, V. K.; Shabani, F.; Baruj, H. D.; Delikanli, S.; Sharma, M.; Demir, H. V. Blue-Emitting CdSe Nanoplatelets Enabled by Sulfur-Alloyed Heterostructures for Light-Emitting Diodes with Low Turn-on Voltage. *ACS Appl. Nano Mater.* **2022**, *5*, 1367−1376.
(335) Rohatgi, A. WebPlotDigitizer, 2021; https://automeris.io/WebPlotDigitizer.
(336) Chen, O.; Zhao, J.; Chauhan, V. P.; Cui, J.; Wong, C.; Harris, D. K.; Wei, H.; Han, H.-S.; Fukumura, D.; Jain, R. K.; et al. Compact High-Quality CdSe−CdS Core−Shell Nanocrystals with Narrow Emission Linewidths and Suppressed Blinking. *Nat. Mater.* **2013**, *12*, 445−451.
(337) Hao, J.; Liu, H.; Miao, J.; Lu, R.; Zhou, Z.; Zhao, B.; Xie, B.; Cheng, J.; Wang, K.; Delville, M.-H. A Facile Route to Synthesize CdSe/ZnS Thick-Shell Quantum Dots with Precisely Controlled Green Emission Properties: Towards QDs Based LED Applications. *Sci. Rep.* **2019**, *9*, 12048.
(338) Steckel, J. S.; Zimmer, J. P.; Coe-Sullivan, S.; Stott, N. E.; Bulović, V.; Bawendi, M. G. Blue Luminescence from (CdS)ZnS Core−Shell Nanocrystals. *Angew. Chem., Int. Ed.* **2004**, *43*, 2154−2158.
(339) Chen, D.; Zhao, F.; Qi, H.; Rutherford, M.; Peng, X. Bright and Stable Purple/Blue Emitting CdS/ZnS Core/Shell Nanocrystals Grown by Thermal Cycling Using a Single-Source Precursor. *Chem. Mater.* **2010**, *22*, 1437−1444.
(340) Ji, B.; Koley, S.; Slobodkin, I.; Remennik, S.; Banin, U. ZnSe/ZnS Core/Shell Quantum Dots with Superior Optical Properties through Thermodynamic Shell Growth. *Nano Lett.* **2020**, *20*, 2387−2395.
(341) Swafford, L. A.; Weigand, L. A.; Bowers, M. J.; McBride, J. R.; Rapaport, J. L.; Watt, T. L.; Dixit, S. K.; Feldman, L. C.; Rosenthal, S. J. Homogeneously Alloyed CdS_xSe_{1-x} Nanocrystals: Synthesis, Characterization, and Composition/Size-Dependent Band Gap. *J. Am. Chem. Soc.* **2006**, *128*, 12299−12306.
(342) Aubert, T.; Cirillo, M.; Flamee, S.; Van Deun, R.; Lange, H.; Thomsen, C.; Hens, Z. Homogeneously Alloyed $CdSe_{1-x}S_x$ Quantum Dots ($0 \leq x \leq 1$): An Efficient Synthesis for Full Optical Tunability. *Chem. Mater.* **2013**, *25*, 2388−2390.
(343) Hamachi, L. S.; Yang, H.; Jen-La Plante, I.; Saenz, N.; Qian, K.; Campos, M. P.; Cleveland, G. T.; Rreza, I.; Oza, A.; Walravens, W.; et al. Precursor Reaction Kinetics Control Compositional Grading and Size of $CdSe_{1-x}S_x$ Nanocrystal Heterostructures. *Chem. Sci.* **2019**, *10*, 6539−6552.
(344) Bailey, R. E.; Nie, S. Alloyed Semiconductor Quantum Dots: Tuning the Optical Properties without Changing the Particle Size. *J. Am. Chem. Soc.* **2003**, *125*, 7100−7106.
(345) Protière, M.; Reiss, P. Highly Luminescent $Cd_{1-x}Zn_xSe$/ZnS Core/Shell Nanocrystals Emitting in the Blue−Green Spectral Range. *Small* **2007**, *3*, 399−403.
(346) Deng, Z.; Yan, H.; Liu, Y. Band Gap Engineering of Quaternary-Alloyed ZnCdSSe Quantum Dots via a Facile Phosphine-Free Colloidal Method. *J. Am. Chem. Soc.* **2009**, *131*, 17744−17745.
(347) Yu, K.; Hrdina, A.; Ouyang, J.; Kingston, D.; Wu, X.; Leek, D. M.; Liu, X.; Li, C. Ultraviolet $ZnSe_{1-x}S_x$ Gradient-Alloyed Nanocrystals via a Noninjection Approach. *ACS Appl. Mater. Interfaces* **2012**, *4*, 4302−4311.
(348) Yu, P.; Cao, S.; Shan, Y.; Bi, Y.; Hu, Y.; Zeng, R.; Zou, B.; Wang, Y.; Zhao, J. Highly Efficient Green InP-Based Quantum Dot Light-

https://doi.org/10.1021/acs.chemrev.3c00097
Chem. Rev. XXXX, XXX, XXX−XXX

Emitting Diodes Regulated by Inner Alloyed Shell Component. *Light Sci. Appl.* **2022**, *11*, 162.
(349) Li, L.; Reiss, P. One-Pot Synthesis of Highly Luminescent InP/ZnS Nanocrystals without Precursor Injection. *J. Am. Chem. Soc.* **2008**, *130*, 11588−11589.
(350) Shen, C.; Zhu, Y.; Tao, H.; Li, J.; Zou, J.; Wang, L.; Liang, J.; Xiao, X.; Xu, X.; Xu, G. Blue-Emitting InP/GaP/ZnS Quantum Dots with Enhanced Stability by Siloxane Capping: Implication for Electroluminescent Devices. *ACS Appl. Nano Mater.* **2022**, *5*, 2801−2811.
(351) Van Avermaet, H.; Schiettecatte, P.; Hinz, S.; Giordano, L.; Ferrari, F.; Nayral, C.; Delpech, F.; Maultzsch, J.; Lange, H.; Hens, Z. Full-Spectrum InP-Based Quantum Dots with Near-Unity Photoluminescence Quantum Efficiency. *ACS Nano* **2022**, *16*, 9701−9712.
(352) Jang, E.; Kim, Y.; Won, Y.-H.; Jang, H.; Choi, S.-M. Environmentally Friendly InP-Based Quantum Dots for Efficient Wide Color Gamut Displays. *ACS Energy Lett.* **2020**, *5*, 1316−1327.
(353) Ramasamy, P.; Kim, N.; Kang, Y.-S.; Ramirez, O.; Lee, J.-S. Tunable, Bright, and Narrow-Band Luminescence from Colloidal Indium Phosphide Quantum Dots. *Chem. Mater.* **2017**, *29*, 6893−6899.
(354) Li, Y.; Hou, X.; Dai, X.; Yao, Z.; Lv, L.; Jin, Y.; Peng, X. Stoichiometry-Controlled InP-Based Quantum Dots: Synthesis, Photoluminescence, and Electroluminescence. *J. Am. Chem. Soc.* **2019**, *141*, 6448−6452.
(355) Srivastava, V.; Dunietz, E.; Kamysbayev, V.; Anderson, J. S.; Talapin, D. V. Monodisperse InAs Quantum Dots from Aminoarsine Precursors: Understanding the Role of Reducing Agent. *Chem. Mater.* **2018**, *30*, 3623−3627.
(356) Srivastava, V.; Janke, E. M.; Diroll, B. T.; Schaller, R. D.; Talapin, D. V. Facile, Economic and Size-Tunable Synthesis of Metal Arsenide Nanocrystals. *Chem. Mater.* **2016**, *28*, 6797−6802.
(357) Ginterseder, M.; Franke, D.; Perkinson, C. F.; Wang, L.; Hansen, E. C.; Bawendi, M. G. Scalable Synthesis of InAs Quantum Dots Mediated through Indium Redox Chemistry. *J. Am. Chem. Soc.* **2020**, *142*, 4088−4092.
(358) Franke, D.; Harris, D. K.; Chen, O.; Bruns, O. T.; Carr, J. A.; Wilson, M. W. B.; Bawendi, M. G. Continuous Injection Synthesis of Indium Arsenide Quantum Dots Emissive in the Short-Wavelength Infrared. *Nat. Commun.* **2016**, *7*, 12749.
(359) Liu, W.; Chang, A. Y.; Schaller, R. D.; Talapin, D. V. Colloidal InSb Nanocrystals. *J. Am. Chem. Soc.* **2012**, *134*, 20258−20261.
(360) Yarema, M.; Kovalenko, M. V. Colloidal Synthesis of InSb Nanocrystals with Controlled Polymorphism Using Indium and Antimony Amides. *Chem. Mater.* **2013**, *25*, 1788−1792.
(361) Busatto, S.; de Ruiter, M.; Jastrzebski, J. T. B. H.; Albrecht, W.; Pinchetti, V.; Brovelli, S.; Bals, S.; Moret, M.-E.; de Mello Donega, C. Luminescent Colloidal InSb Quantum Dots from In Situ Generated Single-Source Precursor. *ACS Nano* **2020**, *14*, 13146−13160.
(362) Jeong, B. G.; Chang, J. H.; Hahm, D.; Rhee, S.; Park, M.; Lee, S.; Kim, Y.; Shin, D.; Park, J. W.; Lee, C.; et al. Interface Polarization in Heterovalent Core−Shell Nanocrystals. *Nat. Mater.* **2022**, *21*, 246−252.
(363) Kim, S.-W.; Zimmer, J. P.; Ohnishi, S.; Tracy, J. B.; Frangioni, J. V.; Bawendi, M. G. Engineering $InAs_xP_{1-x}$/InP/ZnSe III-V Alloyed Core/Shell Quantum Dots for the Near-Infrared. *J. Am. Chem. Soc.* **2005**, *127*, 10526−10532.
(364) Zhao, T.; Oh, N.; Jishkariani, D.; Zhang, M.; Wang, H.; Li, N.; Lee, J. D.; Zeng, C.; Muduli, M.; Choi, H.-J.; et al. General Synthetic Route to High-Quality Colloidal III−V Semiconductor Quantum Dots Based on Pnictogen Chlorides. *J. Am. Chem. Soc.* **2019**, *141*, 15145−15152.
(365) Yu, W. W.; Falkner, J. C.; Shih, B. S.; Colvin, V. L. Preparation and Characterization of Monodisperse PbSe Semiconductor Nanocrystals in a Noncoordinating Solvent. *Chem. Mater.* **2004**, *16*, 3318−3322.
(366) Pietryga, J. M.; Werder, D. J.; Williams, D. J.; Casson, J. L.; Schaller, R. D.; Klimov, V. I.; Hollingsworth, J. A. Utilizing the Lability of Lead Selenide to Produce Heterostructured Nanocrystals with Bright, Stable Infrared Emission. *J. Am. Chem. Soc.* **2008**, *130*, 4879−4885.
(367) Justo, Y.; Geiregat, P.; van Hoecke, K.; Vanhaecke, F.; De Mello Donega, C.; Hens, Z. Optical Properties of PbS/CdS Core/Shell Quantum Dots. *J. Phys. Chem. C* **2013**, *117*, 20171−20177.
(368) Sagar, L. K.; Walravens, W.; Zhao, Q.; Vantomme, A.; Geiregat, P.; Hens, Z. PbS/CdS Core/Shell Quantum Dots by Additive, Layer-by-Layer Shell Growth. *Chem. Mater.* **2016**, *28*, 6953−6959.
(369) Hines, M. A.; Scholes, G. D. Colloidal PbS Nanocrystals with Size-Tunable Near-Infrared Emission: Observation of Post-Synthesis Self-Narrowing of the Particle Size Distribution. *Adv. Mater.* **2003**, *15*, 1844−1849.
(370) Ma, W.; Luther, J. M.; Zheng, H.; Wu, Y.; Alivisatos, A. P. Photovoltaic Devices Employing Ternary PbS_xSe_{1-x} Nanocrystals. *Nano Lett.* **2009**, *9*, 1699−1703.
(371) Akhtar, J.; Afzaal, M.; Banski, M.; Podhorodecki, A.; Syperek, M.; Misiewicz, J.; Bangert, U.; Hardman, S. J. O.; Graham, D. M.; Flavell, W. R.; et al. Controlled Synthesis of Tuned Bandgap Nanodimensional Alloys of PbSxSe1-x. *J. Am. Chem. Soc.* **2011**, *133*, 5602−5609.
(372) Smith, D. K.; Luther, J. M.; Semonin, O. E.; Nozik, A. J.; Beard, M. C. Tuning the Synthesis of Ternary Lead Chalcogenide Quantum Dots by Balancing Precursor Reactivity. *ACS Nano* **2011**, *5*, 183−190.
(373) Kojima, A.; Teshima, K.; Shirai, Y.; Miyasaka, T. Organometal Halide Perovskites as Visible-Light Sensitizers for Photovoltaic Cells. *J. Am. Chem. Soc.* **2009**, *131*, 6050−6051.
(374) Chung, I.; Lee, B.; He, J.; Chang, R. P. H.; Kanatzidis, M. G. All-Solid-State Dye-Sensitized Solar Cells with High Efficiency. *Nature* **2012**, *485*, 486−489.
(375) Kim, H.-S.; Lee, C.-R.; Im, J.-H.; Lee, K.-B.; Moehl, T.; Marchioro, A.; Moon, S.-J.; Humphry-Baker, R.; Yum, J.-H.; Moser, J. E.; et al. Lead Iodide Perovskite Sensitized All-Solid-State Submicron Thin Film Mesoscopic Solar Cell with Efficiency Exceeding 9%. *Sci. Rep.* **2012**, *2*, 591.
(376) Lee, M. M.; Teuscher, J.; Miyasaka, T.; Murakami, T. N.; Snaith, H. J. Efficient Hybrid Solar Cells Based on Meso-Superstructured Organometal Halide Perovskites. *Science* **2012**, *338*, 643−647.
(377) Tsai, H.; Nie, W.; Blancon, J.-C.; Stoumpos, C. C.; Asadpour, R.; Harutyunyan, B.; Neukirch, A. J.; Verduzco, R.; Crochet, J. J.; Tretiak, S.; et al. High-Efficiency Two-Dimensional Ruddlesden−Popper Perovskite Solar Cells. *Nature* **2016**, *536*, 312−316.
(378) Stoumpos, C. C.; Kanatzidis, M. G. Halide Perovskites: Poor Man's High-Performance Semiconductors. *Adv. Mater.* **2016**, *28*, 5778−5793.
(379) Arora, N.; Dar, M. I.; Hinderhofer, A.; Pellet, N.; Schreiber, F.; Zakeeruddin, S. M.; Grätzel, M. Perovskite Solar Cells with CuSCN Hole Extraction Layers Yield Stabilized Efficiencies Greater than 20%. *Science* **2017**, *358*, 768−771.
(380) Yang, W. S.; Park, B.-W.; Jung, E. H.; Jeon, N. J.; Kim, Y. C.; Lee, D. U.; Shin, S. S.; Seo, J.; Kim, E. K.; Noh, J. H.; et al. Iodide Management in Formamidinium-Lead-Halide−Based Perovskite Layers for Efficient Solar Cells. *Science* **2017**, *356*, 1376−1379.
(381) Tsai, H.; Asadpour, R.; Blancon, J.-C.; Stoumpos, C. C.; Durand, O.; Strzalka, J. W.; Chen, B.; Verduzco, R.; Ajayan, P. M.; Tretiak, S.; et al. Light-Induced Lattice Expansion Leads to High-Efficiency Perovskite Solar Cells. *Science* **2018**, *360*, 67−70.
(382) Lin, K.; Xing, J.; Quan, L. N.; de Arquer, F. P. G.; Gong, X.; Lu, J.; Xie, L.; Zhao, W.; Zhang, D.; Yan, C.; et al. Perovskite Light-Emitting Diodes with External Quantum Efficiency Exceeding 20 per Cent. *Nature* **2018**, *562*, 245−248.
(383) Sutherland, B. R.; Sargent, E. H. Perovskite Photonic Sources. *Nat. Photonics* **2016**, *10*, 295−302.
(384) Fang, Y.; Dong, Q.; Shao, Y.; Yuan, Y.; Huang, J. Highly Narrowband Perovskite Single-Crystal Photodetectors Enabled by Surface-Charge Recombination. *Nat. Photonics* **2015**, *9*, 679−686.
(385) Wei, H.; Fang, Y.; Mulligan, P.; Chuirazzi, W.; Fang, H.-H.; Wang, C.; Ecker, B. R.; Gao, Y.; Loi, M. A.; Cao, L.; et al. Sensitive X-Ray Detectors Made of Methylammonium Lead Tribromide Perovskite Single Crystals. *Nat. Photonics* **2016**, *10*, 333−339.

https://doi.org/10.1021/acs.chemrev.3c00097
Chem. Rev. XXXX, XXX, XXX−XXX

(386) Wei, H.; DeSantis, D.; Wei, W.; Deng, Y.; Guo, D.; Savenije, T. J.; Cao, L.; Huang, J. Dopant Compensation in Alloyed $CH_3NH_3PbBr_{3-x}Cl_x$ Perovskite Single Crystals for Gamma-Ray Spectroscopy. *Nat. Mater.* **2017**, *16*, 826−833.
(387) He, Y.; Ke, W.; Alexander, G. C. B.; McCall, K. M.; Chica, D. G.; Liu, Z.; Hadar, I.; Stoumpos, C. C.; Wessels, B. W.; Kanatzidis, M. G. Resolving the Energy of γ-Ray Photons with $MAPbI_3$ Single Crystals. *ACS Photonics* **2018**, *5*, 4132−4138.
(388) He, Y.; Matei, L.; Jung, H. J.; McCall, K. M.; Chen, M.; Stoumpos, C. C.; Liu, Z.; Peters, J. A.; Chung, D. Y.; Wessels, B. W.; et al. High Spectral Resolution of Gamma-Rays at Room Temperature by Perovskite $CsPbBr_3$ Single Crystals. *Nat. Commun.* **2018**, *9*, 1609.
(389) Zhu, H.; Fu, Y.; Meng, F.; Wu, X.; Gong, Z.; Ding, Q.; Gustafsson, M. V.; Trinh, M. T.; Jin, S.; Zhu, X.-Y. Lead Halide Perovskite Nanowire Lasers with Low Lasing Thresholds and High Quality Factors. *Nat. Mater.* **2015**, *14*, 636−642.
(390) Zhang, H.; Liao, Q.; Wu, Y.; Zhang, Z.; Gao, Q.; Liu, P.; Li, M.; Yao, J.; Fu, H. 2D Ruddlesden−Popper Perovskites Microring Laser Array. *Adv. Mater.* **2018**, *30*, 1706186.
(391) Cao, Y.; Wang, N.; Tian, H.; Guo, J.; Wei, Y.; Chen, H.; Miao, Y.; Zou, W.; Pan, K.; He, Y.; et al. Perovskite Light-Emitting Diodes Based on Spontaneously Formed Submicrometre-Scale Structures. *Nature* **2018**, *562*, 249−253.
(392) Maczka, M.ła.; Gagor, A.; Zareba, J. K.; Stefanska, D.; Drozd, M.; Balciunas, S.; Simenas, M.; Banys, J.; Sieradzki, A. Three-Dimensional Perovskite Methylhydrazinium Lead Chloride with Two Polar Phases and Unusual Second-Harmonic Generation Bistability above Room Temperature. *Chem. Mater.* **2020**, *32*, 4072−4082.
(393) Maczka, M.; Ptak, M.; Gagor, A.; Stefanska, D.; Zareba, J. K.; Sieradzki, A. Methylhydrazinium Lead Bromide: Noncentrosymmetric Three-Dimensional Perovskite with Exceptionally Large Framework Distortion and Green Photoluminescence. *Chem. Mater.* **2020**, *32*, 1667−1673.
(394) Petrosova, H. R.; Kucheriv, O. I.; Shova, S.; Gural'skiy, I. A. Aziridinium Cation Templating 3D Lead Halide Hybrid Perovskites. *Chem. Commun.* **2022**, *58*, 5745−5748.
(395) Stoumpos, C. C.; Frazer, L.; Clark, D. J.; Kim, Y. S.; Rhim, S. H.; Freeman, A. J.; Ketterson, J. B.; Jang, J. I.; Kanatzidis, M. G. Hybrid Germanium Iodide Perovskite Semiconductors: Active Lone Pairs, Structural Distortions, Direct and Indirect Energy Gaps, and Strong Nonlinear Optical Properties. *J. Am. Chem. Soc.* **2015**, *137*, 6804−6819.
(396) Weber, D. $CH_3NH_3PbX_3$, Ein Pb(II)-System Mit Kubischer Perowskitstruktur/$CH_3NH_3PbX_3$, a Pb(II)-System with Cubic Perovskite Structure. *Z. Naturforsch., B* **1978**, *33*, 1443−1445.
(397) Goldschmidt, V. M. Die Gesetze Der Krystallochemie. *Naturwissenschaften* **1926**, *14*, 477−485.
(398) Ishihara, T.; Takahashi, J.; Goto, T. Exciton State in Two-Dimensional Perovskite Semiconductor $(C_{10}H_{21}NH_3)_2PbI_4$. *Solid State Commun.* **1989**, *69*, 933−936.
(399) Tanaka, K.; Takahashi, T.; Kondo, T.; Umeda, K.; Ema, K.; Umebayashi, T.; Asai, K.; Uchida, K.; Miura, N. Electronic and Excitonic Structures of Inorganic−Organic Perovskite-Type Quantum-Well Crystal $(C_4H_9NH_3)_2PbBr_4$. *Jpn. J. Appl. Phys.* **2005**, *44*, 5923−5932.
(400) Kitazawa, N.; Aono, M.; Watanabe, Y. Excitons in Organic−Inorganic Hybrid Compounds $(C_nH_{2n+1}NH_3)_2PbBr_4$ (N = 4, 5, 7 and 12). *Thin Solid Films* **2010**, *518*, 3199−3203.
(401) Yamamoto, Y.; Oohata, G.; Mizoguchi, K.; Ichida, H.; Kanematsu, Y. Photoluminescence of Excitons and Biexcitons in $(C_4H_9NH_3)_2PbBr_4$ Crystals under High Excitation Density. *Phys. Status Solidi C* **2012**, *9*, 2501−2504.
(402) Lanty, G.; Jemli, K.; Wei, Y.; Leymarie, J.; Even, J.; Lauret, J.-S.; Deleporte, E. Room-Temperature Optical Tunability and Inhomogeneous Broadening in 2D-Layered Organic−Inorganic Perovskite Pseudobinary Alloys. *J. Phys. Chem. Lett.* **2014**, *5*, 3958−3963.
(403) Kim, Y.-H.; Cho, H.; Lee, T.-W. Metal Halide Perovskite Light Emitters. *Proc. Natl. Acad. Sci. U. S. A.* **2016**, *113*, 11694−11702.
(404) Stranks, S. D.; Eperon, G. E.; Grancini, G.; Menelaou, C.; Alcocer, M. J. P.; Leijtens, T.; Herz, L. M.; Petrozza, A.; Snaith, H. J. Electron-Hole Diffusion Lengths Exceeding 1 Micrometer in an Organometal Trihalide Perovskite Absorber. *Science* **2013**, *342*, 341−344.
(405) Oga, H.; Saeki, A.; Ogomi, Y.; Hayase, S.; Seki, S. Improved Understanding of the Electronic and Energetic Landscapes of Perovskite Solar Cells: High Local Charge Carrier Mobility, Reduced Recombination, and Extremely Shallow Traps. *J. Am. Chem. Soc.* **2014**, *136*, 13818−13825.
(406) Ponseca, C. S.; Savenije, T. J.; Abdellah, M.; Zheng, K.; Yartsev, A.; Pascher, T.; Harlang, T.; Chabera, P.; Pullerits, T.; Stepanov, A.; et al. Organometal Halide Perovskite Solar Cell Materials Rationalized: Ultrafast Charge Generation, High and Microsecond-Long Balanced Mobilities, and Slow Recombination. *J. Am. Chem. Soc.* **2014**, *136*, 5189−5192.
(407) Stoumpos, C. C.; Kanatzidis, M. G. The Renaissance of Halide Perovskites and Their Evolution as Emerging Semiconductors. *Acc. Chem. Res.* **2015**, *48*, 2791−2802.
(408) Yu, P.; Cardona, M. *Fundamentals of Semiconductors*, 4th ed.; Graduate Texts in Physics; Springer Berlin, Heidelberg, 2010.
(409) Nishi, K.; Saito, H.; Sugou, S.; Lee, J.-S. A Narrow Photoluminescence Linewidth of 21 meV at 1.35 μm from Strain-Reduced InAs Quantum Dots Covered by $In_{0.2}Ga_{0.8}As$ Grown on GaAs Substrates. *Appl. Phys. Lett.* **1999**, *74*, 1111−1113.
(410) Even, J.; Pedesseau, L.; Katan, C. Analysis of Multivalley and Multibandgap Absorption and Enhancement of Free Carriers Related to Exciton Screening in Hybrid Perovskites. *J. Phys. Chem. C* **2014**, *118*, 11566−11572.
(411) Diab, H.; Trippé-Allard, G.; Lédée, F.; Jemli, K.; Vilar, C.; Bouchez, G.; Jacques, V. L. R.; Tejeda, A.; Even, J.; Lauret, J.-S.; et al. Narrow Linewidth Excitonic Emission in Organic−Inorganic Lead Iodide Perovskite Single Crystals. *J. Phys. Chem. Lett.* **2016**, *7*, 5093−5100.
(412) Li, X.; Hoffman, J. M.; Kanatzidis, M. G. The 2D Halide Perovskite Rulebook: How the Spacer Influences Everything from the Structure to Optoelectronic Device Efficiency. *Chem. Rev.* **2021**, *121*, 2230−2291.
(413) Hanamura, E.; Nagaosa, N.; Kumagai, M.; Takagahara, T. Quantum Wells with Enhanced Exciton Effects and Optical Non-Linearity. *Mater. Sci. Eng., B* **1988**, *1*, 255−258.
(414) Muljarov, E. A.; Tikhodeev, S. G.; Gippius, N. A.; Ishihara, T. Excitons in Self-Organized Semiconductor/Insulator Superlattices: PbI-Based Perovskite Compounds. *Phys. Rev. B* **1995**, *51*, 14370−14378.
(415) Even, J.; Pedesseau, L.; Katan, C. Understanding Quantum Confinement of Charge Carriers in Layered 2D Hybrid Perovskites. *ChemPhysChem* **2014**, *15*, 3733−3741.
(416) Katan, C.; Mercier, N.; Even, J. Quantum and Dielectric Confinement Effects in Lower-Dimensional Hybrid Perovskite Semiconductors. *Chem. Rev.* **2019**, *119*, 3140−3192.
(417) Blancon, J.-C.; Even, J.; Stoumpos, C. C.; Kanatzidis, M. G.; Mohite, A. D. Semiconductor Physics of Organic−Inorganic 2D Halide Perovskites. *Nat. Nanotechnol.* **2020**, *15*, 969−985.
(418) Wang, K.; Park, J. Y.; Akriti; Dou, L. Two-Dimensional Halide Perovskite Quantum-Well Emitters: A Critical Review. *EcoMat* **2021**, *3*, No. e12104.
(419) Stoumpos, C. C.; Cao, D. H.; Clark, D. J.; Young, J.; Rondinelli, J. M.; Jang, J. I.; Hupp, J. T.; Kanatzidis, M. G. Ruddlesden−Popper Hybrid Lead Iodide Perovskite 2D Homologous Semiconductors. *Chem. Mater.* **2016**, *28*, 2852−2867.
(420) Mitzi, D. B.; Feild, C. A.; Harrison, W. T. A.; Guloy, A. M. Conducting Tin Halides with a Layered Organic-Based Perovskite Structure. *Nature* **1994**, *369*, 467−469.
(421) Saparov, B.; Mitzi, D. B. Organic−Inorganic Perovskites: Structural Versatility for Functional Materials Design. *Chem. Rev.* **2016**, *116*, 4558−4596.
(422) Zibouche, N.; Islam, M. S. Structure−Electronic Property Relationships of 2D Ruddlesden−Popper Tin- and Lead-Based Iodide Perovskites. *ACS Appl. Mater. Interfaces* **2020**, *12*, 15328−15337.

https://doi.org/10.1021/acs.chemrev.3c00097
Chem. Rev. XXXX, XXX, XXX−XXX

(423) Tu, Q.; Spanopoulos, I.; Vasileiadou, E. S.; Li, X.; Kanatzidis, M. G.; Shekhawat, G. S.; Dravid, V. P. Exploring the Factors Affecting the Mechanical Properties of 2D Hybrid Organic−Inorganic Perovskites. *ACS Appl. Mater. Interfaces* **2020**, *12*, 20440−20447.
(424) Kim, D.; Vasileiadou, E. S.; Spanopoulos, I.; Kanatzidis, M. G.; Tu, Q. In-Plane Mechanical Properties of Two-Dimensional Hybrid Organic−Inorganic Perovskite Nanosheets: Structure−Property Relationships. *ACS Appl. Mater. Interfaces* **2021**, *13*, 31642−31649.
(425) Vasileiadou, E. S.; Wang, B.; Spanopoulos, I.; Hadar, I.; Navrotsky, A.; Kanatzidis, M. G. Insight on the Stability of Thick Layers in 2D Ruddlesden−Popper and Dion−Jacobson Lead Iodide Perovskites. *J. Am. Chem. Soc.* **2021**, *143*, 2523−2536.
(426) Vasileiadou, E. S.; Hadar, I.; Kepenekian, M.; Even, J.; Tu, Q.; Malliakas, C. D.; Friedrich, D.; Spanopoulos, I.; Hoffman, J. M.; Dravid, V. P.; et al. Shedding Light on the Stability and Structure−Property Relationships of Two-Dimensional Hybrid Lead Bromide Perovskites. *Chem. Mater.* **2021**, *33*, 5085−5107.
(427) Vasileiadou, E. S.; Kanatzidis, M. G. Structure-Property Relationships and Idiosyncrasies of Bulk, 2D Hybrid Lead Bromide Perovskites. *Isr. J. Chem.* **2021**, *61*, 782−817.
(428) Hoffman, J. M.; Hadar, I.; Li, X.; Ke, W.; Vasileiadou, E. S.; Strzalka, J.; Chen, L. X.; Kanatzidis, M. G. Film Formation Mechanisms in Mixed-Dimensional 2D/3D Halide Perovskite Films Revealed by in Situ Grazing-Incidence Wide-Angle X-Ray Scattering. *Chem.* **2022**, *8*, 1067−1082.
(429) Vasileiadou, E. S.; Jiang, X.; Kepenekian, M.; Even, J.; De Siena, M. C.; Klepov, V. V.; Friedrich, D.; Spanopoulos, I.; Tu, Q.; Tajuddin, I. S.; et al. Thick-Layer Lead Iodide Perovskites with Bifunctional Organic Spacers Allylammonium and Iodopropylammonium Exhibiting Trap-State Emission. *J. Am. Chem. Soc.* **2022**, *144*, 6390−6409.
(430) Cao, D. H.; Stoumpos, C. C.; Farha, O. K.; Hupp, J. T.; Kanatzidis, M. G. 2D Homologous Perovskites as Light-Absorbing Materials for Solar Cell Applications. *J. Am. Chem. Soc.* **2015**, *137*, 7843−7850.
(431) Niu, G.; Guo, X.; Wang, L. Review of Recent Progress in Chemical Stability of Perovskite Solar Cells. *J. Mater. Chem. A* **2015**, *3*, 8970−8980.
(432) Quan, L. N.; Yuan, M.; Comin, R.; Voznyy, O.; Beauregard, E. M.; Hoogland, S.; Buin, A.; Kirmani, A. R.; Zhao, K.; Amassian, A.; et al. Ligand-Stabilized Reduced-Dimensionality Perovskites. *J. Am. Chem. Soc.* **2016**, *138*, 2649−2655.
(433) Mao, L.; Stoumpos, C. C.; Kanatzidis, M. G. Two-Dimensional Hybrid Halide Perovskites: Principles and Promises. *J. Am. Chem. Soc.* **2019**, *141*, 1171−1190.
(434) Proppe, A. H.; Quintero-Bermudez, R.; Tan, H.; Voznyy, O.; Kelley, S. O.; Sargent, E. H. Synthetic Control over Quantum Well Width Distribution and Carrier Migration in Low-Dimensional Perovskite Photovoltaics. *J. Am. Chem. Soc.* **2018**, *140*, 2890−2896.
(435) Zhao, X.; Ng, J. D. A.; Friend, R. H.; Tan, Z.-K. Opportunities and Challenges in Perovskite Light-Emitting Devices. *ACS Photonics* **2018**, *5*, 3866−3875.
(436) Spanopoulos, I.; Ke, W.; Kanatzidis, M. G. In Quest of Environmentally Stable Perovskite Solar Cells: A Perspective. *Helv. Chim. Acta* **2021**, *104*, No. e2000173.
(437) Jayanthi, K.; Spanopoulos, I.; Zibouche, N.; Voskanyan, A. A.; Vasileiadou, E. S.; Islam, M. S.; Navrotsky, A.; Kanatzidis, M. G. Entropy Stabilization Effects and Ion Migration in 3D "Hollow" Halide Perovskites. *J. Am. Chem. Soc.* **2022**, *144*, 8223−8230.
(438) Raval, P.; Kennard, R. M.; Vasileiadou, E. S.; Dahlman, C. J.; Spanopoulos, I.; Chabinyc, M. L.; Kanatzidis, M.; Manjunatha Reddy, G. N. Understanding Instability in Formamidinium Lead Halide Perovskites: Kinetics of Transformative Reactions at Grain and Subgrain Boundaries. *ACS Energy Lett.* **2022**, *7*, 1534−1543.
(439) Calabrese, J.; Jones, N. L.; Harlow, R. L.; Herron, N.; Thorn, D. L.; Wang, Y. Preparation and Characterization of Layered Lead Halide Compounds. *J. Am. Chem. Soc.* **1991**, *113*, 2328−2330.
(440) Tabuchi, Y.; Asai, K.; Rikukawa, M.; Sanui, K.; Ishigure, K. Preparation and Characterization of Natural Lower Dimensional Layered Perovskite-Type Compounds. *J. Phys. Chem. Solids* **2000**, *61*, 837−845.
(441) Yaffe, O.; Chernikov, A.; Norman, Z. M.; Zhong, Y.; Velauthapillai, A.; van der Zande, A.; Owen, J. S.; Heinz, T. F. Excitons in Ultrathin Organic-Inorganic Perovskite Crystals. *Phys. Rev. B* **2015**, *92*, 045414.
(442) Ishihara, T. Optical Properties of PbI-Based Perovskite Structures. *J. Lumin.* **1994**, *60−61*, 269−274.
(443) Nah, Y.; Solanki, D.; Dong, Y.; Röhr, J. A.; Taylor, A. D.; Hu, S.; Sargent, E. H.; Kim, D. H. Narrowing the Phase Distribution of Quasi-2D Perovskites for Stable Deep-Blue Electroluminescence. *Adv. Sci.* **2022**, *9*, 2201807.
(444) Tsai, H.; Nie, W.; Blancon, J.-C.; Stoumpos, C. C.; Soe, C. M. M.; Yoo, J.; Crochet, J.; Tretiak, S.; Even, J.; Sadhanala, A.; et al. Stable Light-Emitting Diodes Using Phase-Pure Ruddlesden−Popper Layered Perovskites. *Adv. Mater.* **2018**, *30*, 1704217.
(445) Dahlman, C. J.; DeCrescent, R. A.; Venkatesan, N. R.; Kennard, R. M.; Wu, G.; Everest, M. A.; Schuller, J. A.; Chabinyc, M. L. Controlling Solvate Intermediate Growth for Phase-Pure Organic Lead Iodide Ruddlesden−Popper $(C_4H_9NH_3)_2$ $(CH_3NH_3)_{n-1}Pb_nI_{3n+1}$ Perovskite Thin Films. *Chem. Mater.* **2019**, *31*, 5832−5844.
(446) Liang, C.; Gu, H.; Xia, Y.; Wang, Z.; Liu, X.; Xia, J.; Zuo, S.; Hu, Y.; Gao, X.; Hui, W.; et al. Two-Dimensional Ruddlesden−Popper Layered Perovskite Solar Cells Based on Phase-Pure Thin Films. *Nat. Energy* **2021**, *6*, 38−45.
(447) He, T.; Li, S.; Jiang, Y.; Qin, C.; Cui, M.; Qiao, L.; Xu, H.; Yang, J.; Long, R.; Wang, H.; et al. Reduced-Dimensional Perovskite Photovoltaics with Homogeneous Energy Landscape. *Nat. Commun.* **2020**, *11*, 1672.
(448) Zhang, L.; Sun, C.; He, T.; Jiang, Y.; Wei, J.; Huang, Y.; Yuan, M. High-Performance Quasi-2D Perovskite Light-Emitting Diodes: From Materials to Devices. *Light Sci. Appl.* **2021**, *10*, 61.
(449) Li, X.; Hoffman, J.; Ke, W.; Chen, M.; Tsai, H.; Nie, W.; Mohite, A. D.; Kepenekian, M.; Katan, C.; Even, J.; et al. Two-Dimensional Halide Perovskites Incorporating Straight Chain Symmetric Diammonium Ions, $(NH_3C_mH_{2m}NH_3)(CH_3NH_3)_{n-1}Pb_nI_{3n+1}$ (m = 4−9; n = 1−4). *J. Am. Chem. Soc.* **2018**, *140*, 12226−12238.
(450) Spanopoulos, I.; Hadar, I.; Ke, W.; Tu, Q.; Chen, M.; Tsai, H.; He, Y.; Shekhawat, G.; Dravid, V. P.; Wasielewski, M. R.; et al. Uniaxial Expansion of the 2D Ruddlesden−Popper Perovskite Family for Improved Environmental Stability. *J. Am. Chem. Soc.* **2019**, *141*, 5518−5534.
(451) Mao, L.; Ke, W.; Pedesseau, L.; Wu, Y.; Katan, C.; Even, J.; Wasielewski, M. R.; Stoumpos, C. C.; Kanatzidis, M. G. Hybrid Dion−Jacobson 2D Lead Iodide Perovskites. *J. Am. Chem. Soc.* **2018**, *140*, 3775−3783.
(452) Fu, Y.; Jiang, X.; Li, X.; Traore, B.; Spanopoulos, I.; Katan, C.; Even, J.; Kanatzidis, M. G.; Harel, E. Cation Engineering in Two-Dimensional Ruddlesden−Popper Lead Iodide Perovskites with Mixed Large A-Site Cations in the Cages. *J. Am. Chem. Soc.* **2020**, *142*, 4008−4021.
(453) Smith, M. D.; Crace, E. J.; Jaffe, A.; Karunadasa, H. I. The Diversity of Layered Halide Perovskites. *Annu. Rev. Mater. Res.* **2018**, *48*, 111−136.
(454) Smith, M. D.; Karunadasa, H. I. White-Light Emission from Layered Halide Perovskites. *Acc. Chem. Res.* **2018**, *51*, 619−627.
(455) Lu, J.; Zhou, C.; Chen, W.; Wang, X.; Jia, B.; Wen, X. Origin and Physical Effects of Edge States in Two-Dimensional Ruddlesden-Popper Perovskites. *iScience* **2022**, *25*, 104420.
(456) Yin, J.; Naphade, R.; Gutiérrez Arzaluz, L.; Brédas, J.-L.; Bakr, O. M.; Mohammed, O. F. Modulation of Broadband Emissions in Two-Dimensional ⟨100⟩-Oriented Ruddlesden−Popper Hybrid Perovskites. *ACS Energy Lett.* **2020**, *5*, 2149−2155.
(457) Cortecchia, D.; Yin, J.; Petrozza, A.; Soci, C. White Light Emission in Low-Dimensional Perovskites. *J. Mater. Chem. C* **2019**, *7*, 4956−4969.
(458) Bidikoudi, M.; Fresta, E.; Costa, R. D. White Perovskite Based Lighting Devices. *Chem. Commun.* **2018**, *54*, 8150−8169.

https://doi.org/10.1021/acs.chemrev.3c00097
Chem. Rev. XXXX, XXX, XXX−XXX

(459) Zhang, Y.; Liu, J.; Wang, Z.; Xue, Y.; Ou, Q.; Polavarapu, L.; Zheng, J.; Qi, X.; Bao, Q. Synthesis, Properties, and Optical Applications of Low-Dimensional Perovskites. *Chem. Commun.* **2016**, *52*, 13637−13655.
(460) Zhou, G.; Su, B.; Huang, J.; Zhang, Q.; Xia, Z. Broad-Band Emission in Metal Halide Perovskites: Mechanism, Materials, and Applications. *Mater. Sci. Eng. R Rep.* **2020**, *141*, 100548.
(461) Smith, M. D.; Jaffe, A.; Dohner, E. R.; Lindenberg, A. M.; Karunadasa, H. I. Structural Origins of Broadband Emission from Layered Pb−Br Hybrid Perovskites. *Chem. Sci.* **2017**, *8*, 4497−4504.
(462) Smith, M. D.; Connor, B. A.; Karunadasa, H. I. Tuning the Luminescence of Layered Halide Perovskites. *Chem. Rev.* **2019**, *119*, 3104−3139.
(463) Williams, R. T.; Song, K. S. The Self-Trapped Exciton. *J. Phys. Chem. Solids* **1990**, *51*, 679−716.
(464) Toyozawa, Y. Self-Trapping of an Electron by the Acoustical Mode of Lattice Vibration. I: *Prog. Theor. Phys.* **1961**, *26*, 29−44.
(465) Dohner, E. R.; Hoke, E. T.; Karunadasa, H. I. Self-Assembly of Broadband White-Light Emitters. *J. Am. Chem. Soc.* **2014**, *136*, 1718−1721.
(466) Hu, T.; Smith, M. D.; Dohner, E. R.; Sher, M.-J.; Wu, X.; Trinh, M. T.; Fisher, A.; Corbett, J.; Zhu, X.-Y.; Karunadasa, H. I.; et al. Mechanism for Broadband White-Light Emission from Two-Dimensional (110) Hybrid Perovskites. *J. Phys. Chem. Lett.* **2016**, *7*, 2258−2263.
(467) Paritmongkol, W.; Powers, E. R.; Dahod, N. S.; Tisdale, W. A. Two Origins of Broadband Emission in Multilayered 2D Lead Iodide Perovskites. *J. Phys. Chem. Lett.* **2020**, *11*, 8565−8572.
(468) Kahmann, S.; Tekelenburg, E. K.; Duim, H.; Kamminga, M. E.; Loi, M. A. Extrinsic Nature of the Broad Photoluminescence in Lead Iodide-Based Ruddlesden−Popper Perovskites. *Nat. Commun.* **2020**, *11*, 2344.
(469) Dhanabalan, B.; Pothuraju, R. D.; Marras, S.; Pasquale, L.; Manna, L.; Krahne, R.; Arciniegas, M. P. Reversible Emission Tunability from 2D-Layered Perovskites with Conjugated Organic Cations. *Adv. Photonics Res.* **2021**, *2*, 2100005.
(470) Li, Y.; Ji, C.; Li, L.; Wang, S.; Han, S.; Peng, Y.; Zhang, S.; Luo, J. (γ-Methoxy Propyl Amine)$_2$PbBr$_4$: A Novel Two-Dimensional Halide Hybrid Perovskite with Efficient Bluish White-Light Emission. *Inorg. Chem. Front.* **2021**, *8*, 2119−2124.
(471) Guo, Y.-Y.; Yang, L.-J.; Biberger, S.; McNulty, J. A.; Li, T.; Schötz, K.; Panzer, F.; Lightfoot, P. Structural Diversity in Layered Hybrid Perovskites, A_2PbBr_4 or $AA'PbBr_4$, Templated by Small Disc-Shaped Amines. *Inorg. Chem.* **2020**, *59*, 12858−12866.
(472) Guo, Y.-Y.; McNulty, J. A.; Mica, N. A.; Samuel, I. D. W.; Slawin, A. M. Z.; Bühl, M.; Lightfoot, P. Structure-Directing Effects in (110)-Layered Hybrid Perovskites Containing Two Distinct Organic Moieties. *Chem. Commun.* **2019**, *55*, 9935−9938.
(473) Li, Y. Y.; Lin, C. K.; Zheng, G. L.; Cheng, Z. Y.; You, H.; Wang, W. D.; Lin, J. Novel ⟨110⟩-Oriented Organic-Inorganic Perovskite Compound Stabilized by N-(3-Aminopropyl) Imidazole with Improved Optical Properties. *Chem. Mater.* **2006**, *18*, 3463−3469.
(474) Dohner, E. R.; Jaffe, A.; Bradshaw, L. R.; Karunadasa, H. I. Intrinsic White-Light Emission from Layered Hybrid Perovskites. *J. Am. Chem. Soc.* **2014**, *136*, 13154−13157.
(475) Yangui, A.; Garrot, D.; Lauret, J. S.; Lusson, A.; Bouchez, G.; Deleporte, E.; Pillet, S.; Bendeif, E. E.; Castro, M.; Triki, S.; et al. Optical Investigation of Broadband White-Light Emission in Self-Assembled Organic−Inorganic Perovskite $(C_6H_{11}NH_3)_2PbBr_4$. *J. Phys. Chem. C* **2015**, *119*, 23638−23647.
(476) Hu, H.; Morris, S. A.; Qiao, X.; Zhao, D.; Salim, T.; Chen, B.; Chia, E. E. M.; Lam, Y. M. Molecular Engineering of Two-Dimensional Hybrid Perovskites with Broadband Emission for White Light-Emitting Diodes. *J. Mater. Chem. C* **2018**, *6*, 10301−10307.
(477) Neogi, I.; Bruno, A.; Bahulayan, D.; Goh, T. W.; Ghosh, B.; Ganguly, R.; Cortecchia, D.; Sum, T. C.; Soci, C.; Mathews, N.; et al. Broadband-Emitting 2 D Hybrid Organic−Inorganic Perovskite Based on Cyclohexane-Bis(Methylamonium) Cation. *ChemSusChem* **2017**, *10*, 3765−3772.
(478) Wang, S.; Yao, Y.; Kong, J.; Zhao, S.; Sun, Z.; Wu, Z.; Li, L.; Luo, J. Highly Efficient White-Light Emission in a Polar Two-Dimensional Hybrid Perovskite. *Chem. Commun.* **2018**, *54*, 4053−4056.
(479) Febriansyah, B.; Giovanni, D.; Ramesh, S.; Koh, T. M.; Li, Y.; Sum, T. C.; Mathews, N.; England, J. Inducing Formation of a Corrugated, White-Light Emitting 2D Lead-Bromide Perovskite via Subtle Changes in Templating Cation. *J. Mater. Chem. C* **2020**, *8*, 889−893.
(480) Li, Y.; Zheng, G.; Lin, J. Synthesis, Structure, and Optical Properties of a Contorted < 110>-Oriented Layered Hybrid Perovskite: $C_3H_{11}SN_3PbBr_4$. *Eur. J. Inorg. Chem.* **2008**, *2008*, 1689−1692.
(481) Mao, L.; Guo, P.; Kepenekian, M.; Hadar, I.; Katan, C.; Even, J.; Schaller, R. D.; Stoumpos, C. C.; Kanatzidis, M. G. Structural Diversity in White-Light-Emitting Hybrid Lead Bromide Perovskites. *J. Am. Chem. Soc.* **2018**, *140*, 13078−13088.
(482) Deng, C.; Zhou, G.; Chen, D.; Zhao, J.; Wang, Y.; Liu, Q. Broadband Photoluminescence in 2D Organic−Inorganic Hybrid Perovskites: $(C_7H_{18}N_2)$ $PbBr_4$ and $(C_9H_{22}N_2)PbBr_4$. *J. Phys. Chem. Lett.* **2020**, *11*, 2934−2940.
(483) Salah, M. B. H.; Mercier, N.; Allain, M.; Zouari, N.; Giovanella, U.; Botta, C. Mechanochromic and Electroluminescence Properties of a Layered Hybrid Perovskite Belonging to the < 110> Series. *Eur. J. Inorg. Chem.* **2019**, *2019*, 4527−4531.
(484) Koegel, A. A.; Mozur, E. M.; Oswald, I. W. H.; Jalarvo, N. H.; Prisk, T. R.; Tyagi, M.; Neilson, J. R. Correlating Broadband Photoluminescence with Structural Dynamics in Layered Hybrid Halide Perovskites. *J. Am. Chem. Soc.* **2022**, *144*, 1313−1322.
(485) Haris, M. P. U.; Bakthavatsalam, R.; Shaikh, S.; Kore, B. P.; Moghe, D.; Gonnade, R. G.; Sarma, D. D.; Kabra, D.; Kundu, J. Synthetic Control on Structure/Dimensionality and Photophysical Properties of Low Dimensional Organic Lead Bromide Perovskite. *Inorg. Chem.* **2018**, *57*, 13443−13452.
(486) Li, X.; Guo, P.; Kepenekian, M.; Hadar, I.; Katan, C.; Even, J.; Stoumpos, C. C.; Schaller, R. D.; Kanatzidis, M. G. Small Cyclic Diammonium Cation Templated (110)-Oriented 2D Halide (X = I, Br, Cl) Perovskites with White-Light Emission. *Chem. Mater.* **2019**, *31*, 3582−3590.
(487) Fateev, S. A.; Petrov, A. A.; Marchenko, E. I.; Zubavichus, Y. V.; Khrustalev, V. N.; Petrov, A. V.; Aksenov, S. M.; Goodilin, E. A.; Tarasov, A. B. FA_2PbBr_4: Synthesis, Structure, and Unusual Optical Properties of Two Polymorphs of Formamidinium-Based Layered (110) Hybrid Perovskite. *Chem. Mater.* **2021**, *33*, 1900−1907.
(488) Mao, L.; Wu, Y.; Stoumpos, C. C.; Wasielewski, M. R.; Kanatzidis, M. G. White-Light Emission and Structural Distortion in New Corrugated Two-Dimensional Lead Bromide Perovskites. *J. Am. Chem. Soc.* **2017**, *139*, 5210−5215.
(489) Mao, L.; Wu, Y.; Stoumpos, C. C.; Traore, B.; Katan, C.; Even, J.; Wasielewski, M. R.; Kanatzidis, M. G. Tunable White-Light Emission in Single-Cation-Templated Three-Layered 2D Perovskites $(CH_3CH_2NH_3)_4Pb_3Br_{10-x}Cl_x$. *J. Am. Chem. Soc.* **2017**, *139*, 11956−11963.
(490) Cortecchia, D.; Yin, J.; Bruno, A.; Lo, S.-Z. A.; Gurzadyan, G. G.; Mhaisalkar, S.; Brédas, J.-L.; Soci, C. Polaron Self-Localization in White-Light Emitting Hybrid Perovskites. *J. Mater. Chem. C* **2017**, *5*, 2771−2780.
(491) Booker, E. P.; Thomas, T. H.; Quarti, C.; Stanton, M. R.; Dashwood, C. D.; Gillett, A. J.; Richter, J. M.; Pearson, A. J.; Davis, N. J. L. K.; Sirringhaus, H.; et al. Formation of Long-Lived Color Centers for Broadband Visible Light Emission in Low-Dimensional Layered Perovskites. *J. Am. Chem. Soc.* **2017**, *139*, 18632−18639.
(492) Cortecchia, D.; Neutzner, S.; Srimath Kandada, A. R.; Mosconi, E.; Meggiolaro, D.; De Angelis, F.; Soci, C.; Petrozza, A. Broadband Emission in Two-Dimensional Hybrid Perovskites: The Role of Structural Deformation. *J. Am. Chem. Soc.* **2017**, *139*, 39−42.
(493) Yuan, Y.; Liu, X.-F.; Ma, X.; Wang, X.; Li, X.; Xiao, J.; Li, X.; Zhang, H.-L.; Wang, L. Large Band Gap Narrowing and Prolonged Carrier Lifetime of $(C_4H_9NH_3)_2PbI_4$ under High Pressure. *Adv. Sci.* **2019**, *6*, 1900240.

https://doi.org/10.1021/acs.chemrev.3c00097
Chem. Rev. XXXX, XXX, XXX−XXX

(494) Billing, D. G.; Lemmerer, A. Synthesis, Characterization and Phase Transitions in the Inorganic−Organic Layered Perovskite-Type Hybrids $[(C_nH_{2n+1}NH_3)_2PbI_4]$, It n = 4, 5 and 6. *Acta Crystallogr. Sect. B* **2007**, *63*, 735−747.
(495) Li, X.; Fu, Y.; Pedesseau, L.; Guo, P.; Cuthriell, S.; Hadar, I.; Even, J.; Katan, C.; Stoumpos, C. C.; Schaller, R. D.; et al. Negative Pressure Engineering with Large Cage Cations in 2D Halide Perovskites Causes Lattice Softening. *J. Am. Chem. Soc.* **2020**, *142*, 11486−11496.
(496) Fu, Y.; Hautzinger, M. P.; Luo, Z.; Wang, F.; Pan, D.; Aristov, M. M.; Guzei, I. A.; Pan, A.; Zhu, X.; Jin, S. Incorporating Large A Cations into Lead Iodide Perovskite Cages: Relaxed Goldschmidt Tolerance Factor and Impact on Exciton−Phonon Interaction. *ACS Cent. Sci.* **2019**, *5*, 1377−1386.
(497) Stoumpos, C. C.; Soe, C. M. M.; Tsai, H.; Nie, W.; Blancon, J.-C.; Cao, D. H.; Liu, F.; Traoré, B.; Katan, C.; Even, J.; et al. High Members of the 2D Ruddlesden-Popper Halide Perovskites: Synthesis, Optical Properties, and Solar Cells of $(CH_3(CH_2)_3NH_3)_2(CH_3NH_3)_4Pb_5I_{16}$. *Chem.* **2017**, *2*, 427−440.
(498) Soe, C. M. M.; Nagabhushana, G. P.; Shivaramaiah, R.; Tsai, H.; Nie, W.; Blancon, J.-C.; Melkonyan, F.; Cao, D. H.; Traoré, B.; Pedesseau, L.; et al. Structural and Thermodynamic Limits of Layer Thickness in 2D Halide Perovskites. *Proc. Natl. Acad. Sci. U. S. A.* **2019**, *116*, 58−66.
(499) Li, X.; Ke, W.; Traoré, B.; Guo, P.; Hadar, I.; Kepenekian, M.; Even, J.; Katan, C.; Stoumpos, C. C.; Schaller, R. D.; et al. Two-Dimensional Dion−Jacobson Hybrid Lead Iodide Perovskites with Aromatic Diammonium Cations. *J. Am. Chem. Soc.* **2019**, *141*, 12880−12890.
(500) Gao, L.; Li, X.; Traoré, B.; Zhang, Y.; Fang, J.; Han, Y.; Even, J.; Katan, C.; Zhao, K.; Liu, S.; et al. M-Phenylenediammonium as a New Spacer for Dion−Jacobson Two-Dimensional Perovskites. *J. Am. Chem. Soc.* **2021**, *143*, 12063−12073.
(501) Mao, L.; Guo, P.; Kepenekian, M.; Spanopoulos, I.; He, Y.; Katan, C.; Even, J.; Schaller, R. D.; Seshadri, R.; Stoumpos, C. C.; et al. Organic Cation Alloying on Intralayer A and Interlayer A' Sites in 2D Hybrid Dion−Jacobson Lead Bromide Perovskites $(A')(A)Pb_2Br_7$. *J. Am. Chem. Soc.* **2020**, *142*, 8342−8351.
(502) Shamsi, J.; Urban, A. S.; Imran, M.; De Trizio, L.; Manna, L. Metal Halide Perovskite Nanocrystals: Synthesis, Post-Synthesis Modifications, and Their Optical Properties. *Chem. Rev.* **2019**, *119*, 3296−3348.
(503) Haydous, F.; Gardner, J. M.; Cappel, U. B. The Impact of Ligands on the Synthesis and Application of Metal Halide Perovskite Nanocrystals. *J. Mater. Chem. A* **2021**, *9*, 23419−23443.
(504) De Trizio, L.; Infante, I.; Abdelhady, A. L.; Brovelli, S.; Manna, L. Guidelines for the Characterization of Metal Halide Nanocrystals. *Trends Chem.* **2021**, *3*, 631−644.
(505) Wang, Y.; Zhao, H.; Piotrowski, M.; Han, X.; Ge, Z.; Dong, L.; Wang, C.; Pinisetty, S. K.; Balguri, P. K.; Bandela, A. K.; et al. Cesium Lead Iodide Perovskites: Optically Active Crystal Phase Stability to Surface Engineering. *Micromachines* **2022**, *13*, 1318.
(506) Wei, Y.; Cheng, Z.; Lin, J. An Overview on Enhancing the Stability of Lead Halide Perovskite Quantum Dots and Their Applications in Phosphor-Converted LEDs. *Chem. Soc. Rev.* **2019**, *48*, 310−350.
(507) Seth, S.; Ahmed, T.; De, A.; Samanta, A. Tackling the Defects, Stability, and Photoluminescence of $CsPbX_3$ Perovskite Nanocrystals. *ACS Energy Lett.* **2019**, *4*, 1610−1618.
(508) Wu, Y.; Li, X.; Zeng, H. Highly Luminescent and Stable Halide Perovskite Nanocrystals. *ACS Energy Lett.* **2019**, *4*, 673−681.
(509) Zhang, X.; Li, L.; Sun, Z.; Luo, J. Rational Chemical Doping of Metal Halide Perovskites. *Chem. Soc. Rev.* **2019**, *48*, 517−539.
(510) Bera, S.; Pradhan, N. Perovskite Nanocrystal Heterostructures: Synthesis, Optical Properties, and Applications. *ACS Energy Lett.* **2020**, *5*, 2858−2872.
(511) Ahmed, G. H.; Yin, J.; Bakr, O. M.; Mohammed, O. F. Successes and Challenges of Core/Shell Lead Halide Perovskite Nanocrystals. *ACS Energy Lett.* **2021**, *6*, 1340−1357.
(512) Yang, Z.; Peng, S.; Lin, F.; Wang, P.; Xing, G.; Yu, L. Self-assembly Behavior of Metal Halide Perovskite Nanocrystals. *Chin. J. Chem.* **2022**, *40*, 2239−2248.
(513) Pham, T. T.; Lee, H.; Lee, J.; Chung, W. J. Perovskite Nanocrystal-Embedded Glasses for Photonic Applications. *J. Korean Ceram. Soc.* **2022**, *59*, 749.
(514) Dong, Y.; Zhao, Y.; Zhang, S.; Dai, Y.; Liu, L.; Li, Y.; Chen, Q. Recent Advances toward Practical Use of Halide Perovskite Nanocrystals. *J. Mater. Chem. A* **2018**, *6*, 21729−21746.
(515) Yan, F.; Tan, S. T.; Li, X.; Demir, H. V. Light Generation in Lead Halide Perovskite Nanocrystals: LEDs, Color Converters, Lasers, and Other Applications. *Small* **2019**, *15*, 1902079.
(516) Chen, H.; Li, Y.; Zhao, B.; Ming, J.; Xue, D. Nanocrystals of Metal Halide Perovskites and Their Analogues as Scintillators for X-Ray Detection. *Nano Futur.* **2022**, *6*, 012001.
(517) Que, M.; Zhu, L.; Guo, Y.; Que, W.; Yun, S. Toward Perovskite Nanocrystalline Solar Cells: Progress and Potential. *J. Mater. Chem. C* **2020**, *8*, 5321−5334.
(518) Chiba, T. Recent Advances in Solution-Processed Organic and Perovskite Nanocrystal Light-Emitting Devices. *Polym. J.* **2022**, *54*, 969−976.
(519) Hao, J.; Xiao, X. Recent Development of Optoelectronic Application Based on Metal Halide Perovskite Nanocrystals. *Front. Chem.* **2022**, *9*, 822106.
(520) Wu, Y.; Jia, R.; Xu, J.; Song, L.; Liu, Y.; Zhang, Y.; Ullah, S.; Dai, J. Strategies of Improving $CsPbX_3$ Perovskite Quantum Dots Optical Performance. *Front. Mater.* **2022**, *9*. DOI: 10.3389/fmats.2022.845977.
(521) Ghosh, S.; Pradhan, B. Lead-Free Metal Halide Perovskite Nanocrystals: Challenges, Applications, and Future Aspects. *ChemNanoMat* **2019**, *5*, 300−312.
(522) DuBose, J. T.; Kamat, P. V. Energy *Versus* Electron Transfer: Managing Excited-State Interactions in Perovskite Nanocrystal−Molecular Hybrids: Focus Review. *Chem. Rev.* **2022**, *122*, 12475−12494.
(523) Kaur, G.; Ghosh, H. N. Hot Carrier Relaxation in $CsPbBr_3$ -Based Perovskites: A Polaron Perspective. *J. Phys. Chem. Lett.* **2020**, *11*, 8765−8776.
(524) Polavarapu, L.; Zhang, Q.; Krahne, R. Nanoscale & Nanoscale Advances Joint Themed Collection on Halide Perovskite Nanocrystals. *Nanoscale* **2019**, *11*, 8648−8650.
(525) Dey, A.; Ye, J.; De, A.; Debroye, E.; Ha, S. K.; Bladt, E.; Kshirsagar, A. S.; Wang, Z.; Yin, J.; Wang, Y.; et al. State of the Art and Prospects for Halide Perovskite Nanocrystals. *ACS Nano* **2021**, *15*, 10775−10981.
(526) Zhang, X.; Quan, Z.; Yang, J.; Yang, P.; Lian, H.; Lin, J. Solvothermal Synthesis of Well-Dispersed $NaMgF_3$ Nanocrystals and Their Optical Properties. *J. Colloid Interface Sci.* **2009**, *329*, 103−106.
(527) Schmidt, L. C.; Pertegas, A.; Gonzalez-Carrero, S.; Malinkiewicz, O.; Agouram, S.; Minguez Espallargas, G.; Bolink, H. J.; Galian, R. E.; Perez-Prieto, J. Nontemplate Synthesis of $CH_3NH_3PbBr_3$ Perovskite Nanoparticles. *J. Am. Chem. Soc.* **2014**, *136*, 850−853.
(528) Protesescu, L.; Yakunin, S.; Bodnarchuk, M. I.; Bertolotti, F.; Masciocchi, N.; Guagliardi, A.; Kovalenko, M. V. Monodisperse Formamidinium Lead Bromide Nanocrystals with Bright and Stable Green Photoluminescence. *J. Am. Chem. Soc.* **2016**, *138*, 14202−14205.
(529) Protesescu, L.; Yakunin, S.; Bodnarchuk, M. I.; Krieg, F.; Caputo, R.; Hendon, C. H.; Yang, R. X.; Walsh, A.; Kovalenko, M. V. Nanocrystals of Cesium Lead Halide Perovskites ($CsPbX_3$, X = Cl, Br, and I): Novel Optoelectronic Materials Showing Bright Emission with Wide Color Gamut. *Nano Lett.* **2015**, *15*, 3692−3696.
(530) Zhang, F.; Zhong, H.; Chen, C.; Wu, X.; Hu, X.; Huang, H.; Han, J.; Zou, B.; Dong, Y. Brightly Luminescent and Color-Tunable Colloidal $CH_3NH_3PbX_3$ (X = Br, I, Cl) Quantum Dots: Potential Alternatives for Display Technology. *ACS Nano* **2015**, *9*, 4533−4542.
(531) Li, X.; Wu, Y.; Zhang, S.; Cai, B.; Gu, Y.; Song, J.; Zeng, H. CsPbX3 Quantum Dots for Lighting and Displays: Room-Temperature

Synthesis, Photoluminescence Superiorities, Underlying Origins and White Light-Emitting Diodes. *Adv. Funct. Mater.* **2016**, *26*, 2435−2445.
(532) Akkerman, Q. A.; Nguyen, T. P. T.; Boehme, S. C.; Montanarella, F.; Dirin, D. N.; Wechsler, P.; Beiglböck, F.; Rainò, G.; Erni, R.; Katan, C. Controlling the Nucleation and Growth Kinetics of Lead Halide Perovskite Quantum Dots. *Science* **2022**, *377*, 1406.
(533) Longo, G.; Pertegás, A.; Martínez-Sarti, L.; Sessolo, M.; Bolink, H. J. Highly Luminescent Perovskite−Aluminum Oxide Composites. *J. Mater. Chem. C* **2015**, *3*, 11286−11289.
(534) Dirin, D. N.; Protesescu, L.; Trummer, D.; Kochetygov, I. V.; Yakunin, S.; Krumeich, F.; Stadie, N. P.; Kovalenko, M. V. Harnessing Defect-Tolerance at the Nanoscale: Highly Luminescent Lead Halide Perovskite Nanocrystals in Mesoporous Silica Matrixes. *Nano Lett.* **2016**, *16*, 5866−5874.
(535) Zhao, Q.; Hazarika, A.; Schelhas, L. T.; Liu, J.; Gaulding, E. A.; Li, G.; Zhang, M.; Toney, M. F.; Sercel, P. C.; Luther, J. M. Size-Dependent Lattice Structure and Confinement Properties in $CsPbI_3$ Perovskite Nanocrystals: Negative Surface Energy for Stabilization. *ACS Energy Lett.* **2020**, *5*, 238−247.
(536) Nedelcu, G.; Protesescu, L.; Yakunin, S.; Bodnarchuk, M. I.; Grotevent, M. J.; Kovalenko, M. V. Fast Anion-Exchange in Highly Luminescent Nanocrystals of Cesium Lead Halide Perovskites ($CsPbX_3$, X = Cl, Br, I). *Nano Lett.* **2015**, *15*, 5635−5640.
(537) Akkerman, Q. A.; D'Innocenzo, V.; Accornero, S.; Scarpellini, A.; Petrozza, A.; Prato, M.; Manna, L. Tuning the Optical Properties of Cesium Lead Halide Perovskite Nanocrystals by Anion Exchange Reactions. *J. Am. Chem. Soc.* **2015**, *137*, 10276−10281.
(538) Swarnkar, A.; Chulliyil, R.; Ravi, V. K.; Irfanullah, M.; Chowdhury, A.; Nag, A. Colloidal $CsPbBr_3$ Perovskite Nanocrystals: Luminescence beyond Traditional Quantum Dots. *Angew. Chem.-Int. Ed.* **2015**, *54*, 15424−15428.
(539) Vashishtha, P.; Halpert, J. E. Field-Driven Ion Migration and Color Instability in Red-Emitting Mixed Halide Perovskite Nanocrystal Light-Emitting Diodes. *Chem. Mater.* **2017**, *29*, 5965−5973.
(540) Zhang, H.; Fu, X.; Tang, Y.; Wang, H.; Zhang, C.; Yu, W. W.; Wang, X.; Zhang, Y.; Xiao, M. Phase Segregation Due to Ion Migration in All-Inorganic Mixed-Halide Perovskite Nanocrystals. *Nat. Commun.* **2019**, *10*, 1088.
(541) Hassan, Y.; Park, J. H.; Crawford, M. L.; Sadhanala, A.; Lee, J.; Sadighian, J. C.; Mosconi, E.; Shivanna, R.; Radicchi, E.; Jeong, M.; et al. Ligand-Engineered Bandgap Stability in Mixed-Halide Perovskite LEDs. *Nature* **2021**, *591*, 72−77.
(542) Swarnkar, A.; Mir, W. J.; Nag, A. Can B-Site Doping or Alloying Improve Thermal- and Phase-Stability of All-Inorganic $CsPbX_3$ (X = Cl, Br, I) Perovskites? *ACS Energy Lett.* **2018**, *3*, 286−289.
(543) Krieg, F.; Ochsenbein, S. T.; Yakunin, S.; ten Brinck, S.; Aellen, P.; Süess, A.; Clerc, B.; Guggisberg, D.; Nazarenko, O.; Shynkarenko, Y.; et al. Colloidal $CsPbX_3$ (X = Cl, Br, I) Nanocrystals 2.0: Zwitterionic Capping Ligands for Improved Durability and Stability. *ACS Energy Lett.* **2018**, *3*, 641−646.
(544) Bohn, B. J.; Tong, Y.; Gramlich, M.; Lai, M. L.; Döblinger, M.; Wang, K.; Hoye, R. L. Z.; Müller-Buschbaum, P.; Stranks, S. D.; Urban, A. S.; et al. Boosting Tunable Blue Luminescence of Halide Perovskite Nanoplatelets through Postsynthetic Surface Trap Repair. *Nano Lett.* **2018**, *18*, 5231−5238.
(545) Nenon, D. P.; Pressler, K.; Kang, J.; Koscher, B. A.; Olshansky, J. H.; Osowiecki, W. T.; Koc, M. A.; Wang, L.-W.; Alivisatos, A. P. Design Principles for Trap-Free $CsPbX_3$ Nanocrystals: Enumerating and Eliminating Surface Halide Vacancies with Softer Lewis Bases. *J. Am. Chem. Soc.* **2018**, *140*, 17760−17772.
(546) Koscher, B. A.; Swabeck, J. K.; Bronstein, N. D.; Alivisatos, A. P. Essentially Trap-Free $CsPbBr_3$ Colloidal Nanocrystals by Postsynthetic Thiocyanate Surface Treatment. *J. Am. Chem. Soc.* **2017**, *139*, 6566−6569.
(547) Yong, Z.-J.; Guo, S.-Q.; Ma, J.-P.; Zhang, J.-Y.; Li, Z.-Y.; Chen, Y.-M.; Zhang, B.-B.; Zhou, Y.; Shu, J.; Gu, J.-L.; et al. Doping-Enhanced Short-Range Order of Perovskite Nanocrystals for Near-Unity Violet Luminescence Quantum Yield. *J. Am. Chem. Soc.* **2018**, *140*, 9942−9951.
(548) Jellicoe, T. C.; Richter, J. M.; Glass, H. F. J.; Tabachnyk, M.; Brady, R.; Dutton, S. E.; Rao, A.; Friend, R. H.; Credgington, D.; Greenham, N. C.; et al. Synthesis and Optical Properties of Lead-Free Cesium Tin Halide Perovskite Nanocrystals. *J. Am. Chem. Soc.* **2016**, *138*, 2941−2944.
(549) Swarnkar, A.; Ravi, V. K.; Nag, A. Beyond Colloidal Cesium Lead Halide Perovskite Nanocrystals: Analogous Metal Halides and Doping. *ACS Energy Lett.* **2017**, *2*, 1089−1098.
(550) Liu, F.; Zhang, Y.; Ding, C.; Kobayashi, S.; Izuishi, T.; Nakazawa, N.; Toyoda, T.; Ohta, T.; Hayase, S.; Minemoto, T.; et al. Highly Luminescent Phase-Stable $CsPbI_3$ Perovskite Quantum Dots Achieving Near 100% Absolute Photoluminescence Quantum Yield. *ACS Nano* **2017**, *11*, 10373−10383.
(551) Protesescu, L.; Yakunin, S.; Kumar, S.; Bär, J.; Bertolotti, F.; Masciocchi, N.; Guagliardi, A.; Grotevent, M.; Shorubalko, I.; Bodnarchuk, M. I.; et al. Dismantling the "Red Wall" of Colloidal Perovskites: Highly Luminescent Formamidinium and Formamidinium−Cesium Lead Iodide Nanocrystals. *ACS Nano* **2017**, *11*, 3119−3134.
(552) Leng, M.; Yang, Y.; Zeng, K.; Chen, Z.; Tan, Z.; Li, S.; Li, J.; Xu, B.; Li, D.; Hautzinger, M. P.; et al. All-Inorganic Bismuth-Based Perovskite Quantum Dots with Bright Blue Photoluminescence and Excellent Stability. *Adv. Funct. Mater.* **2018**, *28*, 1704446.
(553) Leng, M.; Chen, Z.; Yang, Y.; Li, Z.; Zeng, K.; Li, K.; Niu, G.; He, Y.; Zhou, Q.; Tang, J. Lead-Free, Blue Emitting Bismuth Halide Perovskite Quantum Dots. *Angew. Chem., Int. Ed.* **2016**, *55*, 15012−15016.
(554) Li, M.; Zhang, X.; Matras-Postolek, K.; Chen, H.-S.; Yang, P. An Anion-Driven Sn2+ Exchange Reaction in $CsPbBr_3$ Nanocrystals towards Tunable and High Photoluminescence. *J. Mater. Chem. C* **2018**, *6*, 5506−5513.
(555) Vigil, J. A.; Hazarika, A.; Luther, J. M.; Toney, M. F. $FA_xCs_{1-x}PbI_3$ Nanocrystals: Tuning Crystal Symmetry by A-Site Cation Composition. *ACS Energy Lett.* **2020**, *5*, 2475−2482.
(556) Liu, L.; Zhao, R.; Xiao, C.; Zhang, F.; Pevere, F.; Shi, K.; Huang, H.; Zhong, H.; Sychugov, I. Size-Dependent Phase Transition in Perovskite Nanocrystals. *J. Phys. Chem. Lett.* **2019**, *10*, 5451−5457.
(557) Bertolotti, F.; Protesescu, L.; Kovalenko, M. V.; Yakunin, S.; Cervellino, A.; Billinge, S. J. L.; Terban, M. W.; Pedersen, J. S.; Masciocchi, N.; Guagliardi, A. Coherent Nanotwins and Dynamic Disorder in Cesium Lead Halide Perovskite Nanocrystals. *ACS Nano* **2017**, *11*, 3819−3831.
(558) Lanigan-Atkins, T.; He, X.; Krogstad, M. J.; Pajerowski, D. M.; Abernathy, D. L.; Xu, G. N. M. N.; Xu, Z.; Chung, D.-Y.; Kanatzidis, M. G.; Rosenkranz, S.; et al. Two-Dimensional Overdamped Fluctuations of the Soft Perovskite Lattice in $CsPbBr_3$. *Nat. Mater.* **2021**, *20*, 977−983.
(559) Weadock, N. J.; Sterling, T. C.; Vigil, J. A.; Gold-Parker, A.; Smith, I. C.; Ahammed, B.; Krogstad, M. J.; Ye, F.; Voneshen, D.; Gehring, P. M.; et al. The Nature of Dynamic Local Order in $CH_3NH_3PbI_3$ and $CH_3NH_3PbBr_3$. *Joule* **2023**, DOI: 10.1016/j.joule.2023.03.017.
(560) Rainò, G.; Kovalenko, M. V. Locking Exciton Fine-Structure Splitting. *Nat. Mater.* **2022**, *21*, 1219.
(561) Swarnkar, A.; Marshall, A. R.; Sanehira, E. M.; Chernomordik, B. D.; Moore, D. T.; Christians, J. A.; Chakrabarti, T.; Luther, J. M. Quantum Dot−Induced Phase Stabilization of α-$CsPbI_3$ Perovskite for High-Efficiency Photovoltaics. *Science* **2016**, *354*, 92−95.
(562) Hu, F.; Zhang, H.; Sun, C.; Yin, C.; Lv, B.; Zhang, C.; Yu, W. W.; Wang, X.; Zhang, Y.; Xiao, M. Superior Optical Properties of Perovskite Nanocrystals as Single Photon Emitters. *ACS Nano* **2015**, *9*, 12410−12416.
(563) Rainò, G.; Nedelcu, G.; Protesescu, L.; Bodnarchuk, M. I.; Kovalenko, M. V.; Mahrt, R. F.; Stöferle, T. Single Cesium Lead Halide Perovskite Nanocrystals at Low Temperature: Fast Single-Photon Emission, Reduced Blinking, and Exciton Fine Structure. *ACS Nano* **2016**, *10*, 2485−2490.
(564) Makarov, N. S.; Guo, S.; Isaienko, O.; Liu, W.; Robel, I.; Klimov, V. I. Spectral and Dynamical Properties of Single Excitons, Biexcitons,

https://doi.org/10.1021/acs.chemrev.3c00097
Chem. Rev. XXXX, XXX, XXX−XXX

and Trions in Cesium−Lead-Halide Perovskite Quantum Dots. *Nano Lett.* **2016**, *16*, 2349−2362.
(565) Park, Y.-S.; Guo, S.; Makarov, N. S.; Klimov, V. I. Room Temperature Single-Photon Emission from Individual Perovskite Quantum Dots. *ACS Nano* **2015**, *9*, 10386−10393.
(566) Yang, Z.; Surrente, A.; Galkowski, K.; Miyata, A.; Portugall, O.; Sutton, R. J.; Haghighirad, A. A.; Snaith, H. J.; Maude, D. K.; Plochocka, P.; et al. Impact of the Halide Cage on the Electronic Properties of Fully Inorganic Cesium Lead Halide Perovskites. *ACS Energy Lett.* **2017**, *2*, 1621−1627.
(567) Iaru, C. M.; Geuchies, J. J.; Koenraad, P. M.; Vanmaekelbergh, D.; Silov, A. Yu. Strong Carrier−Phonon Coupling in Lead Halide Perovskite Nanocrystals. *ACS Nano* **2017**, *11*, 11024−11030.
(568) Pashaei Adl, H.; Gorji, S.; Muñoz-Matutano, G.; Sánchez-Alarcón, R. I.; Abargues, R.; Gualdrón-Reyes, A. F.; Mora-Seró, I.; Martínez-Pastor, J. P. Homogeneous and Inhomogeneous Broadening in Single Perovskite Nanocrystals Investigated by Micro-Photoluminescence. *J. Lumin.* **2021**, *240*, 118453.
(569) Utzat, H.; Shulenberger, K. E.; Achorn, O. B.; Nasilowski, M.; Sinclair, T. S.; Bawendi, M. G. Probing Linewidths and Biexciton Quantum Yields of Single Cesium Lead Halide Nanocrystals in Solution. *Nano Lett.* **2017**, *17*, 6838−6846.
(570) Yazdani, N.; Nguyen-Thanh, T.; Yarema, M.; Lin, W. M. M.; Gao, R.; Yarema, O.; Bosak, A.; Wood, V. Measuring the Vibrational Density of States of Nanocrystal-Based Thin Films with Inelastic X-Ray Scattering. *J. Phys. Chem. Lett.* **2018**, *9*, 1561−1567.
(571) Tamarat, P.; Hou, L.; Trebbia, J.-B.; Swarnkar, A.; Biadala, L.; Louyer, Y.; Bodnarchuk, M. I.; Kovalenko, M. V.; Even, J.; Lounis, B. The Dark Exciton Ground State Promotes Photon-Pair Emission in Individual Perovskite Nanocrystals. *Nat. Commun.* **2020**, *11*, 6001.
(572) Tamarat, P.; Bodnarchuk, M. I.; Trebbia, J.-B.; Erni, R.; Kovalenko, M. V.; Even, J.; Lounis, B. The Ground Exciton State of Formamidinium Lead Bromide Perovskite Nanocrystals Is a Singlet Dark State. *Nat. Mater.* **2019**, *18*, 717.
(573) Becker, M. A.; Vaxenburg, R.; Nedelcu, G.; Sercel, P. C.; Shabaev, A.; Mehl, M. J.; Michopoulos, J. G.; Lambrakos, S. G.; Bernstein, N.; Lyons, J. L.; et al. Bright Triplet Excitons in Caesium Lead Halide Perovskites. *Nature* **2018**, *553*, 189−193.
(574) Yin, C.; Chen, L.; Song, N.; Lv, Y.; Hu, F.; Sun, C.; Yu, W. W.; Zhang, C.; Wang, X.; Zhang, Y. Bright-Exciton Fine-Structure Splittings in Single Perovskite Nanocrystals. *Phys. Rev. Lett.* **2017**, *119*, 026401 DOI: 10.1103/PhysRevLett.119.026401.
(575) Nestoklon, M. O.; Goupalov, S. V.; Dzhioev, R. I.; Ken, O. S.; Korenev, V. L.; Kusrayev, Yu. G.; Sapega, V. F.; de Weerd, C.; Gomez, L.; Gregorkiewicz, T.; et al. Optical Orientation and Alignment of Excitons in Ensembles of Inorganic Perovskite Nanocrystals. *Phys. Rev. B* **2018**, *97*, 235304.
(576) Sercel, P. C.; Lyons, J. L.; Bernstein, N.; Efros, A. L. Quasicubic Model for Metal Halide Perovskite Nanocrystals. *J. Chem. Phys.* **2019**, *151*, 234106.
(577) Sercel, P. C.; Lyons, J. L.; Wickramaratne, D.; Vaxenburg, R.; Bernstein, N.; Efros, A. L. Exciton Fine Structure in Perovskite Nanocrystals. *Nano Lett.* **2019**, *19*, 4068−4077.
(578) Han, Y.; Liang, W.; Lin, X.; Li, Y.; Sun, F.; Zhang, F.; Sercel, P. C.; Wu, K. Lattice Distortion Inducing Exciton Splitting and Coherent Quantum Beating in $CsPbI_3$ Perovskite Quantum Dots. *Nat. Mater.* **2022**, *21*, 1282−1289.
(579) Knowles, K. E.; Nelson, H. D.; Kilburn, T. B.; Gamelin, D. R. Singlet−Triplet Splittings in the Luminescent Excited States of Colloidal Cu^+:CdSe, Cu^+:InP, and $CuInS_2$ Nanocrystals: Charge-Transfer Configurations and Self-Trapped Excitons. *J. Am. Chem. Soc.* **2015**, *137*, 13138−13147.
(580) Norris, D. J.; Yao, N.; Charnock, F. T.; Kennedy, T. A. High-Quality Manganese-Doped ZnSe Nanocrystals. *Nano Lett.* **2001**, *1*, 3−7.
(581) Lommens, P.; Smet, P. F.; de Mello Donega, C.; Meijerink, A.; Piraux, L.; Michotte, S.; Mátéfi-Tempfli, S.; Poelman, D.; Hens, Z. Photoluminescence Properties of Co^{2+}-Doped ZnO Nanocrystals. *J. Lumin.* **2006**, *118*, 245−250.
(582) Roh, J. Y. D.; Smith, M. D.; Crane, M. J.; Biner, D.; Milstein, T. J.; Krämer, K. W.; Gamelin, D. R. Yb^{3+} Speciation and Energy-Transfer Dynamics in Quantum-Cutting Yb^{3+}-Doped $CsPbCl_3$ Perovskite Nanocrystals and Single Crystals. *Phys. Rev. Mater.* **2020**, *4*, 105405.
(583) Marin, R.; Jaque, D. Doping Lanthanide Ions in Colloidal Semiconductor Nanocrystals for Brighter Photoluminescence. *Chem. Rev.* **2021**, *121*, 1425−1462.
(584) Knowles, K. E.; Hartstein, K. H.; Kilburn, T. B.; Marchioro, A.; Nelson, H. D.; Whitham, P. J.; Gamelin, D. R. Luminescent Colloidal Semiconductor Nanocrystals Containing Copper: Synthesis, Photophysics, and Applications. *Chem. Rev.* **2016**, *116*, 10820−10851.
(585) Lu, C.-H.; Biesold-McGee, G. V.; Liu, Y.; Kang, Z.; Lin, Z. Doping and Ion Substitution in Colloidal Metal Halide Perovskite Nanocrystals. *Chem. Soc. Rev.* **2020**, *49*, 4953−5007.
(586) Kanemitsu, Y.; Ishizumi, A. Luminescence Properties of Impurity-Doped Semiconductor Nanoparticles. *J. Lumin.* **2006**, *119*, 161−166.
(587) Bol, A. A.; Ferwerda, J.; Bergwerff, J. A.; Meijerink, A. Luminescence of Nanocrystalline ZnS:Cu^{2+}. *J. Lumin.* **2002**, *99*, 325−334.
(588) Suyver, J. F.; Wuister, S. F.; Kelly, J. J.; Meijerink, A. Luminescence of Nanocrystalline ZnSe:Mn^{2+}. *Phys. Chem. Chem. Phys.* **2000**, *2*, 5445−5448.
(589) Bol, A. A.; van Beek, R.; Ferwerda, J.; Meijerink, A. Temperature Dependence of the Luminescence of Nanocrystalline CdS/Mn2+. *J. Phys. Chem. Solids* **2003**, *64*, 247−252.
(590) Bol, A. A.; Meijerink, A. Long-Lived Mn^{2+} Emission in Nanocrystalline ZnS: Mn^{2+}. *Phys. Rev. B* **1998**, *58*, R15997−R16000.
(591) Renero-Lecuna, C.; Martín-Rodríguez, R.; González, J. A.; Rodríguez, F.; Almonacid, G.; Segura, A.; Muñoz-Sanjosé, V.; Gamelin, D. R.; Valiente, R. Photoluminescence in ZnO:Co^{2+} (0.01%−5%) Nanoparticles, Nanowires, Thin Films, and Single Crystals as a Function of Pressure and Temperature: Exploring Electron−Phonon Interactions. *Chem. Mater.* **2014**, *26*, 1100−1107.
(592) Wang, G.; Peng, Q.; Li, Y. Upconversion Luminescence of Monodisperse CaF_2:Yb^{3+}/Er^{3+} Nanocrystals. *J. Am. Chem. Soc.* **2009**, *131*, 14200−14201.
(593) Zhao, Y.; Rabouw, F. T.; Puffelen, T. v.; Walree, C. A. v.; Gamelin, D. R.; de Mello Donega, C.; Meijerink, A. Lanthanide-Doped CaS and SrS Luminescent Nanocrystals: A Single-Source Precursor Approach for Doping. *J. Am. Chem. Soc.* **2014**, *136*, 16533−16543.
(594) Chengelis, D. A.; Yingling, A. M.; Badger, P. D.; Shade, C. M.; Petoud, S. Incorporating Lanthanide Cations with Cadmium Selenide Nanocrystals: A Strategy to Sensitize and Protect Tb(III). *J. Am. Chem. Soc.* **2005**, *127*, 16752−16753.
(595) Dähne, S. Der Ideale Polymethinzustand. *Chimia* **1991**, *45*, 288.
(596) Dähne, S. Color and Constitution: One Hundred Years of Research. *Science* **1978**, *199*, 1163−1167.
(597) Marder, S. R.; Gorman, C. B.; Meyers, F.; Perry, J. W.; Bourhill, G.; Brédas, J.-L.; Pierce, B. M. A Unified Description of Linear and Nonlinear Polarization in Organic Polymethine Dyes. *Science* **1994**, *265*, 632−635.
(598) Meyers, F.; Marder, S. R.; Pierce, B. M.; Brédas, J. L. Tuning of Large Second Hyperpolarizabilities in Organic Conjugated Compounds. *Chem. Phys. Lett.* **1994**, *228*, 171−176.
(599) Tolbert, L. M. Solitons in a Box: The Organic Chemistry of Electrically Conducting Polyenes. *Acc. Chem. Res.* **1992**, *25*, 561−568.
(600) Bouit, P.-A.; Aronica, C.; Toupet, L.; Le Guennic, B.; Andraud, C.; Maury, O. Continuous Symmetry Breaking Induced by Ion Pairing Effect in Heptamethine Cyanine Dyes: Beyond the Cyanine Limit. *J. Am. Chem. Soc.* **2010**, *132*, 4328−4335.
(601) Padilha, L. A.; Webster, S.; Przhonska, O. V.; Hu, H.; Peceli, D.; Ensley, T. R.; Bondar, M. V.; Gerasov, A. O.; Kovtun, Y. P.; Shandura, M. P.; et al. Efficient Two-Photon Absorbing Acceptor-π-Acceptor Polymethine Dyes. *J. Phys. Chem. A* **2010**, *114*, 6493−6501.
(602) Tolbert, L. M.; Zhao, X. Beyond the Cyanine Limit: Peierls Distortion and Symmetry Collapse in a Polymethine Dye. *J. Am. Chem. Soc.* **1997**, *119*, 3253−3258.

https://doi.org/10.1021/acs.chemrev.3c00097
Chem. Rev. XXXX, XXX, XXX−XXX

(603) Dost, T. L.; Gressel, M. T.; Henary, M. Synthesis and Optical Properties of Pentamethine Cyanine Dyes With Carboxylic Acid Moieties. *Anal. Chem. Insights* **2017**, *12*, 1177390117711938.
(604) Hudson, B. S.; Kohler, B. E. A Low-Lying Weak Transition in the Polyene α,ω-Diphenyloctatetraene. *Chem. Phys. Lett.* **1972**, *14*, 299−304.
(605) Schulten, K.; Karplus, M. On the Origin of a Low-Lying Forbidden Transition in Polyenes and Related Molecules. *Chem. Phys. Lett.* **1972**, *14*, 305−309.
(606) Bachilo, S. M.; Spangler, C. W.; Gillbro, T. Excited State Energies and Internal Conversion in Diphenylpolyenes: From Diphenylbutadiene to Diphenyltetradecaheptaene. *Chem. Phys. Lett.* **1998**, *283*, 235−242.
(607) Taniguchi, M.; Du, H.; Lindsey, J. S. PhotochemCAD 3: Diverse Modules for Photophysical Calculations with Multiple Spectral Databases. *Photochem. Photobiol.* **2018**, *94*, 277−289.
(608) Taniguchi, M.; Lindsey, J. S. Database of Absorption and Fluorescence Spectra of > 300 Common Compounds for Use in PhotochemCAD. *Photochem. Photobiol.* **2018**, *94*, 290−327.
(609) PhotochemCAD; https://www.photochemcad.com/.
(610) Wang, S.; Cong, T.; Liang, Q.; Li, Z.; Xu, S. Dual Colorimetric and Fluorescent Chemosensor of Fe^{3+} and Cu^{2+} Based on 2,5-Bis[(4-Carboxylic-Piperidylamino) Thiophenyl]-Croconine. *Tetrahedron* **2015**, *71*, 5478−5483.
(611) Martynov, A. G.; Mack, J.; May, A. K.; Nyokong, T.; Gorbunova, Y. G.; Tsivadze, A. Y. Methodological Survey of Simplified TD-DFT Methods for Fast and Accurate Interpretation of UV−Vis−NIR Spectra of Phthalocyanines. *ACS Omega* **2019**, *4*, 7265−7284.
(612) Kasha, M.; Rawls, H. R.; Ashraf El-Bayoumi, M. Exciton Model in Molecular Spectroscopy. *Pure Appl. Chem.* **1965**, *11*, 371−392.
(613) Hestand, N. J.; Spano, F. C. Expanded Theory of H- and J-Molecular Aggregates: The Effects of Vibronic Coupling and Intermolecular Charge Transfer. *Chem. Rev.* **2018**, *118*, 7069−7163.
(614) Spano, F. C. The Spectral Signatures of Frenkel Polarons in H- and J-Aggregates. *Acc. Chem. Res.* **2010**, *43*, 429−439.
(615) Knapp, E. W. Lineshapes of Molecular Aggregates, Exchange Narrowing and Intersite Correlation. *Chem. Phys.* **1984**, *85*, 73−82.
(616) Barotov, U.; Klein, M. D.; Wang, L.; Bawendi, M. G. Designing Highly Luminescent Molecular Aggregates via Bottom-Up Nanoscale Engineering. *J. Phys. Chem. C* **2022**, *126*, 754−763.
(617) Scarpaci, A.; Nantalaksakul, A.; Hales, J. M.; Matichak, J. D.; Barlow, S.; Rumi, M.; Perry, J. W.; Marder, S. R. Effects of Dendronization on the Linear and Third-Order Nonlinear Optical Properties of Bis(Thiopyrylium) Polymethine Dyes in Solution and the Solid State. *Chem. Mater.* **2012**, *24*, 1606−1618.
(618) Dasari, R. R.; Sartin, M. M.; Cozzuol, M.; Barlow, S.; Perry, J. W.; Marder, S. R. Synthesis and Linear and Nonlinear Absorption Properties of Dendronised Ruthenium(II) Phthalocyanine and Naphthalocyanine. *Chem. Commun.* **2011**, *47*, 4547−4549.
(619) Getmanenko, Y. A.; Allen, T. G.; Kim, H.; Hales, J. M.; Sandhu, B.; Fonari, M. S.; Suponitsky, K. Yu.; Zhang, Y.; Khrustalev, V. N.; Matichak, J. D.; et al. Linear and Third-Order Nonlinear Optical Properties of Chalcogenopyrylium-Terminated Heptamethine Dyes with Rigid, Bulky Substituents. *Adv. Funct. Mater.* **2018**, *28*, 1804073.
(620) Barlow, S.; Brédas, J.-L.; Getmanenko, Y. A.; Gieseking, R. L.; Hales, J. M.; Kim, H.; Marder, S. R.; Perry, J. W.; Risko, C.; Zhang, Y. Polymethine Materials with Solid-State Third-Order Optical Susceptibilities Suitable for All-Optical Signal-Processing Applications. *Mater. Horiz.* **2014**, *1*, 577−581.
(621) Davydenko, I.; Benis, S.; Shiring, S. B.; Simon, J.; Sharma, R.; Allen, T. G.; Chi, S.-H.; Zhang, Q.; Getmanenko, Y. A.; Parker, T. C.; et al. Effects of Meso-M$(PPh_3)_2$Cl (M = Pd, Ni) Substituents on the Linear and Third-Order Nonlinear Optical Properties of Chalcogenopyrylium-Terminated Heptamethines in Solution and Solid States. *J. Mater. Chem. C* **2018**, *6*, 3613−3620.
(622) Davydenko, I.; Barlow, S.; Sharma, R.; Benis, S.; Simon, J.; Allen, T. G.; Cooper, M. W.; Khrustalev, V.; Jucov, E. V.; Castañeda, R.; et al. Facile Incorporation of Pd$(PPh_3)_2$Hal Substituents into Polymethines, Merocyanines, and Perylene Diimides as a Means of Suppressing Intermolecular Interactions. *J. Am. Chem. Soc.* **2016**, *138*, 10112−10115.

https://doi.org/10.1021/acs.chemrev.3c00097
Chem. Rev. XXXX, XXX, XXX−XXX